Durham E-Theses

Through-The-Wall Detection Using Ultra Wide Band Frequency Modulated Interrupted Continuous Wave Signals

FIORANELLI, FRANCESCO

How to cite:

FIORANELLI, FRANCESCO (2013) *Through-The-Wall Detection Using Ultra Wide Band Frequency Modulated Interrupted Continuous Wave Signals*, Durham theses, Durham University. Available at Durham E-Theses Online: http://etheses.dur.ac.uk/9432/

Use policy

Through-The-Wall Detection Using Ultra Wide Band Frequency Modulated Interrupted Continuous Wave Signals

by

Francesco Fioranelli

School of Engineering and Computing Sciences

Durham University

A thesis submitted

for the degree of Doctor of Philosophy

2013

Abstract

Through-The-Wall-Detection (TTWD) techniques can improve the situational awareness of police and soldiers, and support first responders in search and rescue operations. A variety of systems for TTWD based on different waveforms have been developed and presented in the literature, e.g. radar systems based on pulses, noise or pseudo-noise waveforms, and frequency modulated continuous wave (FMCW) or stepped frequency continuous wave (SFCW) waveforms. Ultra wide band signals are normally used as they provide suitable resolution to discriminate different targets.

A common problem for active radar systems for TTWD is the strong backscattered signal from the air-wall interface. This undesired signal can overshadow the reflections from actual targets, especially those with low radar cross section like human beings, and limit the dynamic range at the receiver, which could be saturated and blocked.

Although several techniques have been developed to address this problem, frequency modulated interrupted continuous wave (FMICW) waveforms represent an interesting further approach to wall removal, which can be used as an alternative technique or combined with the existing ones. FMICW waveforms have been used in the past for ionospheric and ocean sensing radar systems, but their application to the wall removal problem in TTWD scenarios is novel.

The validation of the effectiveness of the proposed FMICW waveforms as wall removal technique is therefore the primary objective of this thesis, focusing on comparing simulated and experimental results using normal FMCW waveforms and using the proposed FMICW waveforms.

Initially, numerical simulations of realistic scenarios for TTWD have been run and FMICW waveforms have been successfully tested for different materials and internal structure of the wall separating the radar system and the targets. Then a radar system capable of generating FMICW waveforms has been designed and built to perform a measurement campaign in environments of the School of Engineering and Computing Sciences, Durham University. These tests aimed at the localization of stationary targets and at the detection of people behind walls. FMICW waveforms prove to be effective in removing/mitigating the undesired return caused by antenna cross-talk and wall reflections, thus enhancing the detection of targets.

Declaration

No part of the work described in this thesis has been submitted in support of an application for another degree or qualification to this or any other university or institute of learning.

Statement of Copyright

Acknowledgments

I would like to thank a number of people who helped me throughout the course of my PhD and contributed to make the work presented in this thesis possible. First thanks to my supervisor, Professor Sana Salous, for the opportunity of working in such an interesting project and for the suggestions and challenges to improve this work. Thanks to Dr. Stuart Feeney, who provided invaluable advice and help, especially for the hardware part of this project. Many thanks also to all the members of our "crew" in the Communications Lab, Odiri, Nasour, Adnan, and Xavier, for the constructive discussions about our research projects and certainly for their support and friendship (and also for volunteering now and then as targets for my through-wall experiments!). I am also grateful to the staff in the Electronic and Mechanical Workshop for their help and assistance.

Furthermore, I would like to thank Her Majesty's Government Communications Centre (HMGCC), in particular Dr. Howard Cummins, for funding and sponsoring my PhD project.

Last but obviously not least I would like to thank my parents, my family, and my older and newer friends for their precious support throughout the (sometimes not so easy) time of my PhD.

To my parents Valter and Giuseppina

"...e costruire è sapere e potere rinunciare alla perfezione..."

List of symbols

B - Bandwidth of the chirp

c - Speed of propagation of EM waves in vacuum

D - Thickness of the wall

f_0 - Start frequency of the chirp

f_B - Beat-note frequency

f_c – Carrier frequency

f_D - Doppler shift

F_n - Receiver noise figure

f_S - Sampling frequency

G_T, G_R – Gains of the transmitting and receiving antennas

k - Boltzmann's constant

K - Number of bits per gating sequence

L – Length of the aperture

L_G - Additional power loss for gating

L_S - System losses

M - Number of samples per chirp

N - Number of processed chirp

P_T - Transmitted power

R - Range to the target

T - Duration of the chirp

T_0 - Standard temperature

T_B - Bit duration for a gating sequence

T_S - Sequence duration for a gating sequence

v - Target speed

ΔA - Cross range resolution

Δf_D - Doppler resolution

ΔR - Down range resolution

ε_r - Dielectric Permittivity

λ - Wavelength

σ - Radar cross section

τ - Round-trip delay

$\tau_{RX1},\ \tau_{RX2}$ – Additional delays for the gating sequence at the receiver

List of acronyms

ADC – Analogue to Digital Converter

AWG – Arbitrary Waveform Generator

BP – Back Projection

CS – Compressive Sensing

CW – Continuous Wave

DARPA – Defense Advanced Research Projects Agency

DDFS – Direct Digital Frequency Synthesizer

DMSI – Delay-Multiply-Sum-Integration

DSI – Delay-Sum-Integration

FA – Factor Analysis

FCC – Federal Communications Commission

FDTD – Finite Difference in Time Domain

FEM – Finite Element Method

FFT – Fast Fourier Transform

FIR – Finite Impulse Response

FIT – Finite Integration Technique

FMCW – Frequency Modulated Continuous Wave

FMICW – Frequency Modulated Interrupted Continuous Wave

GPR – Ground Penetrating Radar

ICA – Independent Component Analysis

IIR – Infinite Impulse Response

LNA – Low Noise Amplifier

LPF – Low Pass Filter

MIMO – Multiple Input Multiple Output

MLBS – Maximum Length Binary Sequence

MoM – Method of Moment

MRP – Mean Received Power

MRS – Mean Received Signal

PCA – Principal Components Analysis

PLL – Phase Locked Loop

PRBS – Pseudo-Random Binary Sequence

RCS – Radar Cross Section

RF – Radio Frequency

SAR – Synthetic Aperture Radar

SCR – Signal-to-Clutter Ratio

SFCW – Stepped Frequency Continuous Wave

SVD – Singular Value Decomposition

TLM – Transmission Line Matrix

TTWD – Through-The-Wall Detection

UWB – Ultra Wide Band

VNA – Vector Network Analyzer

YIG – Yttrium Iron Garnet

Table of Contents

List of figures and tables

1.1 Introduction

Through-The-Wall-Detection (TTWD) techniques aim at providing information on areas which cannot be seen through conventional methods or directly accessed. Since the late nineties these techniques have been attracting the interest of defence and army departments, law enforcement agencies, and first responders. TTWD sensors can improve the situational awareness of police and soldiers in an urban warfare context, for instance in case of people taken as hostages or before breaking in a room occupied by hostile agents. They can also support first responders in search and rescue operations, for instance in case of people trapped inside burning buildings or buried under rubble after an earthquake. Finally TTWD sensors can be used in civilian applications, for instance to locate metal shells or gas/water pipes while refurbishing buildings.

Traditional radar applications pre-existed TTWD techniques by several decades, since the first military radar systems for air defence date back to the thirties [1]. These systems operate in a free space environment, assuming that atmospheric distortions do not affect significantly the detection performance of the radar. These distortions can also be corrected during the processing of the data. Non-free space applications are more similar to TTWD techniques, and indeed they historically derive from geological research in Ground Penetrating Radar (GPR), in order to locate natural resources deposits (minerals, oil, and gas) by analyzing the discontinuities encountered by waves propagating through the earth [2]. Ultrasound tomography for medical imaging is another example of non-free space application to be compared with TTWD techniques, although each has its own peculiar issues. In geophysical and medical imaging systems the propagation medium (the ground and the patient's body respectively) is discontinuous but dense, i.e. it fills all the volume under test. In TTWD applications there are at least two air-wall material interfaces which have a non negligible impact on the spreading waveforms, but most of the volume is free space, air. In geophysical and medical imaging systems sensors are placed directly on the medium (ground or body respectively) to improve the propagation into the volume under test. In TTWD applications sensors normally operate at a stand-off distance from the wall, since in many operational scenarios it may be not possible or risky placing them in direct contact with the wall.

A first survey of available technologies and existing devices for TTWD was carried out in 1998 by Ferris and Currie for a joint project of the American National Institute of Justice and the Defense Advanced Research Project Agency (DARPA) [3]. Three technologies were identified as potentially appropriate for practical TTWD systems: Radio Frequency (RF), X-ray, and acoustic. However only systems based on RF were reported in their survey because they could provide at the same time suitable through wall penetration and resolution for good imaging performance. Drawbacks of using X-ray systems were highlighted as well, in particular potential safety risks because of the ionizing radiation and the limitation to very short ranges.

A more recent survey can be found in [4], where the researches on TTWD conducted by the US Army since 2002 are summarized. Microwave based radar systems proved to be the most mature technologies among those investigated and a far better option compared with Terahertz, acoustic, or X-ray. After choosing the RF microwave technology other specifications must be taken into account to design a TTWD system, for instance:

- *Frequency*. In TTWD a compromise should be achieved between better through wall penetration at lower frequency and better imaging resolution at higher frequency. TTWD systems should also operate in the field together with other electronic devices, so the operational frequency should be chosen to avoid interference.

- *Resolution*. This is related to the ability to discriminate between two close objects. In TTWD down-range resolution is proportional to the bandwidth, so Ultra Wide Band (UWB) signals are normally used to achieve very fine resolution. Generating UWB signals with the required features is generally not an issue with the current technology, but limitations in the use of some portions of the electromagnetic spectrum may come from the regulatory agencies and from the interference with other systems in the field. Cross-range resolution is proportional to the aperture of the system: larger apertures lead to finer resolution, but may require larger antennas or longer arrays of sensors. This may not comply with the size and weight constraints of some TTWD systems.

- *Range and Dynamic Range*. This refers to the maximum distance of a detectable target from the TTWD radar system, and the ability to record weak signals when strong signals are present. The strongest signal for TTWD systems is normally caused by wall reflections.

- *Power Usage*. This takes into account how much power the TTWD system needs, and consequently its life time when operated from portable batteries in the field.

- *Weight and Size*. If handheld, the TTWD system should be carried and deployed easily, without interfering with other tasks of the operator. Bulkier devices can be developed if mounted on vehicles.

- *Reading Time*. The time for the TTWD system to provide operators with a useful piece of information, possibly in a few seconds for a practical system in the field.

TTWD systems can be classified by the level of information they provide [2, 4]. The simplest systems are so-called 0-D, which detect the presence of motion in the area under surveillance, but without providing information about the location or the number of targets. The design of these systems can be extremely easy, with just a single antenna (monostatic radar) and a Continuous Wave (CW) waveform. 1-D TTWD systems provide range measurement to the targets, but not an angle. Therefore the precise location of the targets cannot be obtained, but range information may be enough to discriminate between close and far targets, and possibly gate out reflections from ranges which are considered not interesting. The design complexity increases just slightly compared with previous 0-D systems: monostatic radar can still be used, but modulated or pulsed waveforms are needed to get range estimation. 2-D TTWD systems provide planar images of the area under surveillance in Cartesian or Polar coordinates through a graphical interface. This allows the user to determine how many possible targets are present in the area and where they are, improving greatly the situational awareness of the operators. At least 2 (bistatic radar) or more (multistatic radar) receiving sensors are needed for 2-D systems. These sensors can be arranged in a 1-D array belonging to a single system or physically distributed in several cooperating systems. Another possibility is moving a single sensor to different positions and coherently combining the data, the so-called Synthetic Aperture Radar (SAR) approach. Finally 3-D TTWD

systems provide a volumetric image, adding the dimension of height to 2-D systems. 3-D systems need a bi-dimensional array of sensors.

TTWD has been defined as a "multifaceted technology" since it requires integrated knowledge across several fields of engineering, in particular antennas and array design, signal processing, radar theory, and imaging algorithms [5]. A deep understanding of the propagation of electromagnetic waves and their interaction with materials is also very important, especially the propagation effects through air/wall interfaces and through composite wall structures, like air gaps or internal metallic parts, on the wavefront. Given the heterogeneity of disciplines involved in TTWD and the different level of information sought, many different systems have been proposed in the literature and validated.

1.2 Contributions

Wall reflections are a common problem of TTWD being significantly stronger than the desired backscattered signal from people or objects behind the wall. The required dynamic range for correct detection may therefore be too wide and not easily achievable, and the strong reflected signal may compromise the performance of the receiver.

This thesis proposes a novel wall removal technique based on Frequency Modulated Interrupted Continuous Wave (FMICW) waveforms to address the near-far problem posed by wall reflections, and investigates its effectiveness. A comprehensive review of existing wall removal techniques applied in different TTWD systems is provided, highlighting advantages and disadvantages in comparison with the proposed technique. A mathematical model of FMICW waveforms is presented, focusing on the parameters of interest for through-the-wall radar applications and their adaptation to different wall materials and structures. The proposed technique is successfully validated through results from numerical simulations in CST Microwave Studio and TTWD experiments performed in different realistic scenarios at the School of Engineering and Computing Sciences, Durham University.

1.3 Organisation of the thesis

Chapter 2 reviews systems for TTWD proposed in the literature and using different ultra wide band waveforms. Wall removal techniques are also discussed and compared with the proposed approach based on FMICW waveforms.

Chapter 3 describes the well-established theory of Frequency Modulated Continuous Wave (FMCW) radar systems and analyzes the proposed FMICW waveforms. The main parameters of the waveform and their impact on the radar performance are also discussed.

Chapter 4 presents numerical simulations of different scenarios for TTWD. Comparisons of results using FMCW and FMICW waveforms are shown to demonstrate the effectiveness of the proposed technique. This chapter describes also the imaging algorithms used to produce radar images from the data.

Chapter 5 describes the radar system built for the experimental validation of the proposed FMICW waveforms; a block diagram of the whole system is provided and the synchronization of all the components is discussed. The value of FMCW-FMICW parameters used for the experimental campaign are also discussed.

Chapter 6 presents experimental results to validate the effectiveness of the proposed FMICW technique. Experiments are performed in indoor environments with different kinds of walls, aiming at the detection of stationary targets behind walls and at the detection of people through their movement or breathing.

Chapter 7 includes the conclusions and suggests possible improvements which arise from the work performed to date.

The **Appendix** includes the programs written to control and synchronize the components of the radar system.

1.4 References

[1]   M. Skolnik, *Radar Handbook, Third Edition*: McGraw-Hill Education, 2008.

[2]   E. J. Baranoski, "Through-wall imaging: historical perspective and future directions," *Journal of the Franklin Institute,* vol. 345, pp. 556-569, 2008.

[3]   J. D. D. Ferris and N. C. Currie, "Survey of current technologies for through-the-wall surveillance (TWS)," pp. 62-72, 1999.

[4]   M. Farwell*, et al.*, "Sense through the wall system development and design considerations," *Journal of the Franklin Institute,* vol. 345, pp. 570-591, 2008.

[5]   M. G. Amin, *Through-the-Wall Radar Imaging*: CRC PressINC, 2010.

2.1 UWB Waveforms for Through-The-Wall Detection Systems

In this section different UWB waveforms for TTWD systems are presented. UWB signals are defined by the US Federal Communications Commission (FCC) as those with fractional bandwidth (the ratio of the 3 dB bandwidth to the centre frequency) greater than 25%, or with actual bandwidth greater than 500 MHz [1-2]. UWB waveforms have been used successfully in TTWD radar systems for several years, mainly because the wide bandwidth provides a fine down-range resolution and thus improves the detection of the targets [3].

Impulse radar systems transmit pulse trains with duration of a single pulse T_p and pulse repetition frequency equal to $1/T_t$, where T_t is the separation between pulses. The duration of a single pulse is the reciprocal of the bandwidth of the signal and it is proportional to the range resolution of the radar system; the shorter the duration T_p, the wider the bandwidth and the finer the time delay or range resolution. Normally single bipolar pulses defined as the derivative of a Gaussian pulse are used in TTWD systems [1]. One of the challenges when using this waveform is the possibility of producing a pulse short enough to achieve the desired bandwidth, i.e. with suitable fast rise and fall times. The transmitter antenna should be carefully designed to avoid ringing effects or distortion on the pulse shape. Another challenge arises if the received pulses are sampled in real time at the analogue-to-digital converter (ADC), since the ADC should work at very high frequency to digitize correctly the waveforms, generally around several GHz. The so-called sequential sampling simplifies the ADC, either reducing its working frequency by sampling only a few or even one sample per pulse, or reducing the bit resolution required to sample each pulse. The drawback of these two approaches is that more pulses are required to obtain a radar range profile, so the measurement time is longer. The system dynamic range is also reduced when this non-optimal sampling is used [2].

Frequency modulated radar systems transmit continuous waves (CW) whose frequency is swept in a certain time interval between a start and a stop frequency, either in steps through a set of intermediate frequencies (Stepped Frequency Continuous Wave, SFCW) or linearly (Frequency Modulated Continuous Wave, FMCW). The bandwidth of the waveform is given by the difference between the stop and start frequency, and the

wider the bandwidth the finer the range resolution of the system. As described in detail in chapter 3, information on the distance of the targets is related to frequency components extracted at the receiver through heterodyne detection; the frequency of these components depends on the duration and bandwidth of the transmitted waveform. Frequency modulated waveforms are easier to generate compared with impulses. Stepped Frequency Continuous Wave signals can be generated by a Direct Digital Frequency Synthesizer (DDFS) or by a step oscillator and Phase-Locked-Loop (PLL), Frequency Modulated Continuous Wave signals can be generated by swept oscillators, for instance Yttrium Iron Garnet (YIG), or arbitrary waveform generators (AWG). A more detailed description of FMCW waveforms and their radar performance is given in chapter 3 of this thesis.

Noise radars transmit noise-like waveforms and correlate the received signal with a delayed copy of the transmitted signal. A strong correlation peak is expected when this delay is equal to the round-trip delay of the received signal (the time for the signal to reach a target and be reflected back to the receiver). These waveforms have uniform power spectral density between a lower and a higher frequency, so their bandwidth can be defined as the difference of these two frequencies [1]. The relation between bandwidth and down-range resolution is the same as for frequency modulated waveforms. In TTWD applications, noise waveforms have the advantage of low probability of detection and intercept since they appear like noise.

Waveforms based on M-sequences (maximum length binary sequences, MLBS) are pseudo-random noise signals and they can be used in TTWD radar systems. They are normally generated by a linear feedback shift register controlled by a stable clock. The system maximum operational frequency is half the value of this clock. Since a pseudo-random signal is periodic, sequential sampling can be applied to reduce the sampling frequency of the ADC, as seen before for impulse radars. The sampling clock can easily derive from the clock to the shift register after suitable division.

Normally it is possible to satisfy conventional requirements of TTWD, like spatial and Doppler resolution or operational range, with systems using one of the aforementioned waveforms, even if the overall performance may differ. A comparison in terms of system dynamic range for the same requirements (bandwidth, centre frequency,

operational range, and integration time for recording one radar profile) when using different waveforms is given in [2]. Impulse and noise waveforms have high dynamic range if the received signal is sampled at the ADC in real time, whereas there is a reduction in dynamic range if sequential sampling techniques are used to simplify the ADC. These techniques imply that several transmitted pulses are necessary to create a single range profile and that the receiver is not optimally matched to the transmitted signal, hence the dynamic range is reduced. FMCW and SFCW can have comparable good performance if the system offers good quality of the frequency sweep (for instance a very short setup time between the frequency steps of the SFCW waveform, which a good DDFS can normally achieve). An assessment of the requirements of radar systems aimed at detecting people through the wall is provided in [4-5]. These requirements are expressed in terms of maximum operational range, desired resolution in both down-range and cross-range directions, Doppler resolution, and maximum losses due to the two-way wall penetration to be taken into account. In figure 2.1 the physical meaning of down-range and cross-range directions is explained with reference to a typical through-wall detection scenario with a radar system outside a room. The cross-range direction is parallel to the wall separating the area with possible targets and the radar system, whereas the down-range direction is perpendicular to the wall.
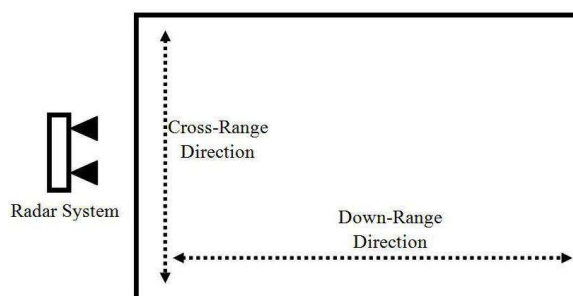
Figure 2.1 Sketch of a through-wall detection scenario to highlight down-range and cross-range directions

In [4] an estimation of the total through-wall propagation loss as a function of the frequency and of the different wall materials (wood, bricks, and concrete) is provided; the radar cross section (RCS) of a human being from experimental results was taken into account in this estimation. Total losses increase with frequency as expected, and they vary between about 100 and 130 dB for an operational range of 10 m. The analysis in [4] shows that all the aforementioned UWB waveforms can meet the requirements,

but the systems differ in terms of dynamic range and speed to provide a reading. In [5] similar conclusions are presented, but the FMCW system appears to offer the best compromise in terms of speed and dynamic range compared with the other systems.

However advantages and disadvantages of different UWB waveforms for TTWD are always dependent also on operational requirements of the final system, like weight and size, power consumption, complexity and off the shelf availability of the hardware, and therefore its cost. In force spectral regulations can also play a role in choosing the operational frequency and bandwidth, with effects on the achievable resolution and through-wall penetration, as well as on the design of the antennas.

As previously mentioned in chapter 1, FMCW waveforms are used in this work, aiming at exploring the possibility of gating them to solve the near-far problem of wall reflections. FMCW waveforms to which a gating sequence has been applied are the so-called Interrupted FMCW, or FMICW. FMCW and FMICW waveforms can be generated by an AWG, which has the advantage of changing flexibly the parameters of the waveform and of the gating sequence. A more detailed description of both waveforms and their radar performance is given in chapter 3 of this thesis.

2.2 Review of TTWD Systems

Effective TTWD systems in the literature based on the waveforms previously described are summarized in the following section, focusing on what these radar systems are able to detect and on possible wall removal techniques.

2.2.1 Impulse radar systems

A TTWD radar system based on impulse waveforms has been developed at the Department of Electrical Engineering and Computing Science of the University of Tennessee. A first study to characterize the propagation losses through different wall materials and the fidelity in the transmission and reception of pulses suitable for TTWD is presented in [6]. Good fidelity in using a pulse waveform centred at 10 GHz and with 600 MHz of bandwidth is shown, as well as reduced through-wall losses for most

materials at that frequency. In [7] the first experimental results in the hallway of an office building are demonstrated, placing a 5 cm plywood panel between the radar and the area under test. The detection of static metallic targets is achieved, as well as the tracking of a moving person carrying a gas tank. This radar system is based on a customized pulse generator with duration 0.6-2 ns, an array of antennas optimized for the frequency range around 10 GHz, and an FPGA for real-time control and acquisition of the signals. In [8] the authors present another pulse radar system integrated with RF instruments to perform some tasks, for instance a sampling oscilloscope to digitize the signals. This system is experimentally tested to detect static metallic targets behind a 1.25 cm drywall panel at the frequency range 8-12 GHz, but it can be reconfigured to work at lower frequencies to penetrate thicker walls just by changing the antennas and a few transceiver components. In [9] the system presented in [6-7] is improved including a near field beam-forming algorithm to take into account refraction and losses within the walls. Experimental validation is provided with static metallic targets (a plate and a pipe) behind 8 cm brick wall and with tracking of a person moving behind 4 cm drywall. Some components of this system including the antennas can operate across a wide range of frequencies (2-10 GHz), but some of them (local oscillator, mixer, and band pass filters) need to be changed depending on the selected operational bandwidth. A detailed description of the hardware components involved in this radar system is given in [10], and a first example of time-frequency analysis for detection of breathing is also shown. The latest developments of the pulse radar system of this research group are given in [11-12]. In [11] localization of people through their breathing is presented, even in case of two people at the same distance from the radar. In [12] hardware improvements of the system compared with the old version in [10] are discussed, in particular a new design achieving more compact size and reduced jitter in the clock to the ADC, as well as better performing components (for instance ADC with more resolution bits). Experimental validation of the improved system is provided through detection of static metallic targets behind cement wall, and micro-Doppler signature of a person walking due to the swinging of the limbs.

In [13] results from the UWB pulse radar system developed at the UWB Radar Imaging Lab of Institute of Electronics, Chinese Academy of Sciences are presented. The radar operates in the frequency range 0.5-3 GHz and has multiple input multiple output

(MIMO) capability, in particular two transmitters and four receivers. The successful tracking of a person moving behind a 24 cm solid concrete wall is demonstrated. The movement is a "stop-go" walking, i.e. the person stops and stands still for a while and then starts walking again. In [14] the aforementioned pulse radar system is employed successfully in experimental scenarios where a person trapped under rubble should be located through breathing detection.

In [15] the pulse based radar system developed by the US Army Research Laboratory is presented. This radar uses a commercial monocycle impulse generator, with roughly 90% of the transmitted energy concentrated in the 800-2400 MHz frequency range. An array with 16 receiving Vivaldi antennas and 2 transmitting horn antennas is used, with FPGA boards dealing with the synchronization and control of all the components. This system is mounted on a vehicle and is capable of working both in the forward-looking and side-looking directions while the vehicle is moving. This system has been successfully tested in open air scenarios with obstacles (trees, light poles, and high grass) and target (a metallic trihedral). In [16] the same system is used to detect moving targets, in particular a pick-up and a walking man, with the latter detected successfully also behind a cinder block wall. The tracking of these targets is demonstrated via radar images created using the back-projection algorithm. The motion detection is based on the change detection paradigm: the difference between consecutive sets of data is calculated before forming the images so that static clutter is reduced. In these experiments the targets were moving on a trajectory parallel to the radar array, which would make them very hard to detect by a Doppler based approach.

In [17] detection of human beings behind concrete walls using UWB short pulses is presented. The experiment was carried out at La Rochelle University, France. This radar system uses a Gaussian pulse with bandwidth 3.2 GHz and centre frequency 4.7 GHz in a bistatic configuration, with one transmitting and one receiving antenna. The presence of a man behind 15 cm concrete wall was successfully demonstrated.

In [18] results from a pulse based radar system developed at the Radar Imaging Lab, Centre for Advanced Communications of the Villanova University, US, are presented. The focus of this paper is the combination of change detection approach (subtraction of data belonging to consecutive measurements to enhance the detection of moving targets

and to reduce the stationary clutter) with compressive sensing (techniques to reduce the required amount of data while maintaining the same quality of the resulting radar image [1]). This radar system uses a 0.7 ns pulse at the frequency range 1.5-4.5 GHz. The detection of both walking movements and sudden head movements behind 1 cm cement board is successfully demonstrated. In [19] the same impulse waveform is used, but wall reflections are time-gated out, without using the change detection approach. This allows detecting also a stationary target (here a metallic sphere), together with moving targets (here a man walking).

2.2.2 SFCW radar systems

Many results in different aspects of TTWD have been presented in the research at the Radar Imaging Lab, Centre for Advanced Communications of the Villanova University, US, using SFCW waveforms generated by Vector Network Analyzer (VNA). In [20] the successful detection of several static metallic targets (spheres, cylinders, dihedrals, and trihedrals) in an office-like environment is demonstrated through radar images created by a beam-forming algorithm taking into account the effects of the through-wall propagation. Four horn antennas are used to exploit polarization diversity and the bandwidth of the SFCW signal is 2-3 GHz. The wall consists of two panels (1.9 cm plywood and 1.6 cm drywall), and side and back wall of the scene under test are covered with absorbing material to prevent reflections, like in an anechoic chamber. Reflections from the wall and clutter are removed by background subtraction, i.e. subtraction of data from a scenario without targets. In [21] a similar experimental setup investigates the possibility of combining multiple data of the same scene, but taken from different angles/views ("multilocation") to improve the detection. The data are first processed to have a uniform coordinate system, and then combined together accordingly. The SFCW signal covers the bandwidth 0.7-3.1 GHz to penetrate through 14 cm solid concrete wall. A horn antenna is used in monostatic approach and moved across a bidimensional position grid. Static metallic targets and a revolving table with chair are included in the scene. In [22] the same experimental setup (SFCW signal from VNA in the frequency range 2-3 GHz, static metallic targets, and wall made of plywood and gypsum panels) as in [20] is used, but an alternative technique based on Singular

Value Decomposition (SVD) is proposed to mitigate the undesired reflections from the wall. This technique is modified to be used also in case of MIMO radar scenario in [23], and successfully detects two human beings standing in an office-like scene with computer, table, and chair behind 14 cm solid concrete wall. Here the SFCW signal covers the bandwidth 1-3 GHz; three horn antennas are used, one as transmitter and two as receivers. This technique to reduce wall reflections is suitable for detection in stationary scenarios, where change detection or Doppler based techniques relying on the motion of the targets would not work. Any a-priori knowledge of the scene under test, for instance background data without the targets, is not required either. In [24] an alternative technique to deal with the wall reflections problem is presented and applied to an experimental scenario using SFCW waveforms with bandwidth 1-3 GHz, monostatic approach with a horn antenna, a metallic dihedral as target, and three different kinds of wall: plywood and plaster panels, 14 cm solid concrete, and 30 cm hollow cinder blocks. The technique is the so-called "spatial filtering" and relies on having similar wall reflections at all the antenna positions of the receiving array. In [25] the wall removal techniques mentioned in [22, 24], namely subspace projection and spatial filtering, are applied jointly with compressive sensing, proving that they can still work if applied on a reduced amount of data. Experimental validation is given using SFCW signals with 1-3 GHz bandwidth and detection of a metallic dihedral behind 14 cm solid concrete wall. In [26] change detection and MIMO processing are combined and results of detection of walking persons from a SFCW based system are presented. The signal bandwidth is here 1.5-2.5 GHz, three horn antennas are used (one receiver and two transmitters), and the wall is 14 cm solid concrete. Two possible change detection approaches are tested: the former is the pixel by pixel subtraction of complex amplitude data, equivalent to the time domain subtraction of two profiles by a delay line, the latter is the subtraction of pixel intensity values followed by a zero-threshold operation.

A flat-panel antenna array has been developed at the Department of Electrical and Computer Engineering of the Ohio State University and used for TTWD applications in conjunction with VNA generating SFCW signals [27]. This array is particularly suitable for TTWD systems being relatively small and light, and a *Labview* graphical interface simply controls the overall system, including the switches for the antenna array and the

VNA generating the signal. Results when detecting static metallic trihedrals behind 20 cm cinder block wall are presented; the bandwidth of the SFCW signal is 0.9-2.3 GHz. The imaging algorithm is back-projection based and assumes free-space propagation for simplicity. As the authors suggest, this algorithm may be improved including refocusing beam-forming taking into account the effects of the through-wall propagation, and adaptive CLEAN algorithm to reduce the reflection from the wall [28]. Experimental results of this approach are provided in a scenario where metallic static targets (a sphere and a trihedral) are detected behind 19 cm cinder block wall. The waveform was again SFCW with bandwidth 0.5-2 GHz and generated by a VNA. The effectiveness of the imaging algorithm proposed in [28] relies on having accurate parameters of the wall, which is generally not possible in realistic scenarios. In [29] the SFCW radar system presented in [27] is used to test an improved imaging algorithm based on Lagrange multipliers. The reflections from the wall are simply removed by subtraction of data from an empty scenario.

A SFCW radar system has been developed for TTWD applications at the National University of Defence Technology, China [30]. Unlike the aforementioned systems in this subsection, for which a VNA is used, the SFCW signal is generated in this system by a synthesizer, which is combined with the transceiver in a compact module. An array of 15 Archimedean spirals antennas is used at the receiver, whereas 2 similar antennas are used at the transmitters. Results of tracking a person walking behind 30 cm concrete wall are provided using SFCW signals with bandwidth 1-2 GHz. Change detection approach, i.e. subtracting time domain data of two consecutive frames is applied to reduce the reflections from the front wall and enhance the target motion detection. In [31] the same radar system is used to detect human motion (walking and swinging of limbs) behind 30 cm cinder block wall. The change detection approach is applied here directly on the image domain, and the phase difference is exploited to discard residual stationary clutter and improve motion detection.

TTWD experiments using SFCW signals have been carried out at the Indian Institute of Technology to test wall reflections and statistical clutter reduction techniques [32-33]. The SFCW signal is generated by VNA in the 3.95-5.85 GHz bandwidth; a horn antenna is moved along a synthetic array in monostatic configuration to produce data

for radar images. Targets are plates of metal and Teflon placed at the same distance from the radar; 1.2 cm plywood wall is used in [32], whereas a more challenging 28 cm brick wall in [33]. A more detailed description of the wall removal techniques proposed in these papers is given in section 2.3 of this chapter.

The Norwegian Defence Research Establishment has developed an interesting radar system based on SFCW waveforms for GPR operations, in particular aiming at the ExoMars space mission on the surface of Mars, carried out by the European Space Agency [34-35]. The SFCW signal with bandwidth 0.5-3 GHz is generated by DDFS and all the components (antennas excluded) are integrated in a very compact board; a detailed hardware block diagram is given in [34]. This system is interesting to compare with the work of this project as it introduces the possibility of gating the SFCW signal through switches at the transmitter and at the receiver, in order to reduce the cross-talk between the antennas and the strong reflection from the air-ground interface, thus increasing the system dynamic range. More details are given in section 2.4 of this thesis and in chapter 3 which describes extensively the FMICW waveforms used in our work.

2.2.3 FMCW radar systems

TTWD experiments using FMCW waveforms have been carried out at the Radar and Electromagnetism Department, ONERA, France [36-40]. Common aspects of the referenced papers are the use of a YIG oscillator to generate FMCW signals with high linearity, and the presence of a fixed filter at intermediate frequency to remove the contribution of the cross-talk and of the wall reflections, assuming they are located at fixed frequencies. Change detection based on subtraction of images from different time steps is applied to track the motion of targets. Different walls are used (rubble stone in [38], plasterboard in [39], and cinder block wall in [40]), but the bandwidth of the FMCW signal is the same (1-4 GHz) since it provides a good compromise in terms of down-range resolution and penetration through most wall materials. An array of receiving antennas is used to produce radar images via real-time beam-forming algorithm in the most recent papers [39-40].

A FMCW based radar system for TTWD applications has been developed and improved over the past years at the Michigan State University and later at the MIT Lincoln Laboratory, US. In [41] a first setup is presented to work in the 7.5-12.5 GHz frequency range and to detect metallic targets (a model of an aircraft and some pushpins) in free space. The main hardware features are already implemented in this first prototype, namely the use of a YIG oscillator to generate the FMCW waveform, and the use of a high-Q band pass filter at intermediate frequency (7.5 kHz pass band centred at 10.7 MHz) to remove the undesired signals from antenna cross-talk and wall reflections. This filter reduces also the noise bandwidth of the receiver, thus increasing its sensitivity. This system consisted of one transmitting and one receiving antenna in a bistatic approach, and SAR multiple measurements were needed to create an image. In [42] the same system was used in the frequency range 1.926-4.069 GHz which is more suitable for penetration through dielectric slabs. Examples of experimental images with metallic carriage bolts and cylinder through 10 cm solid concrete wall were provided. In [43-44] the system is improved with a MIMO array consisting of 13 transmitting and 8 receiving linear tapered slot antennas. The array is used in sequential bistatic mode, activating one transmitter and one receiver at a time, through fast switches controlled by a *Labview* interface. This reduces the time to get a radar image from roughly 20 minutes for the previous SAR approach to roughly 2 seconds. Examples of detection of static metallic targets in free space are provided in [43], and through 10 cm concrete wall in [44]. A further improvement of this FMCW based radar system is given in [45]. The antennas are designed as hybrid of linear tapered slot and Vivaldi, and above all the processing for the SAR imaging algorithm is improved, so that the system produces an image every 0.1 s rather than 2 s as in the previous references. Three experimental scenarios behind 10 cm concrete wall are successfully tested: a man rotating a metallic rod, a small metallic sphere rolling close to another which stays stationary, and a man walking. Besides the range gating due to the band pass filter mentioned in reference [41], coherent change detection based on subtraction of consecutive data frame is applied to improve motion detection. In [46] results from other experimental scenarios are presented: a man walking, a man standing/sitting while breathing or holding his breath, and a human moving close to a strong metallic object. Different walls are used, namely 10 cm concrete, 20 cm concrete, and cinder blocks wall.

At the National University of Science and Technology, Kaohsiung, Taiwan, experiments for TTWD have been carried out using narrowband FMCW waveforms. A prototype using a narrowband FMCW signal (2.4-2.484 GHz) in the ISM band is presented in [47]. A person standing still behind 1.5 cm wood panel could be detected through his breathing; coherent change detection is applied by subtracting data frames measured in different time periods in order to enhance the detection of the breathing motion. In [48] the system is improved: the capability of measuring the azimuth of possible targets through CW waveforms and two receiving antennas is added to the range capability of FMCW waveforms already showed in [47]. Experimental results are presented for two subjects sitting behind 3 cm wood panel, who are successfully detected through background subtraction of FMCW spectra: the differences in these spectra due to the breathing are indeed easily detected. The bandwidth of the FMCW signal is 2.4-2.7 GHz, therefore this is not an UWB signal according to the standard definition.

2.2.4 Noise and pseudo-random noise radar systems

A system for TTWD based on pure noise continuous waveforms has been developed at the Pennsylvania State University [49]. This system is based on a thermal noise source located in the frequency range 350-750 MHz, and the components are integrated in compact FPGA hardware, able to perform real-time range operations and store measurements in SAR approach to produce bidimensional radar images. A person moving behind 14 cm cinder block wall in an empty and in an office-like room is successfully detected by this system. In [50] older experiments using a similar noise based system are presented, in particular for through foliage and through wall detection of static metallic targets. In [51] a more recent version of the system is presented. Hardware for range detection based on UWB noise waveforms in the frequency range 400-720 MHz is combined with components for Doppler detection based on single CW tone at 750 MHz, resulting in a compact system. Log-periodic antennas are used in bistatic configuration with one receiver and one transmitter; SAR approach is applicable to create bidimensional radar images. Several experimental results are presented: radar range profiles of a metallic plate behind 19 cm solid concrete wall, radar range profile

of a man inside a shed with thin (a few mm) plastic and wood wall but at a long stand-off distance (3-11 m), radar images of one or two human standing behind 15 cm wall, and micro Doppler signature of several human movements (moving arms, shifting position, and breathing) through empirical mode decomposition and Hilbert transform analysis. Background subtraction with an empty scenario is applied for detection of stationary targets; coherent change detection with subtraction of correlation signals referring to consecutive data frames is applied for motion detection. Time gating is mentioned as a feasible way to gate out the undesired signals due to the antenna cross-talk and reflections from the wall.

TTWD systems based on UWB Maximum Length Binary Sequences, therefore pseudo-random noise waveforms, have been developed and successfully tested at the University of Ilmenau, Germany over the past years. A first description of the theory and suitable block diagram is presented in [52], with a prototype board generating a 511 points M-sequence with roughly 400 MHz bandwidth. In [53] hardware improvements increase the frequency of the clock to the shift register up to 10 GHz, allowing M-sequence bandwidth up to 5 GHz. Examples of GPR applications are provided. In [54] TTWD applications are presented to track the walking movement of a person behind 20 cm brick wall and locate his position in an office like environment, assuming static scenario (nothing else is moving). The system is clocked at 9 GHz, with actual bandwidth 0.7-4.5 GHz. Trilateration approach is used with one transmitting and two receiving antennas, the easiest configuration to provide azimuth localization of targets. Coherent background subtraction is applied, after estimation through an adaptive exponential method of the background response to be subtracted from the data. The detection of a person sitting behind 40 cm brick wall through breathing using a similar M-sequence based radar is showed in [55]. In [56] other experimental results can be found: motion tracking for a person walking, breathing detection for a person buried under rubble, and reconstructions of room interiors. Spiral antennas in the aforementioned trilateration configuration are used in this paper, with operational bandwidth 2.5 GHz. In [57] recent results regarding remote detection of vital signs for people trapped under rubble are presented. The system here is clocked at 4.5 GHz, and the operational bandwidth is 0.1-2 GHz allowing good through rubble penetration. Methods to remove the clutter and enhance the desired breathing signal are mentioned: stationary clutter can be removed

by high pass filtering in the observation time domain, assuming that breathing frequency is higher than 0.2 Hz, whereas non-stationary clutter needs to be separated through algorithmic methods (for instance sub-space decomposition methods like SVD, or exploiting the fact that the clutter frequency is generally lower than the breathing). The importance of reducing antenna cross-talk to prevent saturation of the receiver is mentioned.

2.2.5 Passive radar systems

In [58] a different and alternative approach for TTWD of moving people using a passive radar is presented from the researches at University College London, UK. Whereas the systems described so far involve through-wall transmission of waveforms towards the area under test, this passive radar collects and exploits the 2.4 GHz signals transmitted from a WiFi access point already inside the area under test. Doppler shifts are expected in these signals because of the motion of targets and they can be extracted through suitable processing. Experimental Delay-Doppler results are showed for a person moving inside a storage building behind 30 cm composite wall, consisting of an external layer of bricks and an internal layer of concrete, separated by 10 cm air gap. Static clutter and the strong direct signal from the transmitter of opportunity, in this case the access point inside the storage building, are removed through an implementation of the CLEAN algorithm which is adapted to the system presented in [58]. As its name suggests, CLEAN is a procedure which searches and removes the brightest contribution in a scene of interest, thus "cleaning" the final image from all the undesired contributions through several iterations of the algorithm. It should be noted that for passive radar systems there is no exterior wall reflection problem, which on the contrary needs always to be addressed for active systems to avoid masking of actual targets and receiver saturation. However the strong direct signal from the transmitter may saturate the receiver even in passive systems, and post-processing algorithms as the CLEAN proposed in [58] cannot address this problem.

2.3 Review of Wall Removal Techniques

Any TTWD active radar system has to confront with the problem of reflections from the exterior wall, which complicate the detection of possible targets placed behind this wall. Depending on wall parameters like thickness, dielectric constant, conductivity, and internal structure, the presence of the air/wall interface scatters back most of the transmitted signal and drastically reduces the amount of power available to sense the area under test. Therefore at the receiver wall reflections appear far stronger than the backscattered signal from actual targets, especially from targets with low RCS as human beings, which are masked and difficult to detect (the so-called "near-far problem"). Walls with air gaps or hollow structures are especially challenging, since they tend to trap the electromagnetic waves as if in resonant cavities, making the duration of the wall reflection signals far longer than the physical thickness, thus overshadowing targets close to the interior wall [24, 40].

Increasing simply the transmitted power to detect these hidden targets may be beneficial in impulse based systems, but it is not a viable solution for SFCW or FMCW systems where transmitter and receiver are always active. In case of monostatic scenarios it is hard to maintain the required isolation between the transmitter and the receiver circuitry through circulators or similar hardware. In case of bistatic or multistatic scenarios there is strong signal leakage from transmitters to receivers because of the cross-talk between the antennas. In all these cases a strong undesired signal is present at the receiver, thus heavily limiting the dynamic range of the TTWD system and increasing the possibility of saturating and blocking the receiver [42].

Being considered as clutter, wall reflections decrease also the signal-to-clutter ratio (SCR) of radar images of the area under test. It has been observed that this prevents the application of compressive sensing (CS) techniques, which aim at producing radar images of same quality and resolution using far fewer data, allowing faster measurements [1, 19].

Because of these reasons different wall mitigation or removal techniques have been developed and applied to TTWD systems. In the rest of this section a summary of these techniques is given, followed by a description of the wall removal approach proposed in this thesis.

2.3.1 Subspace projection methods

These wall removal techniques structure the received signals from different receivers in a matrix, the so-called B-scan; the receivers can be physically different or a single receiver is moved to different positions in SAR approach. Suitable decomposition methods are then applied to this matrix aiming at separating the clutter (cross-talk signal and wall reflections included), target, and noise subspaces, and at removing or at least mitigating the first. After removal of the clutter subspace radar images are produced from the data. The advantage of these techniques is that they do not require any a-priori knowledge of the wall parameters or structure, nor they try to estimate them. Their drawback is that, being applied only on measured data, they do not address the problem of reduced system dynamic range because of cross-talk or wall reflections.

An early example of subspace projection approach can be found in [59], where through-wall experiments are performed using SFCW waveforms and a single metallic target behind plywood and brick walls. SVD method is applied to the B-scan matrix to decompose it in the sum of its eigen-components. The authors conclude empirically that the first eigen-component is the wall reflection subspace, the second is the target reflection subspace, and the remaining components are the noise subspace. They therefore extract only the second eigen-component to make radar images. In [32] the same authors present three other decomposition methods alternative to SVD: factor analysis (FA), principal component analysis (PCA), and Independent Component Analysis (ICA). All these four methods decompose the B-scan matrix of measured data and aim at extracting only the contribution due to target reflections to create radar images. The performance of these four methods is compared using experimental data from a SFCW based radar system. Two targets, one made of metal and one made of Teflon, are placed behind a plywood wall at the same down-range distance, so that the dielectric target is more difficult to detect because of the high reflections from the metal target. ICA outperforms the other three methods detecting correctly both targets. Compared with the other methods, ICA exploits stronger statistical properties to separate clutter and target subspaces, but it is more complicated to implement. In [33] further performance comparisons of the aforementioned methods are presented using experimental data from a scenario with brick wall. The authors draw similar

conclusions, with ICA outperforming the other methods when both metallic and dielectric targets are present in the scene under test.

In [60] ICA is applied by a different research group on experimental data from a SFCW based through-wall system; two metallic targets behind wood wall and concrete wall are used. Both targets are correctly detected for both types of wall applying ICA approach.

In [22] a substantial correction to the SVD method proposed in [32-33] is presented. The authors prove that the target subspace is not simply and only the second eigen-component of the B-scan, but it spans across several eigen-components, depending on the number of targets in the scene under test and on their location. So the target subspace is extracted as a weighted and smoothed combination of eigen-components, rather than simply a single eigen-component. The effectiveness of this new approach is demonstrated through experimental data with multiple metallic targets behind wood and gypsum wall. In [23] this approach is extended to the case of MIMO radar systems. Additional processing to extract the target subspace is required because the wall subspace spans across more eigen-components than in monostatic scenarios. This is caused by the MIMO approach, where wall reflections are no longer similar for each antenna position, but depend on the transmitting/receiving antenna pairs.

So far these subspace projection methods have been discussed to remove wall reflections for detection of static targets, but they may be used also in other applications when two different signals need to be separated relying on their uncorrelation properties. For instance in [57] singular value decomposition is mentioned as a way to separate breathing signature from non-stationary clutter in the context of detection of people buried under rubble.

Although developed for a different context, namely breast cancer detection through UWB signals, it is worth also mentioning the method proposed in [61]. The aim is reducing the strong backscattered signal from the air/skin interface, far stronger than the reflections from tumours inside the breast. The approach is not dissimilar to the methods discussed in this subsection, since it aims at separating the contributions of desired (tumours) and undesired (skin) signals. Each received signal is decomposed in a

frequency domain model as a sum of components, and the required parameters for this model are extracted from the data. The components related to the skin are expected to be far stronger than those related to the targets, so they can be isolated through a suitable threshold and removed before creating the image.

2.3.2 Spatial filtering method

This method is introduced in [24] and successfully tested on experimental data from a static target (metallic dihedral) behind three different types of walls (solid, multilayered, and cinder blocks). It is particularly effective for detection of stationary targets, when methods based on change detection (change caused by the motion of targets in the area under test) or on Doppler effect are not applicable. The method has the advantage of not needing a-priori knowledge of the wall parameters and structure, and it is effective when the reflections from the wall and from the targets are overlapped in the time domain because the targets are close to the interior wall. This overlapping would make unsuitable methods based on discriminating and gating out in the time domain the undesired wall reflections.

The method assumes monostatic approach with a series of measurements along an array parallel to the wall, and relies on the similarity of the wall reflections for all the antenna positions, whereas echoes from the targets change for each antenna position along the array. This assumption is realistic for many TTWD systems, since the wall normally has a spatial extent larger than the array of measuring positions, whereas targets like human beings occupy a limited space, just a portion along the array. The proposed method models the received signal, which contains both reflections from walls and targets, as a function of the antenna position index along the array, and then applies a spatial frequency transform. Wall and targets reflections can be separated in this new spatial frequency domain: the former have zero or very low component, since they do not change along the array, the latter have higher spatial frequency because of the changes along the array. Once the targets and wall spatial frequency bandwidth are identified, a filter can be designed and applied to remove or at least mitigate wall reflections. However this estimation and the consequent filter design is not trivial. The wall spatial frequency bandwidth can extend longer because of instabilities in the antenna positions,

antenna patterns, or local non-homogeneous areas inside the wall. The target spatial frequency bandwidth depends on the target down-range and on the extent of its signal return along the array, so it may overlap the wall spatial frequency bandwidth and therefore be altered by filtering. Since this method is applied before beam-forming and creation of images, the filter should be designed to minimize smearing and distortions on the targets reflections. The authors propose a parametric notch IIR filter, which can be flexibly adjusted to the environment. They compare its performance with a moving average background subtraction method, which can be modelled as a FIR filter; this consists in subtracting from each received signal the average of the previous received signals. The proposed notch filter outperforms the moving average filter for inhomogeneous walls, giving results closer to those ideally obtained by subtraction of the empty scenario.

The authors suggest an analogy between their filtering approach in the spatial frequency domain for detection of static targets and the filtering in the Doppler frequency domain for detection of moving targets in cluttered environments, where clutter is the stationary or slow moving background. The easiest filter is the subtraction between two consecutive received signals, but more refined high-pass filters can be used to improve flexibility. An attempt using the easy approach of subtraction between signals received at neighbouring antennas is performed in [24] with ideal data from a simulated point scatterer, but it is discarded because of the distortion introduced on the target spatial frequency spectrum.

In [25] the authors show that the aforementioned wall removal method, as well as the subspace projection method described in the previous subsection, can work together with compressive sensing. Normally it is assumed that wall removal methods are applied on full set of data before compressive sensing, whereas this paper using experimental data prove that these methods are effective even when operating on a reduced set of data.

2.3.3 Background subtraction methods

If data from the area under test without potential targets (the so-called empty scenario) are available, they can be simply subtracted from the actual measured data to remove wall reflections before applying beam-forming algorithms; this is effective for detection of stationary targets. Unfortunately this approach is not realistic for most of the real-time, in-field applications of TTWD systems, but empty scenario data may be available for long time surveillance operations of an area. This easy approach can be applied for simplicity purposes when the focus is really not wall removal techniques: for instance to perform experiments aimed at testing beam-forming algorithms [29] and TTWD systems at early stage of development [20], to simplify the detection of stationary targets with low RCS for demonstration purposes [51], and to extract human breathing parameters through suitable signal processing techniques (for instance using Hilbert-Huang transform in [62]).

An alternative approach for wall removal which does not require access to background data is proposed in [63], where a model of the target image in TTWD SAR approach is developed and a refocusing method is applied to compensate for wall effects. This method assumes that wall reflectivity and transmissivity matrices are known, which is rather unlikely in realistic scenarios, but a procedure to estimate these parameters is suggested. Wall reflections can be gated out from the backscattered time domain signal, and the required parameters can be estimated from them after conversion into the frequency domain. The wall reflection signal can be computed analytically according to a suitable model, and then subtracted from the actual measured data to enhance the SCR of the final refocused images; it should be noted that only the wall contribution is cancelled, whereas stationary targets are preserved in the resulting images. Experimental validation using a SFCW radar system is given; a metallic trihedral behind 9.2 cm concrete wall is used as target. This method is effective, but it is subject to errors in the estimation of wall parameters and response.

2.3.4 Change detection methods

Change detection can be considered a special case of background subtraction when the aim is motion detection, either of large scale movements given by people walking and swinging limbs, or small scale movements given by breathing [26]. This approach assumes that wall reflections and stationary clutter do not change over the measurement time, whereas the contribution of moving targets does. Therefore a simple subtraction of data referring to different measurement instants can remove undesired signals. This subtraction can be performed either in the image domain after the application of beam-forming algorithms (non-coherent subtraction), or in the raw data domain (coherent subtraction).

Non-coherent change detection is applied for instance in [31], followed by a further step exploiting the image phase differences to improve detection. Coherent and non-coherent change detection are also applied and compared in [64]. The authors suggest that non-coherent change detection produces better final images, with less artefacts, but further studies are required to confirm this conclusion. A zero-threshold operation is applied after non-coherent processing to remove possible pixels with negative values which would appear as artefacts.

Coherent change detection can be applied to data from TTWD radar systems using different waveforms. For instance in [16] the method is used on data from a pulse based system, subtracting the time domain received signals at different measurement times; in [48] on data from a FMCW based radar system, subtracting the spectra of the intermediate frequency signal, which contains information on the target's range; in [65] on simulated data from a noise waveform based radar system, subtracting the cross-correlation between transmitted and received signals.

In [18] coherent change detection is applied before compressive sensing on data from a pulse based system. The authors propose two different models for detection of sudden movements of head, limbs, or torso, and for detection of a translational motion like walking. In the former case data from two consecutive frames are subtracted, whereas in the latter data belonging to frames which are separated by a relatively long time delay. In [26] further results from the same authors are presented when change detection approach is combined with MIMO radar. Coherent (before beam-forming) and non-

coherent (after beam-forming) change detection are applied to the same experimental data and the performance of both methods is compared. Coherent approach seems to perform better for change detection applied to consecutive frames, whereas both approaches are equivalent for change detection applied to non consecutive frames.

In the previous examples change detection was implemented simply subtracting data from two frames, but more refined estimations of the stationary background to be subtracted have been suggested in the literature. In [11] the average of a set of previous received signals is subtracted from each signal, instead of only the previous signal. In [13] an improved estimation of the average static background is presented to take into account the possibility that the target stops and stays for a while. If the target does not move, its signature would not appear in the simple difference of two consecutive frames and it would be treated as clutter. In [54] a similar approach with weights and thresholds in the average formula is presented. The focus of this work is avoiding that the area where a movement is detected contributes to the background estimation; this benefits the detection of movements along the azimuth direction or small movements like breathing.

2.3.5 Polarization based methods

Numerical simulations show that wall and target reflections can be distinguished by their polarization. Reflections from the wall are mostly co-polarized with the transmitted signal, whereas reflections from human beings excite cross-polarization components, or more generally different polarizations, due to the body's irregular shape [1, 66]. Very promising simulated results have been presented, but practical exploitation of cross-polarized components is very challenging. Cross-polarized components are far weaker than co-polarized: in the simulations the cross-polarized signature for a standing human being is 20-30 dB (depending on the wall) weaker than the co-polarized case [1]. In realistic TTWD systems cross-polarized components may be buried in the noise and therefore not detectable. Another issue is the generation/reception of pure polarizations through the antennas, which is challenging for typical wide-beam antennas like horn, especially at the low frequencies required for through-wall penetration [1]. At the

current stage of technology, polarization based techniques are still more investigated through numerical simulations than in realistic experiments.

2.3.6 Hardware filtering method

Apart from polarization based approaches, all the wall removal methods described so far are applied after the digitization and recording of the received signals, wall reflections and clutter included. Even if these methods remove the undesired contributions, the recording of backscattered signals from low RCS targets when also wall reflections are present can be challenging because of the required system dynamic range. The risk is that the signals from the targets are buried in the noise floor of the system, and therefore cannot be correctly extracted even after the application of wall removal techniques.

A possible solution to this problem for FMCW based radar systems is presented in details in [41-42] and also quickly mentioned in [40]; the former refers to the system built at the Michigan State University and then MIT Lincoln Laboratory, US, the latter to the system developed by ONERA, France. FMCW radar systems are described in details in chapter 3 of this thesis, but for the sake of brevity it should be noted that the information on the range to the targets is converted into frequency tones of a signal usually called "beat note": the farther the target, the higher the frequency of the beat note. Since the air/wall interface is closer to the radar compared with any other possible targets, the beat note frequency related to its reflection is the lowest; there may also be a beat note caused by the antenna cross-talk in bistatic/multistatic scenarios, but its frequency is still low, since the distance between the antennas is shorter than the distances to the targets. These undesired beat note frequencies can be filtered out with a suitable band pass filter, provided that its stop/pass band transition is steep enough to remove the contributions from cross-talk and wall, without distorting the contributions of the targets.

The beat note frequencies at which wall and target contributions appear in FMCW systems depend not only on their distance from the radar, but also on the duration and bandwidth of the FMCW signal itself. If the radar system is meant for fixed surveillance

applications where the stand-off distance radar-wall does not change, then an optimum filter can be designed because the beat note frequency of the wall reflections is known and fixed, provided that the duration and bandwidth of the FMCW signal do not change as well. If the radar system is movable or the duration and bandwidth of the FMCW signal change, then some degrees of flexibility are required. One option could be a variable filter that can be tuned, or a set of different filters which can be switched in and out. A more interesting solution is proposed in [42], where an oscillator can slightly shift the bandwidth of the transmitted FMCW signal, and consequently the beat note frequencies related to undesired and desired reflections. In this way the filter is fixed, while the beat note frequencies are accordingly adjusted to place contributions of the targets in the pass band and wall reflections in the stop band. The filter proposed in [42] is a 4 pole crystal, operating at intermediate frequency: centre frequency 10.7 MHz and a 7.5 kHz 3 dB bandwidth.

It should be noted that the authors still apply change detection techniques as described in sub-section 2.3.4 on the data collected with these systems; this improves the detection of moving targets, removing any residual static clutter or wall reflections. For instance in [40] non-coherent image subtraction is applied, whereas in [45] coherent change detection is used.

2.3.7 Gating methods

When short pulses are used as transmitted waveforms, time gating can be a suitable technique to remove early reflections from the wall [19, 67]. Basically pulses reflected by the air/wall interface arrive at the receiver before those reflected by the targets, which are farther away from the radar. If pulses are short enough in terms of time duration, the early signal related to the wall can be simply gated out before applying beam-forming or other additional processing on the remaining data. It should be noted that the dispersion effect given by some kinds of wall, especially those with lots of internal cavities and layers, may distort and broaden the received pulses, compromising the effectiveness of this technique.

In the aforementioned approach the strong reflection from the wall is still acquired and digitized at the receiver, and this gives problem in terms of required system dynamic range, as already discussed in this section. Assuming that the reflection from the wall and the reflection from the targets are sufficiently separated in time, a solution to this problem could be switching on the receiver just slightly after the time when the wall reflection comes back and slightly before the target reflection. In case of pulse based systems different backscattered pulses should be easy to separate in the time domain, whereas for FMCW or SFCW systems, where the transmitter and the receiver are always active, this is not an easy task.

In the following section the proposed wall removal technique based on gated FMCW waveforms is quickly described to compare with other existing techniques; a more detailed analysis follows in chapter 3.

2.4 Proposed Wall Removal Technique: FMICW

As mentioned in the previous section, this thesis presents a technique to mitigate/remove cross-talk signal and wall reflections for TTWD based on gating FMCW waveforms (gated FMCW or interrupted FMCW).

Intuitively the idea is switching on the receiver only after the transmission of the waveform (to avoid signal leakage from the transmitter) and after the reception of the wall backscattered reflection (which comes before reflections from the targets since the air/wall interface is closer to the radar). For FMCW radar systems, which normally work with the transmitter and the receiver always active, suitable on-off patterns have to be provided to ensure that transmission and reception are not simultaneous. These on-off patterns can be modelled through complementary gating sequences multiplied by the transmitted and received waveforms, in order to get a range-dependent sensitivity of the radar system [68]. These gating sequences can be designed accordingly so that the receiver is active and listening only when the desired backscattered reflections from the targets are present.

The required on-off patterns can be physically implemented with switches at the transmitter and the receiver, with suitable gating sequences to control them. An example

of this approach for a SFCW based system for GPR applications is presented in [34]. A block diagram of the hardware is provided, with a DDFS generating the normal SFCW signal, plus another DDFS to generate the gating sequences to control the switches.

Unlike the aforementioned approach, the radar system proposed in this thesis uses arbitrary waveform generators to generate at the same time FMCW waveforms with the gating sequences applied. Compared with a normal FMCW system, no extra hardware is needed with this approach (no switches and their controlling units as in [34]). Another advantage is the flexibility in changing via software all the parameters of the FMCW waveform (duration and bandwidth of the signal) and of the gating sequences. This permits taking into account changes in the scenario under test in field applications, for instance a change in the stand-off distance, and to react by simply correcting the generated waveform and/or the gating sequences. It should be noted that how quickly these changes can be made depends on the chosen arbitrary waveform generator, on its hardware implementation, and also on its interface with the user.

A more detailed description of the parameters of the gating sequences and a model of their effect on the FMCW signal is given in chapter 3. It is interesting to conclude this section comparing advantages and disadvantages of the proposed wall removal technique with those presented in the previous section.

The ideal background subtraction with "empty scenario data" is not realistic for in field applications since it would require a-priori data on the scenario under test, so it can be immediately discarded. Like our proposed technique, the approach of estimating and subtracting the wall response from the data does not require a-priori knowledge, but it is subject to errors in the estimation and modelling of the response itself. Subspace projection and spatial filtering techniques do not need any a-priori knowledge of the wall and they are not subject to errors in estimating the wall parameters. However, being algorithmic techniques applied on the recorded data, they do not address the problem of insufficient system dynamic range or receiver saturation which may arise because of the strong wall reflections. This drawback is also shared with the estimation and subtraction of the wall response.

Polarization based techniques can be discarded, since their practical application still pose lots of problems as pointed out previously.

Change detection approaches do not address again the problem of the required dynamic range when cross-talk signal and wall reflections are present at the receiver. Furthermore they are not suitable for detection of stationary targets.

Hardware filtering for FMCW systems is an interesting technique and its effectiveness is proved. The approach proposed in this thesis can be an alternative to it which does not require extra hardware, like the filter itself and the additional oscillator to adjust the frequency of the received signals to the fixed filter.

So the application of gated FMCW waveforms can be an interesting alternative to the wall removal techniques so far proposed in the literature. This method does not require any a-priori knowledge of the scene under test or estimation of wall parameters. It can increase the system dynamic range allowing detection of low RCS targets and avoiding receiver saturation. Being implemented through AWG, it allows flexible adaptation of the parameters of the waveforms to the scenario under test. The proposed approach can also be combined with pre-existing techniques to enhance their performance: subspace projections, spatial filtering, and change detection can indeed still be applied on data from gated FMCW systems, to eliminate the residual clutter and enhance the overall performance of the system.

2.5 Summary of the chapter

Different UWB waveforms for TTWD applications have been discussed in this chapter, namely impulses, SFCW, FMCW, noise, and pseudo-noise waveforms. A non-exhaustive review of existing TTWD radar systems has been presented, with focus on the near-far problem caused by the wall reflections and techniques to mitigate/remove them. The wall removal technique proposed in this thesis has been mentioned and its advantages and disadvantages compared with existing techniques have been discussed.

The following two tables summarize the existing TTWD radar systems and the wall removal techniques presented in this chapter.

Ref.	Waveform and Frequency Range [GHz]	Antennas	Targets, Type of Wall, and Wall Removal Technique
[7]	Pulse 7-13	1 horn at the transmitter 16 Vivaldi at the receiver	Detection of static metallic targets and of a person carrying a metallic gas tank behind 5 cm plywood panel.
[8]	Pulse 8-12	As in [7]	Detection of static metallic targets behind 1.25 cm drywall panel.
[9]	Pulse 2-4 or 8-10	2 sub-arrays of 8 Vivaldi elements	Detection of static metallic targets behind 8 cm brick wall and of a person walking behind 4 cm drywall panel.
[11]	Pulse 1.5-4.5	8 sub-arrays, each integrating 8 Vivaldi elements	Detection of multiple people through their breathing. Wall removal by change detection.
[12]	Pulse 1.5-4.5	1 horn at the transmitter 8 Vivaldi at the receiver	Detection of static metallic targets behind cement wall and Doppler signature of a person walking and swinging limbs.
[13]	Pulse 0.5-3	Not specified what type, but 2 elements at the transmitter and 4 at the receiver	Detection of a person moving and standing behind 24 cm concrete wall. Wall removal by change detection.
[15]	Pulse 0.8-2.4	2 horns at the transmitter, 16 Vivaldi at the receiver	Detection of static metallic targets in open-air scenario with some obstacles.
[16]	Pulse 0.3-3 or 0.6-1.5	As in [15]	Detection of moving targets in open air scenario and behind cinder block wall. Wall removal by change detection.

[17]	Pulse 3.1-6.3	Not specified	Detection of the presence of a person behind 15 cm concrete wall.
[18]	Pulse 1.5-4.5	1 horn at the transmitter, 8 Vivaldi at the receiver	Detection of a person walking and of sudden movements of the head behind 1 cm cement board. Wall removal by change detection.
[19]	Pulse 1.5-4.5	As in [18]	Detection of both stationary metallic targets and of a walking person behind 1 cm cement board. Wall removal by time gating.
[20]	SFCW 2-3	4 horns for 4 port VNA	Detection of static metallic targets behind 1.9 cm plywood plus 1.6 cm drywall. Wall removal by background subtraction.
[21]	SFCW 0.7-3.1	1 horn in monostatic approach	Detection of static metallic targets behind 14 cm solid concrete wall.
[22]	SFCW 2-3	1 horn in monostatic approach	Detection of static metallic targets behind 1.9 cm plywood plus 1.6 cm drywall. Wall removal by subspace projection.
[23]	SFCW 1-3	2 horns at the transmitter, 1 horn at the receiver	Detection of two people standing in an office-like scenario behind 14 cm solid concrete wall. Wall removal by subspace projection.
[24]	SFCW 1-3	1 horn in monostatic approach	Detection of static metallic dihedral behind plywood and plaster panels, 14 cm solid concrete, and 30 cm hollow cinder blocks wall. Wall removal by spatial filtering.

[25]	SFCW 1-3	1 horn in monostatic approach	Detection of static metallic dihedral behind 14 cm solid concrete wall. Wall removal by spatial filtering and subspace projection.
[26]	SFCW 1.5-2.5	2 horns at the transmitter, 1 horn at the receiver	Detection of one person and then two people walking behind 14 cm solid concrete wall. Wall removal by change detection.
[27, 29]	SFCW 0.9-2.3	12 printed "flower-shape" elements	Detection of static metallic targets behind 20 cm cinder blocks wall. Wall removal by background subtraction in [29].
[28]	SFCW 0.5-2	1 horn in monostatic approach	Detection of static metallic targets behind 19 cm cinder blocks wall. Wall removal by adaptive CLEAN algorithm.
[30]	SFCW 1-2	2 Archimedean spirals at the transmitter, 15 at the receiver	Detection of a person walking behind 30 cm concrete wall. Wall removal by change detection.
[31]	SFCW 1-2	Archimedean spirals; 2 at the transmitter, 15 at the receiver	Detection of a person walking and swinging limbs behind 30 cm concrete wall. Wall removal by change detection.
[32-33]	SFCW 3.95-5.85	1 horn in monostatic approach	Detection of static metallic and Teflon targets behind 1.2 cm plywood wall [32] and 28 cm brick wall [33]. Wall removal by subspace projection.
[36]	FMCW 2-4	2 exponentially tapered slot	Detection of a person walking behind brick partition. Wall removal by hardware filtering plus change detection or SVD.

[38-40]	FMCW 1-4	1 ridged horn at the transmitter. Array at the receiver, e.g. 8 Vivaldi or 16 exponentially tapered slot	Detection and tracking of a person walking behind rubble stone [38], plasterboard [39], and cinder blocks wall [40]. Wall removal by hardware filtering and change detection.
[42]	FMCW 1.926-4.069	2 linearly tapered slot	Detection of static metallic targets behind 10 cm solid concrete wall (SAR approach). Wall removal by hardware filtering.
[44]	FMCW 1.926-4.069	21 linearly tapered slot (13 at the transmitter and 8 at the receiver)	Detection of static metallic targets behind 10 cm solid concrete wall (physical array). Wall removal by hardware filtering.
[45]	FMCW 2-4	21 Vivaldi and linear slot hybrid antenna elements	Detection of movements (man rotating metallic rod, metallic sphere rolling, and man walking) behind 10 cm solid concrete wall. Wall removal by change detection and hardware filtering.
[46]	FMCW 2-4	As in [45]	Detection of a moving and standing person (either breathing or holding breath) behind 10 cm concrete, 20 cm concrete, and cinder blocks wall. Wall removal by hardware filtering.
[47]	FMCW 2.4-2.484	2 printed elements	Detection of breathing behind 1.5 cm wood panel. Wall removal by change detection.

[48]	FMCW 2.4-2.7	1 horn at the transmitter 2 horns at the receiver	Detection and localization of breathing of two people behind 3 cm wood panels. Wall removal by change detection.
[49]	Noise 0.35-0.75	Not specified	Detection of a person moving behind 14 cm cinder blocks wall in empty and office-like room.
[51]	Noise 0.4-0.72	2 log-periodic	Several results: static metallic targets behind 19 cm solid concrete wall, range profiles of one/two people standing inside a shed, two people standing behind 15 cm wall, and micro-Doppler signature of human movements behind 10 cm concrete wall. Wall removal by background subtraction.
[54]	Pseudo-noise 0.7-4.5	1 horn at the transmitter 2 horns at the receiver	Detection and tracking of a person moving behind 20 cm brick wall in office-like environment. Wall removal by change detection.
[55]	Pseudo-noise 0.7-4.5	Not specified	Detection of breathing behind 40 cm brick wall. Wall removal by background subtraction.
[56]	Pseudo-noise 0.008-2.5	1 spiral at the transmitter 2 spirals at the receiver	Several results: motion tracking for a person walking behind wall, breathing detection for a person under rubble, and reconstruction of room interiors. Wall removal by change detection.

[58]	Passive WiFi 2.4	1 SD24 antenna from *Stella Doradus Ltd* for each passive node	Detection of a person moving inside a storage building behind 30 cm composite wall (bricks, air gap, and concrete).

Table 2.1 Summary of existing TTWD radar systems

Wall Removal Technique	Reference Number
Subspace projection	[22-23, 25, 32-33, 59-60]
Spatial filtering	[24-25]
Background subtraction	[20, 29, 51, 62] – Subtraction of the wall response (with a-priori knowledge) [63] – Estimation and subtraction of the wall response (without a-priori knowledge)
Change detection	[26, 31, 40, 64] – Non-coherent approach [16, 18, 26, 45, 47, 65] – Coherent approach [11, 13, 54] – More refined static background estimation
Polarization based	[66] – Only simulation based
Hardware filtering	[39-46]
Gating	[19, 67]

Table 2.2 Summary of existing wall removal techniques

2.6 References

[1]   M. G. Amin, *Through-the-Wall Radar Imaging*: CRC Press, 2010.

[2]   Hamran, *Radar Performance of Ultra Wideband Waveforms*, 2010.

[3]   M. Farwell*, et al.*, "Sense through the wall system development and design considerations," *Journal of the Franklin Institute,* vol. 345, pp. 570-591, 2008.

[4]   X. Zhuge*, et al.*, "Assessment of electromagnetic requirements for UWB through-wall radar," in *Electromagnetics in Advanced Applications, 2007. ICEAA 2007. International Conference on*, 2007, pp. 923-926.

[5]   A. G. Yarovoy*, et al.*, "Comparison of UWB technologies for human being detection with radar," in *Radar Conference, 2007. EuRAD 2007. European*, 2007, pp. 295-298.

[6]   Y. Yunqiang and A. E. Fathy, "See-through-wall imaging using ultra wideband short-pulse radar system," in *Antennas and Propagation Society International Symposium, 2005 IEEE*, 2005, pp. 334-337 vol. 3B.

[7]   Y. Yunqiang and A. Fathy, "Design and implementation of a low-cost real-time ultra-wide band see-through-wall imaging radar system," in *Microwave Symposium, 2007. IEEE/MTT-S International*, 2007, pp. 1467-1470.

[8]   Y. Yunqiang*, et al.*, "Development and implementation of ultra-wideband see-through-wall imaging system based on sampling oscilloscope," *Antennas and Wireless Propagation Letters, IEEE,* vol. 7, pp. 465-468, 2008.

[9]   W. Yazhou*, et al.*, "A reconfigurable UWB system for real-time through wall imaging applications," in *Radio and Wireless Symposium (RWS), 2010 IEEE*, 2010, pp. 633-636.

[10]   Y. Yunqiang and A. E. Fathy, "Development and implementation of a real-time see-through-wall radar system based on FPGA," *Geoscience and Remote Sensing, IEEE Transactions on,* vol. 47, pp. 1270-1280, 2009.

[11]   Y. Wang, *et al.*, "Simultaneous localization and respiration detection of multiple people using low cost UWB biometric pulse Doppler radar sensor," in *Microwave Symposium Digest (MTT), 2012 IEEE MTT-S International*, 2012, pp. 1-3.

[12]   L. Quanhua, *et al.*, "A compact integrated 100 GS/s sampling module for UWB see through wall radar with fast refresh rate for dynamic real time imaging," in *Radio and Wireless Symposium (RWS), 2012 IEEE*, 2012, pp. 59-62.

[13]   W. Shiyou, *et al.*, "A simple strategy for moving target imaging via an experimental UWB through-wall radar," in *Ground Penetrating Radar (GPR), 2012 14th International Conference on*, 2012, pp. 961-965.

[14]   X. Yanyun, *et al.*, "A novel method for automatic detection of trapped victims by ultrawideband radar," *Geoscience and Remote Sensing, IEEE Transactions on,* vol. 50, pp. 3132-3142, 2012.

[15]   M. Ressler, *et al.*, "The Army Research Laboratory (ARL) synchronous impulse reconstruction (SIRE) forward-looking radar," pp. 656105-656105, 2007.

[16]   K. Ranney, *et al.*, "Recent MTI experiments using ARL's synchronous impulse reconstruction (SIRE) radar," 2008, p. 694708.

[17]   O. Sisma, *et al.*, "UWB radar: vision through a wall," *Telecommunication Systems,* vol. 38, pp. 53-59, 2008/06/01 2008.

[18]   F. Ahmad and M. G. Amin, "Through-the-wall human motion indication using sparsity-driven change detection," *Geoscience and Remote Sensing, IEEE Transactions on,* vol. 51, pp. 881-890, 2013.

[19]   J. Qian, *et al.*, "Joint localization of stationary and moving targets behind walls using sparse scene recovery," *Journal of Electronic Imaging,* vol. 22, pp. 021002-021002, 2013.

[20]   F. Ahmad and M. G. Amin, "Through-the-wall radar imaging experiments," in *Signal Processing Applications for Public Security and Forensics, 2007. SAFE '07. IEEE Workshop on*, 2007, pp. 1-5.

[21]   F. Ahmad and M. G. Amin, "Multi-location wideband synthetic aperture imaging for urban sensing applications," *Journal of the Franklin Institute,* vol. 345, pp. 618-639, 2008.

[22]   F. H. C. Tivive*, et al.*, "An SVD-based approach for mitigating wall reflections in through-the-wall radar imaging," in *Radar Conference (RADAR), 2011 IEEE*, 2011, pp. 519-524.

[23]   F. Ahmad and M. G. Amin, "Wall clutter mitigation for MIMO radar configurations in urban sensing," in *Information Science, Signal Processing and their Applications (ISSPA), 2012 11th International Conference on*, 2012, pp. 1165-1170.

[24]   Y. Yeo-Sun and M. G. Amin, "Spatial filtering for wall-clutter mitigation in through-the-wall radar imaging," *Geoscience and Remote Sensing, IEEE Transactions on,* vol. 47, pp. 3192-3208, 2009.

[25]   E. Lagunas*, et al.*, "Joint wall mitigation and compressive sensing for indoor image reconstruction," *Geoscience and Remote Sensing, IEEE Transactions on,* vol. 51, pp. 891-906, 2013.

[26]   M. G. Amin and F. Ahmad, "Change detection analysis of humans moving behind walls," *IEEE Trans. Aerosp. Electronic Syst,* 2013.

[27]   K. E. Browne*, et al.*, "Through-wall opportunistic sensing system utilizing a low-cost flat-panel array," *Antennas and Propagation, IEEE Transactions on,* vol. 59, pp. 859-868, 2011.

[28]   P. C. Chang*, et al.*, "Adaptive CLEAN with target refocusing for through-wall image improvement," *Antennas and Propagation, IEEE Transactions on,* vol. 58, pp. 155-162, 2010.

[29]   K. E. Browne*, et al.*, "Fast optimization of through-wall radar images via the method of lagrange multipliers," *Antennas and Propagation, IEEE Transactions on,* vol. 61, pp. 320-328, 2013.

[30]   L. Biying*, et al.*, "A SFCW radar for through wall imaging and motion detection," in *Radar Conference (EuRAD), 2011 European*, 2011, pp. 325-328.

[31]   L. Biying*, et al.*, "Detection of human beings in motion behind the wall using SAR interferogram," *Geoscience and Remote Sensing Letters, IEEE,* vol. 9, pp. 968-971, 2012.

[32]   P. K. Verna*, et al.*, "Analysis of clutter reduction techniques for through wall imaging in UWB range," *Progress In Electromagnetics Research B,* vol. 17, pp. 29-48, 2009.

[33]   A. N. Gaikwad*, et al.*, "Application of clutter reduction techniques for detection of metallic and low dielectric target behind the brick wall by stepped frequency continuous wave radar in ultra-wideband range," *Radar, Sonar & Navigation, IET,* vol. 5, pp. 416-425, 2011.

[34]   M. J. Oyan*, et al.*, "Ultrawideband gated step frequency ground-penetrating radar," *Geoscience and Remote Sensing, IEEE Transactions on,* vol. 50, pp. 212-220, 2012.

[35]   S. E. Hamran*, et al.*, "A prototype for the WISDOM GPR on the ExoMars mission," in *Advanced Ground Penetrating Radar, 2007 4th International Workshop on*, 2007, pp. 252-255.

[36]   N. Maaref*, et al.*, "FMCW ultra-wideband radar for through-the- wall detection of human beings," in *Radar Conference - Surveillance for a Safer World, 2009. RADAR. International*, 2009, pp. 1-5.

[37]   N. Maaref*, et al.*, "Ultra-wideband frequency modulated continuous wave synthetic aperture radar for through-the-wall localization," in *Microwave Conference, 2009. EuMC 2009. European*, 2009, pp. 1880-1883.

[38]   N. Maaref*, et al.*, "Ultra wide band radar system for through-the-wall microwave localization and imaging," in *Synthetic Aperture Radar (EUSAR), 2010 8th European Conference on*, 2010, pp. 1-4.

[39]   N. Maaref and P. Millot, "Array-based UWB FMCW through-the-wall radar," in *Antennas and Propagation Society International Symposium (APSURSI), 2012 IEEE*, 2012, pp. 1-2.

[40]   N. Maaref and P. Millot, "Array-based ultrawideband through-wall radar: prediction and assessment of real radar abilities," *International Journal of Antennas and Propagation,* vol. 2013, p. 9, 2013.

[41]   G. Charvat*, et al.*, "A low-power high-sensitivity X-band rail SAR imaging system [Measurement's Corner]," *Antennas and Propagation Magazine, IEEE,* vol. 50, pp. 108-115, 2008.

[42]   G. L. Charvat*, et al.*, "A through-dielectric radar imaging system," *Antennas and Propagation, IEEE Transactions on,* vol. 58, pp. 2594-2603, 2010.

[43]   G. L. Charvat*, et al.*, "An ultrawideband (UWB) switched-antenna-array radar imaging system," in *Phased Array Systems and Technology (ARRAY), 2010 IEEE International Symposium on*, 2010, pp. 543-550.

[44]   G. L. Charvat*, et al.*, "A through-dielectric ultrawideband (UWB) switched-antenna-array radar imaging system," *Antennas and Propagation, IEEE Transactions on,* vol. 60, pp. 5495-5500, 2012.

[45]   T. S. Ralston*, et al.*, "Real-time through-wall imaging using an ultrawideband multiple-input multiple-output (MIMO) phased array radar system," in *Phased Array Systems and Technology (ARRAY), 2010 IEEE International Symposium on*, 2010, pp. 551-558.

[46]   G. L. Charvat*, et al.*, "Detection algorithm implementation and measured results for a real-time, through-wall radar system using a TDM MIMO antenna array," in *Radar Conference (RADAR), 2012 IEEE*, 2012, pp. 0240-0246.

[47]   W. Fu-Kang*, et al.*, "Seeing through walls with a self-injection-locked radar to detect hidden people," in *Microwave Symposium Digest (MTT), 2012 IEEE MTT-S International*, 2012, pp. 1-3.

[48]   W. Fu-Kang*, et al.*, "Detection of concealed individuals based on their vital signs by using a see-through-wall imaging system with a self-injection-locked radar," *Microwave Theory and Techniques, IEEE Transactions on,* vol. 61, pp. 696-704, 2013.

[49]   C. Pin-Heng*, et al.*, "Through wall ranging and imaging using UWB random noise waveform: System design considerations and preliminary experimental results," in *Antennas and Propagation Society International Symposium, 2009. APSURSI '09. IEEE*, 2009, pp. 1-4.

[50]   R. M. Narayanan*, et al.*, "Radar penetration imaging using ultra-wideband (UWB) random noise waveforms," *Radar, Sonar and Navigation, IEE Proceedings -,* vol. 151, pp. 143-148, 2004.

[51]   C. Pin-Heng*, et al.*, "A portable real-time digital noise radar system for through-the-wall imaging," *Geoscience and Remote Sensing, IEEE Transactions on,* vol. 50, pp. 4123-4134, 2012.

[52]   J. Sachs*, et al.*, "A new UWB-principle for sensor-array application," in *Instrumentation and Measurement Technology Conference, 1999. IMTC/99. Proceedings of the 16th IEEE*, 1999, pp. 1390-1395 vol.3.

[53]   J. Sachs, "M-sequence ultra-wideband-radar: state of development and applications," in *Radar Conference, 2003. Proceedings of the International*, 2003, pp. 224-229.

[54]   R. Zetik*, et al.*, "Detection and localization of persons behind obstacles using M-sequence through-the-wall radar," pp. 62010I-62010I, 2006.

[55]   R. Zetik*, et al.*, "UWB short-range radar sensing - The architecture of a baseband, pseudo-noise UWB radar sensor," *Instrumentation & Measurement Magazine, IEEE,* vol. 10, pp. 39-45, 2007.

[56]   J. Sachs*, et al.*, "Detection and tracking of moving or trapped people hidden by obstacles using ultra-wideband pseudo-noise radar," in *Radar Conference, 2008. EuRAD 2008. European*, 2008, pp. 408-411.

[57]   J. Sachs*, et al.*, "Remote vital sign detection for rescue, security, and medical care by ultra-wideband pseudo-noise radar," *Ad Hoc Networks,* 2012.

[58]   K. Chetty*, et al.*, "Through-the-wall sensing of personnel using passive bistatic WiFi radar at standoff distances," *Geoscience and Remote Sensing, IEEE Transactions on,* vol. 50, pp. 1218-1226, 2012.

[59]   R. Chandra and et al., "An approach to remove the clutter and detect the target for ultra-wideband through-wall imaging," *Journal of Geophysics and Engineering,* vol. 5, p. 412, 2008.

[60]   C. R. P. Dionisio*, et al.*, "Experiments on through-wall imaging using ultra wideband radar," *Microwave and Optical Technology Letters,* vol. 54, pp. 339-344, 2012.

[61]   A. Maskooki*, et al.*, "Frequency domain skin artifact removal method for ultra-wideband breast cancer detection," *Progress In Electromagnetics Research* vol. 98, pp. 299-314, 2009.

[62]   L. Lanbo*, et al.*, "Through-wall bio-radiolocation with UWB impulse radar: observation, simulation and signal extraction," *Selected Topics in Applied Earth Observations and Remote Sensing, IEEE Journal of,* vol. 4, pp. 791-798, 2011.

[63]   M. Dehmollaian and K. Sarabandi, "Refocusing through building walls using synthetic aperture radar," *Geoscience and Remote Sensing, IEEE Transactions on,* vol. 46, pp. 1589-1599, 2008.

[64]   A. Martone*, et al.*, "Coherent and non-coherent change detection for through the wall sensing of moving targets," in *Radar Conference (RADAR), 2011 IEEE*, 2011, pp. 256-261.

[65]   W. Hong*, et al.*, "Through-wall imaging of moving targets using UWB random noise radar," *Antennas and Wireless Propagation Letters, IEEE,* vol. 8, pp. 802-805, 2009.

[66]   T. Dogaru and C. Le, "SAR images of rooms and buildings based on FDTD computer models," *Geoscience and Remote Sensing, IEEE Transactions on,* vol. 47, pp. 1388-1401, 2009.

[67]   W. Yazhou and A. E. Fathy, "Advanced system level simulation platform for three-dimensional UWB through-wall imaging SAR using time-domain approach," *Geoscience and Remote Sensing, IEEE Transactions on,* vol. 50, pp. 1986-2000, 2012.

[68]   S. Salous, *Radio Propagation Measurement and Channel Modelling*: Wiley, 2013.

3.1 FMCW Signals for Radar Applications

In this section FMCW signals, also known as chirps, are analyzed mathematically and their performance for radar applications is discussed. FMCW signals are suitable waveforms for pulse compression techniques, which allow to avoid the high peak power limitation of pulse based radar systems by continuous transmission of waveforms [1]. High peak power or longer pulse durations are desirable to increase the maximum range detectable by pulse based radars, but higher power would complicate the transmitter architecture and interfere with other existing systems, whereas longer pulses would reduce the system resolution. Pulse compression techniques overcome these problems by spreading power across different frequencies as a function of time.

Besides the use of simpler transmitters (solid-state transmitters for instance), another advantage of pulse compression techniques is the reduction of the produced interference with other systems and the increased rejection of narrowband interference. Interference may still worsen the overall radar performance by increasing the noise floor, or by causing a near-far problem, where the receiver is blocked by the interference and unable to detect weaker desired signals [1-2]. As previously mentioned, an example of this problem is the presence of wall reflections in TTWD, which is addressed in this thesis.

Besides FMCW, pulse compression can be implemented also using codes to modulate the carrier. Several codes have been proposed in the literature for this purpose, namely Barker, PRBS (Pseudo-Random Binary Sequences), Gold, Kasami, and loosely synchronous [1]. A disadvantage of this approach, especially for PRBS codes, is that the spectrum of the transmitted signal is not limited within the desired bandwidth, but a portion of it spreads to out-of-band regions. This may require further spectrum shaping to reduce these out-of-band components, for instance a band-pass filter at the carrier frequency, or a low-pass structure before the modulator. On the contrary FMCW does not require additional spectrum shaping for practical radar applications.

Advantages of FMCW signals over impulses for TTWD systems have been mentioned in some of the research works reviewed in chapter 2 of this thesis. In [3] the authors present their FMCW radar and then analyze how more complicated it would be to get similar performance using a pulse based system. A much faster digitizer would be needed, as well as more expensive and complex hardware at the transmitter to generate

the required peak power. In addition to this, in [4] other authors mention the difficulty in generating jitter-free impulses at the transmitter as a drawback of pulse based systems, and the advantage of adapting the chirp duration to the Doppler shifts produced by different targets and different motion in case of FMCW systems. Besides being easier to generate, if compared with impulses FMCW signals do not require special antenna design, for instance loading to prevent ringing [5].

FMCW signals or chirps consist of a linear sweep from a start to a stop frequency within a time interval. Although non-linear frequency sweeps are possible [6], only linear sweeps are analyzed here because they are used in this thesis. Mathematically a chirp in a time interval T is given by:

$$v(t) = A cos[\Phi(t)] = A cos\left(2\pi f_c t \pm \pi \frac{B}{T} t^2\right), \quad -\frac{T}{2} \leq t \leq \frac{T}{2} \tag{3.1}$$

where A is a constant denoting the amplitude, f_c is the carrier frequency, B is the bandwidth swept by the chirp, and T the sweep duration. Figures 3.1 and 3.2 show the time domain representation of a chirp signal with bandwidth 1 MHz and duration 20 μs: the former shows how the frequency is changing linearly with time, the latter is an amplitude-time representation. It can be seen that the frequency sweeps in a time T from a start value to a stop value denoting the bandwidth B.
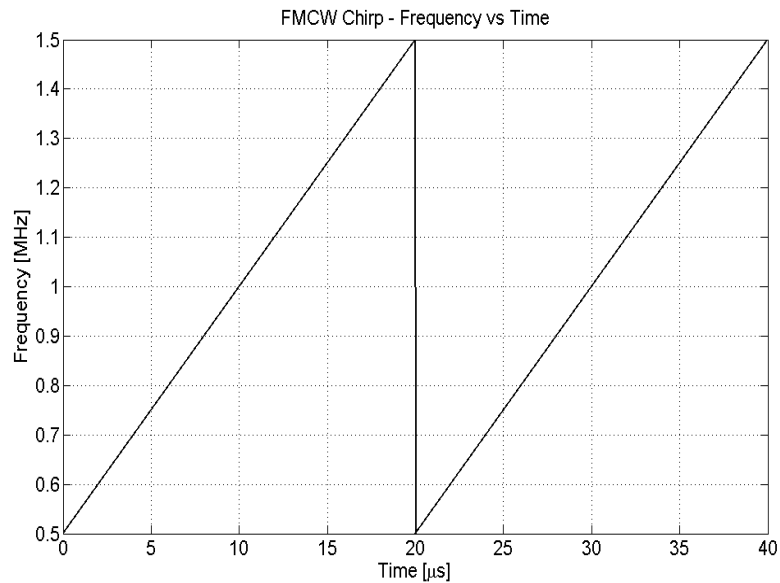
Figure 3.1 Frequency-Time relation of a linear FMCW Chirp
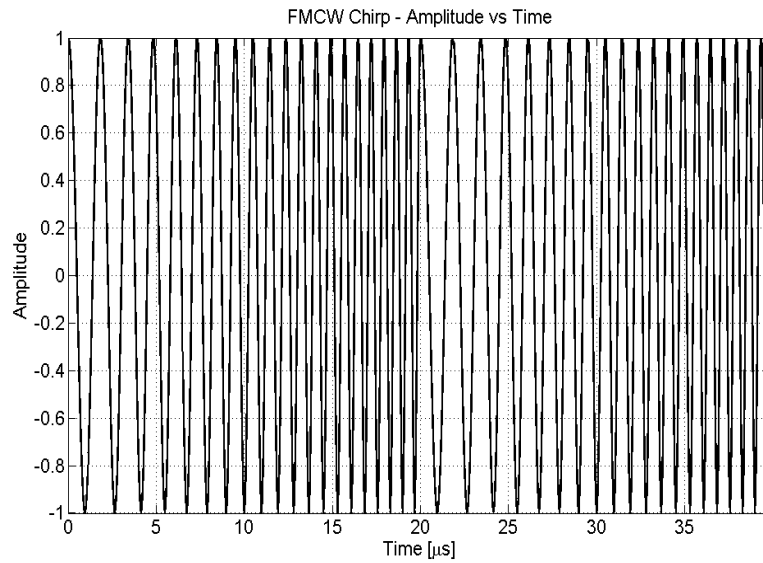
Figure 3.2 Time domain waveform of a linear FMCW Chirp

The analytical expression of the spectrum is given in [1]. It should be noted that the amount of energy not contained within the bandwidth B depends on the time-bandwidth product BT: for instance 5% if BT=10 and roughly 1-2% if BT=100. For practical UWB radar applications, the product BT is much higher and therefore the totality of the energy is considered to be located within B. The practical absence of out-of-band energy for FMCW systems eliminates the need for spectrum shaping before transmission, in contrast to PRBS based systems. In figure 3.3 the spectrum of a chirp signal with time-bandwidth product equal to 200 is presented.
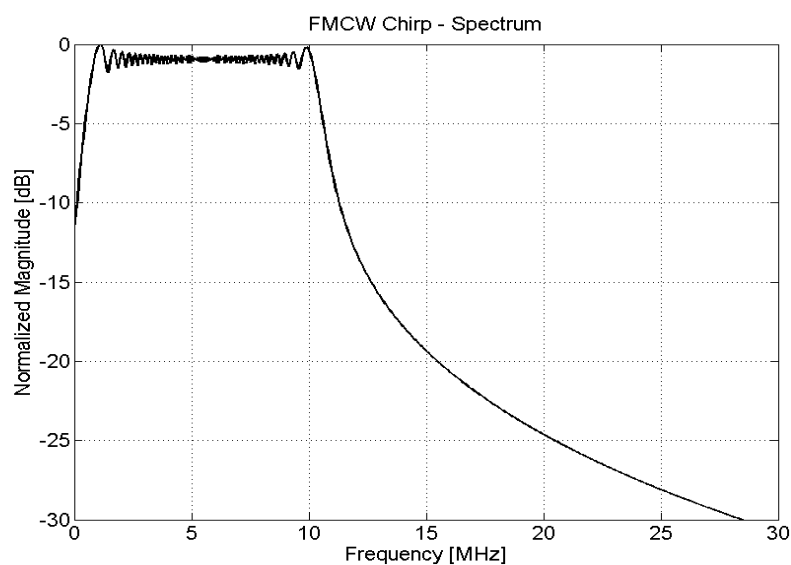
Figure 3.3 Spectrum of a linear FMCW Chirp

FMCW signals can be compressed either through matched filter or heterodyne detection. Matched filter approach uses a filter with transfer function which is equal to the mirror image of the transmitted signal, and delayed accordingly to ensure causality. This approach compresses the signal in time but not in frequency, and thus the digitization of the output would require fast ADC, compromising one of the advantages of FMCW over impulse based systems. In this thesis heterodyne detection is used instead of the matched filter, and this approach is described in detail in subsection 3.1.1.

It is however interesting to look at the magnitude of the output of a matched filter detector [1]:

$$y(t) = \sqrt{BT}\frac{\sin{(\pi Bt)}}{\pi Bt} \tag{3.2}$$

Equation (3.2) shows that the peak magnitude of the signal is 10 log(BT), and this quantity is normally called compression gain of the radar. Furthermore the envelope of this signal is a so-called sin *x/x* function, which presents side-lobes in the time domain; for large values of the time-bandwidth product, the peak side-lobe level is roughly -13 dB and the 3dB width is 0.886/B [6]. In case of multiple targets side-lobes from highly reflective targets can mask low RCS targets, so their level has to be reduced. One approach is the transmission of a non-linear chirp, where the frequency modulation is designed to shape the spectrum and produce the required low level for the time domain side-lobes [6]. The other common approach is weighting the transmitted or the received signal, either in time or in frequency domain, by a suitable window; however this reduces the actual resolution of the system because of the broadening of the main lobe. Different windows introduce different trade-offs between the side-lobe level and the main-lobe width expansion [1, 7].

3.1.1 Heterodyne detection for FMCW signals

Heterodyne detection for FMCW signals consists of multiplying the received chirp by a replica of the transmitted chirp, followed by low-pass filtering to remove high frequency components. The frequency of the resulting signal, normally called beat-note, is related to the time delay of the targets, i.e. multiple targets at different distances from

the radar produce different frequencies in the beat-note signal. Unlike the matched filter approach, heterodyne detection compresses the signal in the frequency domain, so that slower (and therefore simpler and cheaper) ADC can be used at the receiver. The frequency of the beat note for usual radar applications is indeed in the range of tens of kHz or a few MHz, which are easy to digitize.

The mathematical analysis of the heterodyne detection follows [1, 8], assuming that the transmitted signal is the chirp in the following equation:

$$v_T(t) = A_T cos[\Phi(t)] = A_T cos\left(2\pi f_0 t + \pi \frac{B}{T}t^2\right), \quad -\frac{T}{2} \le t \le \frac{T}{2} \tag{3.3}$$

where f_0 is the start frequency of the sweep. Considering for simplicity the presence of a single stationary target, the received signal is a delayed copy of the transmitted signal:

$$v_R(t) = A_R cos[\Phi(t - \tau)] = A_R cos\left(2\pi f_0(t - \tau) + \pi \frac{B}{T}(t - \tau)^2\right) \tag{3.4}$$

where A_R is the amplitude of the received signal, depending on the RCS of the target. The multiplication of transmitted and received signals is performed at the receiver through a mixer. Therefore the output of the mixer consists of the multiplication of two cosine functions as in (3.5), which can be rewritten using trigonometric identities as in equation (3.6):

$$v_M(t) = A_T A_R cos\left(2\pi f_0 t + \pi \frac{B}{T}t^2\right) cos\left(2\pi f_0(t - \tau) + \pi \frac{B}{T}(t - \tau)^2\right) \tag{3.5}$$

$$v_M(t) = \frac{A}{2} cos\left(\omega_0 t + \pi \frac{B}{T}t^2 - \omega_0(t - \tau) - \pi \frac{B}{T}t^2(t - \tau)^2\right)$$
$$+ \frac{A}{2} cos\left(\omega_0 t + \pi \frac{B}{T}t^2 + \omega_0(t - \tau) + \pi \frac{B}{T}t^2(t - \tau)^2\right) \tag{3.6}$$

where $\omega_0 = 2\pi f_0$ and $A = A_T A_R$. The second term in equation (3.6) has frequency of about twice f_0, so it is removed by the low-pass filter placed after the mixer. The remaining signal, which is the so-called beat-note, is in equation (3.7):

$$v_B(t) = \frac{A}{2} cos\left(2\pi \frac{B}{T}t\tau + \omega_0 \tau - \pi \frac{B}{T}\tau^2\right) \tag{3.7}$$

The frequency of this signal can be extracted by the derivative of the cosine argument as it follows:

$$f_B = \frac{1}{2\pi} \frac{d}{dt} \left(2\pi \frac{B}{T} t\tau + \omega_0 \tau - \pi \frac{B}{T} \tau^2 \right) = \frac{B}{T} \tau \qquad (3.8)$$

Equation (3.8) shows that the frequency of the beat-note signal f_B after heterodyne detection is related to the time delay τ in which the signal is reflected by the target and propagates back to the receiver. This equation can be rewritten to show the range to the target R (range including the transmitter-target and the target-receiver paths), which is related to the time delay through the propagation speed. From equation (3.9) the range to the target can be estimated in FMCW radar systems.

$$f_B = \frac{B}{T} \tau = \frac{BR}{cT} \qquad (3.9)$$

If the target (or the receiver) is moving at constant radial velocity v, then the time delay for the target echo to reach the receiver changes in time because of the change in the range from the radar. As it can be seen in equation (3.10), the time delay has a first fixed term related to the original range R_0, and a second term depending on the speed with which the target is moving:

$$\tau = \frac{R(t)}{c} = \frac{R_0}{c} \pm \frac{vt}{c} \qquad (3.10)$$

The dependency of the time delay τ on time t from equation (3.10) is applied in equation (3.8) to estimate the frequency of the beat-note. Assuming that the velocity of the target is very small compared with the speed of light c, and therefore some of the terms can be ignored, equation (3.11) is obtained:

$$f_B = \frac{1}{2\pi} \frac{d}{dt} \left(\frac{2\pi B}{T} t(\frac{R_0}{c} \pm \frac{vt}{c}) + \omega_0(\frac{R_0}{c} \pm \frac{vt}{c}) - \frac{\pi B}{T}(\frac{R_0}{c} \pm \frac{vt}{c})^2 \right) = \frac{B}{T} \tau_0 + f_0 \frac{v}{c} \qquad (3.11)$$

In equation (3.11) the frequency of the beat-note shows the first component depending on the time delay τ_0 due to the range to the target, and the second component due to the Doppler shift. The assumption of target velocity much smaller than speed of light is perfectly reasonable for TTWD scenarios, where targets of interest are human beings walking or moving limbs behind walls. Therefore the beat-note frequency in a single

chirp duration T is mainly proportional to the target range, and this piece of information can be extracted through spectral analysis. It should be noted that if the Doppler shift is large enough to move the beat-note frequency to another frequency bin, the estimation of the target range within a single chirp will be ambiguous. This is the so-called range/Doppler ambiguity for FMCW radars and can be dealt with using suitable waveform design [1]. For the work presented in this thesis, the duration of the chirp is such to avoid ambiguity for the context of TTWD and human motion.

If N consecutive chirps are analyzed, the time delay τ_n at the nth chirp can be expressed as in equation (3.12), which yields instantaneous frequency of the beat-note f_{Bn} as in (3.13) after elimination of terms which are small compared with others or with one radian:

$$\tau = \frac{R_n(t)}{c} = \frac{R_0}{c} \pm \frac{v(t + nT)}{c} \tag{3.12}$$

$$f_{Bn} = \frac{B}{T}\tau_0 + f_0\frac{v}{c} + Bn\frac{v}{c} \tag{3.13}$$

Comparing equation (3.13) with (3.11) it can be seen that an additional term Bn(*v*/c) appears in the beat-note frequency because of the movement of the target during the n chirp. For large values of bandwidth B, number of chirps n, or fast target speed *v*, this term is not negligible.

3.1.2 Double FFT Processing

Equation (3.13) shows that information on the target time delay/range and on its Doppler shift can be extracted through spectral analysis of the beat-note frequency. There are two possible methods based on Fast Fourier Transform (FFT), and they are equivalent in terms of extracted information and computational complexity [8]. The former employs double FFT processing: the first FFT is applied on a single chirp to extract time delay and therefore range information, the second FFT is applied on N consecutive chirps to extract Doppler and therefore target speed information. The latter method employs a single, longer, FFT over several consecutive chirps to extract both

delay and Doppler information. In this work the double FFT processing is used, and it is discussed in details in this subsection.

With the assumption of no range/Doppler ambiguity, the Fourier transform of a single chirp is as in equation (3.14), where the integral is solved:

$$V(f) = \int_{-\frac{T}{2}}^{\frac{T}{2}} A\cos[\Phi_B(t)]\, e^{-j2\pi ft} dt =$$

$$= \frac{AT}{2} \frac{\sin\left[\frac{2\pi(f - f_B)T}{2}\right]}{\frac{2\pi(f - f_B)T}{2}} e^{-j\varphi_0 + j\omega_0 nT\frac{v}{c}} + \frac{AT}{2} \frac{\sin\left[\frac{2\pi(f + f_B)T}{2}\right]}{\frac{2\pi(f + f_B)T}{2}} e^{j\varphi_0 - j\omega_0 nT\frac{v}{c}} \quad (3.14)$$

Equation (3.14) shows that the spectrum of a single chirp is a sin *x/x* function centred at the beat-note frequency f_B related to the target time delay. This Fourier Transform is performed digitally through FFT algorithm on digitized beat-note signals. The sampling frequency f_S has to match Nyquist criterion, so it must be greater than twice the maximum expected beat-note frequency. If M time samples per chirp are used, M/2 samples are available in the frequency domain from 0 to $f_S/2$; these frequency domain samples can be converted into time delay samples and into range samples using equation (3.9).

If N chirps are digitized and converted separately into the frequency domain, they can be arranged in a matrix with dimensions N-by-M/2 which is shown in equation (3.15). Each row represents the FFT of single chirp, so each element is a frequency bin, related to the time delay and therefore to the target range within a chirp duration T. The time to fill in a row is the duration of a single chirp T, so NT time is required to fill the whole matrix. The elements in each column represent digital samples at a particular frequency bin of the beat-note which has been sampled every T times. So each column can be considered a function of time and a second FFT can be applied to them to extract various pieces of information.

$$
\begin{bmatrix}
C_{11} & C_{12} & \cdots & C_{1m} & \cdots & C_{1\frac{M}{2}} \\
C_{21} & C_{22} & \cdots & C_{2m} & \cdots & C_{2\frac{M}{2}} \\
\cdots & \cdots & \cdots & \cdots & \cdots & \cdots \\
C_{n1} & C_{n2} & \cdots & C_{nm} & \cdots & C_{n\frac{M}{2}} \\
\cdots & \cdots & \cdots & \cdots & \cdots & \cdots \\
C_{N1} & C_{N2} & \cdots & C_{Nm} & \cdots & C_{N\frac{M}{2}}
\end{bmatrix}
\tag{3.15}
$$

In a frequency bin m the column elements change because of the relative movement of the target and the radar which causes Doppler shift. This can be seen in equation (3.14) where the phase of the spectrum of a single chirp is a function of the Doppler shift; this phase factor is rewritten in equation (3.16) for an element C_{nm} of the matrix, where nT is rewritten as t_n to represent the discrete flow of time from chirp to chirp:

$$
C_{nm}(f) = K(f)e^{j2\pi f_0 nT\frac{v}{c}} = K(f)e^{j2\pi f_0\frac{v}{c}t_n}
\tag{3.16}
$$

The second FFT of this expression in t_n over N chirps, i.e. from 0 to NT, yields:

$$
C_m(f) = NTK(f)\frac{\sin\left[2\pi\left(f - \frac{v}{c}f_0\right)\frac{NT}{2}\right]}{2\pi\left(f - \frac{v}{c}f_0\right)\frac{NT}{2}}
\tag{3.17}
$$

The Doppler shift causes displacement of the sin *x/x* function shown in equation (3.17). Therefore a target moving with speed *v* appears as a peak at value $f_0(v/c)$ in the Doppler domain after performing the second FFT.

The output of this second FFT consists of N discrete samples. In this work it is assumed that the duration of the chirp T is such to avoid range/Doppler ambiguity: this means that the maximum detectable Doppler shift without ambiguity is within ±1/2T. Since N samples are distributed in this Doppler range, the Doppler resolution of this approach is 1/NT.

Equations (3.14) and (3.17) show that the outputs of the two FFT are sin *x/x* functions, respectively in the frequency and Doppler domain. As previously mentioned, this function has high level of side-lobes, which can overlap and mask the main lobe of other sin *x/x* pulses related to other targets. This problem can be overcome multiplying the data by suitable window functions prior to FFT processing. Hamming window is

typically used: this reduces the side-lobes level to -43 dB, with the drawback of broadening the main lobe to 1.8 bins at -6 dB [1, 7].

3.1.3 Summary of FMCW radar parameters

In this subsection typical requirements of a TTWD radar system are discussed and related to FMCW and processing parameters. The actual values used for the experimental campaign of this thesis are discussed in chapter 5, where the radar system built at the Centre for Communications Systems of Durham University is described in details.

The down-range resolution ΔR of the radar system is related to the bandwidth as it can be seen in equation (3.18): the wider the bandwidth of the chirp B, the finer the down-range resolution [9]. UWB systems therefore provide very fine down-range resolution. Down-range and cross-range resolution have been defined in section 2.1 of this thesis.

$$\Delta R = \frac{c}{2B} \qquad (3.18)$$

The cross-range resolution ΔA is related to the length of the receiving array L, which may be a physical array with different antennas, or a synthetic array with SAR approach where a single antenna is moved along a grid of positions [9]. In equation (3.19) it can be seen that, given a range to the target R, the cross-range resolution becomes finer, the longer the array is; λ is the wavelength. It should be noted that the length of the array depends heavily on the actual in-field conditions of the radar system (size and weight, or stand-off distance for instance), so it is not always possible to increase it arbitrarily to improve the cross-range resolution.

$$\Delta A = \frac{\lambda R}{L} \qquad (3.19)$$

The maximum range of a detectable target R_{MAX} can be derived from the radar equation for pulse compression shown in (3.20) and related to the minimum signal-to-noise ratio SNR_{MIN} necessary for detection [1, 9-10]: given a minimum SNR at which a radar system works, detection is possible only up to a maximum spatial range. In equation (3.20) P_T is the transmitted power, τ_0 is the duration of the compressed pulse, G_T and G_R

are the gains of the transmitting and receiving antennas, σ is the target RCS, k is Boltzmann's constant, T_0 is the standard temperature of 290 K, F_n is the receiver noise figure, and L_S represents the system losses, including the energy lost within the wall in TTWD applications.

$$SNR_{MIN} = \frac{P_T \tau_0 G_T G_R \sigma \lambda^2}{(4\pi)^3 k T_0 F_n L_S (R_{MAX})^4} \tag{3.20}$$

For FMCW radar systems the range is related to the beat-note frequency as in equation (3.9), so the maximum expected beat-note frequency can be derived. Since this signal is digitized at the ADC, Nyquist criterion states that the sampling frequency f_S must be at least twice the maximum expected beat-note frequency. Combining this relation with equation (3.9) and (3.18), the maximum range and the desired down-range resolution can be related to the number of samples M for each digitized chirp, as in equation (3.21):

$$f_S \geq 2 f_{bMAX} \equiv M \geq \frac{2 R_{MAX}}{\Delta R} \tag{3.21}$$

Given a maximum target speed expected for scenarios under test, the maximum expected Doppler shift can be computed as in equation (3.22), where f_0 is the carrier frequency.

$$f_{DMAX} = f_0 \frac{v_{MAX}}{c} \tag{3.22}$$

As previously mentioned, it is desirable to choose the duration of the chirp T so that there is no range/Doppler ambiguity. This yields equation (3.23). Basically the faster a target is moving, the larger is the expected Doppler shift, and therefore the shorter the chirp duration must be to avoid ambiguity.

$$f_{DMAX} < \frac{1}{2T} \ or \ T < \frac{1}{2 f_{DMAX}} \tag{3.23}$$

The Doppler resolution Δf_D is related to the number of consecutive chirps analyzed to extract Doppler information, as in equation (3.24). Basically the finer the desired Doppler resolution is, the higher the number of chirps to be processed N must be. This number has an effect on the total reading time for the radar system to provide the user

with information: intuitively, more chirps to process means longer time and more intensive computation to produce information.

$$\Delta f_D = \frac{1}{NT} \tag{3.24}$$

3.2 FMICW Signals for Radar Applications

In chapter 2 FMICW (also called gated/interrupted FMCW) signals are mentioned as a possible wall removal technique in radar systems for TTWD. In this section these signals are presented and analyzed mathematically, highlighting the differences with normal FMCW signals described in the previous section.

It has been mentioned that in the context of radar for TTWD the strong signal leakage from the transmitter to the receiver and strong reflections from the air/wall interface worsen the performance and compromise the detection of targets. The dynamic range of the system may be insufficient to detect low RCS targets which appear masked by strong undesired signals, and the receiver may saturate and be blocked by such strong signals. To avoid this, in short impulse based radar systems the receiver can be simply switched on after the transmission of the pulse, but this is not possible for FMCW radar systems where the transmitter and the receiver are both active at the same time.

FMICW technique solves this problem with suitable switching sequences applied to the transmitter and to the receiver to ensure that they are not simultaneously on [1]. This provides the receiver with listening intervals when only the echoes from the targets are received and the undesired signals are not.

FMICW signals date back to the eighties for applications like ionospheric sounding and ocean surface sensing, for which monostatic approach would be preferable. For instance in [11] FMICW is mentioned as a way to mitigate the required high isolation between transmitter and receiver for FMCW radar systems. In [12] the effects of introducing switching sequences on FMCW signals is mathematically analyzed, and examples for an ionospheric chirp sounder provided. In [13-14] the performance of FMICW radars for ocean surface sensing are discussed, focusing on the comparison between bistatic FMCW and monostatic FMICW radar [13], and on different gating sequences which

can be applied [14]. A more recent paper [15] provides an overview of existing oceanographic radar networks across the Pacific coastal area, among which several systems are based on FMICW signals. However, to the best of our knowledge, FMICW signals have not been applied so far to tackle the wall reflections problem in the context of TTWD.

3.2.1 Model and effects of FMICW signals

FMICW signals are generated by switching on and off the transmitter and the receiver with complementary sequences to ensure that they are not simultaneously active. These gating sequences can be mathematically modelled through binary functions with duration T_S and with bit duration T_B equal simply to T_S/K, where K is the number of bits. The transmitter (or receiver) is switched on when the sequence assumes value 1, and off when the value is 0.

The received FMICW signal can be written as in equation (3.25): the FMCW chirp in equation (3.4) is multiplied by the delayed copy of the transmitted switching sequence g(t). The replica of the transmitted signal from equation (3.3) which is used at the receiver is multiplied by the complementary gating sequence, as in equation (3.26).

$$v_R(t) = A_R cos[\Phi(t - \tau)]g(t - \tau) \qquad (3.25)$$

$$v_T(t) = A_T cos[\Phi(t)][1 - g(t)] \qquad (3.26)$$

Assuming heterodyne detection to mix the previous two signals, the output of the mixer after low-pass filtering, which is basically the beat-note signal, is given in equation (3.27). It is an interrupted CW signal with frequency related to the target time delay τ as in equation (3.7) for FMCW chirp, but with power related to the switching sequences and the time delay τ. So the power of the beat-note, which is the signal containing both range and Doppler information, is time-delay sensitive.

$$v_B(t) = \left[\frac{A}{2} cos\left(2\pi \frac{B}{T} t\tau + \omega_0 \tau - \pi \frac{B}{T} \tau^2\right)\right] g(t - \tau)[1 - g(t)] \qquad (3.27)$$

A figure of merit to investigate the effect of the gating sequences on the beat-note power is the so-called Mean Received Power (MRP), or alternatively its square root

Mean Received Signal (MRS) [1]. The MRS is basically the cross-correlation between the transmitted and the received gating sequences as in equation (3.28):

$$MRS(\tau) = \frac{1}{T_S} \int_0^{T_S} g(t - \tau) \left[1 - g(t)\right] dt \qquad (3.28)$$

The MRS depends on the properties of the gating sequences, bit duration and number of bits for instance, and on the target time delay τ. So the MRS and consequently the beat-note power in equation (3.28) are reduced for some values of time delay, i.e. for some spatial ranges. Designing carefully the gating sequences, it is possible to get MRS profiles which attenuate undesired signals within a certain range of values of time delay, and which possibly do not alter desired signals within other time delay ranges. This is basically the principle to employ FMICW signals to mitigate/remove wall reflections in TTWD applications: the MRS of suitable gating sequences is such to attenuate at time delays corresponding to air/wall interface, and to minimize attenuation at time delays corresponding to the targets in the area under test.

The overall transmitted power for FMICW signals is reduced of a factor which is proportional to the transmitter off-time. The FMCW radar equation shown in (3.20) can be updated for FMICW signals with an additional loss term L_G as in (3.29). In [12] it is shown that gating sequences with 50% duty cycle provide maximum power efficiency, so they minimize this factor L_G. Gating sequences with lower duty cycle increase these losses and worsen the SNR, but they may be useful in TTWD scenarios to improve the effect of wall reflections mitigation. More details are given in subsection 3.2.2.

$$SNR_{MIN} = \frac{P_T \tau_0 G_T G_R \sigma \lambda^2}{(4\pi)^3 k T_0 F_n L_G L_S (R_{MAX})^4} \qquad (3.29)$$

Looking at equation (3.28), it can be seen that the MRS is equal to zero when the target time delay τ is multiple of the sequence duration T_S, and this means that the beat-note power is zero. These values of time delay are related to the so-called "blind ranges" because targets placed at the corresponding ranges are not detected. In order to avoid this problem, the duration of the gating sequence should be longer than the maximum

expected time delay for the scenario under test, as in equation (3.30). This ensures that any blind range is outside the considered range of interest.

$$T_S = KT_B > \tau_{MAX} \tag{3.30}$$

As seen in equations (3.25) and (3.26), FMICW signals are multiplication of FMCW chirps by gating sequences in the time domain; in the frequency domain this multiplication is a convolution of the spectra. Being periodic signals, the spectrum of the gating sequences is made of impulse functions enveloped by the spectrum of a single period of the sequence; these functions are placed every multiple of the sequence frequency f_S, which is the reciprocal of the sequence duration T_S. The overall effect of this convolution is that the original FMCW spectrum of the beat-note signal is replicated at the positions of the impulse functions [13]. Therefore it should be ensured that the sequence frequency is greater than twice the highest expected beat-note frequency, in order to avoid aliasing which would compromise the detection of targets. This condition can be expressed as in (3.31), where the number of bits of the sequence K and their duration T_B is related to the parameters of the FMCW chirp (bandwidth B and duration T) and to the maximum target range R_{MAX} (which here is the one-way range from target to radar assuming a monostatic scenario).

$$f_S > 2f_{BMAX}$$

$$\frac{1}{T_S} = \frac{1}{KT_B} > 2\frac{2BR_{MAX}}{cT} \ or \ T_B < \frac{cT}{4BKR_{MAX}} \tag{3.31}$$

Basically this anti-aliasing condition put constraints on the choice of the gating sequence parameters, given the FMCW chirp and the desired maximum target range.

It should be noted that there may be a conflict between equations (3.30) and (3.31) to obtain a suitable value for the bit duration T_B, therefore a compromise to satisfy both equations should be sought in practical applications.

3.2.2 Gating sequences for FMICW signals in TTWD context

In this subsection several examples of gating sequences from the literature and used in this thesis' work are presented and their MRS analyzed, focusing on the suitability in the context of TTWD. For each gating sequence, figures with a few periods of their pattern in time domain and the corresponding MRS are presented.

Square wave [1 0] with 50 % duty cycle (as in figure 3.4) is the simplest gating sequence and it has been used in radar systems for ocean surface sensing in [13], and more recently in GPR applications [16]. Looking at the MRS in figure 3.5, it can be seen that there is a pattern of maxima and minima, at odd and even integer multiples of the bit duration T_B respectively. This is expected from the analysis of the sequence "blind ranges" in the previous section, which discussed the presence of a "blind range" every multiple of the sequence duration. Normally the bit duration of square wave sequences is chosen to locate the first maximum of the MRS at the time-delay corresponding to the range to desired targets; this ensures that there are no "blind ranges" in the area under test located between the radar and the expected target range [13, 16].

A drawback of this approach is that the detection of targets closer to the radar can be compromised. These targets have low time delay values, which may be located on the slope of the MRS too close to the minimum; this means that the beat-note components related to these targets may be strongly attenuated. In the TTWD context echoes of targets close to the internal side of the wall may suffer this problem.

If the range to an interesting target is known or suspected, square wave sequences can be useful to tune the maximum MRS at this position and focus their detection, while attenuating neighbouring targets; this could be a useful approach to enhance a low RCS target (a human being for instance) when it is close to highly reflective nearby targets. This approach could be generalized in surveillance applications where an area is scanned repeatedly using square waves with increasing bit duration; in this way the detection is focused in sub-areas which are checked one after the other in a loop.
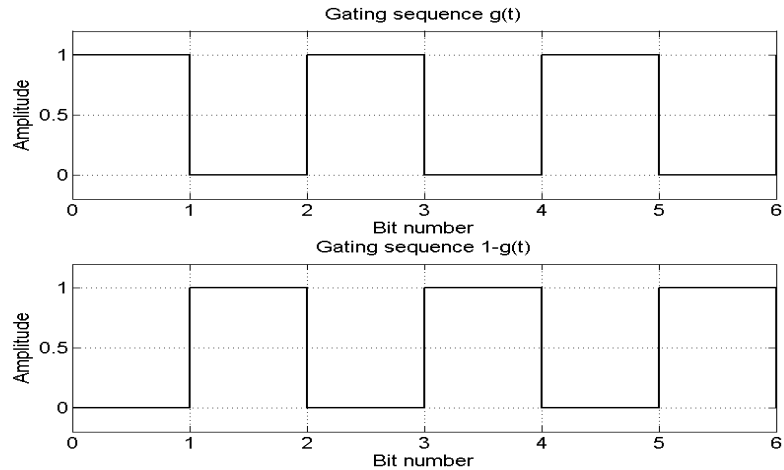
Figure 3.4 Bit pattern of the square wave gating sequence
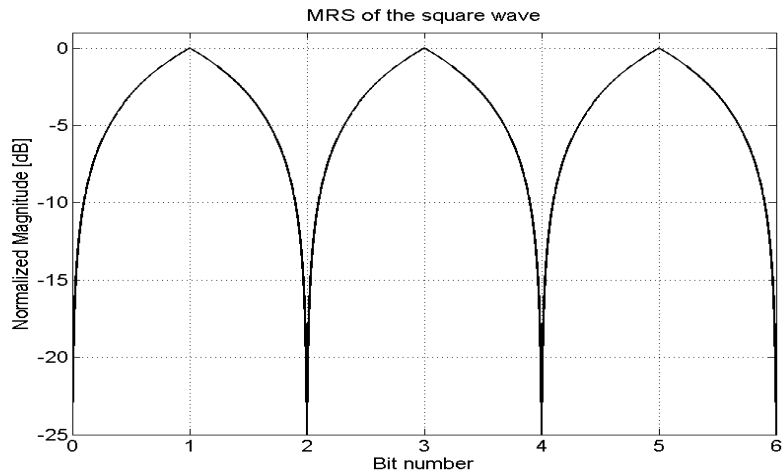
Figure 3.5 MRS of the square wave

M (or maximum length binary sequence) sequences have been previously mentioned as waveforms used in pseudo-random noise radar systems, but they are suitable as gating sequences for FMICW signals as well. M-sequences have length equal to a power of 2 minus one, so the shortest M-sequence consists of 3 bit [1 1 0], as shown in figure 3.6, followed by 7 bit M-sequence [1 0 0 1 1 1 0], as shown in figure 3.8.

Looking at the MRS in figures 3.7 and 3.9, an interesting property of these sequences can be seen: apart from the first and the last bit where there is a slope, the MRS is flat. From detection perspective this means that there is a range of time delay values, and therefore a corresponding spatial distance, where there are no "blind ranges" and no

additional attenuation of the beat-note power. This is a useful property for TTWD applications: the bit duration can be chosen so that the reflections from the wall fall within the first bit, thus they are attenuated, whereas the area with possible targets is located in the flat portion of the MRS where there is no additional attenuation.
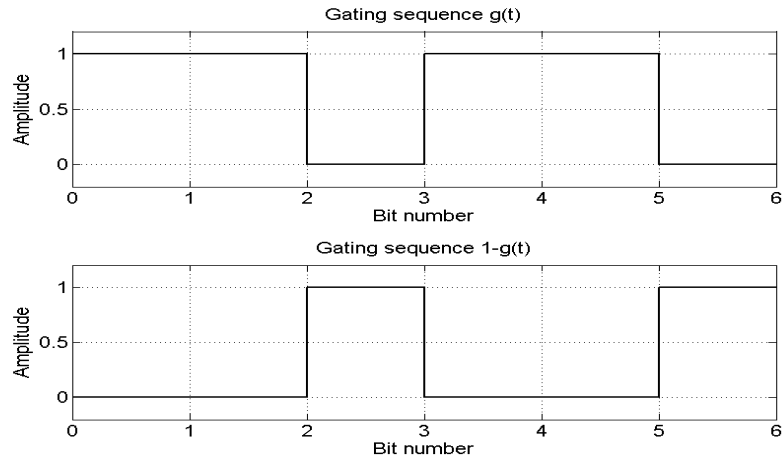
Figure 3.6 Bit pattern of the 3 bit M gating sequence
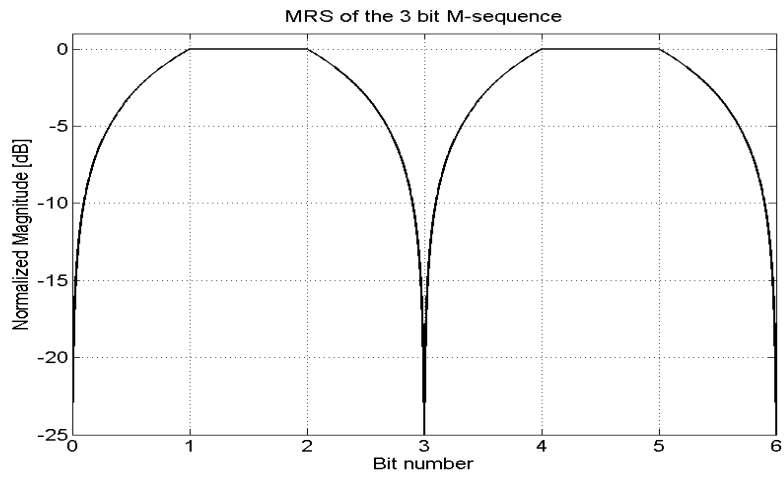
Figure 3.7 MRS of the 3 bit M-sequence
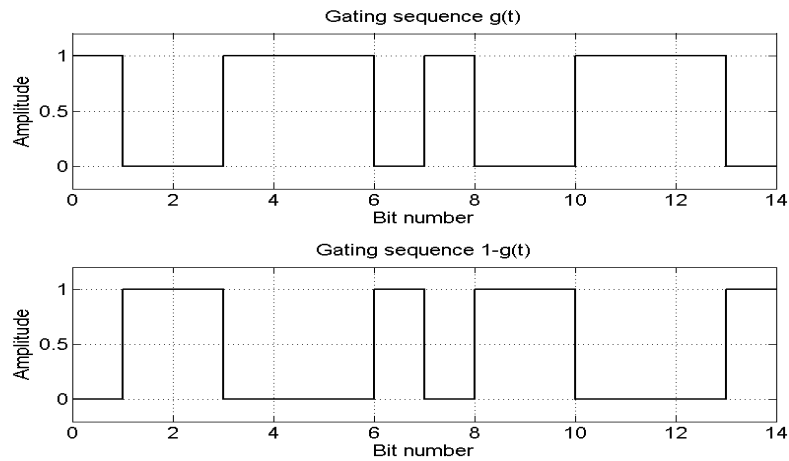
Figure 3.8 Bit pattern of the 7 bit M gating sequence
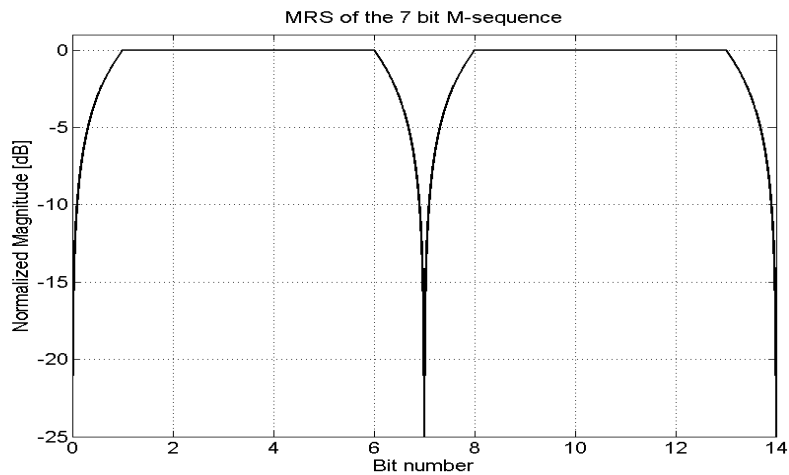
Figure 3.9 MRS of the 7 bit M-sequence

Barry sequence [1 1 0 0 0 1 1 1 1 0 0 0 0 0 0 0] has been used in the past for ionospheric channel sounding and it consists of 16 bit, as shown in figure 3.10 [1]. An interesting feature of the MRS of this sequence as shown in figure 3.11 is the rise time which takes three bits. In TTWD this may be useful to attenuate wall reflections which extend for a long range of time delays, but the MRS is not flat at intermediate time delay values as it was for M-sequences, and this may cause additional attenuation on the response of the targets. It should be noted that the MRS has the same value in the flat area between bit 5 and 11 where targets are supposed to be located, and around bit 2 and 3 where part of the wall reflections is supposed to be. Therefore there may be no additional attenuation

on the wall reflections, which makes this sequence not the best option for TTWD applications; in this thesis' work square waves and M-sequences are indeed preferred.
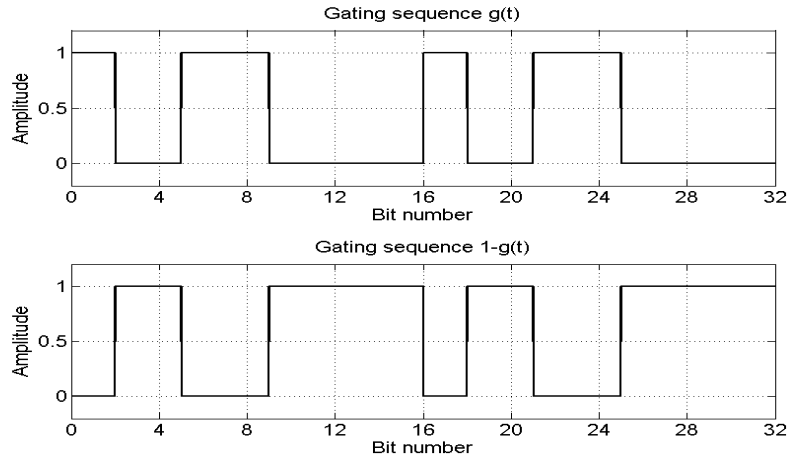
Figure 3.10 Bit pattern of the Barry gating sequence
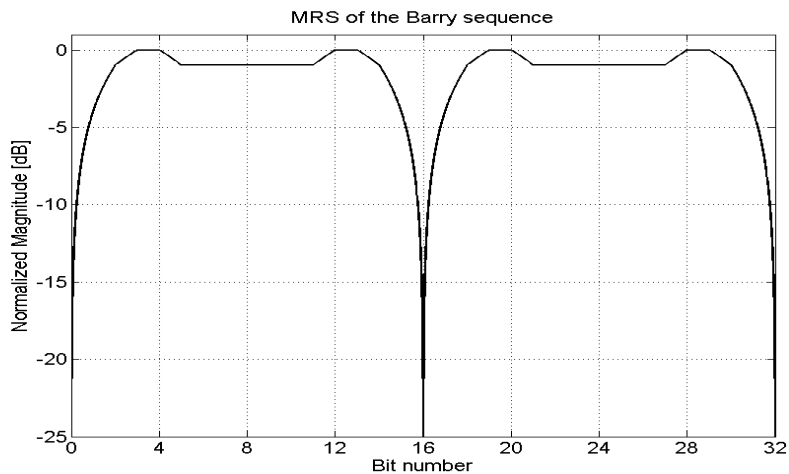
Figure 3.11 MRS of the Barry sequence

It has been mentioned that square waves and M-sequences present potential advantages for TTWD applications: the former can enhance the detection at particular ranges where maximum MRS is located, the latter have flat MRS which provide no "notches" of additional attenuation for areas where the targets are supposed to be located. In both cases the effectiveness of these sequences in mitigating/removing the reflections from the wall relies on the assumption that the values of time delay related to the undesired signals are within the first bit of the sequence, and thus these signals are strongly attenuated.

However, as in figures 3.5, 3.7 and 3.9, the MRS within the first bit is a rising slope, which means that the value of attenuation on the beat-note power is small, only a few dB, for time delays just below T_B. Furthermore, the reflections from the wall produce a beat-note component which is extended over a range of time delay values, because of the non-infinite resolution and the effect of windowing which broadens the main lobe. As a consequence of these facts, the attenuation given by the aforementioned MRS on the wall reflections may be not enough to mitigate them effectively and to enhance the detection of the targets.

This problem arises particularly in TTWD, where reflections from the wall and targets' echoes are very close in terms of corresponding time delays, especially for targets near the internal wall. This leads to a compromise when choosing the bit duration T_B for M-sequences. On the one hand T_B should be short enough so that all the echoes from the targets fall after T_B itself, in the range where the MRS is flat; however the wall reflections may be not attenuated enough and they may still hide the targets. On the other hand T_B should be long enough to have strong attenuation on the wall reflections because of the steep slope of the MRS; however the targets' echoes may be on the slope of the MRS and be attenuated as well, so that their detection is still compromised.

A solution to this problem comes from modifications in the gating sequences at the receiver, where additional off-time is introduced. The gating sequences shown so far are perfectly complementary: the receiver is switched on at the exact instant when the transmitter is switched off. With these modifications the receiver is switched on slightly after the switching-off of the transmitter, and switched off a bit before the switching-on of the transmitter. This can be seen in figure 3.12 for a 3 bit M-sequence, where these additional time intervals are called τ_{RX1} and τ_{RX2} for the receiver gating sequence. The effect on the MRS can be seen in figure 3.13, where both τ_{RX1} and τ_{RX2} are 20% of bit duration long, just to give an example.

Comparing figure 3.13 with figure 3.7, it can be seen that at the beginning of the slope and close to bit duration 0 there is an additional interval where the MRS is practically zero, so it is not seen using logarithmic scale; this interval of zero MRS is τ_{RX2} long. At bit duration 3, there are two intervals of zero MRS, one on the left τ_{RX1} long and one on the right τ_{RX2} long, respectively; this is repeated at each multiple of the sequence

duration T_S. Basically these additional delays at the receiver gating sequence extend the duration of the "blind ranges", so that they can be exploited to remove undesired signals. It should be noted that also the interval where the MRS is flat is extended according to the values of τ_{RX1} and τ_{RX2}, making the MRS slope steeper.

In TTWD context two approaches are possible. The value of τ_{RX2} can be chosen so that a great portion of the wall reflections fall within this interval close to bit duration 0, so that they are cancelled while at the same time the MRS slope is steep enough to provide no attenuation on the targets. Alternatively, the sequence bit duration and the values of τ_{RX1} and τ_{RX2} can be chosen so that the wall reflections fall within the second "blind range", which appear at a time delay corresponding to the first period of the sequence (at bit 3 in these examples). This provides a broader "blind range" to cancel long undesired signals.

This approach can be seen as a reduction of the duty cycle of the gating sequence at the receiver, and this reduces the overall received power since the off-time at the receiver is increased. Looking at equation (3.29) this causes an increase of the loss factor L_G in the radar equation, which is proportional to the ratio of the additional off-time (τ_{RX1} plus τ_{RX2}) to the bit duration T_B. This can compromise the system dynamic range and the detection of low RCS targets. Therefore the values of the additional delays τ_{RX1} and τ_{RX2} cannot be chosen arbitrarily long and a compromise must be sought.
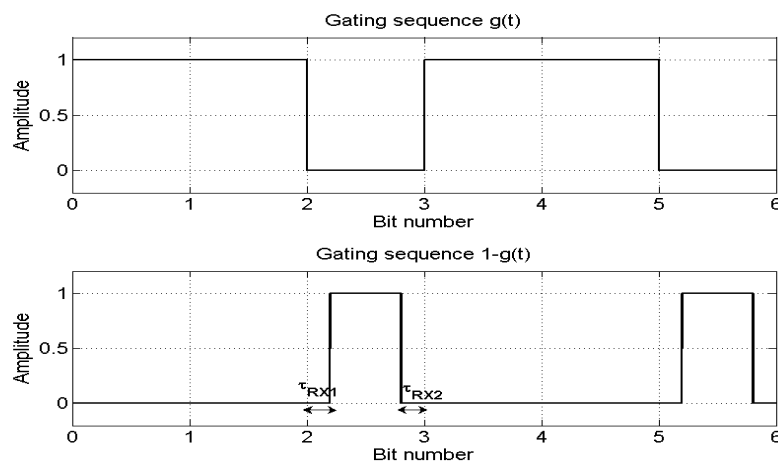
Figure 3.12 Bit pattern of the 3 bit M gating sequence with τ_{RX1} and τ_{RX2} equal to 20% bit duration
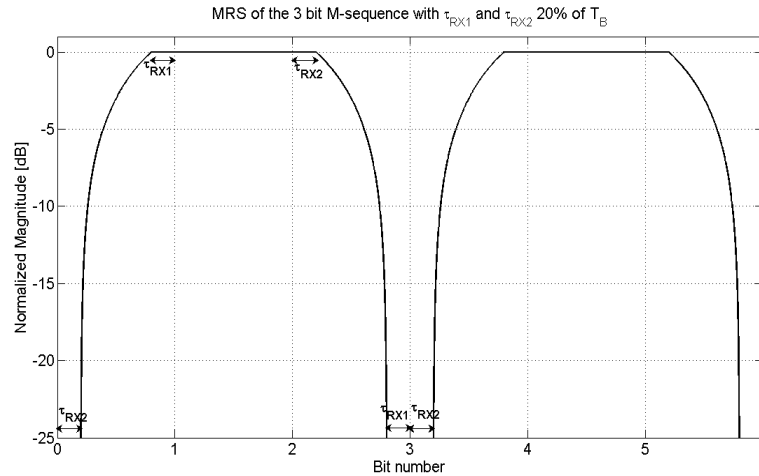
Figure 3.13 MRS of the 3 bit M-sequence with τ_{RX1} and τ_{RX2} equal to 20% bit duration

A partial mitigation for this problem can be the use of just one additional delay, τ_{RX2}, which still provides broader "blind ranges" to remove undesired signals, but at the same time reduces the additional loss of power in the radar equation. The gating sequence for this approach is shown in figure 3.14, with MRS in figure 3.15. Comparing figure 3.15 with figure 3.13, it can be seen that the extended "blind range" close to zero bit duration is preserved, whereas the "blind range" at bit duration 3 is shorter. The MRS shown in figure 3.15 is more effective in terms of mitigation of wall reflections for TTWD compared with the MRS in figure 3.7 for the same sequence, where τ_{RX2} was set to zero and thus the "blind range" was a single point.
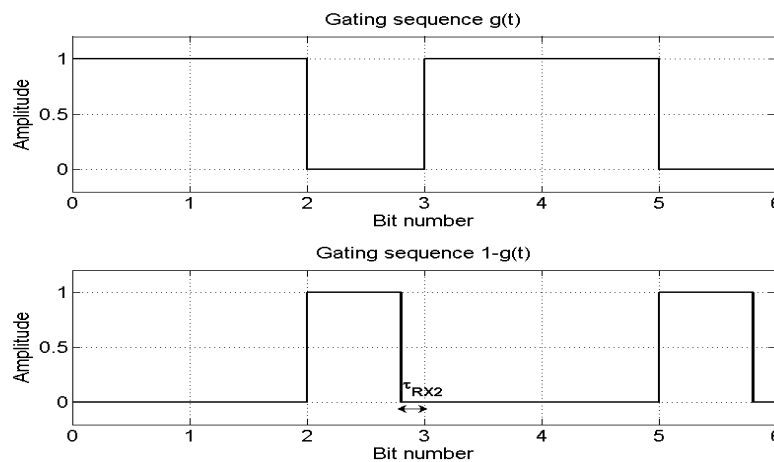
Figure 3.14 Bit pattern of the 3 bit M gating sequence with τ_{RX2} equal to 20% bit duration
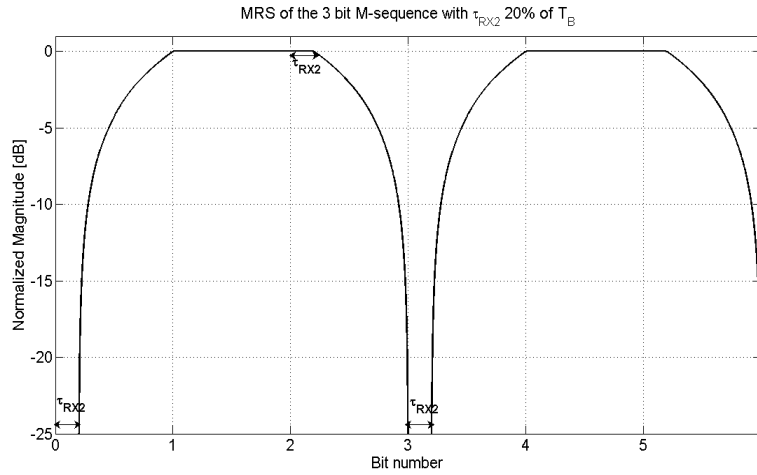
Figure 3.15 MRS of the 3 bit M-sequence with τ_{RX2} equal to 20% bit duration

The approach of using additional delays τ_{RX1} and τ_{RX2} can be applied to square waves as well. For further information figure 3.16 shows the gating sequence and figure 3.17 the corresponding MRS. Looking at figure 3.17 it can be seen that the "blind ranges" are extended as expected, as well as the MRS maxima, which are no longer single points as in figure 3.5, but they are extended as well.
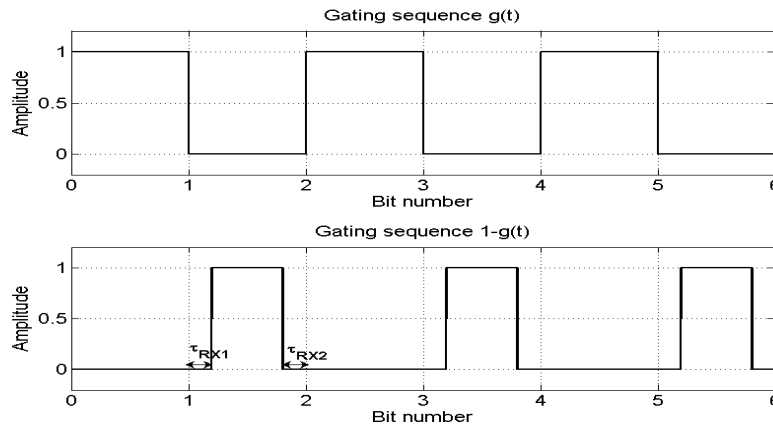
Figure 3.16 Bit pattern of the square wave gating sequence with τ_{RX1} and τ_{RX2} equal to 20% bit duration
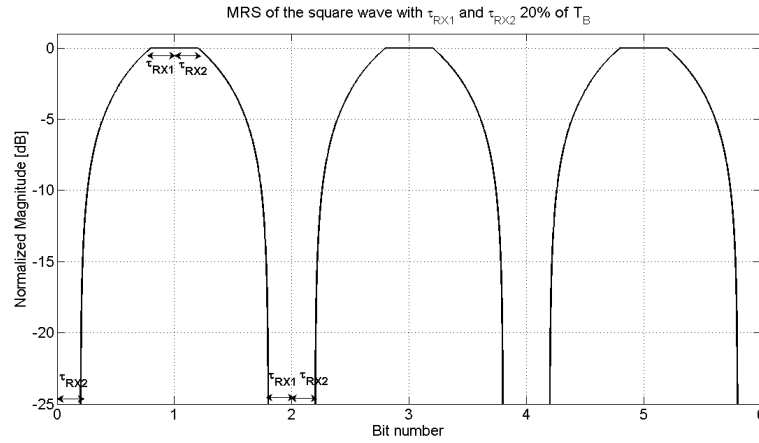
Figure 3.17 MRS of the square wave gating sequence with τ_{RX1} and τ_{RX2} equal to 20% bit duration

Clearly a compromise between effective mitigation of undesired signals and additional power losses must always be sought when the values of the parameters of the gating sequence are chosen. This depends also on the features of the scenario under test, for instance the type of wall reflections and how long they extend in terms of round-trip delay. Examples of how designing gating sequences suitable for a particular scenario can be found in chapter 4 with reference to data from numerical simulations and in chapter 6 referring to experimental data.

3.3 Summary of the chapter

In this chapter FMCW signals for radar systems have been presented and mathematically modelled assuming heterodyne detection and double FFT processing over multiple chirps to extract range and Doppler information. The first FFT set is performed within each single chirp at M points to extract M/2 frequency bins, related to the target range. The second FFT set is performed over N chirps to extract Doppler bins for each range bin.

FMICW signals have been discussed and modelled as well, highlighting their additional effects on normal FMCW, namely range-dependent received power according to the MRS of the gating sequence, presence of "blind ranges", risk of aliasing, and overall reduction of the received power.

The suitability of FMICW signals as wall mitigation/removal technique in TTWD applications has been discussed, focusing on the features of the MRS of the chosen sequences.

The following table summarizes useful relations which link FMCW and FMICW parameters and radar requirements, and can be useful to design effective systems.

Table 3.1 FMCW and FMICW parameters and radar requirements

Down-range resolution ΔR and chirp bandwidth B	$\Delta R = \dfrac{c}{2B}$
Cross-range resolution ΔA and array length L	$\Delta A = \dfrac{\lambda R}{L}$
Maximum expected range R_{MAX} and maximum expected beat-note frequency f_{bMAX}	$f_{bMAX} = \dfrac{B R_{MAX}}{cT}$
ADC sampling frequency f_S and maximum expected beat-note frequency	$f_S \geq 2f_{bMAX}$
Expected number of samples per chirp M given f_S	$M \geq \dfrac{2R_{MAX}}{\Delta R}$
Chirp duration T and maximum Doppler shift f_{DMAX} to avoid ambiguity	$T < \dfrac{1}{2f_{DMAX}}$
Doppler resolution Δf_D and number of chirps to process N	$\Delta f_D = \dfrac{1}{NT}$
Bit duration T_B of a K-bit gating sequence and maximum expected target delay τ_{MAX} to avoid "blind ranges"	$T_S = KT_B > \tau_{MAX}$
Bit duration T_B to avoid aliasing given the other parameters	$T_B < \dfrac{cT}{4BNR_{MAX}}$

3.4 References

[1]   S. Salous, Radio Propagation Measurement and Channel Modelling: Wiley, 2013.

[2]   A. G. Stove, "Linear FMCW radar techniques," Radar and Signal Processing, IEE Proceedings F, vol. 139, pp. 343-350, 1992.

[3]   G. L. Charvat, et al., "A through-dielectric radar imaging system," Antennas and Propagation, IEEE Transactions on, vol. 58, pp. 2594-2603, 2010.

[4]   N. Maaref, et al., "Ultra-wideband frequency modulated continuous wave synthetic aperture radar for through-the-wall localization," in Microwave Conference, 2009. EuMC 2009. European, 2009, pp. 1880-1883.

[5]   M. G. Amin, Through-the-Wall Radar Imaging: CRC PressINC, 2010.

[6]   M. Skolnik, Radar Handbook, Third Edition: McGraw-Hill Education, 2008.

[7]   F. Harris, "On the use of windows for harmonic analysis with the discrete Fourier transform," Proceedings of the IEEE, vol. 66, pp. 51-83, 1978.

[8]   D. E. Barrick and E. R. Laboratories, FM/CW radar signals and digital processing: Environmental Research Laboratories, 1973.

[9]   M. Farwell, et al., "Sense through the wall system development and design considerations," Journal of the Franklin Institute, vol. 345, pp. 570-591, 2008.

[10]   B. R. Mahafza, Radar Signal Analysis and Processing Using MATLAB: Taylor & Francis, 2010.

[11]   H. D. Griffiths, "New ideas in FM radar," Electronics & Communication Engineering Journal, vol. 2, pp. 185-194, 1990.

[12]   A. Poole, "On the use of pseudorandom codes for "Chirp" radar," Antennas and Propagation, IEEE Transactions on, vol. 27, pp. 480-485, 1979.

[13]   J. A. McGregor, et al., "Switching system for single antenna operation of an S-band FMCW radar," Radar, Sonar and Navigation, IEE Proceedings -, vol. 141, pp. 241-248, 1994.

[14]   R. H. Khan and D. K. Mitchell, "Waveform analysis for high-frequency FMICW radar," Radar and Signal Processing, IEE Proceedings F, vol. 138, pp. 411-419, 1991.

[15]   S. Fujii, et al., "An overview of developments and applications of oceanographic radar networks in Asia and Oceania countries," Ocean Science Journal, vol. 48, pp. 69-97, 2013/03/01 2013.

[16]   M. J. Oyan, et al., "Ultrawideband gated step frequency ground-penetrating radar," Geoscience and Remote Sensing, IEEE Transactions on, vol. 50, pp. 212-220, 2012.

4.1 Numerical Simulations of Radar Systems for TTWD

In this section the reasons for running computer-based numerical simulations of radar systems are discussed, focusing on the context of TTWD. A quick review of some of the most interesting works from the literature is presented, with particular emphasis on the effects of the through-wall propagation and the need of suitable models.

Numerical simulations allow the analysis of the capabilities and limitations of a radar system prior to building it and to performing measurements. Through these simulations it is possible to predict the performance of the system and its sensitivity to the variations of the many parameters involved. This is very important in the context of TTWD, where the successful detection of the targets is influenced by a multiplicity of parameters: waveform parameters like shape, duration, and bandwidth, antenna parameters like number, polarization, position, and beam-width, target parameters like RCS, and scenario parameters like thickness, materials, and internal structure of the wall. The performance of the system can therefore be tested while changing one or more of these parameters, avoiding at the same time measurement errors which may be specifically due to the hardware.

An extremely easy example of numerical simulation for TTWD is shown in [1]. This simulation is not realistic since the scenario under test is simply modelled in two dimensions, with a metallic square as target placed inside a rectangle which models a room. The source of the excitation is simply modelled as a point, and the excitation is a pulse centred at 2 GHz. The interesting element of this paper is the implementation of the Back-Projection (BP) imaging algorithm, with a proposed easy estimation of the additional delay caused by the propagation within the wall. More details about suitable numerical methods for TTWD simulations are given in section 4.2, whereas a deeper analysis of some of the suitable imaging algorithms is given in section 4.3.

A first example of realistic through-wall simulation is given in [2], where a 3D model of a room imported from a CAD software is used; the wall is modelled as brick material and 16 cm thick. The target is a human phantom whose internal tissues are realistically modelled as well, using data from medical research. The excitation is a pulse centred at 1.1 GHz. The transmitter is simply modelled as a dipole antenna, moved in a grid of positions in SAR approach; the receivers are single points where the electric and

magnetic fields are sampled and recorded. BP algorithm is used to create radar images in monostatic and multistatic approach. Another 3D simulation is presented in [3], where the room has realistic sizes with 15 cm thick walls, and the target is a model of a man carrying a weapon; the excitation is a pulse with bandwidth 1.5-2.5 GHz.

Many remarkable results on simulations of TTWD scenarios have been presented by the Army Research Laboratory, US, such as the possibility of using different numerical methods to perform the simulations, and the study of the RCS of the human body. In [4] the importance of adding ceiling and floor to simulations of rooms with targets is highlighted, in order to make the model more realistic and to avoid artefacts in the radar image caused by the waveform diffraction at the top and bottom edges of the wall. A comparison between simulations with a time-domain exact method and with a ray-tracing approximation method is also performed in [4]. The focus is on the model of a room with a human phantom inside and with different wall materials (bricks, concrete, and cinder blocks). The conclusion is that the two methods give similar results. This ray-tracing method is preferred because it requires less computational resources.

In [5-6] a similar comparison between the two numerical methods is performed when computing the RCS of the human body, and useful results are reported. The average RCS for two different human phantoms, namely the "fit model" and the "fat model", and for different body positions does not seem to change a great deal in the frequency range generally used in TTWD, i.e. between 200 MHz and up to 3 GHz. As long as the body trunk stays upright, the values of the RCS varies indeed in a tight range, from -4 to 0 dBsm, and it is not much influenced by the position of the limbs. A reduction of about 5 dB is recorded when looking at the side of the body, rather than at the front or back. The RCS does not change much if the human phantom is modelled as a uniform object without the details of the internal tissues, but just using the electrical parameters of the skin (the authors suggest dielectric permittivity ε_r 50 and conductivity σ 1 S/m). This happens because at the frequency range relevant for TTWD the electromagnetic waves are mostly reflected by the skin, without penetration into the internal tissues. Therefore simplified human phantoms can be used in numerical simulations for TTWD, reducing the computational burden in terms of simulation time and computer memory. Furthermore, the RCS of these uniform phantoms is not very sensitive to variations in

electrical permittivity and conductivity of the skin-like material, at least for values higher than 20 and 0.5 S/m, respectively. The validation of the ray-tracing method against the time-domain method is performed for the RCS of human phantoms as well, and it is found that the faster ray-tracing method can be used without significant differences above 1 GHz.

A summary of the aforementioned results can be found in [7] and in chapter 9 of [8], where radar images from numerical simulations of different realistic scenarios are presented. The scenarios are a room with a human phantom, the same room where a metallic cabinet is added, and a complex room with more phantoms, realistic pieces of furniture, and internal partition walls. Three different wall materials are tested, namely bricks, solid concrete, and cinder blocks. This last wall structure appears to be particularly challenging for the detection of targets close to the wall because it produces a smeared, extended reflection which may mask them. Pulse excitations are used, with bandwidth 1 or 2 GHz, centred at 1.5 and 2.5 GHz respectively. The use of cross-polarization components to create radar images without wall reflections is discussed in [7]; this was mentioned in chapter 2 of this thesis among the possible wall removal techniques, but only on simulated data.

In [9] the same authors present a comparison of experimental data with simulations performed with the aforementioned ray-tracing method. The scenario under test is a big abandoned barracks; therefore its numerical simulation would be extremely intensive in terms of computational resources if a time-domain method was used. The experimental data are collected by a radar system mounted on a vehicle, which is moved in SAR approach at different positions outside the building. Reasonable agreement between simulated and experimental data is shown in this paper.

4.1.1 More on the effects of through-wall propagation

Good knowledge of the electromagnetic properties of materials is extremely important to model with accuracy the effects of the through-wall propagation on waveform parameters like time-delay, amplitude, and shape. In [10] a quick summary of these effects is provided. It has been already mentioned in chapter 2 of this thesis that the

reflection at the air/wall interface produces a strong back-scattered signal which can compromise the performance of radar systems for TTWD and therefore needs to be mitigated with suitable techniques. The amount of reflected energy depends on the dielectric contrast between air and wall material, but also on the angle of incidence and surface smoothness of the wall. Electromagnetic waves are slowed down when they propagate within dielectric materials like walls, so there is an additional time delay for the waves to propagate to the target and back to the radar system which should be taken into account. This delay depends on the wall thickness and dielectric permittivity ε_r. The air/wall dielectric contrast causes also refraction of the electromagnetic waves, and at the same time the presence of particles or irregularities inside the wall causes diffraction. The combined effect of these two phenomena is the distortion of the wavefront, which needs to be addressed to reconstruct the phase of the waves for imaging purposes. Furthermore walls absorb part of the electromagnetic energy because of conductivity losses. These losses are proportional to the conductivity σ of the wall material, and also to the water content. Normally, for dry walls and at not too high frequency ranges (up to roughly 3 GHz) these losses are small. The main contribution to the losses comes indeed from the back-scattered reflection.

Since the dielectric permittivity and the conductivity vary with frequency, the aforementioned wall effects on the waveform are frequency dependent as well. This is particularly important in TTWD applications where UWB waveforms are used to increase the down-range resolution of the system. As a result, walls have a dispersion effect on the waveforms because different spectral components are attenuated and slowed down differently. In time domain this causes broadening of the actual pulse waveforms compared with the transmitted pulses, thus reducing the actual bandwidth available in the system [8].

It is therefore important to characterize the frequency dependence of dielectric parameters for the most common wall construction materials. In [11] the complex dielectric constant for ten common wall materials, among which wood, plywood, drywall, glass, concrete, and brick, are provided in the frequency range above 2 GHz. The range 3.1-10.6 GHz was indeed assigned originally by the FCC in the US for UWB

applications. Values for brick and reinforced concrete at lower frequencies, 0.5-3 GHz, can be found in [12].

In chapter 1 of [8] a summary of the most relevant researches investigating dielectric properties of wall materials is provided. It is beyond the scope of this thesis to describe the techniques to measure dielectric parameters, but it is useful to mention quickly the range of values found for the most common materials. These values are then used in the processing of simulated and experimental data of this thesis. As previously mentioned, losses due to back reflection of the energy are far more consistent than those caused by conductivity losses. Therefore the focus is more on the material permittivity than on its conductivity. Dry wood has permittivity in the range 1.2-4.5, depending on the wood type, density, moisture content, and temperature. Bricks have values in the range 3-10, with strong influence of the water content: the higher the water percentage, the higher the permittivity. Concrete present the same strong dependence on the water content, but also on the presence of aggregates, additives, and reinforcing internal structures; for solid and dry concrete values in the range 5-7 have been found. Obviously it should be taken into account the variability of the material samples from structure to structure, and also the age of the building since these parameters may change with time because of internal molecular changes.

In conclusion, through-wall propagation has a multiplicity of effects on radar waveforms. These effects depend not only on the dielectric parameters of the wall material, but also on its internal structure and on the presence of mixed or multi-layered materials, which is common in realistic buildings. Numerical simulations can be therefore extremely useful to predict and analyze these effects, allowing to study the sensitivity of the radar performance to certain wall parameters and to optimize the waveforms to compensate for undesired wall effects.

4.2 CST Microwave Studio for Simulations of FMICW-based Radar Systems

In this section the suitability of the commercial software CST Microwave Studio to perform numerical simulations of through-wall radar systems based on FMICW waveforms is explored. An overview of the time-domain based method used in this software is given, focusing on the required steps to implement FMICW signals.

Performing numerical simulations of an environment or of an object means basically predicting information on the behaviour of the electromagnetic fields or corresponding voltages/currents in a certain volume of space. Mathematically this implies to solve Maxwell's equations, which represent the exact electromagnetic behaviour of the system under test. Since these simulations are computer based, continuous quantities like time and space which appear in the equations need to be discretized. Different numerical methods have been developed to approach this problem, but a discussion on the details of the implementation and pros and cons of these methods is beyond the scope of this thesis. A quick overview of some aspects of the different methods can be found in [13-14], and more details in specialized books on this topic like [15].

Numerical methods can be divided into time domain and frequency domain based. The former include Finite Integration Technique (FIT), Finite Difference in Time Domain (FDTD), and Transmission Line Matrix (TLM); the latter include Finite Element Method (FEM) and Method of Moment (MoM). All the aforementioned methods divide the volume under test in small geometric elements (for instance cubic cells or tetrahedra) and solve Maxwell's equations referring to these small elements; MoM is an exception since it is applied on surfaces rather than on volumes. Normally a multiplication of two matrices is performed for time domain methods at each time-step, whereas a linear system is solved for frequency domain methods by inverting a matrix.

CST Microwave Studio provides the user with different methods to approach simulated scenarios, namely a time domain solver based on FIT, a frequency domain solver based on tetrahedral mesh of the volume under test, and integral and asymptotic solvers based on surface and not volumetric mesh. The time domain FIT method proves to be the best choice for simulations of TTWD scenarios, which are electrically large, non-resonant, and rich in realistic details structures. Frequency domain methods would need more

computational resources to simulate the same scenario, being more suitable to analyse resonating structures. Integral and asymptotic solvers can characterize the field scattered by electrically large structures like ships or airplanes, and their RCS, but in case of TTWD the focus is in modelling the electromagnetic propagation within and through the wall, and thus time domain methods are more suitable.

FIT method discretizes the volume under test in hexahedral cells; the electric voltages on the edges and the magnetic flux through the faces of these cells are the unknown quantities from Maxwell's equations in integral form. The time derivatives of these equations are discretized in time-steps, generating an iterative process where the unknown are updated at each time-step and depend on the unknown of the neighbouring cells. This iterative algorithm is suitable for parallelization on high performance computing machines. The cell size must be small enough to give a good approximation of small parts and curved surfaces of the volume under test. It depends also on the frequency range of the simulation, since a minimum number of cells is expected to be included in one wavelength. A rule of thumb is taking the largest cell size equal to or smaller than one tenth of the shortest wavelength, corresponding to the highest frequency of interest, taking into account the dielectric permittivity of the material. Values of dielectric permittivity, conductivity, and magnetic permeability are normally assigned to each cell to simulate a material. Conformal techniques have been developed to model a single cell with two different materials, allowing the use of less and bigger cells to model curved surfaces or interfaces between materials. This implies faster and less computationally intensive simulations. Once the grid of hexahedral cells is assigned, the maximum value of the time-step is limited by the so-called Courant stability criterion. Basically the time-step has to be small enough for the information to propagate to all the neighbouring cells within a time-step.

A summary of the interesting features of the FIT method of CST Microwave Studio for TTWD simulations is:

- It is a "full wave" method based on the exact solution of Maxwell's equations, without any approximation. Therefore it can model precisely all the wave propagation phenomena, including near field effects or multiple scattering, neglected by other approximated methods.

- The combination of hexahedral grid and conformal techniques allow to model heterogeneous and complex structures, like human body phantoms and pieces of furniture in a room imported from specialized CAD software

- Being a time domain method, the UWB frequency response of the scenario under test is available with a single FFT operation, whereas a frequency domain method would need to run the simulations at many frequency points. All the transient features of antennas or components are recorded as well in the time domain.

- The method can be easily implemented in parallel architecture of high performance computing machines. Nevertheless, the computational burden in terms of required memory and CPU hours can be very heavy, especially to simulate big rooms or many targets, and if the frequency range increases.

As previously mentioned, the simulations performed in the context of this thesis' work aim at testing FMICW signals: basically FMCW signals plus gating sequences. Although CST Microwave Studio uses Gaussian pulses as default excitation waveform for the FIT method, FMCW signals can be implemented as user-defined waveforms. This causes a series of issues that need to be addressed in order to perform effective simulations, and they are discussed in the rest of this section. To the best of our knowledge, FMCW and FMICW signals have not been simulated so far in CST, therefore the following notes may be useful to establish a simulation approach also beneficial to contexts other than TTWD.

- **Pre-windowing**. As described in chapter 3, FMCW signals are mathematically cosine functions with sweeping frequency. At time 0 these functions are equal to 1, assuming normalized amplitude. This strong transition at the beginning of these user-defined waveforms introduces in CST potential instability and strong ripple artefacts on the recorded signals at the simulated receivers, compromising the effectiveness of the simulation. It should be noted that these ripples are artefacts due to the implementation of the FIT method in the software, and they have nothing to do with the actual scenario under test. A solution to this is

applying a window function to the FMCW signal to reduce its value at time 0, as if to simulate that the actual transmitted signal was already weighted by the window. Normally window functions are instead applied to the beat-note signal at the receiver, as mentioned in chapter 3. The beat-note signal is obtained by multiplying the received signal by a replica of the transmitted signal, and by low-pass filtering the result. If in the simulations a window is applied to the transmitted signal, at the heterodyne receiver both the received signal and the replica of the transmitted signal are multiplied by the window function, so that the beat-note itself is multiplied by the square power of the window. Therefore the square root of the window function is applied to the transmitted signal in the simulation, so that the beat-note is weighted by the actual window. In the simulations performed in this thesis' work and described in section 4.4 Hamming window is used. Equation (4.1) summarizes this issue: $v_M(t)$ is the beat-note signal given by the multiplication of the received signal $v_R(t)$ and the transmitted replica $v_T(t)$, each multiplied by the square root of the window function $w(t)$.

$$v_M(t) = v_T(t)\sqrt{w(t)}\,v_R(t - \tau)\sqrt{w(t - \tau)} \tag{4.1}$$

- **Postponed gating.** FMICW signals present sharp transitions between the time intervals when the transmitter/receiver is active and when it is not; the signal goes immediately to zero when the corresponding gating sequence assume value 0. These transitions cause the same problem mentioned before to the numerical implementation of the FIT method in CST, i.e. the introduction of instability and ripple artefacts. FMICW signals cannot therefore be directly simulated in CST. The solution is running the simulations using normal FMCW signals and postponing the application of the gating sequences to a later stage, after all the FMCW simulated signals have been collected from CST. In this thesis' work the FMCW signals from CST are loaded and processed externally through MATLAB. This provide flexibility since the same set of FMCW data from a single simulated scenario can be used in conjunction with different gating sequences without running again the simulation. This is an important advantage,

taking into account the heavy computational burden of each through-wall simulation.

- **Plane wave excitation.** In this thesis' work a plane wave excitation is used at the transmitter, and the electromagnetic fields are recorded at certain points in the volume to simulate the receivers; these points are called "probes" in CST. This allows to avoid modelling the antennas and their small physical parts, which may require a very fine volumetric mesh and make the simulations more intensive. Although ideal, plane waves can be considered a fairly realistic model for excitations coming from transmitter antennas located at great distance, in the far field. As in equation (4.2), CST probes record the total field, which is the superposition of the incident field (the plane wave itself) and the scattered field (signals reflected back by the targets), which the radar system should actually measure.

$$E_{TOT} = E_{INC} + E_{SCAT} \tag{4.2}$$

Since the FMCW signal is always active during the simulation, there is no direct way in CST to remove the incident field and extract the scattered field. The solution comes from simulating an empty copy of the scenario under test with the same excitation, where the electrical parameters of the vacuum are assigned to all the objects. In this case the field recorded at the probes is just incident field since there are no scatterers in the empty scenario, as in (4.3).

$$E_{TOT}^{empty} = E_{INC}^{empty} = E_{INC} \tag{4.3}$$

Finally the desired scattered field for the scenario under test can be computed by subtracting the recorded field for the empty scenario from the total field, as in equation (4.4). The assumption is that the incident field is the same for the scenario under test and the empty scenario, which is true if the plane wave and the FMCW signals are set with the same options in both simulations.

$$E_{SCAT} = E_{TOT} - E_{INC}^{empty} \tag{4.4}$$

Following the aforementioned suggestions it is possible to simulate effectively FMICW signals for TTWD scenarios using the time domain solver of CST Microwave Studio.

Results aimed at showing the effectiveness of FMICW waveforms as wall removal technique are presented in section 4.4 of this chapter.

4.3 Overview of Imaging Algorithms

In the previous section it has been mentioned that FMCW signals recorded at the probes and simulating the received signals of a real system are loaded onto MATLAB for processing. This processing may include the application of gating sequences to get FMICW signals, and it simulates the operation of a heterodyne detector described in chapter 3, namely multiplication and low-pass filtering. The results are range profiles for each probe, which can be combined to create radar images through suitable imaging algorithms.

The algorithms used to process simulated and experimental data of this thesis' work are briefly described in this section. Many more algorithms have been proposed in the literature (Stolt and Kirchhoff migration, or Capon beam-former among them [8]), but their rigorous analysis is beyond the scope of this work, which is more focused on investigating the suitability of FMICW as wall removal technique. A useful overview of imaging algorithms in the context of TTWD can be found in [16].

Back Projection (BP) is one of the simplest imaging algorithms for TTWD [1]. The area under test is divided into a grid of pixels, and for each transmitter/receiver pair the round-trip delay related to each pixel is computed. The round-trip delay is the time for the waveform to propagate from the transmitter to the target, and to be reflected back to the receiver. The values of the received signals at these round-trip delay values are added together to get the intensity value of each pixel, thus forming an image when the procedure is repeated for all the pixels.

Since a plane wave is used as excitation for the numerical simulations performed in this thesis' work, there is a single transmitter and multiple probes as receivers. The pixel intensity for the BP algorithm can be written therefore as in equation (4.5)

$$I(x_i, y_j) = \sum_{k=1}^{N} E_k(\tau_{ijk}) \qquad (4.5)$$

where the indices (i,j) denote the coordinates of the pixels in the X and Y directions respectively, and the index k denotes one of the N receivers. E_k is therefore the recorded signal at one of the receivers, and τ_{ijk} is the round-trip delay related to a particular pixel-receiver combination.

The following two imaging algorithms are originally applied to the context of breast cancer detection using UWB signals [17-18]. Delay-Sum-Integration (DSI) algorithm differs from BP in the use of integration over a time window to generate the pixel intensity values, rather than simply picking a point from the received response at the corresponding value of round-trip delay. This generates radar images where the coloured spots related to the targets appear more focused.

For each pixel the N received signals are considered up to the round-trip delay corresponding to the maximum expected target range, while the remaining samples are discarded. Each signal is then circularly shifted by the round-trip delay corresponding to that particular pixel-receiver pair. Finally all the shifted signals are added together and the result is integrated over a suitable window to get the pixel intensity value, as in equation (4.6). The radar image is obtained by repeating this process for all the pixels.

$$I(x_i, y_j) = \int_0^W \sum_{k=1}^N E_k(t - \tau_{ijk}) dt \qquad (4.6)$$

The length of the integration window W is equal to the pulse duration in [17-18], where pulse-based systems are discussed. When using FMCW signals, a good estimation of this window is the main lobe width of the frequency components of the beat-note signal. Therefore the reciprocal of the chirp bandwidth is a good value. Assuming 1.5 GHz, the window is roughly 0.667 ns long.

Delay-Multiply-Sum-Integration (DMSI) is an interesting extension of the previous algorithm, with the addition of multiplications in pairs of the responses after the circular shifting. The mathematical formulation is modified as in (4.7):

$$I(x_i, y_j) = \int_0^W \sum_{k=1}^{N-1} \sum_{l=k+1}^N E_k(t - \tau_{ijk}) E_l(t - \tau_{ijl}) dt \qquad (4.7)$$

where the indices k and l denote which receivers are involved in the multiplication in pairs, and τ_{ijk} and τ_{ijl} are the round-trip delays of each response, depending on the pixel and on the receiver taken into account. Compared with the previous algorithm, the additional multiplications contribute to increase further the focus of the coloured spots related to the targets.

It should be noted that for both DSI and DMSI an additional square or fourth power operation can be added to the resulting functions in (4.6) and (4.7) before the integration, in order to get further focused images. However, increasing too much the focusing may lead to cancel some targets in the final radar images if their reflections are too weak compared with other targets or with the clutter level. In other words, the focusing procedure may be thought of as a scale, which tends to get narrower when the focus is increased in the imaging algorithm, so that weaker targets are included at the bottom of the scale together with the noise/clutter. Therefore a compromise should always be sought between nicely focused images and the probability of missing weak targets.

The effectiveness of the aforementioned algorithms relies on accurate estimations of the round-trip delays, which in the context of TTWD is not a trivial task because of the effects of the through-wall propagation. More details are given in the next subsection.

4.3.1 Round-trip delay estimation in the context of TTWD

In equations (4.5)-(4.7) it can be seen that the effective implementation of these imaging algorithms depend on the accurate estimation of the round-trip delay for the transmitter-pixel-receiver path. Assuming the position of transmitters and receivers to be known, the estimation of this delay would be easy if the scenario under test was in free space, since the delay would be simply equal to the spatial distance divided by the propagation speed c (3×10^8 m/s).

Unfortunately the presence of the wall complicates this estimation. As discussed in subsection 4.1.1, the presence of the wall slows down the electromagnetic waves and this effect is proportional to the square root of the dielectric permittivity ε_r. Therefore materials with high permittivity like concrete exhibit stronger effects. An additional

factor should be therefore added to the estimation of the round-trip delay compared with the ideal free space situation. The value of this correction depends on the length of the through-wall path: the longer the waves are propagating within the wall, the longer the correction delay factor will be. So the actual problem is the estimation of the through-wall propagation path.

Failure to considering this additional delay causes displacement and blurring of the targets in the final radar images. In [19] the authors analyze these effects when the estimation of either the thickness or the permittivity of a uniform wall has inaccuracies. They propose methods to reduce this uncertainty combining data of measurements at different stand-off distances from the wall. The same authors propose in [20] an auto-focusing technique based on high order statistic extracted from the data in order to mitigate the undesired effects on the final image.

Rather than applying additional processing to compensate for the bad effects of inaccurate values of the through-wall propagation path, several techniques have been proposed in the literature to provide reliable estimations of this quantity. In [21] a beam-forming algorithm is proposed to take into account the effects of a uniform wall once its thickness and permittivity, as well as the angle of incidence are known. This approach relies on the Newton-Raphson numerical method to solve a set of transcendental equations derived from taking into account the refraction at the air-wall interfaces. In [22] this approach is extended to 3D imaging with data from a planar array. In [16] the actual round-trip delay is estimated referring to a mock scenario where the internal wall is touching the target, so there is no air layer between wall and target itself. In this way some approximations in the refraction equations are possible, in order to simplify the numerical method (here Newton-Horner method is suggested) and speed up its convergence. In [1] an extremely easy estimation is applied, which does not require any numerical method. The through-wall path is simply equal to the wall thickness, neglecting refraction and unrealistically assuming that all the waves impinge perpendicularly on the wall.

In this thesis' work the round-trip delay is estimated without solving equations through numerical methods for simplicity, but the oblique trajectory of the electromagnetic waves is considered. This approach can be called "straight-ray approximation" since it

does not take into account the refraction at the air/wall interfaces, thus avoiding to solve transcendental equations with angles, but still providing a sufficiently accurate estimation.

The round-trip delay τ_{ijk} from equations (4.5)-(4.7) can be written as the sum of the part related to the transmitter-pixel path and the pixel-receiver path, as in equation (4.8):

$$\tau_{ijk} = \tau_{TX} + \tau_{RX} \tag{4.8}$$

As mentioned, the transmitter is a plane wave in the numerical simulations performed in this thesis' work; therefore the excitation wavefront is uniform for all the pixels in the volume under test and the wave impinges perpendicularly to the wall. This allows the simplification of the estimation of the round-trip delay for the transmitter-pixel path, since the actual through-wall path is simply the thickness of the wall D, as in equation (4.9)

$$\tau_{TX} = \frac{R_{TX}(i,j)}{c} + \frac{D}{c}\sqrt{\epsilon_r - 1} \tag{4.9}$$

R_{TX} is the transmitter-pixel distance, which in case of plane wave excitation is the distance from the pixel to the boundary of the simulated volume where the plane wave ideally starts to propagate; R_{TX} depends only on the pixel coordinates (i,j) since the plane wave wavefront is uniform. It should be noted that the first term in equation (4.9) refers to the free space case, with the second term correcting for the presence of the wall. The round-trip delay related to the pixel-receiver path can be written as in (4.10):

$$\tau_{RX} = \frac{R_{RX}(i,j,k)}{c} + \frac{L}{c}\sqrt{\epsilon_r - 1} = \frac{R_{RX}(i,j,k)}{c} + \frac{D}{c \cdot cos\theta}\sqrt{\epsilon_r - 1} \tag{4.10}$$

where the first term of the equation is referred to the free space delay for the pixel-receiver path, and the second term corrects for the presence of the wall assuming "straight-ray approximation", with L through-wall path length and θ the angle between the pixel-receiver path and the perpendicular to the wall. This angle can be computed from the coordinates of pixel and receiver as in equation (4.11), with reference to the mock geometry shown in figure 4.1.

$$\theta = arctg\left(\frac{|y_p - y_r|}{|x_p - x_r|}\right) \tag{4.11}$$
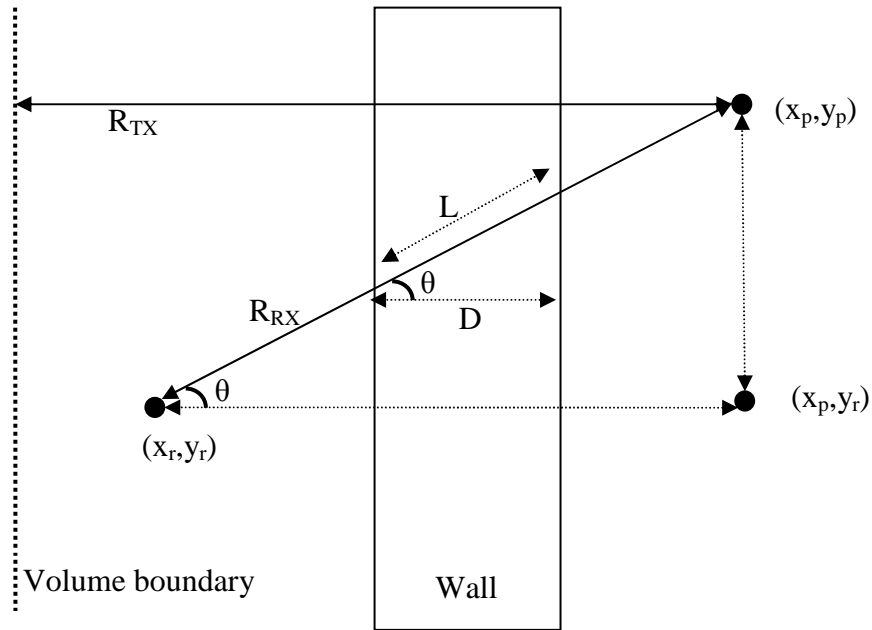
Figure 4.1 Mock geometry of the through-wall scenario for θ estimation

The methods presented so far to estimate the actual through-wall path and consequently correct the round-trip delay assume homogeneity of the wall structure, and knowledge of the thickness and permittivity. Inaccuracies in these two parameters may compromise the effectiveness of the correction, and again lead to displacement and blurring in the final images.

Unfortunately in realistic operational conditions these parameters are not known. Techniques for their estimation have been developed as in [8, 11], but their application can be time consuming or not practical in operational scenarios (for instance if one antenna needs to be placed on the other side of the wall). Furthermore, real walls are rarely homogeneous: they present multi-layered structures, internal gaps, and irregularities (reinforcement structures or pipes for instance) for which the through-wall path estimation would be far more complex. It is therefore easier in real applications applying the aforementioned estimations assuming homogeneous walls and using values of permittivity in the range of those reported in the literature for common wall materials. A margin of displacement for the position of the targets in images from real through-wall scenarios should be always expected.

4.4 Results from Numerical Simulations

In this section the application of the proposed FMICW technique to remove wall reflections is discussed. Results from numerical simulations of realistic environments and its effectiveness are shown through radar images. The process to select suitable gating sequences and parameters for each scenario under test is also described. Comparisons of the performance of the different imaging algorithms presented in the previous section are provided.

The simulated environments are three-dimensional rooms with walls having different materials and structure; floor and ceiling are simulated as well for more realism and to prevent artefacts from diffraction at the edges of the wall, as suggested in [4]. Targets are placed inside these rooms, in particular a metallic cabinet and a human phantom; the phantom is modelled with uniform material reproducing the parameters of human skin (dielectric permittivity 31.29 at 1.25 GHz frequency), as suggested in [5-6]. This allows speeding up the simulation time since the internal tissues of the human body are not modelled. As previously mentioned, the transmitter is modelled for simplicity's sake as a plane wave, whereas the receivers are modelled as probes which sample the electromagnetic fields in the volume under test. The images shown in this section are created using 9 probes, which are placed 25 cm apart, thus forming a 2m long array. The colour scale of all the images presented in this section is in decibel and indicated next to each image. When FMICW waveforms are used, the values of bit duration and delays τ_{RX1} and τ_{RX2} for the gating sequences are multiple of 0.125 ns, which is the time step provided by the AWG used for the radar experiments. Details about FMICW waveforms are given in chapter 3 of this work, whereas the hardware components of the radar system used for the experimental campaign are described in chapter 5.

Figure 4.2 shows a view of the first simulated scenario, where the room area is 235×200 cm and the stand-off distance of the probes from the wall is 30 cm. The wall is solid, 15 cm thick, and made of 1 year old concrete (with dielectric permittivity ε_r 5.657 at 1.25 GHz, as provided by CST). The metallic cabinet and the human phantom are placed at 220 cm and roughly 150 cm from the array of probes, respectively. The simulated FMCW chirp has bandwidth 0.5-2 GHz and duration 1200 ns. Assuming for simplicity

maximum range of 5 m in the anti-aliasing condition in equation (3.31), the maximum bit duration is 12/N ns for a gating sequence with N bits.

Figures 4.3-4.5 compare radar images for this scenario using FMCW (top) and FMICW (bottom) waveforms with BP, DSI, and DMSI imaging algorithms, respectively. Focusing on the FMCW images only, it can be seen that wall reflections are the strongest contribution recorded in the images as expected; the metallic cabinet can be detected, whereas the human phantom cannot even if it is closer to the probes than the cabinet. Given the stand-off distance of this scenario, wall reflections are expected to be received at a round-trip delay of 2 ns. A 3 bit M-sequence is chosen as gating sequence because it is the shortest sequence in terms of number of bits providing a flat area in its MRS in order not to attenuate the reflections from the targets; fewer bits allow longer bit duration according to the anti-aliasing condition in equation (3.31). With bit duration sufficiently long, the reflections from the wall can be placed at the blind range at the beginning of the MRS slope and thus attenuated. The MRS of the sequence used in this scenario can be seen in figure 4.6, with the chosen bit duration 7.5 ns.

In figures 4.3-4.5 (bottom) both targets can be successfully detected thanks to the application of the gating sequence. It should be noted that the scale of the images is the same in comparing FMCW with FMICW results. Comparing results from different algorithms, it can be seen that DSI and DMSI provide better images than BP. The coloured spots are more focused on the actual positions of the targets and they are surrounded by less clutter.

Figure 4.2 View of simulated scenario 1

Figure 4.3 Comparison of FMCW-FMICW images for simulated scenario 1 – BP algorithm

Figure 4.4 Comparison of FMCW-FMICW images for simulated scenario 1 – DSI algorithm

Figure 4.5 Comparison of FMCW-FMICW images for simulated scenario 1 – DMSI algorithm

Figure 4.6 MRS of the 3 bit M-sequence used in simulated scenario 1

The second simulated scenario is a copy of the previous one, but with two modifications: the stand-off distance of the probes from the wall is now increased to 250 cm, and a different material is used for walls, ceiling, and floor (40 years old concrete, with permittivity 4.642 at 1.25 GHz). A view of this scenario can be seen in figure 4.7, where the green points on the left represent the probes where the electromagnetic fields are sampled and recorded. The targets are the usual metallic cabinet and the human phantom, placed at 440 cm and 370 cm from the probes, respectively. The duration of the simulated chirp has been increased to 3000 ns, so that the maximum allowed bit duration from the anti-aliasing condition is increased as well. Assuming a maximum range of 6 m, this condition yields maximum bit duration of 25/N ns for a gating sequence with N bits.

Figures 4.8-4.10 compare results with FMCW (top) and FMICW (bottom) waveforms using BP, DSI, and DMSI algorithms respectively. As expected wall reflections only are detected in the FMCW images, therefore a gating sequence should be applied to mitigate them and to detect the targets. However the longer stand-off distance prevents the application of the gating approach used in the previous scenario, i.e. choosing a bit duration long enough to place wall reflections at the beginning of the slope of the MRS. The round-trip delay corresponding to 250 cm stand-off distance for the wall is indeed roughly 16.67 ns, whereas the maximum bit duration allowed from the anti-aliasing condition is 12.5 ns for a square wave or 8.33 ns for a 3 bit M-sequence, therefore not enough to mitigate wall reflections.

A solution is to design the gating sequence so that wall reflections are placed at the second blind range of the MRS of the gating sequence. Assuming again a 3 bit M-sequence, the suitable bit duration to implement this approach is 5.75 ns as in the MRS shown in figure 4.11; with this bit duration the second blind range is located at 17.25 ns, effective in mitigating wall reflections at 16.67 ns. Looking at figures 4.8-4.10 (bottom), it can be seen that reflections from the first air/wall interface are removed, but there are residual reflections from the internal back wall interface. The detection of both targets is obtained thanks to the use of the FMICW waveforms. As expected the coloured spot related to the metallic cabinet is brighter than the spot related to the human phantom, which can be correctly detected. As previously observed, DSI and DMSI provide better

images, in particular the two artefacts recorded in the BP image are removed, as well as the residual of the external air/wall interface.
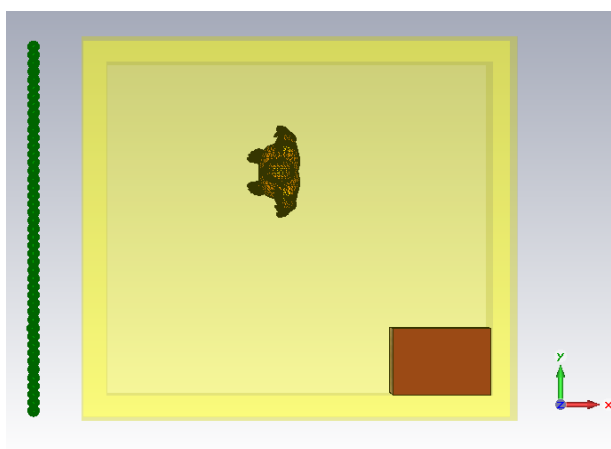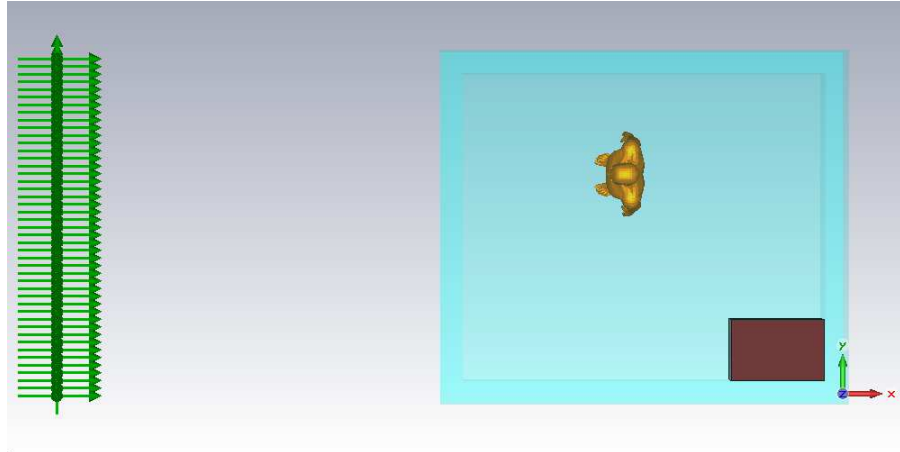

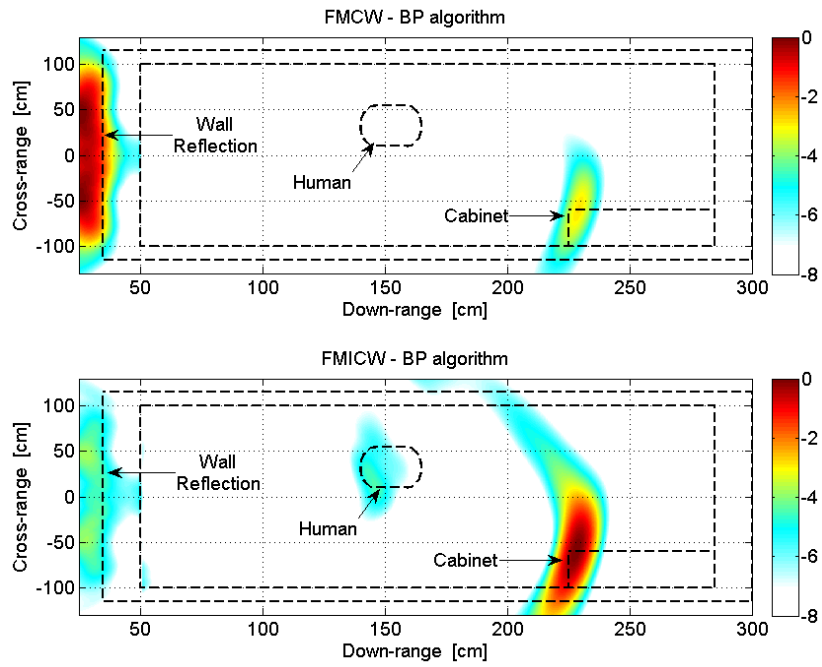**Figure 4.7 View of simulated scenario 2**
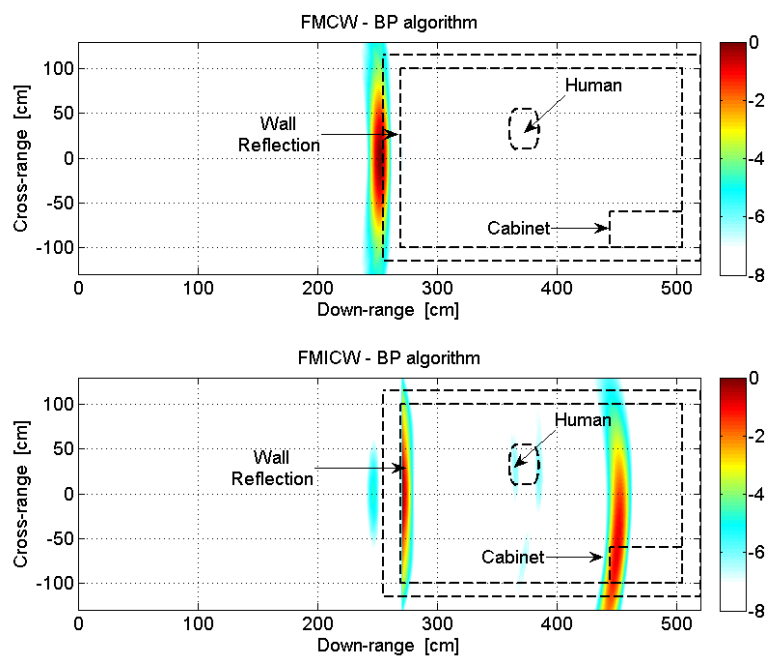
Figure 4.8 Comparison of FMCW-FMICW images for simulated scenario 2 – BP algorithm
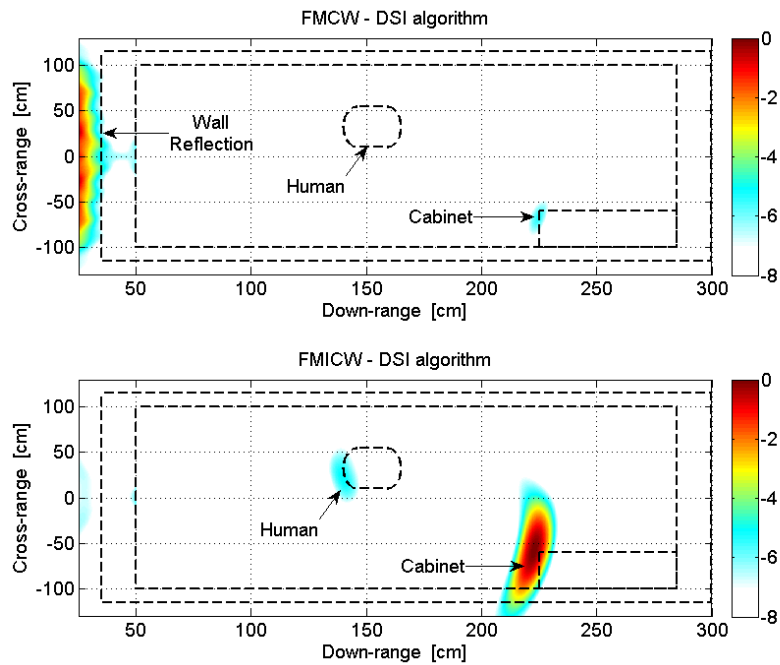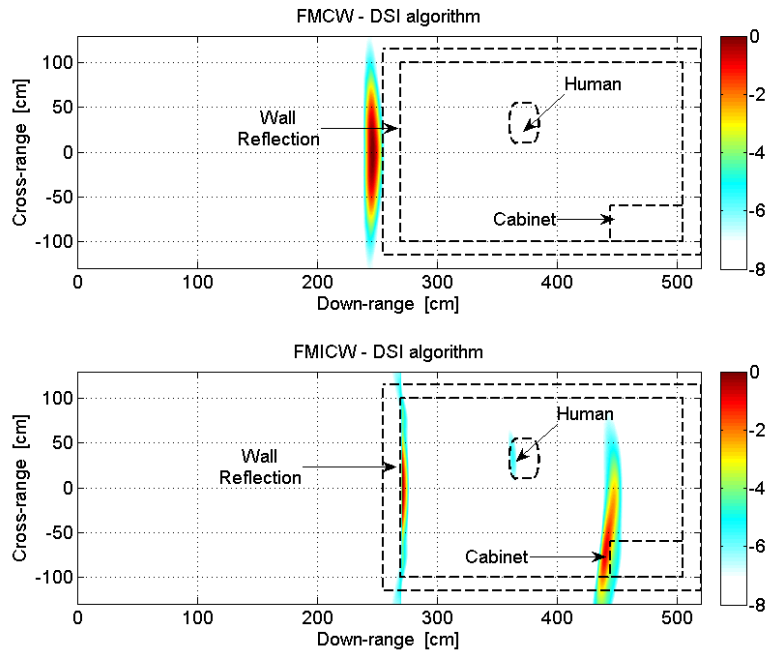
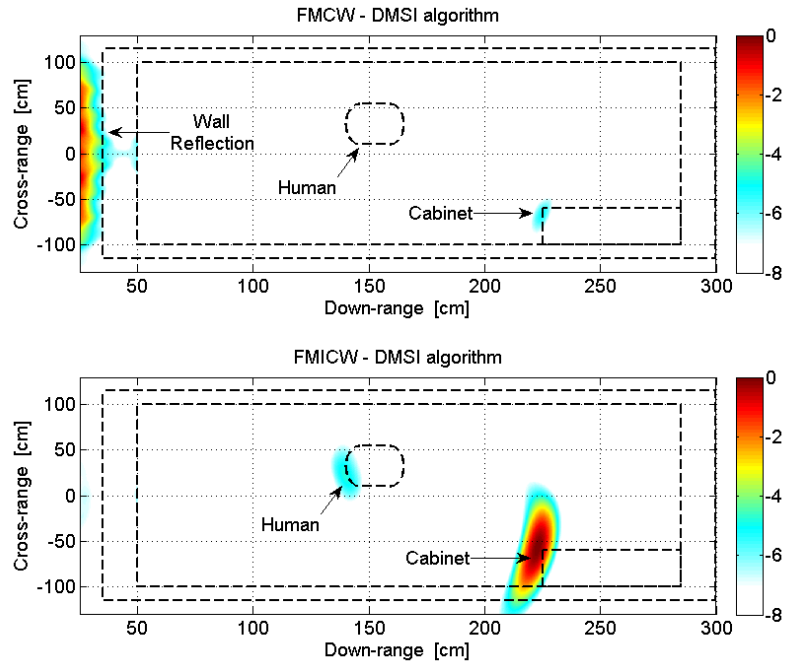**Figure 4.9 Comparison of FMCW-FMICW images for simulated scenario 2 – DSI algorithm**

Figure 4.10 Comparison of FMCW-FMICW images for simulated scenario 2 – DMSI algorithm
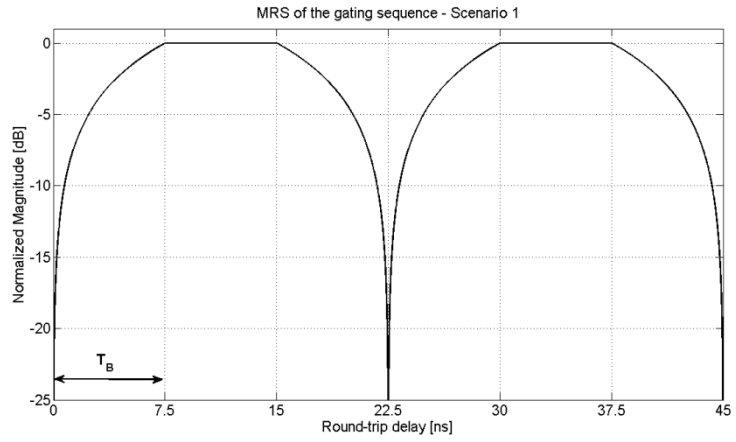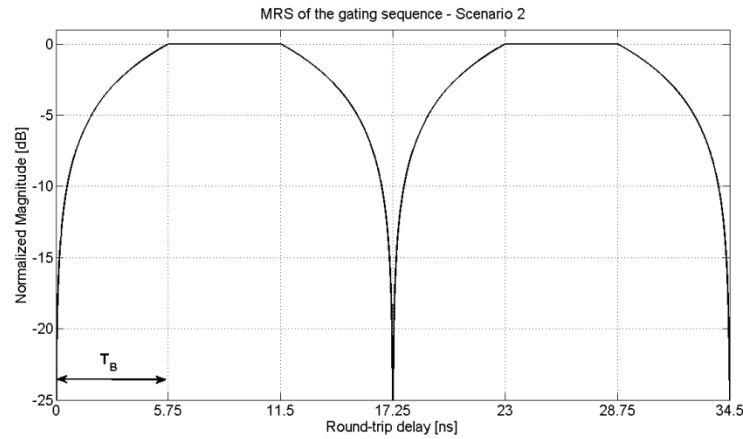
Figure 4.11 MRS of the 3 bit M-sequence used in simulated scenario 2

In the third scenario the wall material is turned into wood (permittivity ε_r 2.017 at 1.25 GHz), whereas the ceiling and floor are still made of 40 years old concrete as in the previous scenario. The targets and their positions inside the room are still the same as shown in figure 4.7. The simulated FMCW signal is the same, with 1.5 GHz bandwidth and duration 3000 ns, and thus the anti-aliasing condition does not change.

Figure 4.12 compares radar images obtained using FMCW (top) with FMICW (bottom) waveforms; images on the left are created using the BP algorithm, whereas those on the right using the DMSI algorithm. Although in this scenario the metallic cabinet is already detected using FMCW waveforms, as in both top figures, and even the human phantom is detected for the DMSI image, the application of the FMICW waveforms improve the detection of both targets and remove the contribution from the wall. The fact that the targets can be already detected using normal FMCW waveforms is due to the small value of permittivity for wood used as wall material in comparison with concrete used in the previous simulated scenarios. As expected, images produced by the DMSI algorithm are better focused than those by BP. DSI results are not shown since they are very similar to those using DMSI, as already observed in figures 4.4-4.5 and 4.9-4.10 for the previous scenarios.

The FMICW gating approach for this scenario is the same as in the previous one, i.e. the second blind range of the MRS is used to remove wall reflections. The MRS of the

gating sequence shown in figure 4.13 is a 3 bit M-sequence with bit duration 5.625 ns and delays τ_{RX1} and τ_{RX2} equal to 0.5 ns each. This gives an actual blind range duration of 1 ns long centred at round-trip delay of 16.875 ns (wall reflections for stand-off distance 250 cm are placed at round-trip delay of roughly 16.67 ns).

Figure 4.12 Comparison of FMCW-FMICW images for simulated scenario 3 – BP and DMSI algorithm
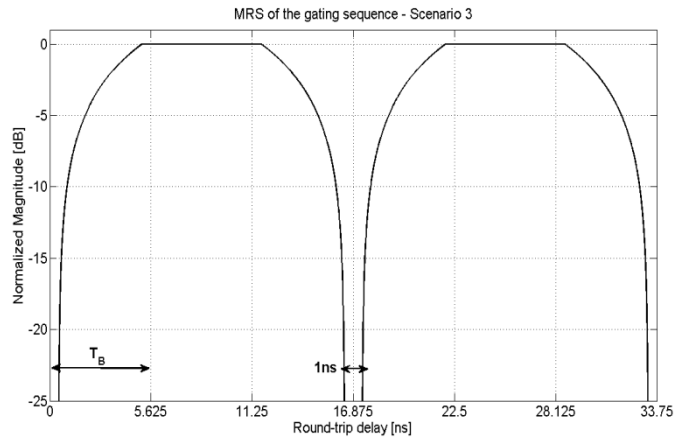
Figure 4.13 MRS of the 3 bit M-sequence used in simulated scenario 3

The fourth simulated scenario presents the same environment as the previous two scenarios, but the material for walls, ceiling, and floor is 1 year old concrete. The FMCW signal and anti-aliasing condition are the same as in scenarios 2 and 3.

Figure 4.14 compares FMCW and FMICW results with two different imaging algorithms, BP and DMSI. Unlike the previous scenario with walls made of wood and similarly to scenario 2 with 40 years old concrete, here the targets cannot be detected using normal FMCW signals, whereas the application of the gating sequence allows detection of both targets, human phantom included. The MRS of the chosen gating sequence is shown in figure 4.15: it is the usual 3 bit M-sequence, with bit duration 5.75 ns and delays τ_{RX1} and τ_{RX2} equal to 0.5 ns, giving a blind range which is 1 ns long. Comparing FMICW images with BP and DMSI, it can be seen that the latter removes the artefacts close to the human phantom which are present in the BP image; this was already observed in scenario number 2, as in figures 4.8 (bottom) and 4.10 (bottom).

Figure 4.14 Comparison of FMCW-FMICW images for simulated scenario 4 – BP and DMSI algorithm

Figure 4.15 MRS of the 3 bit M-sequence used in simulated scenario 4

So far simulated rooms with solid wall structures and different materials have been presented, either with short stand-off distance as in scenario number 1, or with longer distance as in scenarios 2 to 4. Now the fifth simulated scenario presents a different wall structure: a 5 cm layer made of 1 year old concrete is followed by a 5 cm air gap, and then by another 5 cm solid layer made of concrete, as seen in figure 4.16. This wall structure is more realistic since real walls often present internal air gaps for insulation purposes. From a radar perspective this structure is more challenging than a solid wall since it tends to trap the electromagnetic energy, so that wall reflections have extended duration and therefore longer blind ranges in the MRS are needed to cancel them through FMICW waveforms. Successful detection of both targets can be achieved by having longer delays τ_{RX1} and τ_{RX2} for the gating sequence, as shown in figures 4.17-4.18. Figure 4.17 compares images with FMCW and FMICW waveforms and with BP and DMSI imaging algorithms; figure 4.18 shows the MRS of the gating sequence used in this scenario. Anti-aliasing condition and gating approach are the same as in the previous scenarios with long stand-off distance, but here a square wave sequence is used, with bit duration 8.625 ns and τ_{RX1} and τ_{RX2} equal to 1 ns each, and thus the blind range is 2 ns long. This gating sequence is designed so that the blind range at round trip-delay values 16.25-18.25 ns can remove the reflections from the wall expected at roughly 16.67 ns, including their extension due to the air gap. The flat part of the MRS is located at the round-trip delay corresponding to the human phantom (distance 370 cm from the probes, thus roughly 24.67 ns delay), whereas the reflection from the metallic

cabinet (expected at roughly 29.33 ns being its distance 440 cm) are located in the falling slope of the MRS; this should not be a problem since the metallic cabinet is a high reflective target compared with the human phantom. The effectiveness of this approach can be seen in figure 4.17, where both targets can be detected with the FMICW waveform.

Figure 4.16 View of simulated scenario 5

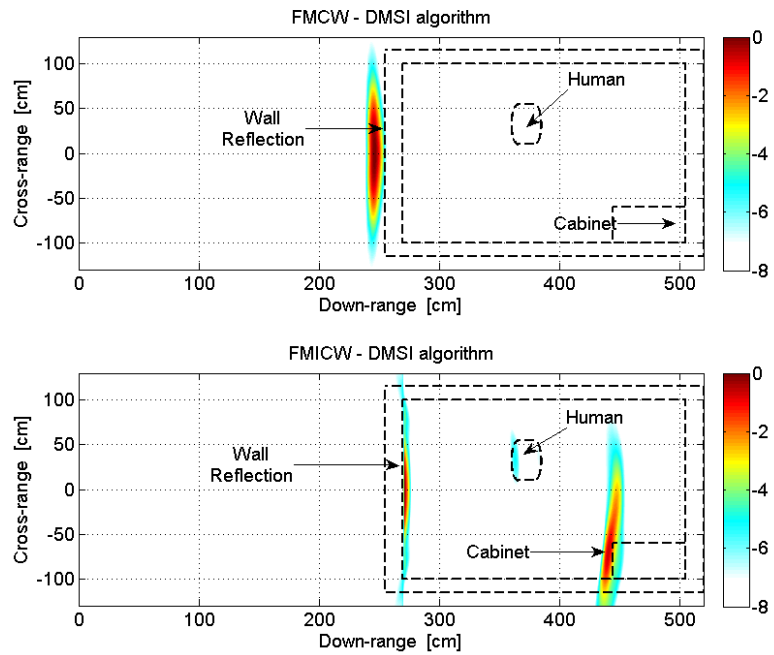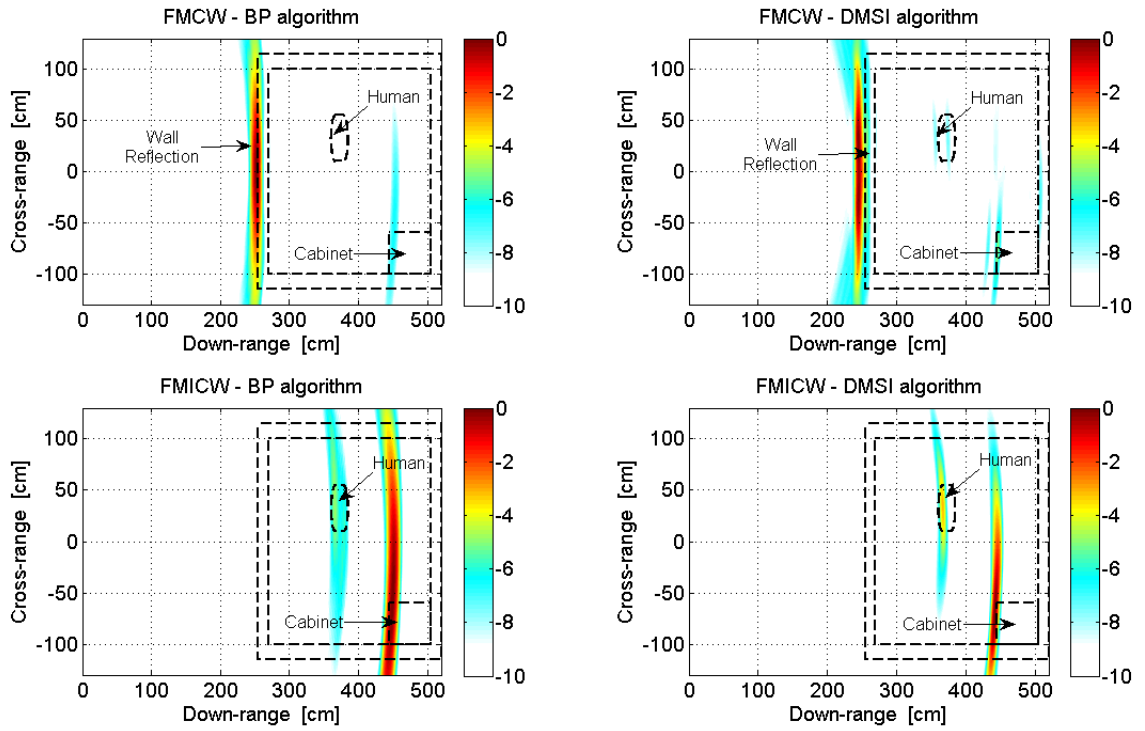**Figure 4.17 Comparison of FMCW-FMICW images for simulated scenario 5 – BP and DMSI algorithm**
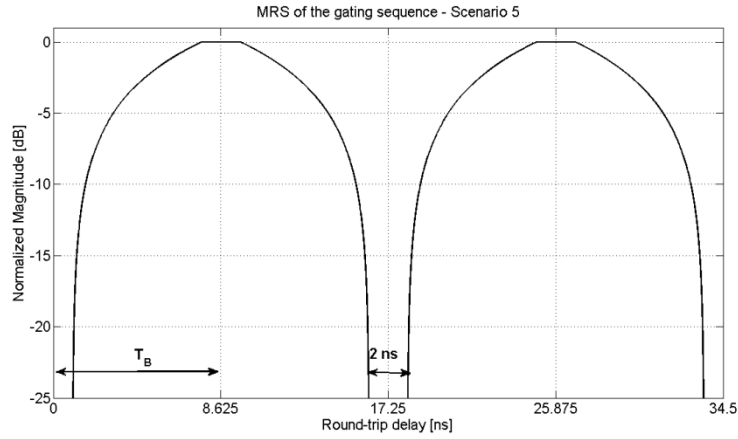
Figure 4.18 MRS of the square wave sequence used in simulated scenario 5

In scenario number 6 a room with another wall structure is simulated and analyzed. The wall is made of cinder blocks and the material is the usual 1 year old concrete; each cinder block has overall size 24×15 cm with two 9×7.5 cm air cavities. The overall area of the simulated room is 258×192 cm, with wall thickness 15 cm; the metallic cabinet and the human phantom are placed at 460 and 370 cm from the probes, respectively. Similarly to the previous scenario, this realistic wall structure is particularly challenging for radar detection because of the internal cavities and multiple reflections which take place inside the wall [7]. These phenomena extend the wall reflections contribution in terms of round-trip delay, so that a much longer blind range in the MRS of the FMICW gating sequence is needed. More artefacts are also introduced in the images by this wall structure.

Figure 4.20 shows the usual comparison of results with FMCW and FMICW waveforms, using BP and DMSI imaging algorithms. Figure 4.21 shows the MRS of the gating sequence used in this scenario: it is a square wave with bit duration 10 ns and τ_{RX1} and τ_{RX2} equal to 3.625 ns, so that the blind range is 7.25 ns long. Such a wide blind range is required to remove the extended wall reflection due to the cinder blocks wall. This undesired signal is indeed expected to start at round-trip delay 16.67 ns since the stand-off distance is 250 cm, and the blind range shown in figure 4.21 covers the range 16.375 ns up to 23.625 ns, thus it is suitable for wall removal. In the bottom sub-figures of figure 4.20 the effectiveness of the chosen gating sequence in removing wall reflections can be seen, as well as the successful detection of both targets. DMSI

algorithm is preferable since it removes some of the artefacts due to this wall structure, which are otherwise present in the BP image. The slight displacement of the detected human phantom in figure 4.20 (bottom-left) could be caused by the inaccuracy in the estimation of the permittivity of this composite wall structure.

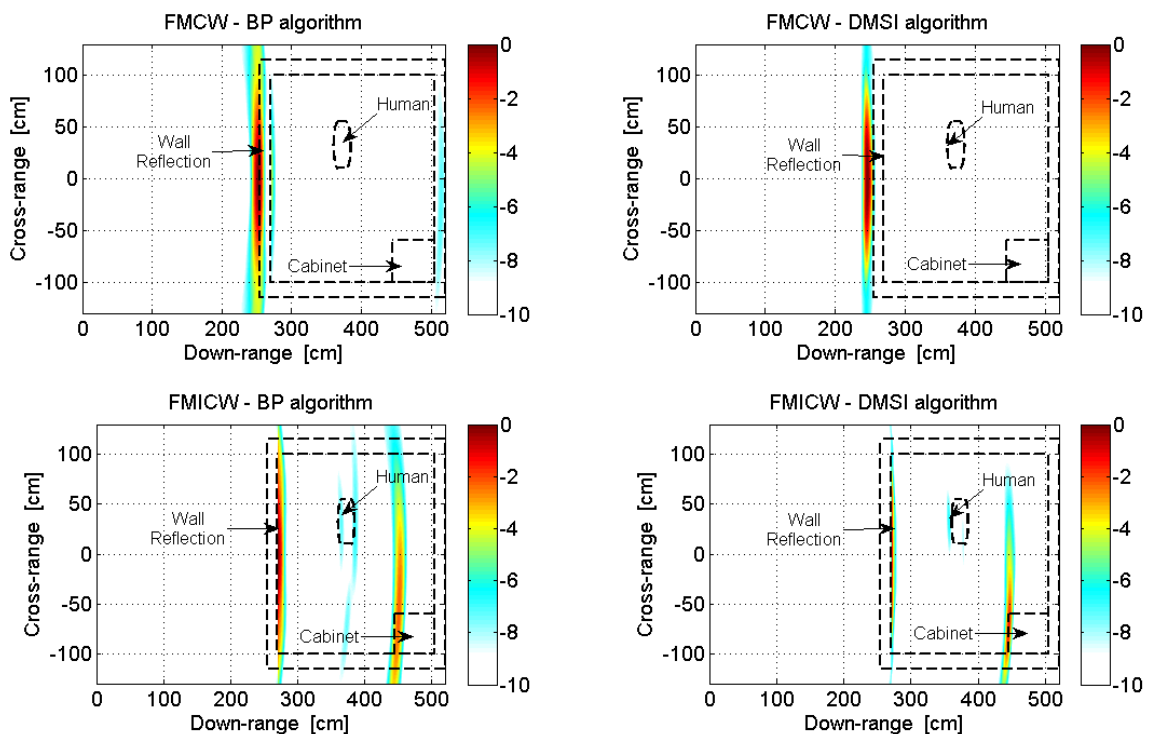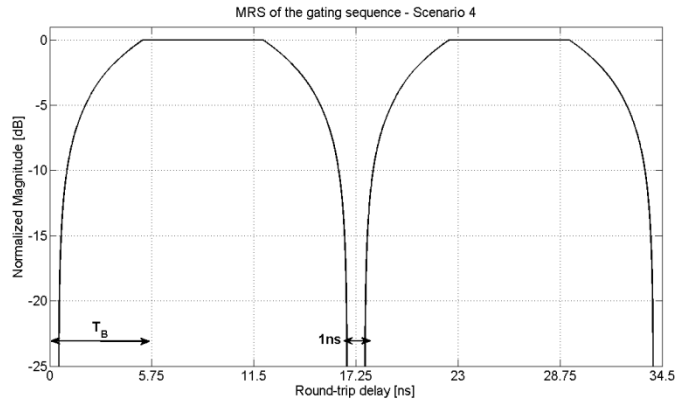**Figure 4.19 View of simulated scenario 6**

Figure 4.20 Comparison of FMCW-FMICW images for simulated scenario 6 – BP and DMSI algorithm
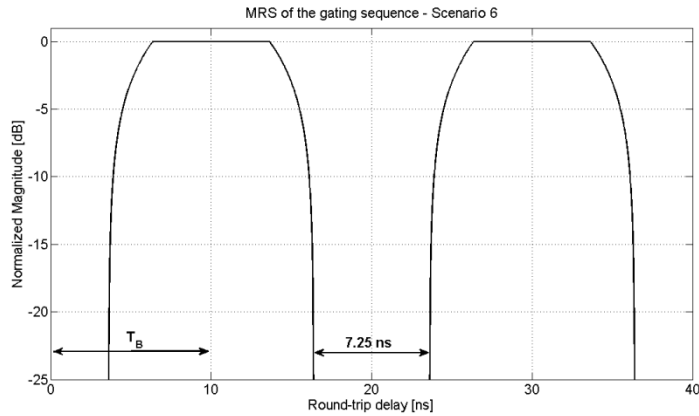
Figure 4.21 MRS of the square wave sequence used in simulated scenario 6

In scenario number 7 the stand-off distance is reduced to 25 cm. The room has an area of 290×170 cm (thus larger than the previous ones) and solid wall with thickness 15 cm; walls, ceiling, and floor are made of 40 years old concrete. The targets are two human phantoms, one facing the array of probes with its chest and one with its back, placed at roughly 160 and 240 cm from the probes, respectively; both phantoms are uniformly modelled with skin-like material. The FMCW signal duration has been increased to 5000 ns, so that the maximum bit duration given by the anti-aliasing condition increases as well. Assuming maximum range to the target 5 m for simplicity, the maximum allowed bit duration is 50/N ns for a gating sequence of N bits. Two different gating sequences have been tested in this scenario, namely the 3 bit M-sequence with bit duration 8.75 ns and the square wave with bit duration 16 ns. The MRS of both sequences can be seen in figure 4.24. The first gating sequence provides flat MRS, i.e. no attenuation, at values of round-trip delay corresponding to the reflections of the two targets, 10.67 and 16 ns, respectively, whereas wall reflections are attenuated by the blind range at the beginning of the MRS. In figure 4.23 (top) images using FMCW and FMICW waveforms gated through the M-sequence are compared and the effectiveness of the FMICW waveform in detecting both targets is shown. In the bottom-left sub-figure the FMICW image is created using DMSI rather than BP algorithm to get better focused images; however the farthest target appears attenuated with this algorithm, since its backscattered reflection is much weaker compared with the closer target. If the square wave gating sequence is applied as in the bottom-right sub-figures, both targets appear well detected in the image even with DMSI algorithm. The MRS of the chosen

square wave is designed to have zero attenuation at the round-trip delay related to the farthest target (16 ns) and to moderately attenuate the reflection of the closest target. The overall effect is that both targets appear having the same level of intensity in the image. This scenario was useful to highlight the effect of different gating sequences and how a square wave can be applied to enhance the detection of far, less reflective targets.
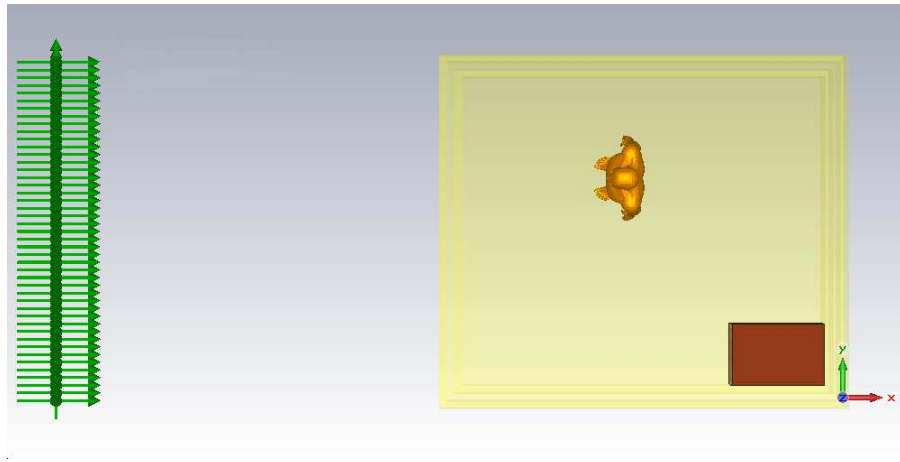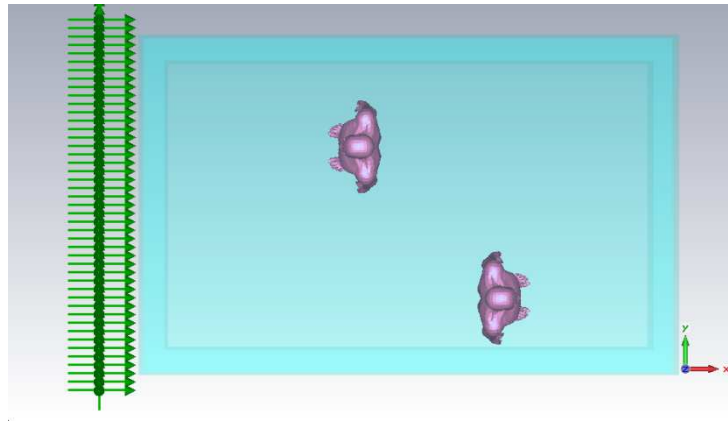

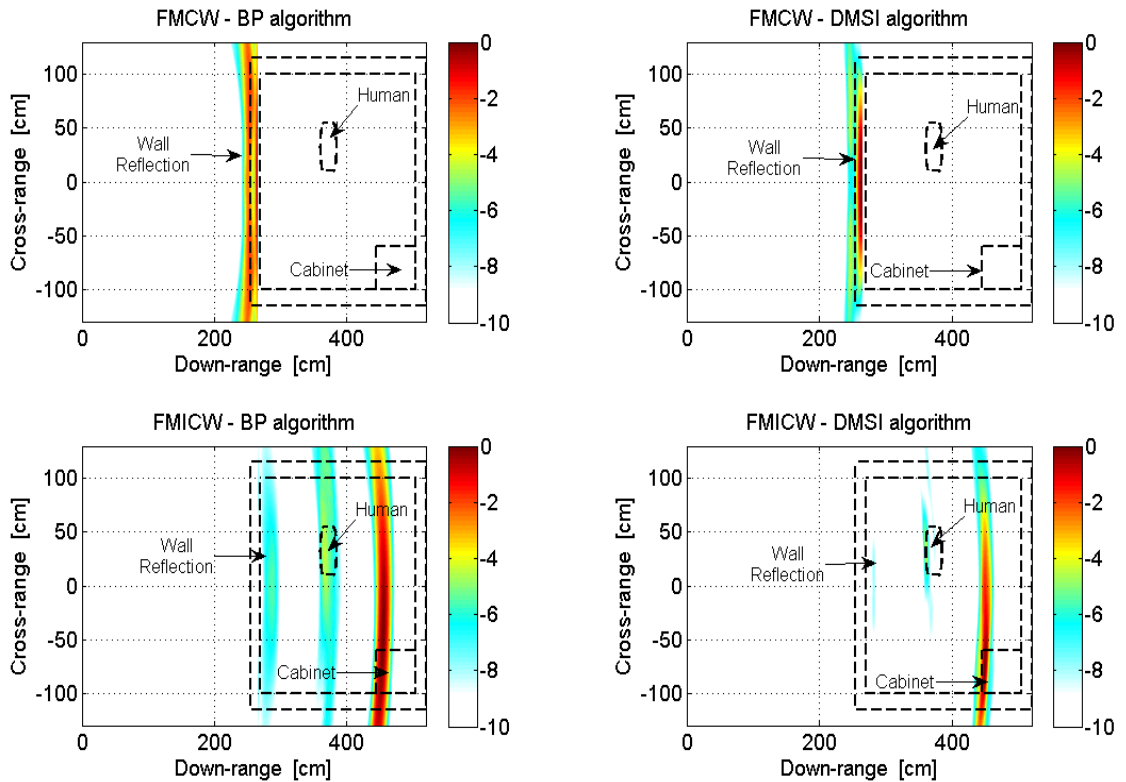**Figure 4.22 View of simulated scenario 7**
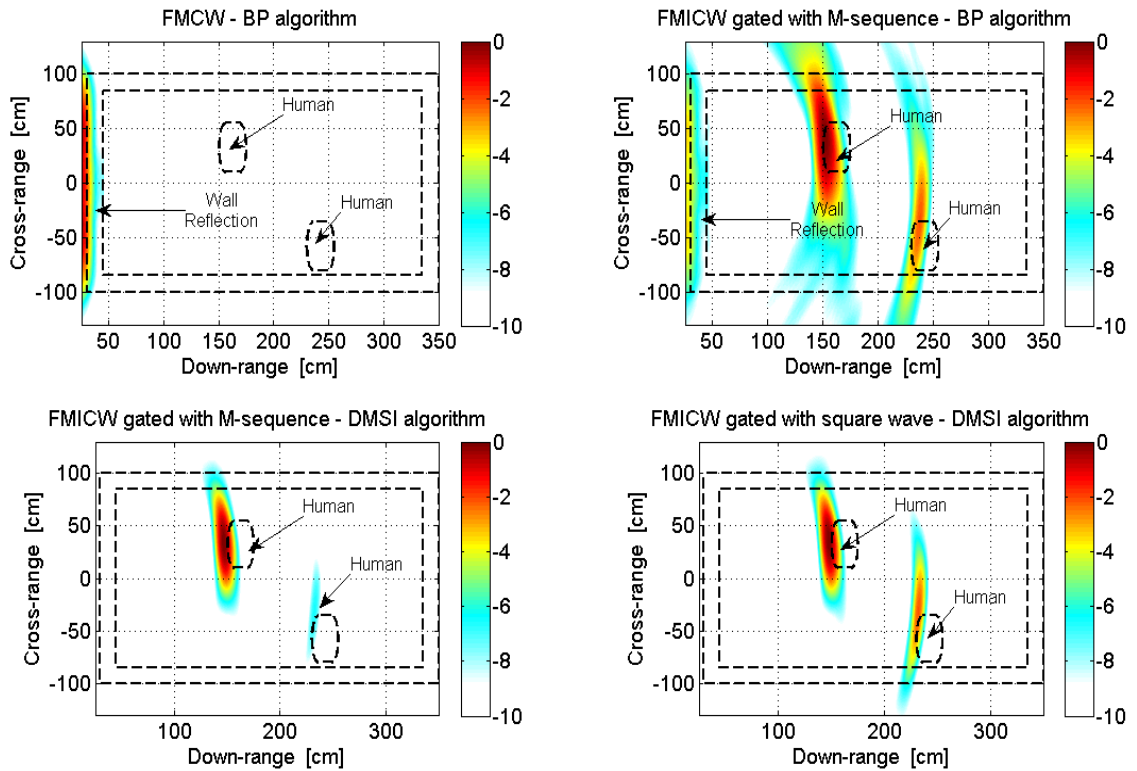
**Figure 4.23 Comparison of FMCW-FMICW images for simulated scenario 7 – BP and DMSI algorithm**
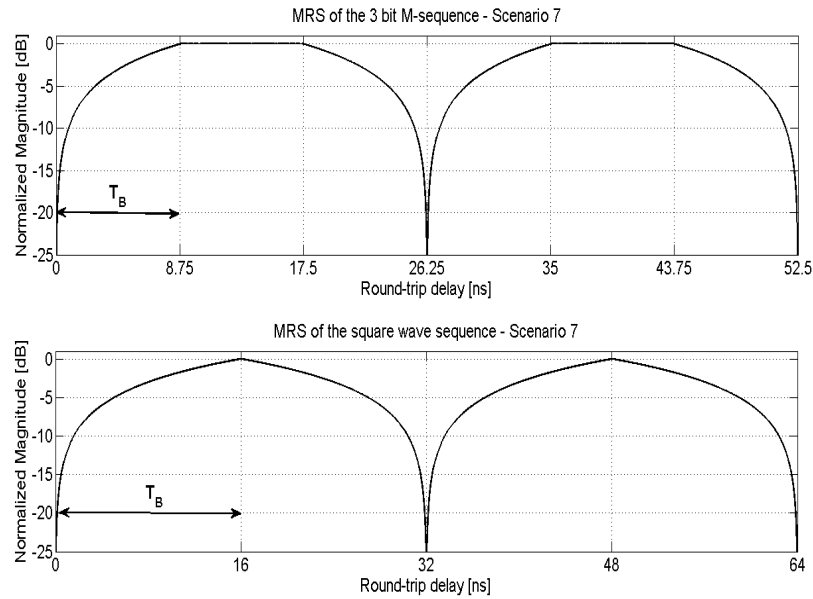
Figure 4.24 MRS of the gating sequences used in simulated scenario 7

In scenario number 8 a 10 cm thick partition wall which separates the two human phantoms is inserted into the previous simulated environment. This partition wall is placed at 200 cm from the array of probes and there is a wooden door through it, just in front of the farthest human phantom, as it can be seen in figure 4.25. The two phantoms have been slightly shifted compared with the previous scenario, at distances of 150 cm and 250 cm from the probes, respectively. The duration of the simulated chirp is here 4000 ns, giving for a gating sequence with N bits maximum bit duration 40/N ns in order to avoid aliasing. The detection of the farthest target is particularly challenging because of the partition wall, as it can be seen in figure 4.26, where images with FMCW and FMICW waveforms are compared when different gating sequences are used. All the sub-figures are created with the BP algorithm. In the top-left sub-figure FMCW waveforms are used: in this case only wall reflections from the main wall and from the partition wall are shown and the targets are not detected.

Different gating sequences have been applied to create the other sub-figures in figure 4.26, and the MRS of these sequences are shown in figure 4.27. The first is the 3 bit M-sequence with bit duration 11 ns, which removes the reflection from the main wall through its first blind range, but is not effective in dealing with the contribution of the

partition wall. In the sub-figure referring to this sequence, the top-right in figure 4.26, the reflection from the partition wall is indeed the strongest signal and it completely prevents the detection of the farthest target; the first target is successfully detected.

In order to remove the reflection of the partition wall, the second blind range of the MRS can be used, as done for the second gating sequence for this scenario, a square wave with bit duration 7 ns. Its blind range is located at 14 ns, corresponding to the round-trip delay of the partition wall at 200 cm. In the corresponding image for this gating sequence (bottom-left in figure 4.26) the reflection from the partition wall is removed, as it can be seen in comparison with the top figures, but the reflection from the main wall is strong because the slope of the MRS is too steep with only 7 ns of bit duration, and therefore the first blind range is too short to mitigate the undesired contribution.

A solution is the introduction of the delays τ_{RX1} and τ_{RX2} equal to 1.25 ns for the square wave gating sequence, getting the third MRS shown in figure 4.27. The first blind range is extended to increase the attenuation on the reflection from the main wall; the second blind range is extended as well to remove the reflection form the partition wall, without attenuating the contribution from the targets. In the image corresponding to this third gating sequence (the bottom-right in figure 4.26) both targets are successfully detected despite the residual reflection from the main wall, and the partition wall is completely removed.
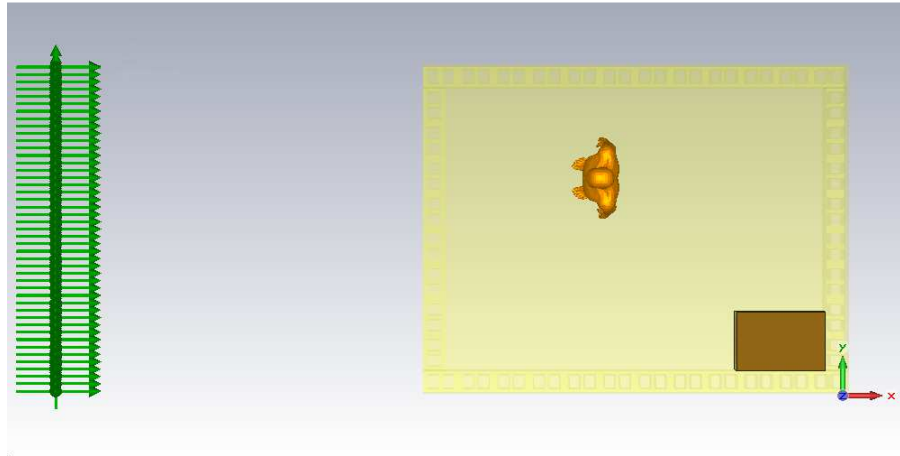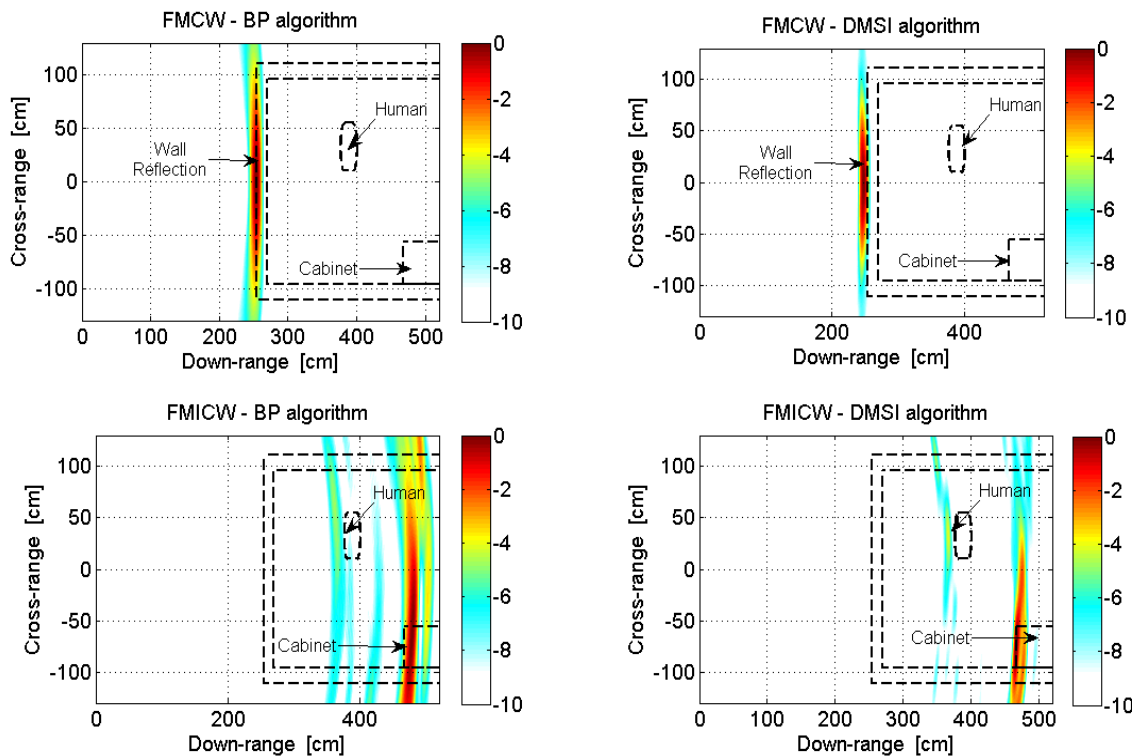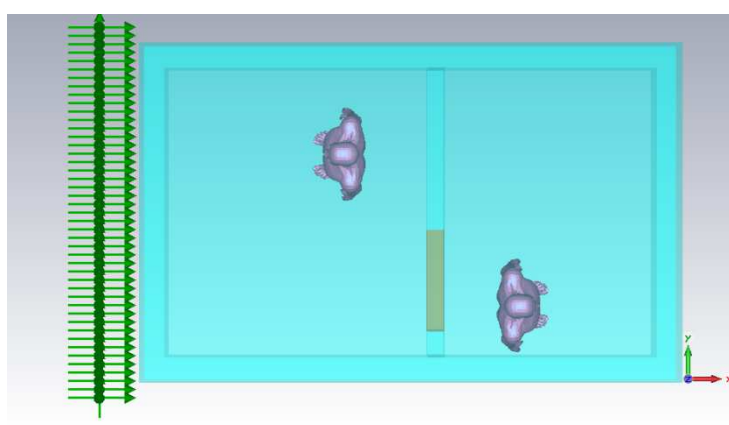

Figure 4.25 View of simulated scenario 8
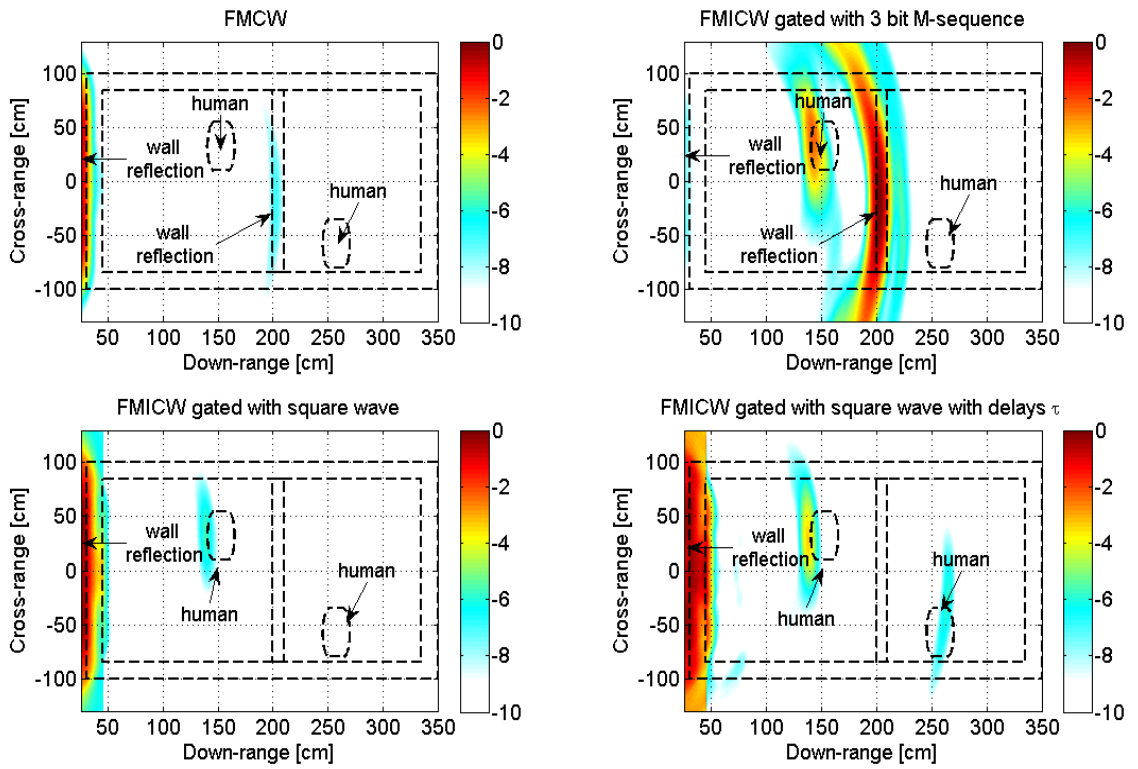
**Figure 4.26 Comparison of FMCW-FMICW images for simulated scenario 8 – BP algorithm**
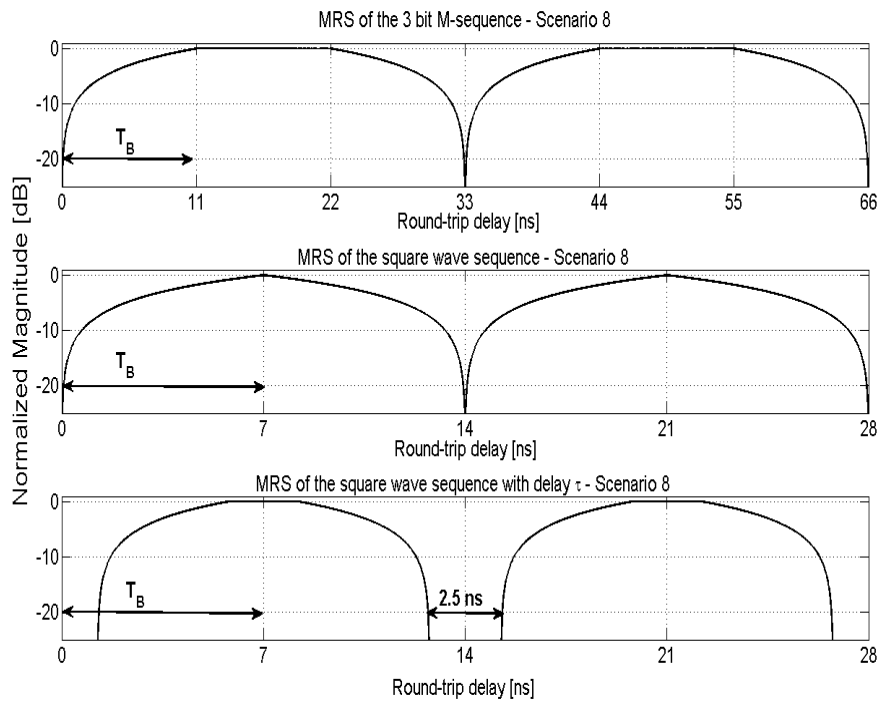
Figure 4.27 MRS of the gating sequences used in simulated scenario 8

110

It has been mentioned in section 3 of chapter 2 that the use of cross-polarized signal components for image formation can strongly reduce the contribution of wall reflections and enhance the detection of human phantoms. Although the challenges of the practical implementation of this approach makes it unsuitable in real applications, its effectiveness has been investigated through numerical simulations in [7]. Figures 4.28 and 4.29 show a few examples of images created using the cross-polarized signals in the simulated scenarios number 3 and 6, which have already been presented in this section. Comparisons of images using cross-polarized and co-polarized signal components are provided, when normal FMCW waveforms are used without gating. In both figures it can be seen that the use of cross-polarized components enhances greatly the reflection from the human phantom and from the back wall of the room, whereas the reflection from the main wall and from the metallic cabinet are strongly attenuated; in both cases only the human phantom is detected when the DMSI imaging algorithm is applied. These results are in line with what already discussed in chapter 2.
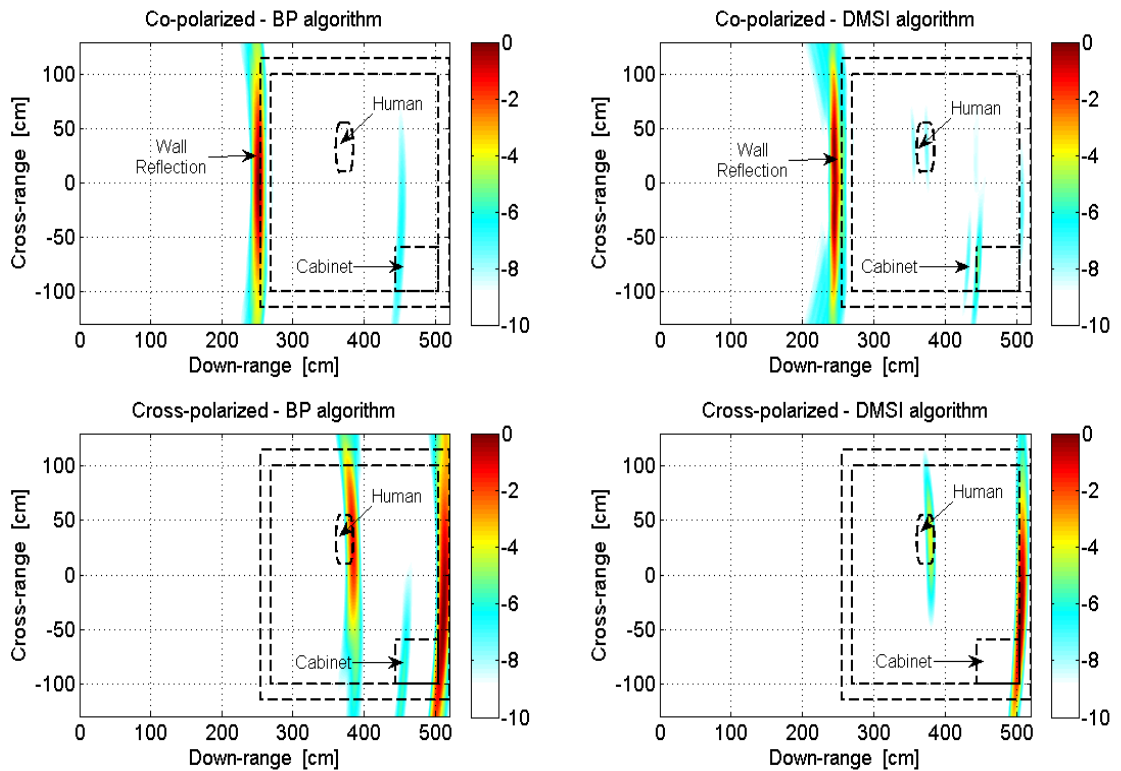
Figure 4.28 Comparison of FMCW images with co- and cross-polarized signal components for simulated scenario 3 – BP and DMSI algorithm
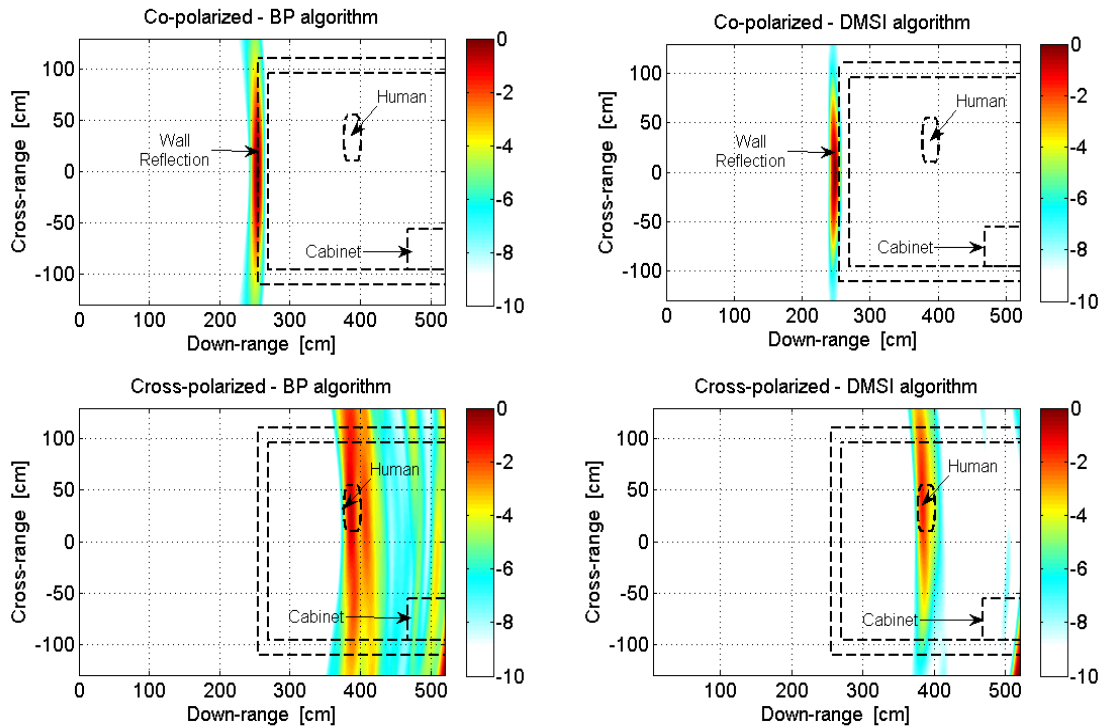
Figure 4.29 Comparison of FMCW images with co- and cross-polarized signal components for simulated scenario 6 – BP and DMSI algorithm

As a conclusion of this section where the results from numerical simulations have been presented, it is worth discussing briefly the computational requirements of these simulations. One of the drawbacks of the FIT method when simulating electrically large structures as three-dimensional rooms is the amount of memory and CPU time required. The amount of memory depends on the number of hexahedral mesh cells in the environment to be simulated, which increases with the size of the environment itself (for instance using longer stand-off distances), and with the electrical permittivity of the simulated objects (higher permittivity implies smaller cells, so more cells are needed to model the volume under test). The amount of CPU time depends on the duration of the user-defined FMCW signal (longer waveforms imply longer simulation time), and on the geometry and materials of the simulated environment (the smaller the mesh cells are, the shorter the maximum allowed time-step is in order to ensure a stable simulation, so that more time-steps are necessary to simulate a certain waveform). It should be noted that, given the high permittivity of the skin-like material used for the human phantom and the frequency range 0.5-2 GHz of the FMCW signal, the average duration

of a single time step is a few picoseconds. Therefore simulations of waveforms which are 1200-5000 ns long require hundreds of thousands of time-steps.

The simulations presented in this section have been run on a Dell workstation T7500, with 48 GB of RAM, 2 CPU Intel Xeon E5640 (with 8 cores in total), and Windows 7 operating system. Table 4.1 summarizes the number of mesh cells, the duration of the FMCW waveform, and the required simulation time. The strong correlation between the duration of the simulated FMCW waveform and the simulation time can be seen from the data. Compared with scenario 1, the other scenarios have more cells because of the increased stand-off distance, with the exception of scenario 3 where the walls are made of wood, which has a lower electrical permittivity compared with concrete. It should be noted that the overall simulation time depends also on other tasks and programs which may be running at the same time with the numerical simulation. The simulation can be far slower if other tasks, for instance in MATLAB, are running at the same time with CST Microwave Studio.

	Number of mesh cells [million]	FMCW chirp duration [ns]	Overall simulation time [hours]
Scenario 1	28.7	1200	53
Scenario 2	30.1	3000	119
Scenario 3	24.6	3000	115
Scenario 4	34.6	3000	142
Scenario 5	31.9	3000	166
Scenario 6	32.4	3000	158
Scenario 7	31.9	5000	227
Scenario 8	33.5	4000	205

Table 4.1 Summary of computational requirements for the simulated scenarios of this chapter

4.5 Summary of the chapter

In this chapter the importance of numerical simulations to analyze capabilities and limitations of radar systems for TTWD has been discussed with reference to some of the works proposed in the literature. Particular emphasis has been given to the possibility of modelling the effects that the through-wall propagation causes on radar waveforms, depending on the electrical parameters and on the internal structure of walls. The commercial software CST Microwave Studio is presented as a suitable tool to simulate through-wall scenarios based on FMICW waveforms using the FIT method. Three algorithms to process the data from CST and create images have been presented, with particular emphasis on the estimation of the round-trip delay taking into account the presence of the wall.

Finally, results have been presented for eight different simulated scenarios, focusing on the effectiveness of the proposed FMICW technique in mitigating wall reflections and enhancing the detection of the targets in comparison with normal FMCW waveforms. The selection of suitable gating sequences for each scenario has been discussed when applying FMICW waveforms. Images from different algorithms have been compared, showing that using DSI and DMSI adapted from medical imaging the results are better focused than those created using the classic BP algorithm.

The following table summarizes the main features of the simulated scenarios, in particular the thickness, permittivity, and internal structure of the wall, the type of targets and their distance, and the type of gating sequences used for the FMICW waveforms.

Scenario	Stand-off distance	Room area	Targets and their distance	Wall thickness and structure	Gating sequences for FMICW
1	30 cm	235×200 cm	Metallic cabinet 220 cm Human phantom 150 cm	15 cm solid 1 year concrete ($\varepsilon_r = 5.657$)	3 bit M-sequence with $T_B = 7.5$ ns
2	250 cm	235×200 cm	Metallic cabinet 440 cm Human phantom 370 cm	15 cm solid 40 years concrete ($\varepsilon_r = 4.642$)	3 bit M-sequence with $T_B = 5.75$ ns
3	250 cm	235×200 cm	Metallic cabinet 440 cm Human phantom 370 cm	15 cm solid wood ($\varepsilon_r = 2.017$)	3 bit M-sequence with $T_B = 5.625$ ns, $\tau_{RX1} = \tau_{RX2} = 0.5$ ns
4	250 cm	235×200 cm	Metallic cabinet 440 cm Human phantom 370 cm	15 cm solid 1 year concrete ($\varepsilon_r = 5.657$)	3 bit M-sequence with $T_B = 5.75$ ns, $\tau_{RX1} = \tau_{RX2} = 0.5$ ns
5	250 cm	235×200 cm	Metallic cabinet 440 cm Human phantom 370 cm	15 cm with 5 cm air gap 1 year concrete ($\varepsilon_r = 5.657$)	Square wave with $T_B = 8.625$ ns, $\tau_{RX1} = \tau_{RX2} = 1$ ns
6	250 cm	258×192 cm	Metallic cabinet 460 cm Human phantom 370 cm	15 cm cinder blocks 1 year concrete ($\varepsilon_r = 5.657$)	Square wave with $T_B = 10$ ns, $\tau_{RX1} = \tau_{RX2} = 3.625$ ns
7	25 cm	290×170 cm	Human phantom 160 cm Human phantom 240 cm	15 cm solid 40 years concrete ($\varepsilon_r = 4.642$)	3 bit M-sequence $T_B = 8.75$ ns Square wave $T_B = 16$ ns
8	25 cm	290×170 cm	Human phantom 150 cm Human phantom 250 cm	Main wall: 15 cm solid Partition wall: 10 cm solid 40 years concrete ($\varepsilon_r = 4.642$)	3 bit M-sequence $T_B = 11$ ns Square wave $T_B = 7$ ns Square wave $T_B = 7$ ns, $\tau_{RX1} = \tau_{RX2} = 1.25$ ns

Table 4.2 Summary of the main features of the simulated scenarios presented in this chapter

4.6 References

[1]   L. Chen and O. Shan, "Through-wall surveillance using ultra-wideband short pulse radar: numerical simulation," in Industrial Electronics and Applications, 2007. ICIEA 2007. 2nd IEEE Conference on, 2007, pp. 1551-1554.

[2]   W. A. Chamma, "FDTD modelling of a realistic room for through-the-wall radar applications," in Computational Electromagnetics in Time-Domain, 2007. CEM-TD 2007. Workshop on, 2007, pp. 1-4.

[3]   R. S. Schechter and S.-T. Chun, "High-resolution 3-D imaging of objects through walls," Optical Engineering, vol. 49, p. 113204, 2010.

[4]   T. Dogaru and C. Le, "Simulated radar range profiles of a simple room as computed by FDTD and Xpatch," Army Research Laboratory, Adelphi, MD Tech. Rep. ARL-TR-4420, 2008.

[5]   T. Dogaru, et al., "Computer Models of the Human Body Signature for Sensing Through the Wall Radar Applications," Army Research Laboratory, Adelphi, MD, Tech. Rep. ARL-TR-4290, 2007.

[6]   T. Dogaru and C. Le, "Validation of Xpatch computer models for human body radar signature," Army Research Laboratory, Adelphi, MD, Tech. Rep. ARL-TR-4403, 2008.

[7]   T. Dogaru and C. Le, "SAR images of rooms and buildings based on FDTD computer models," Geoscience and Remote Sensing, IEEE Transactions on, vol. 47, pp. 1388-1401, 2009.

[8]   M. G. Amin, Through-the-Wall Radar Imaging: CRC Press, 2010.

[9]   C. Le, et al., "Ultrawideband (UWB) radar imaging of building interior: measurements and predictions," Geoscience and Remote Sensing, IEEE Transactions on, vol. 47, pp. 1409-1420, 2009.

[10]   L. M. Frazier, "Radar surveillance through solid materials," Proc. SPIE 2938, Command, Control, Communications, and Intelligence Systems for Law Enforcement, pp. 139-146, 1997.

[11]   A. Muqaibel, et al., "Ultrawideband through-the-wall propagation," Microwaves, Antennas and Propagation, IEE Proceedings -, pp. 581-588, 2005.

[12]   Y. Chang-Fa, et al., "A free space approach for extracting the equivalent dielectric constants of the walls in buildings," in Antennas and Propagation Society International Symposium, 1996. AP-S. Digest, 1996, pp. 1036-1039 vol.2.

[13]   T. Weiland, et al., "A practical guide to 3-D simulation," Microwave Magazine, IEEE, vol. 9, pp. 62-75, 2008.

[14]   I. Munteanu, et al., "It's about time," Microwave Magazine, IEEE, vol. 11, pp. 60-69, 2010.

[15]   A. Taflove and S. C. Hagness, Computational Electrodynamics: The Finite-Difference Time- Domain Method: Artech House, Incorporated, 2005.

[16]   M. Aftanas, Through-Wall Imaging With UWB Radar System: Lambert Academic Publishing, 2010.

[17]   L. Hooi Been, et al., "Confocal microwave imaging for breast cancer detection: delay-multiply-and-sum image reconstruction algorithm," Biomedical Engineering, IEEE Transactions on, vol. 55, pp. 1697-1704, 2008.

[18]   D. Byrne, et al., "Data independent radar beamforming algorithms for breast cancer detection," Progress in Electromagnetic Research, vol. 107, pp. 331-348, 2010.

[19]   W. Genyuan and M. G. Amin, "Imaging through unknown walls using different standoff distances," Signal Processing, IEEE Transactions on, vol. 54, pp. 4015-4025, 2006.

[20]   F. Ahmad, et al., "Autofocusing of through-the-wall radar imagery under unknown wall characteristics," Image Processing, IEEE Transactions on, vol. 16, pp. 1785-1795, 2007.

[21]   F. Ahmad, et al., "Synthetic aperture beamformer for imaging through a dielectric wall," Aerospace and Electronic Systems, IEEE Transactions on, vol. 41, pp. 271-283, 2005.

[22]   F. Ahmad, et al., "Three-Dimensional Wideband Beamforming for Imaging Through a Single Wall," Geoscience and Remote Sensing Letters, IEEE, vol. 5, pp. 176-179, 2008.

5.1 Block Diagram of the FMICW based radar system

In this chapter the description of the hardware components of the FMICW based radar system built at the Centre for Communications Systems, Durham University is presented. The synchronization of all the components through a common stable clock is also discussed.

Figure 5.1 shows the block diagram of the proposed radar system; the meaning of the acronyms is summarized in table 5.1, with a detailed description of each block following in this section.
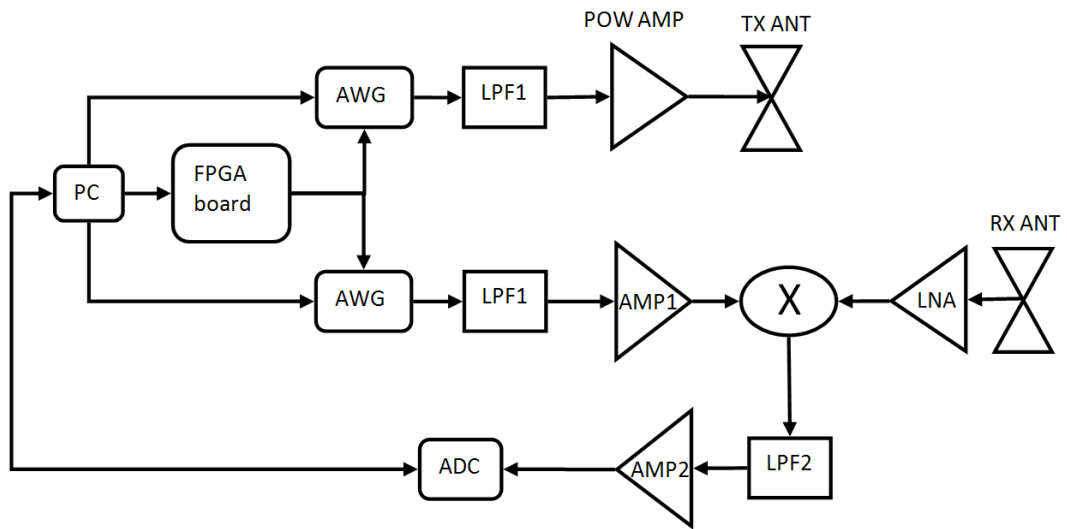
Figure 5.1 Block diagram of the proposed radar system

AWG	Arbitrary Waveform Generator
LPF1	Low Pass Filter (pass-band up to 3.5 GHz)
POW AMP	Power Amplifier
LNA	Low Noise Amplifier
X	Mixer
AMP1	Medium Power Amplifier
LPF2	Low Pass Filter (pass-band up to 10 MHz)
AMP2	Base Band Amplifier
ADC	Analogue to Digital Converter
FPGA	Field Programmable Gate Array board

Table 5.1 Summary of the acronyms of the hardware block diagram

The two AWGs are the core element of the radar system and they are used to generate FMCW or FMICW waveforms. They are programmed through a PC and synchronized through a FPGA board, which provides their trigger signals. At the transmitter side the waveform generated by the AWG is filtered and amplified before transmission through the antenna. At the receiver side the replica of the transmitted waveform is filtered and amplified accordingly to drive the mixer. This signal is multiplied with the received waveform, which is amplified by the LNA. As discussed in chapter 3, the resulting signal after low-pass filtering is the beat-note signal, which carries information on the range to the targets and on Doppler shifts in case of moving targets. This signal is therefore amplified, digitized through the ADC, and stored in a PC for processing and image formation. All the radio-frequency components and also the low pass filter and the amplifier for the beat-note signal (LPF_2 and AMP_2 in figure 5.1) have been placed in a portable rack assembled for the purpose, which is shown in figure 5.2.

Figure 5.2 Portable rack with RF components

5.1.1 Arbitrary Waveform Generator

The arbitrary waveform generators are commercial modules AWG801 produced by Euvis; figure 5.3 shows the two units used for the proposed radar system. Each unit can generate user-defined or built-in standard waveforms with frequency up to 4 GHz and duration up to slightly less than 1 ms. The duration is limited by the size of the on-board memory and the maximum frequency is limited by the frequency of the input clock, in

this case 4 GHz. The sampling rate of the waveforms is 8 GHz, thus the minimum time-step between digital samples is 0.125 ns. In the proposed radar system the AWG's are controlled by a C program which loads into their memory the desired waveforms generated through MATLAB (these programs have been included in the appendix). It is a very flexible approach which allows the generation of FMICW waveforms with different gating sequences for different scenarios under test just via software from the PC. For the through-wall experiments performed in the measurement campaign presented in chapter 6 the FMCW-FMICW signal covers the bandwidth 0.7-2.2 GHz. Figure 5.4 shows the spectrum of this signal at the output of the AWG with data captured by a spectrum analyzer; the power level is roughly -5.8 dBm and it is reasonably flat across the desired bandwidth, with the magnitude of the ripple around 1 dB.

Figure 5.3 Arbitrary Waveform Generators
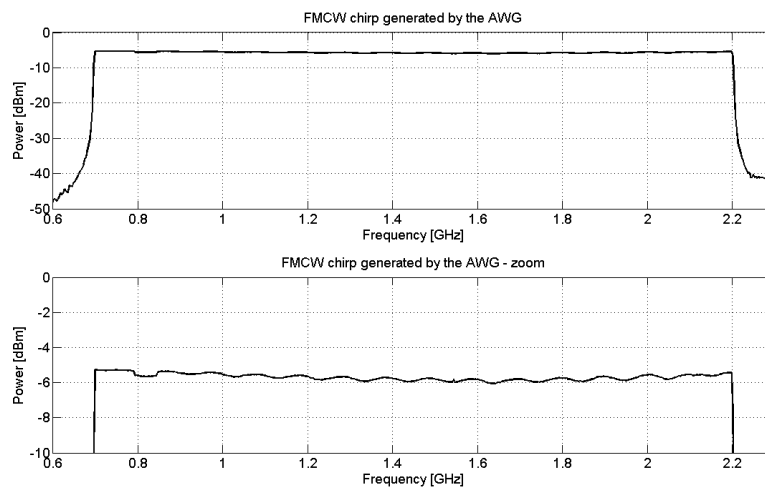
Figure 5.4 Spectrum of the FMCW chirp generated by the AWG

5.1.2 Low Pass Filter with 3.5 GHz pass-band

A low pass filter is generally required at the output of the AWG to attenuate the residual clock and the alias image. For our system the residual clock is placed at 4 GHz with power of roughly -50 dBm, and the alias starts at 5.8 GHz, which is the symmetric frequency of the maximum frequency of the FMCW signal (2.2 GHz) with respect to the clock. The low pass filter, called LPF_1 in figure 5.1, has been however designed assuming a general waveform with frequency up to 3.5 GHz, so that it may be used in future systems and not only for the through-wall radar described in this section. In this case the pass-band of the filter has to extend up to 3.5 GHz and the alias to be attenuated would start at 4.5 GHz.

The design of this filter has been therefore based on these requirements: 60 dB attenuation in the stop-band (frequencies higher than 4.5 GHz), S11 parameter not higher than -15 dB across the pass-band, and 0.1 dB ripple Chebyshev response with 15 sections. An initial design using ideal lumped elements has been made according to [1] and using AWR software. The required values of inductance (a few nH) and capacitance (not higher than 3 pF) are too low to be reached with lumped elements. Therefore a distributed design based on microstrip lines has been adopted: series inductors are approximated by high impedance transmission lines, which are folded to reduce the overall length of the filter, and shunt capacitors are approximated by low impedance open stubs. The substrate Rogers 4003 with 0.5 mm thickness has been chosen. Figure 5.5 shows the layout of the distributed design of the filter. After simulations with AWR of the distributed model, the expected attenuation for the residual clock and for the alias is satisfactory: 37 dB for the former at 4 GHz, and 61 dB for the latter at 4.5 GHz.
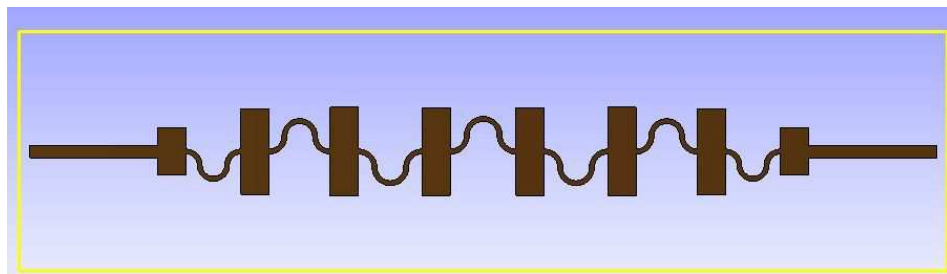
Figure 5.5 Layout of the low pass filter with 3.5 GHz pass-band

The filters have been manufactured using the facilities at the School of Engineering and Computing Sciences, Durham University and mounted onto a metallic base for mechanical stability. SMA connectors with flat central pins have been used to fit the narrow width of the microstrip at the two extremities of the filters. Figures 5.6-5.7 show respectively the transmission (S12 and S21 parameters) and reflection (S11 and S22) patterns of the manufactured filter.
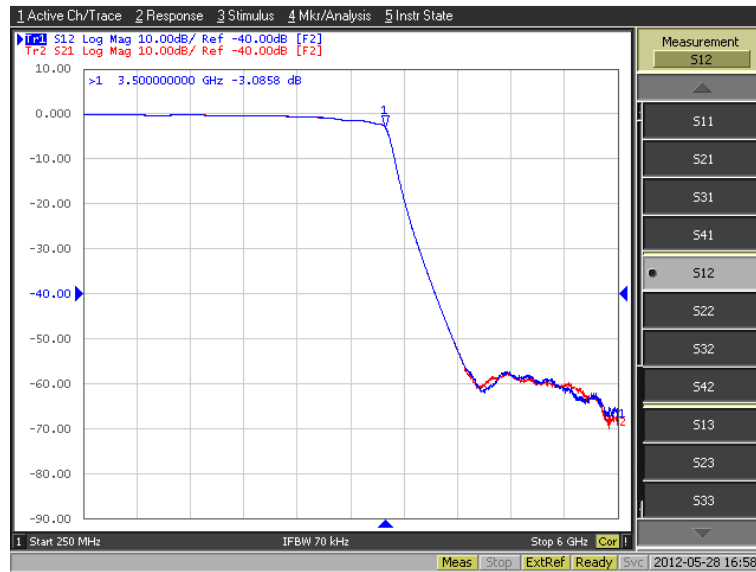
Figure 5.6 S12 and S21 parameters of the 3.5 GHz LPF
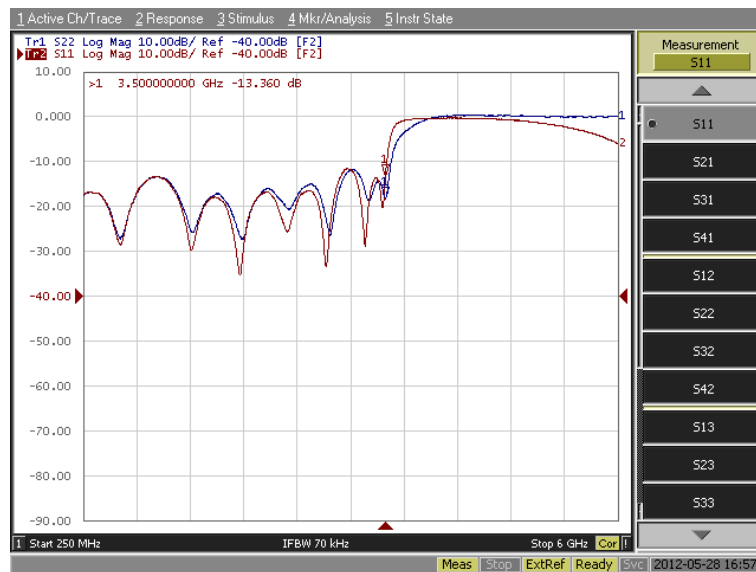
Figure 5.7 S11 and S22 parameters of the 3.5 GHz LPF

The attenuation across the stop-band after 4.5 GHz is 60 dB or lower, in line with the values expected from the AWR simulation, whereas the reflection parameters across the band-pass before 3.5 GHz present discrepancies in comparison with the simulated model. Some degradation on the reflection pattern was somewhat expected because of the manufacturing process of these filters based on etching the copper rather than removing it by a chemical process, which generally gives results closer to the simulations in AWR. The good transmission pattern makes these filters suitable for the radar system presented in this section.

5.1.3 Power Amplifier

A power amplifier is needed at the transmitter side to amplify the waveform up to a power level suitable for through-wall penetration and detection. In our system this amplifier is placed between the low pass filter at the output of the AWG and the transmitter antenna, as in figure 5.1. The model used is Mini-Circuits ZHL-4240 operating across the bandwidth 700-4200 MHz, with minimum gain 40 dB and maximum output power around 28 dBm. Figure 5.8 shows the FMCW signal across the bandwidth 0.7-2.2 GHz after amplification by this power amplifier. Since the data are recorded by a spectrum analyzer with 20 dB attenuator at the input, it can be seen that the actual power level across the desired bandwidth is around 28 dBm. This signal is then applied to the antenna for transmission.
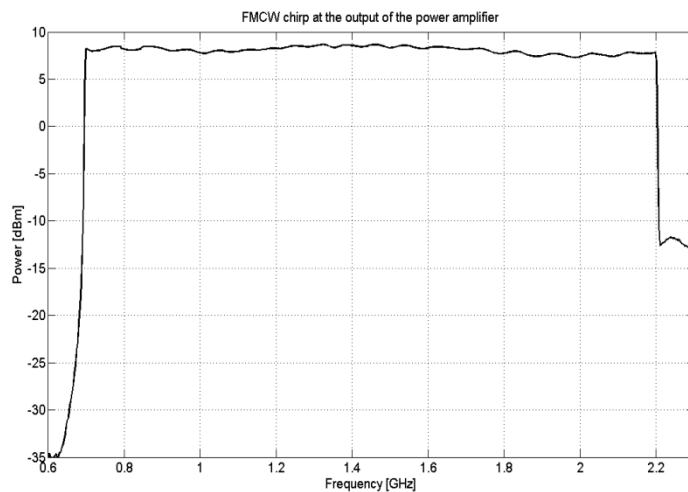
Figure 5.8 Spectrum of the FMCW chirp at the output of the power amplifier

5.1.4 Transmitter and Receiver Antennas

Our radar system operates in a bistatic mode with two antennas, one at the receiver and one at the transmitter. Two different models of antenna have been designed and manufactured to work across the desired frequency bandwidth (0.7-2.2 GHz) and have a directional radiation pattern, so that the energy can be focused towards the wall and the targets to be detected, avoiding the reception of clutter and undesired signals from side lobes. Both antennas can be used for frequencies starting from 500 MHz, in case lower frequencies are required for penetration through very thick walls.

The first model is a patch-like antenna developed in collaboration with the Fraunhofer Institute for Reliability and Microintegration in Berlin, Germany [2]. It is the result of an optimization process on a basic square patch antenna with the purpose of reducing its size and getting a radiation pattern with a single main lobe. The antenna has been simulated with CST Microwave Studio and Ansoft HFSS, and printed on common FR4 substrate; simulated and measured results of the S11 and of the radiation pattern show good agreement. The antenna is relatively compact (14×17 cm), taken into account that its bandwidth starts at 500 MHz. Figure 5.9 shows the patch-like antennas mounted on a wooden and cardboard support placed next to a brick wall while performing through-wall measurements.

Figure 5.9 Patch-like antennas close to a brick wall

The second model is an antipodal Vivaldi antenna. Figure 5.10 shows two of these antennas placed on a wooden support next to a concrete wall during a measurement.
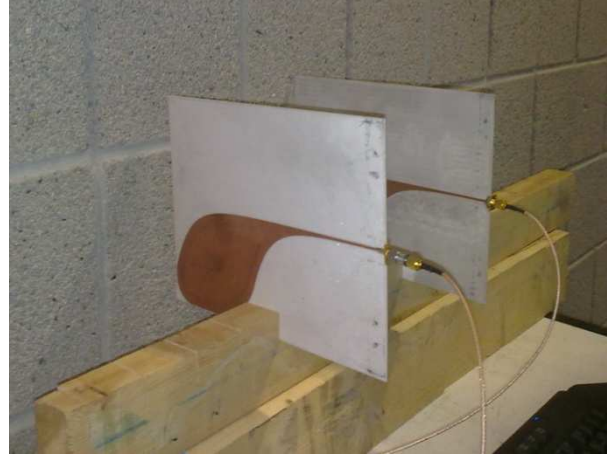
Figure 5.10 Vivaldi antennas close to a concrete wall

The dimensions of this antenna are 26×18.5 cm. These antennas have been simulated and optimized with CST Microwave Studio to work across the desired bandwidth, and then manufactured on Taconic CER10 substrate with thickness 1.5 mm. Figure 5.11 compares simulated and measured S11 parameters for this antenna. The simulations have been performed using both the time domain and the frequency domain solver of CST to compare the results. Good agreement can be seen between measured and simulated data. The antenna is well matched above 0.5 GHz, with the S11 parameter below the -10 dB threshold.
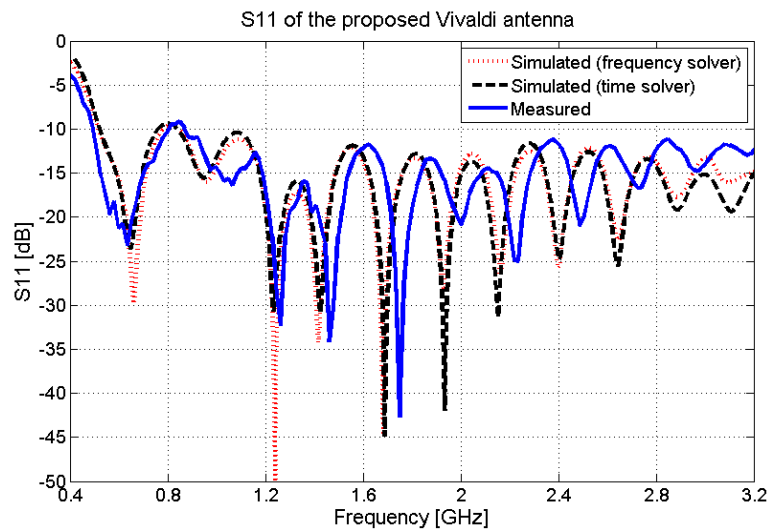
Figure 5.11 Simulated and measured S11 parameter of the proposed Vivaldi antenna

5.1.5 Low Noise Amplifier

At the receiver side a low noise amplifier is placed just after the receiver antenna, as in figure 5.1; a limiter is placed at the input of the LNA for protection from possible static discharges when the antenna is touched by the operator. The LNA is the Mini-Circuits ZX60-3011 operating across the bandwidth 400-3000 MHz, with gain 15-11.5 dB and noise figure 1.4-1.7 dB.

5.1.6 Mixer

The mixer multiplies the received waveform (at the RF port) with the replica of the transmitted waveform (at the LO port) to generate the beat-note signal (at the IF port). The chosen mixer is the level 13 ZEM-4300 MH from Mini-Circuits, operating across the bandwidth 300-4300 MHz at the LO and RF ports, and DC-1000 MHz at the IF port.

5.1.7 Medium Power Amplifier

This amplifier is placed at the output of the AWG after the filter LPF_1, as in figure 5.1 where it is called AMP_1. It is necessary to amplify the replica of the transmitted waveform at the required power level to drive the LO port of the mixer, which in our case is roughly 13 dBm. The chosen amplifier is the ZKL-2R7 from Mini-Circuits, operating across the bandwidth 10-2700 MHz with gain 24 dB and maximum output power 13 dBm.

5.1.8 Low Pass Filter with 10 MHz pass-band

As shown in figure 5.1, this low pass filter (LPF2) is placed at the IF port of the mixer to pass only the beat-note signal carrying information on range and/or Doppler shift related to the targets. Given the duration and the bandwidth of the FMCW chirp used in this thesis' work, 400 μs and 1.5 GHz respectively, the expected beat-note is in the range of hundreds of kHz. The cut-off frequency of this filter has been however set at 10 MHz, in order to have more flexibility for possible different uses of the whole

system. This filter is made of lumped capacitors and inductors and its S parameters are shown in figure 5.12.
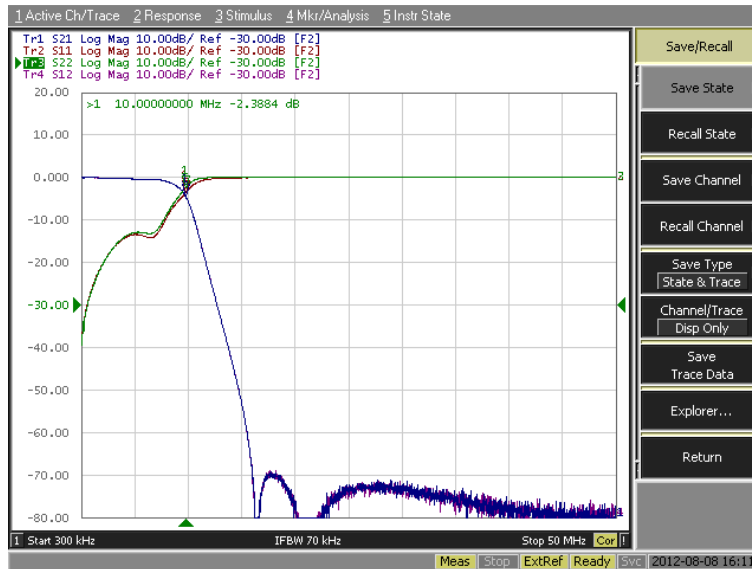
Figure 5.12 S-parameters for the 10 MHz LPF

5.1.9 Base-band Amplifier

This amplifier increases the power level of the beat-note signal before its digitization. The chosen model is the Mini-Circuits ZHL-6A, operating across the bandwidth 2.5 kHz – 500 MHz, with 25 dB gain and maximum power output around 22 dBm.

5.1.10 Analogue-to-Digital Converter

The analogue-to-digital converter digitizes the beat-note signal into files stored in a PC for further processing and image formation. The chosen ADC is the dual-channel PX14400A from Signatec, with 14 bits of resolution. In the measurements performed for this thesis' work the ADC is provided with a stable 10 MHz clock to which the internal clock generator of the ADC can lock. The beat-note is digitized at 20 MHz, the minimum allowed sampling frequency. The ADC is triggered by the "marker", which is a programmable signal generated by the AWG at the beginning of each FMCW signal.

5.2 Clock Distribution and Synchronization

Figure 5.13 shows the distribution of the stable clock used to synchronize the AWG and the ADC in the proposed radar system. The synchronization of these components is of paramount importance to measure correctly Doppler shifts caused by the movement of the targets. Jittering clocks and the consequent not well synchronized start of each FMCW chirp would indeed create strong Doppler artefacts which have nothing to do with the actual targets.
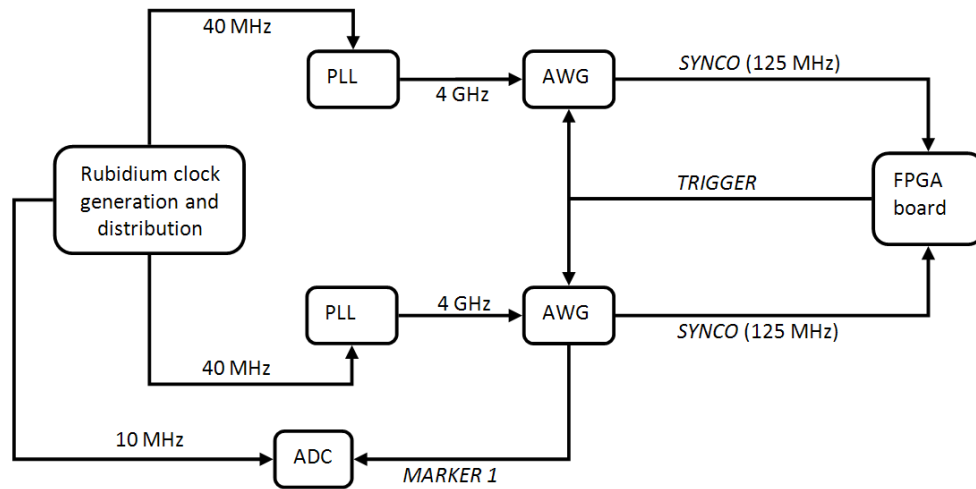
Figure 5.13 Block diagram of the distribution of the stable clock for synchronization

The core element of the diagram shown in figure 5.13 is the block for generation and distribution of the clock. It contains a PRS10 rubidium module from Stanford Research Systems, which generates a very stable 10 MHz sine wave. This module presents frequency accuracy of $\pm5\times10^{-11}$, Allan variance for short-time stability below 10^{-11} at 1 second and 10 seconds, temperature coefficient of $\pm5\times10^{-11}$ over -20 to 65 Celsius degrees, and low aging rate below $\pm5\times10^{-11}$ monthly. In the actual block of figure 5.13 this 10 MHz signal is accordingly split, multiplied, and amplified to derive the outputs at each of the following frequencies: 10 MHz sine wave, 10 MHz square wave, 20 MHz sine, 40 MHz sine, and 80 MHz sine. The block includes batteries to work even in case of disconnection from the main electricity grid, allowing for portable operation of the block up an hour. This block is shown in figure 5.14; its complete design and manufacturing has been made using the facilities of the School of Engineering at Durham University.

Figure 5.14 Rubidium clock generation and distribution block

As in figure 5.13, a 10 MHz square wave from the rubidium clock distribution block is given to the ADC to lock to it. The internal clock generator of the ADC can then generate sampling clocks with frequency 20-400 MHz. A trigger signal must also be given to the ADC in order to start the digitization. This signal is the so-called *MARKER1* generated by the AWG together with the desired output waveform and it is a 1.8 V TTL pulse with duration 40 ns. The ADC is by default activated at the raising edge of this trigger.

The two 40 MHz sine waves are given as input to two PLL modules, which generate two stable 4 GHz clock signals for the AWG. The desired waveform is digitally stored in the memory of the AWG and its amplitude samples are produced at the output with rate equal to twice the value of the given clock, i.e. 8 GHz corresponding to time-step of 0.125 ns. Inside the AWG the clock is divided down to 1/32 (125 MHz) generating the *SYNCO* signal, which is internally used to sense incoming trigger signals to the AWG. The trigger signals must therefore be phase-locked to the *SYNCO* signals in order to ensure that all the AWGs sense the trigger signals at the same time, and therefore their output waveforms are well synchronized. As in figure 5.13, the two SYNCO signals are given to the FPGA board which divides them accordingly to generate the *TRIGGER* signals for the AWG. The trigger signals are 3.3 V TTL and the AWGs are activated at the falling edge. The division factor to generate the trigger signals depends on the duration of the waveform to be generated by the AWG. It is advisable to choose this factor so that the period of the trigger signal is slightly longer than the duration of the

generated waveform. In the measurements presented in this thesis the duration of the FMCW/FMICW chirp is 400 μs and the period of the trigger signals 500 μs, corresponding to a division of the 125 MHz *SYNCO* signals by 62500. If the duration of the chirp is changed, the FPGA board needs to be reprogrammed to generate the trigger signals with suitable period. This can be easily performed via software from a PC.

Figure 5.15 shows a simplified synchronization diagram of the signals related to the AWG, assuming 400 μs for the duration of the FMCW chirp (called *OUTPUT* in figure 5.15) and 500 μs for the period of the trigger (called *TRIGGER*), as in the measurements performed for this thesis. It should be noted that the different signal durations are not in scale. The AWG has been set to generate a single waveform for each trigger. When the AWG senses the falling edge of the trigger signal, it starts to generate the output and at the same time a short pulse (with duration 40 ns, called *MARKER1*) to trigger the ADC and start the digitization. The generated waveform is shorter than the period of the trigger, so the AWG remains inactive (for 100 μs with the numbers given in figure 5.15) until the next trigger. The ADC can be operated either acquiring a long block of data after a single trigger (post-trigger mode), or acquiring shorter amounts of data after each trigger event (segmented mode). Normally we operate the ADC with the first approach, digitizing a long block of data including the inactivity periods of the AWG and then separating each FMCW/FMICW chirp during the processing of the recorded data.
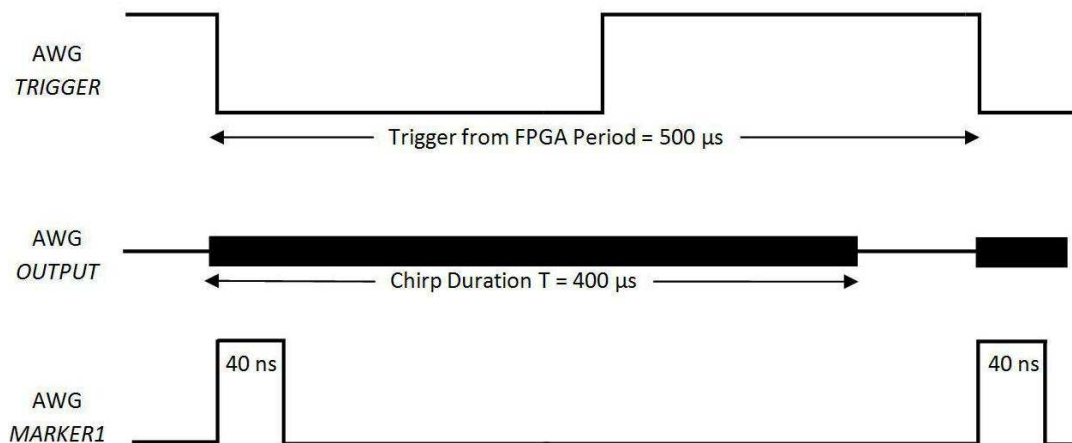
Figure 5.15 Simplified synchronization diagram of the AWG signals

5.3 Waveform and Radar Parameters for the Proposed System

FMCW and FMICW parameters have been discussed and linked to radar requirements and performance in chapter 3. In this section the specifications of the presented TTWD radar system are given with reference to those parameters and the sensitivity of the system is analyzed taking into account the expected power loss caused by the presence of the wall.

The waveform used in the experimental measurements of this work is a FMCW/FMICW with duration 400 μs and bandwidth 1.5 GHz, covering the frequency range 0.7-2.2 GHz. The chosen bandwidth yields 10 cm down-range resolution, which is an acceptable value for TTWD, and the frequency range is such as to penetrate common construction materials including concrete walls without excessive attenuation [3-4]. The cross-range resolution depends on the length of the aperture as in equation (3.19). For the measurements presented in this thesis, both the transmiting and the receiving antennas were moved in 10 cm steps along a 60 cm length parallel to the wall. Assuming a 1-4 m target range, the resulting resolution is approximately 35-140 cm at the centre frequency 1.45 GHz.

Since the focus of this work is testing the effectiveness of the proposed FMICW waveforms as wall mitigation/removal technique, there is no need to consider very long ranges to the target. Assuming for simplicity a maximum expected range 4 m, the maximum beat-note frequency given the aforementioned duration and bandwidth of the chirp is 100 kHz. For practical experiments this value is however higher because of the internal propagation delays of the radar system which have to be added to the round-trip delay related to the target. The minimum allowed sampling frequency of the ADC is 20 MHz, which implies maximum beat-note frequency of 10 MHz to digitize without aliasing. Each 400 μs chirp is therefore sampled at 20 MHz, producing 8000 digital samples.

Given the duration of the chirp, the maximum Doppler shift to avoid ambiguity is ±1250 Hz, which does not pose any problems for detection of human movements, whose shift is much smaller. The Doppler resolution depends on the number of processed waveforms: normally overall data duration of 10 s has been considered for walking detection, corresponding to 0.1 Hz Doppler resolution, whereas 20 s duration

has been considered for breathing detection, corresponding to 0.05 Hz Doppler resolution.

When gating sequences are applied in FMICW waveforms, the bit duration for a sequence made of K bits is 5μs/K (from the anti-aliasing condition in chapter 3), with the aforementioned bandwidth and duration of the chirp and assuming a 4 m maximum range to the target. Since in practical experiments only square waves and M-sequences with 3 bit have been used, this condition yields a bit duration longer than 1 μs, more than enough in through-wall scenarios which are a few meters long. Table 5.2 summarizes the aforementioned FMCW/FMICW parameters.

Chirp frequency range and duration T	0.7-2.2 GHz, T = 400 μs
Chirp bandwidth B and down-range resolution ΔR	B = 1.5 GHz, ΔR = 10 cm
Cross-range resolution ΔA (for aperture length L = 60 cm and target range 1-4 m)	At 1.45 GHz $\Delta A = (c/f_c) \times R/L$ = 35-140 cm
Maximum expected range R_{MAX} and maximum expected beat-note frequency f_{bMAX}	R_{MAX} = 4 m, f_{bMAX} = 100 kHz
ADC sampling frequency f_S	f_S = 20 MHz
Expected number of samples per chirp M (given f_S and T)	8000
Maximum Doppler shift f_{DMAX} to avoid ambiguity (given T)	$f_{DMAX} = \pm 1250$ Hz
Doppler resolution Δf_D (given N chirps of duration T)	Δf_D = 0.1 Hz (if NT = 10 s) or 0.05 Hz (if NT = 20 s)
Bit duration T_B to avoid aliasing for a sequence with K bits (given T, B, and R_{MAX} = 4 m)	$T_B < 5$ μs/K

Table 5.2 Summary of the waveform and radar parameters for the proposed radar system

Besides the aforementioned radar parameters, the power level at the transmitter and at different stages of the receiver has to be considered to ensure that the desired reflections from the targets can be successfully detected in typical through-wall scenarios. The expected overall power loss in through-wall detection, especially of human beings, has been investigated in several works in the literature. In [5] a modified radar equation is provided, taking into account the through-wall losses together with those already expected in free space scenarios, such as path loss, loss due to the target RCS, and polarization mismatch. The effect of the wall depends on its transmission coefficient, which is computed from the measured complex permittivity of the wall material; the RCS of possible targets is obtained from numerical simulations. Assuming a monostatic approach with the same antenna for transmission and reception, 10 dBi antenna gain, and 5 m range to the target, the expected power loss for through-wall detection of a standing human being is roughly 85 dB for a 9.2 cm brick wall and 115 dB for a 14.6 cm solid concrete wall; these values refer to 2.2 GHz frequency, and as expected the losses increase with frequency. It should be noted that the power loss increases with the bistatic angle in case two different antennas are used as transmitter and receiver. In [5] an additional loss up to 18 dB for concrete walls is assumed in case the bistatic angle increases up to 75 degrees. In [6-7] a similar approach combining the knowledge of the RCS of a standing human being and of the dielectric properties of different wall materials is applied to estimate the power loss. Assuming 20 cm thickness for different walls, the power loss across the 1-3 GHz frequency range and at 2 m range is 84-113 dB for brick wall and 93-124 dB for concrete wall.

Compared with the estimation presented in [5], the brick and concrete walls used in the experiments of this work are thicker (16 cm and 25 cm respectively) and the antennas have lower gain than 10 dBi, but the maximum range to the target is shorter than 5 m and the operational frequency is lower (0.7-2.2 GHz). Compared with the estimation in [6-7], the operational frequency is slightly lower (the maximum frequency is 2.2 GHz instead of 3 GHz) but the maximum distance of the target is slightly longer (4 m instead of 2 m). Taking these differences into account, an estimated overall through-wall power loss between approximately 100-136 dB can be considered from the aforementioned estimations, so that the expected power at the input of the ADC of the system presented in this chapter can be calculated.

Assuming 100 dB of through-wall power loss at 4m range, the expected power at the receiving antenna is therefore -72 dBm since the transmitted power is 28 dBm as shown in sub-section 5.1.3. Considering 12 dB gain for the LNA and 6 dB conversion loss at the mixer in the block diagram in figure 5.1, the beat-note power at the IF port of the mixer is about -66 dBm. After amplification by the base-band amplifier with 25 dB gain, the expected power of the signal at the ADC input is -41 dBm. Since the smallest voltage input range of the ADC is 220 mV, this power level may be too weak to detect the reflections from stationary human beings targets and discriminate them from the surrounding clutter due to the environment.

A sensitivity test has been carried out in order to identify the performance of the radar system when detecting weak signals. The test has been performed in back-to-back configuration, where the transmitter is directly connected to the receiver through cables and several attenuators. The ADC has been set with its smallest voltage input range and the starting value of attenuation between the transmitter and receiver was 60 dB, a value still too low in comparison with realistic TTWD scenarios. The value of attenuation was then increased in 10 dB steps until the received signal is not distinguishable from the noise. Fig. 5.16 shows the FMCW range profiles for this test, with values normalized to the initial test with 60 dB attenuation. As expected from a back-to-back test, there is a single beat-note frequency peak at roughly 89.7 kHz. It can be seen that with 100 dB attenuation the peak is still fairly distinguishable from the noise (approximately 10 dB above the noise), whereas this is no longer true for 110 dB attenuation.

Furthermore, an additional loss caused by the off-time at the receiver when FMICW waveforms are applied should be considered for the practical use of the system. The value of this additional loss depends on the gating sequence used and on the off-time over on-time ratio at the receiver. The gating loss should be added to the attenuation values used for the FMCW sensitivity test.
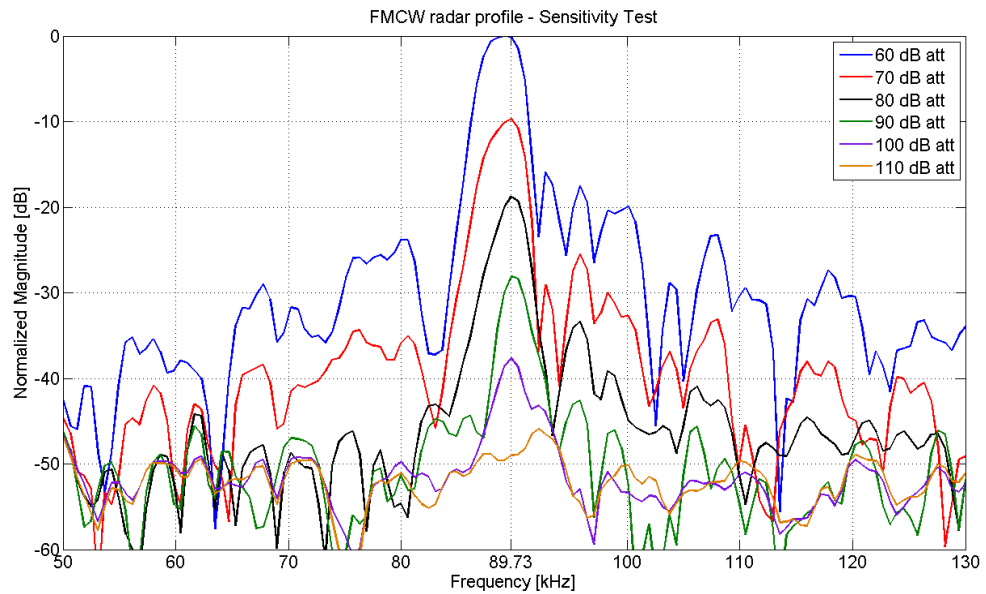
Figure 5.16 FMCW radar profiles of the back-to-back sensitivity test

Therefore, in performing the experimental campaign presented in chapter 6 of this thesis, the extraction of Doppler shifts due to the motion or breathing of human targets is explored as a solution to overcome this problem for the detection of human beings. The effectiveness of the proposed wall removal technique can be still appreciated when dealing with Doppler processing and patterns.

A possible hardware improvement to make the system able to detect stationary human beings without using Doppler could be the use of ad hoc modules at the receiver chain to replace the off-the-shelf LNA and base-band amplifier, for instance the automatic gain control unit or "signal conditioning" block developed at the Centre for Communications System, Durham University, providing gain up to 53 dB for the beat-note signal.

5.4 Summary of the chapter

The hardware description of the proposed FMICW based radar system has been provided in this chapter, focusing on each component of its block diagram. Off-the-shelf, already available components have been used when possible for simplicity's sake, or when required ad hoc components have been designed and manufactured, for instance the low pass filter at 3.5 GHz and the antennas. The distribution of the stable

rubidium clock and its use for the synchronization of the whole system has been also described, with emphasis on the use of the divided clock from the two AWGs for the trigger, in order to avoid jittering and Doppler artefacts. Finally radar performance parameters for the proposed system have been presented, showing its suitability to test the effectiveness of FMICW waveforms as wall removal technique in TTWD. Details about the programs written to control the AWG and the FPGA board, and to generate suitable FMCW and FMICW waveforms are provided in the appendix of this thesis.

5.5 References

[1]   G. L. Matthaei, et al., Microwave filters, impedance-matching networks, and coupling structures: McGraw-Hill, 1964.

[2]   F. Fioranelli, et al., "Optmized patch-like antennas for through the wall radar imaging and preliminary results with frequency modulated interrupted continuous wave," in Signals, Systems, and Electronics (ISSSE), 2012 International Symposium on, 2012, pp. 1-5.

[3]   M. Farwell, et al., "Sense through the wall system development and design considerations," Journal of the Franklin Institute, vol. 345, pp. 570-591, 2008.

[4]   M. G. Amin, Through-the-Wall Radar Imaging: CRC Press, 2010.

[5]   C. Thajudeen, et al., "Measured complex permittivity of walls with different hydration levels and the effect on power estimation of twri target returns," Progress In Electromagnetics Research B, vol. 30, pp. 177-199, 2011.

[6]   X. Zhuge, et al., "Assessment of electromagnetic requirements for UWB through-wall radar," in Electromagnetics in Advanced Applications, 2007. ICEAA 2007. International Conference on, 2007, pp. 923-926.

[7]   A. G. Yarovoy, et al., "Comparison of UWB technologies for human being detection with radar," in Radar Conference, 2007. EuRAD 2007. European, 2007, pp. 295-298.

6.1 Introduction and Environments of the Measurement Campaign

In this chapter experimental results on the effectiveness of the proposed FMICW waveforms as wall mitigation/removal technique for TTWD are presented. Particular emphasis is given to the comparison of radar images (for stationary targets) or Delay-Doppler patterns (for movement detection) when using normal FMCW and gated FMCW or FMICW waveforms. It is shown that FMICW waveforms reduce/remove the contribution of wall reflections and allow the detection of targets even when normal FMCW do not. Details on the architecture of the radar system and on the parameters of the waveforms used in the measurement campaign are provided in chapter 5 of this thesis.

Three different kinds of experiments have been performed: detection of different stationary objects behind walls, detection of people walking, and detection of people through breathing. For the first kind of experiments radar images have been created using the SAR approach, which combines measurements taken at different positions while the antennas are moved on a linear trajectory parallel to the wall. For motion detection the approach based on extracting Doppler shifts through double FFT processing as described in chapter 3 is adopted; this means that it is possible to detect the presence of a moving target, its speed, and if it is moving closer to or farther away from the radar, but the target cannot be precisely localized because only one transmitting and one receiving antenna in fixed positions have been used.

The experiments have been performed in realistic environments of the School of Engineering and Computing Sciences, Durham University, with three different kinds of walls.

In the rest of this section a description of walls and environments is provided. The first kind of wall is fairly common for office-like environments; it is 8 cm thick and made of plastered plywood panels with a honeycomb internal structure made of cardboard. Figure 6.1 shows the room where the targets have been placed during the measurements, in this case a wooden panel covered with aluminium foil to increase its RCS. The room is used for meetings and contains office-like pieces of furniture like tables, chairs, a blackboard, and a computer with projector. The radar system is placed

outside during the measurements, behind the wall that can be seen on the right-hand side of figure 6.1b.

(a)   **(b)**

Figure 6.1 View of the scenario with plastered plywood wall: (a) the inside of the meeting room, and (b) the inside of the room with view of the plywood wall

The second wall is 15 cm thick and made of bricks with layers of plaster on both sides. Through-wall measurements have been performed in two different environments with this kind of wall. The first environment is a landing close to a staircase, with the brick wall separating this area from a corridor. This environment is shown in figure 6.2a where a person is standing in front of the wall during the measurement and in 6.2b where the antennas and part of the radar system are mounted on a trolley on the other side of the wall. The second environment is a small storage room shown in figure 6.3. This room contains several pieces of electronic equipment which contribute to the clutter and make the through-wall detection more challenging. The person is moving or breathing inside this room while the radar system is placed outside, behind the wall.

(a)   **(b)**
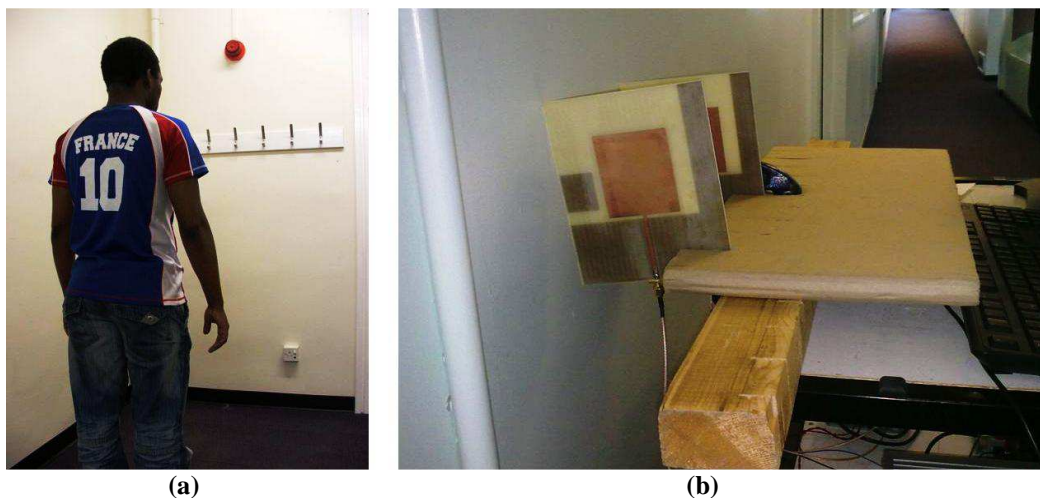
Figure 6.2 View of the scenario with brick wall: (a) person standing on the landing during the measurements, and (b) radar system on the corridor behind the brick wall

Figure 6.3 View of the scenario with brick wall (storage room)

The third kind of wall is 25 cm thick and is made of concrete blocks. Figure 6.4a shows the room where the targets are placed during the measurements (in this case a person holding a metallic panel), and figure 6.4b shows the antennas of the radar system placed outside the room, on the other side of the wall. The room where the measurements have been performed is a teaching room with several desks and chairs.

(a)   (b)

Figure 6.4 View of the scenario with concrete wall: (a) person inside the teaching room, and (b) antennas of the radar system behind the concrete wall

6.2 Methodology of the Measurements: Back-to-back Examples

In this section the methodology of the experiments presented in this chapter is discussed with reference to a couple of simple back-to-back examples, which are scenarios where the transmitter is directly connected to the receiver through cables, with no antennas involved. The process of selecting gating sequences for FMICW waveforms in order to mitigate/remove an undesired return is explained in details. Figure 6.5 displays the block diagram of the back-to-back tests. The transmitted signal is split and fed into two cables of different lengths and with different attenuation, and the resulting two signals are combined and fed into the receiver. The two different propagation paths simulate the presence of two targets placed at two different distances from the radar and having different RCS.
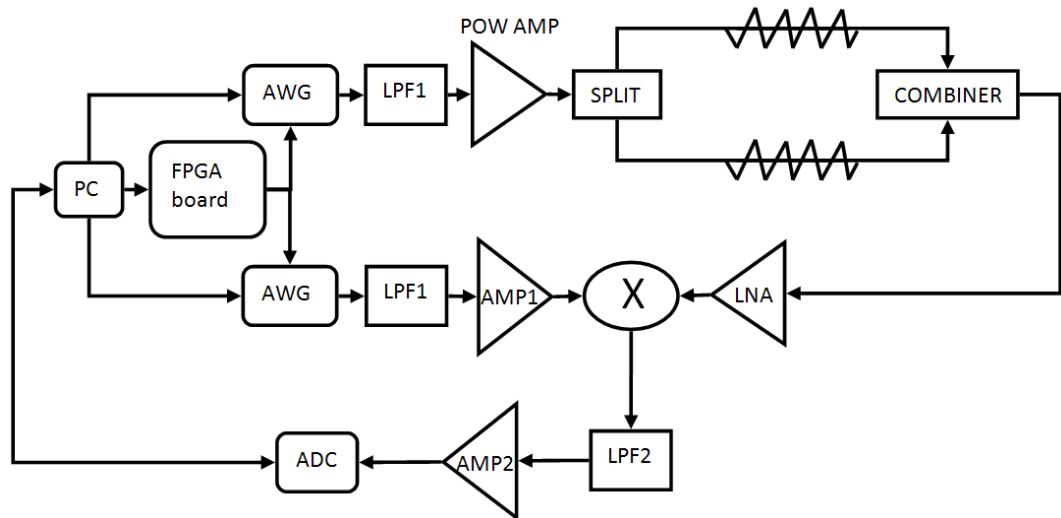
Figure 6.5 Block diagram of the back-to-back measurements

Normal FMCW waveforms are initially used to identify the frequency components of the beat-note signal which are related to the targets, or in this case to the two different propagation paths. Once the peak of the undesired return has been identified and its frequency has been converted into values of round-trip delay, a suitable gating sequence for FMICW waveforms is loaded into the AWG and the resulting radar profile can be obtained and used for further processing. Figures 6.6-6.7 show the comparison of the profiles using FMCW and FMICW waveforms and the MRS of the chosen gating sequence, respectively.

In the first back-to-back example the values of attenuation for the two propagation paths are 50 dB and 47 dB; as in figure 6.6, the corresponding frequency components are 79.4 kHz and 641 kHz, which are equal to 21.17 ns and 171 ns in terms of round-trip delay. A 3 bit M sequence with bit duration 40 ns and delay τ_{RX2} 22 ns is used to remove the first beat-note component. In figure 6.7 we can see that the MRS has indeed a blind range up to 22 ns, whereas it is providing no additional attenuation to the second component at 171 ns. As a result, in figure 6.6 the first component has been completely removed from the FMICW radar profile. It should be noted that the second component has been slightly attenuated because of the reduction of the received power due to the application of the gating sequence, as discussed in section 3.2.
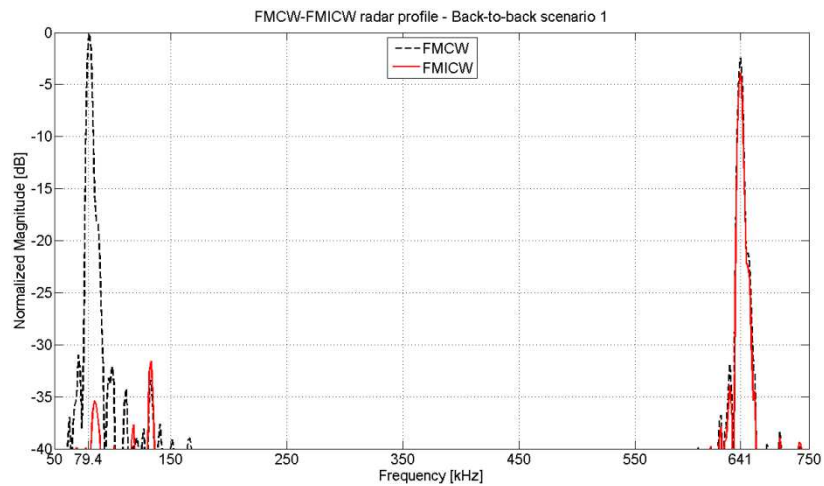
Figure 6.6 FMCW and FMICW radar profile of the back-to-back scenario 1
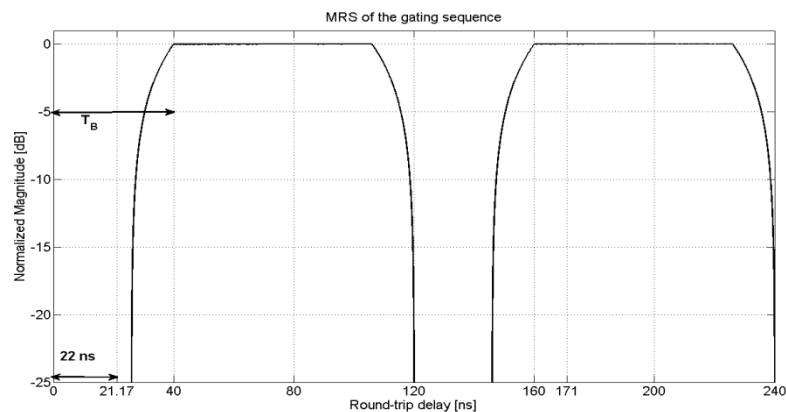
Figure 6.7 MRS of the gating sequence used in the back-to-back scenario 1

In the second back-to-back example the attenuation of the second propagation path has been increased to 66 dB and a much shorter cable has been used in order to have the two beat-note components much closer. This makes the back-to-back test more similar to realistic through-wall scenarios where the components related to the wall and those related to the targets are separated only by tens of kHz, which for the proposed system are equal to a few nanoseconds in terms of round-trip delay (with each nanosecond of round-trip delay corresponding to a range to the target of 15 cm in free space). In the FMCW profile shown in figure 6.8 we can see the two components at 79.4 kHz and 126.7 kHz, corresponding to 21.17 ns and 33.78 ns, respectively. The MRS of the gating sequence used to mitigate the first peak and at the same time not to attenuate the second one is shown in figure 6.9. It is a 3 bit M sequence with bit duration 30 ns and delay τ_{RX2} 21.125 ns. Using the FMICW waveform, the first peak has been removed from the radar profile and the second peak is the strongest component of the profile. Looking at figure 6.8, the first peak in the FMCW profile is roughly 12 dB higher than the second one, whereas in the FMICW profile the second peak is about 20 dB higher than the residual of the first peak.
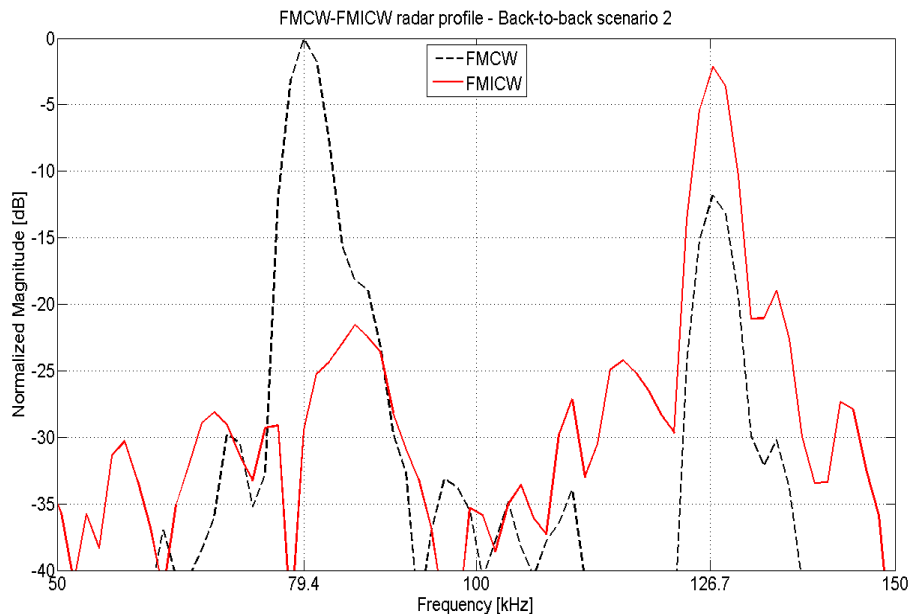
Figure 6.8 FMCW and FMICW radar profile of the back-to-back scenario 2
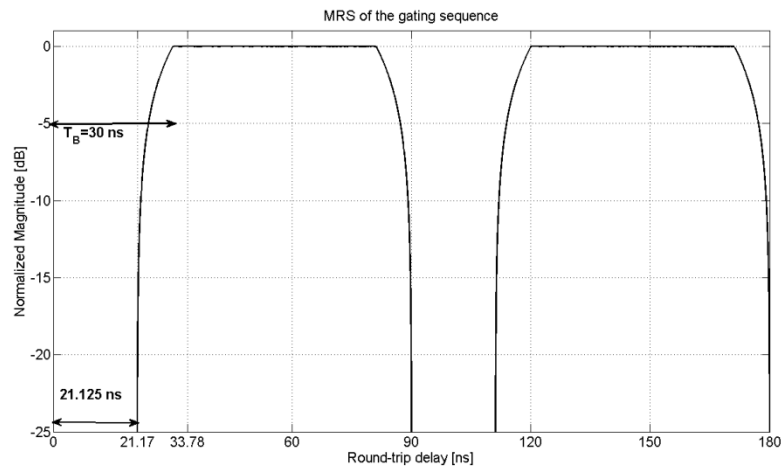
Figure 6.9 MRS of the gating sequence used in the back-to-back scenario 2

These two simple examples in back-to-back configuration show the methodology of the experiments presented in the next three sections of this chapter. Initially FMCW waveforms are used and the corresponding radar profile is analyzed to identify the frequency components related to the cross-talk between the antennas and to the wall reflections. These are normally the first and the second peak of the FMCW profile, or the first, large peak in case both signals are somewhat merged when the stand-off distance of the antennas from the wall is very short. Then the AWG are programmed to provide FMICW waveforms gated with suitable sequences to mitigate/remove the undesired components. Comparison of results when using normal FMCW and proposed FMICW waveforms are provided to show the effectiveness of the FMICW based technique in removing undesired components and enhancing the detection of the targets.

6.3 Experimental Results: Detection of Stationary Targets

In this section experimental results related to the through-wall detection of metallic and non-metallic stationary targets of different shapes are presented. The measurements have been performed in the first two environments described in section 6.1, namely the meeting room with plywood wall and the landing separated by a brick wall from the corridor. The measurements are performed using the SAR approach: the transmitting and the receiving antennas are placed 20 cm apart, and moved on a linear trajectory to 7 different positions which are placed 10 cm apart. The overall length of the synthetic array is therefore 60 cm. Images are created combining the radar profiles taken at each position through the imaging algorithms presented in chapter 4.

6.3.1 Scenario with plastered plywood wall

Figure 6.10 shows the FMCW radar profile of the scenario under test when there are no targets inside the room. The main peak caused by the antenna cross-talk and wall reflections is located at 78 kHz, corresponding to 20.8 ns in terms of round-trip delay. In this scenario the stand-off distance of the antennas from the wall is zero, as the tips of the antennas are touching the external side of the wall.

The thickness and the permittivity of the wall are assumed to be known when estimating the round-trip delay in order to create images. Values of 8 cm and 1.6 are chosen, respectively for thickness and permittivity. The thickness has been simply measured, whereas the permittivity has been estimated as an average between the value of air (1) and wood (around 2), since the plywood panel is mostly hollow inside, where the honeycomb structure made of cardboard is placed. As already discussed in chapter 4, errors in the estimation of these two parameters lead to displacements and blurring in the images, but a rigorous investigation of these effects or the development of a precise estimation procedure is beyond the scope of this work. Nevertheless the chosen values allow the creation of radar images where the displacement of the targets is within the down-range resolution of the proposed radar system (10 cm with 1.5 GHz bandwidth). The images presented in this section are suitable to compare the performance of different imaging algorithms and above all of FMCW and FMICW waveforms, which is the main focus of this work.

Once identified the peak of the undesired signal at 78 kHz (20.8 ns), a 3 bit M sequence with bit duration 7 ns and delays τ_{RX1} and τ_{RX2} equal to 0.75 ns was chosen. As it can be seen from the MRS in figure 6.11, the second blind range, which is centred at 21 ns and 1.5 ns long, is used to remove the undesired peak.
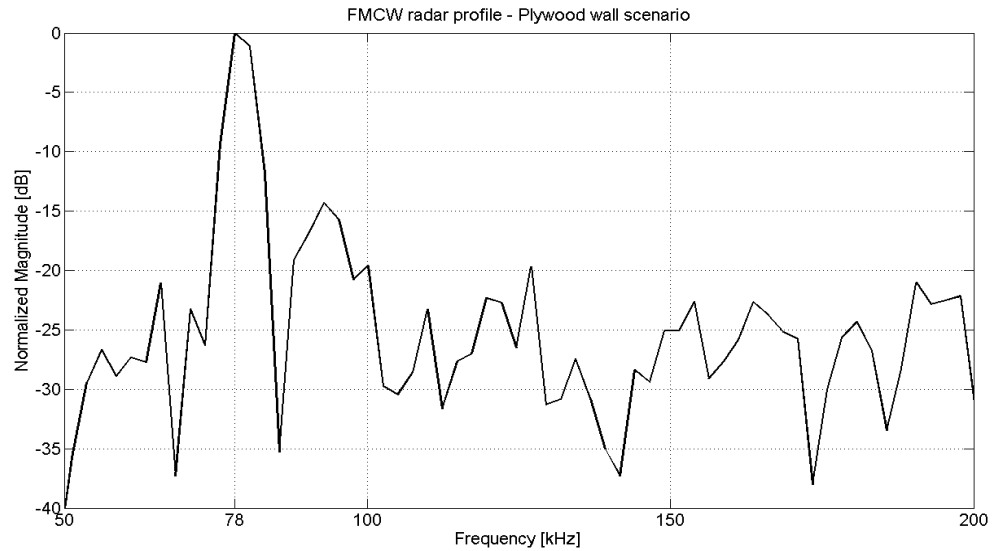
Figure 6.10 FMCW radar profile of the plywood wall scenario for stationary target detection
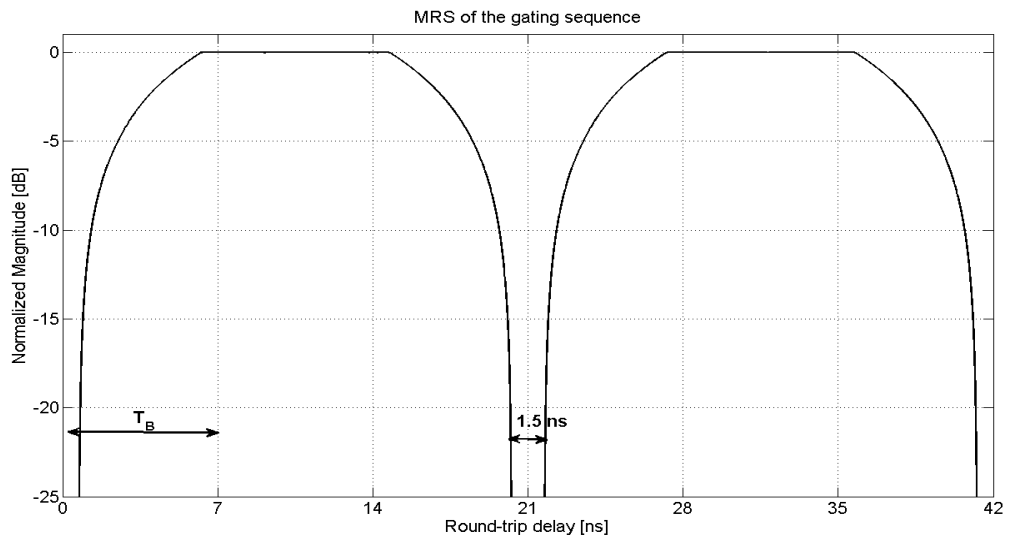
Figure 6.11 MRS of the gating sequence used for stationary target detection (plywood wall scenario)

Five different objects have been used as targets in these measurements and placed behind the plywood wall: a wooden panel covered with aluminium foil to increase its RCS, a cake tin, a plastic jerrycan filled with water, a metallic bin, and a fire extinguisher. For each object figures comparing images created using different algorithms and FMCW-FMICW waveforms are presented. The structure of each figure is the following: sub-figure (a) is created with FMCW waveform and BP algorithm, sub-figure (b) with FMICW and BP algorithm, sub-figure (c) with FMICW and DSI algorithm, and sub-figure (d) with FMICW and DMSI algorithm. The colour scale is the same for all the sub-figures in each figure and is in decibel.

Figure 6.12 Wooden panel covered with aluminium foil behind plywood wall

Figure 6.13 Detection of the wooden panel covered with aluminium foil behind plywood wall: (a) with FMCW and BP algorithm, (b) with FMICW and BP algorithm, (c) with FMICW and DSI algorithm, and (d) with FMICW and DMSI algorithm

Figure 6.14 Cake tin behind plywood wall
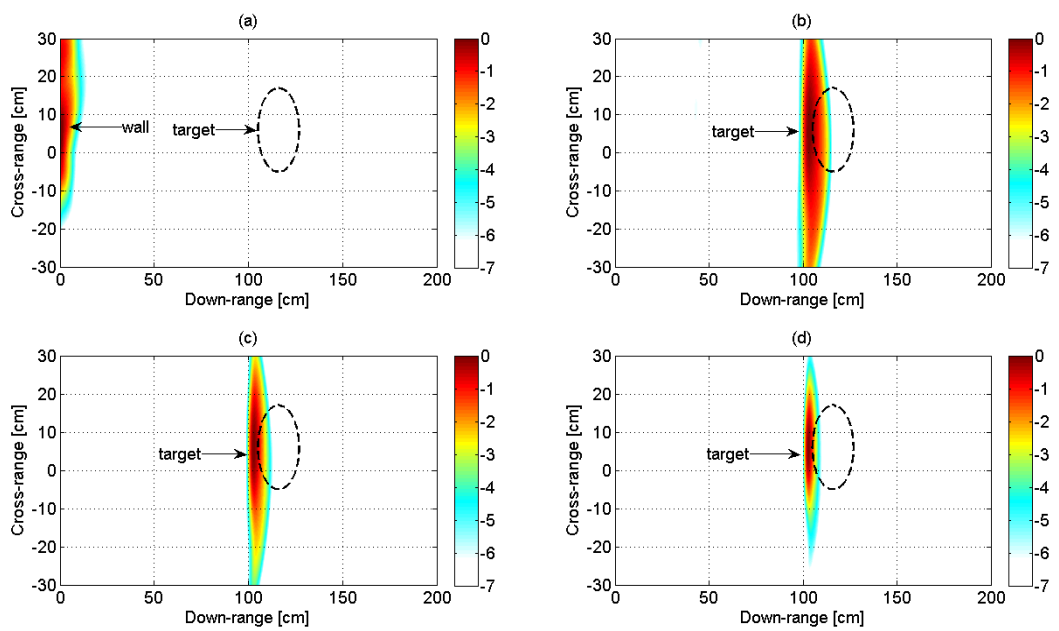
Figure 6.15 Detection of the cake tin behind plywood wall: (a) with FMCW and BP algorithm, (b) with FMICW and BP algorithm, (c) with FMICW and DSI algorithm, and (d) with FMICW and DMSI algorithm

Figure 6.16 Plastic jerrycan filled with water behind plywood wall
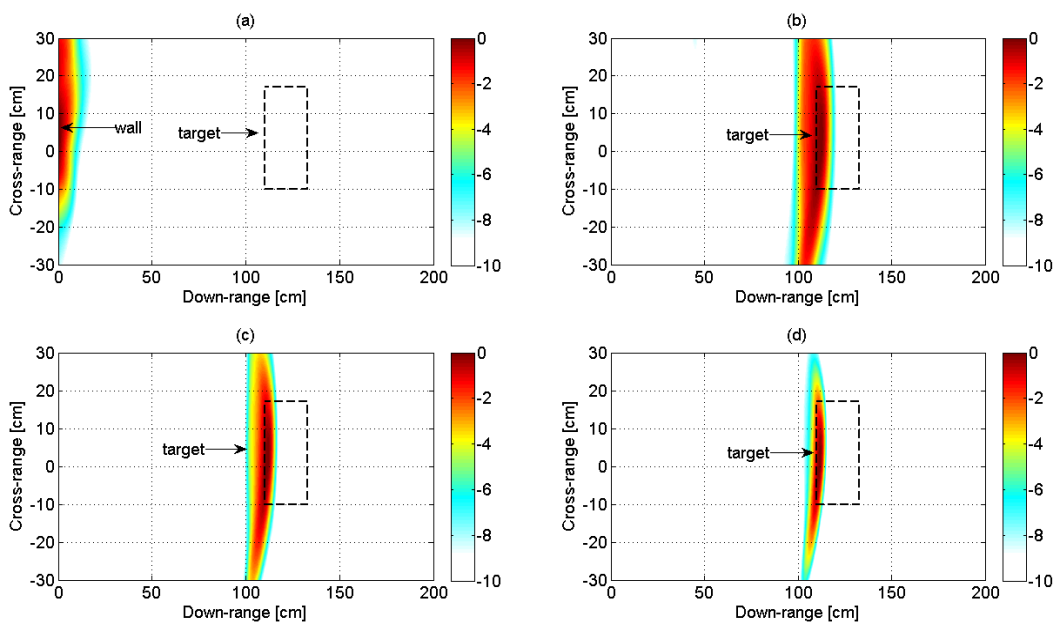
Figure 6.17 Detection of the plastic jerrycan filled with water behind plywood wall: (a) with FMCW and BP algorithm, (b) with FMICW and BP algorithm, (c) with FMICW and DSI algorithm, and (d) with FMICW and DMSI algorithm

Figure 6.18 Metallic bin behind plywood wall
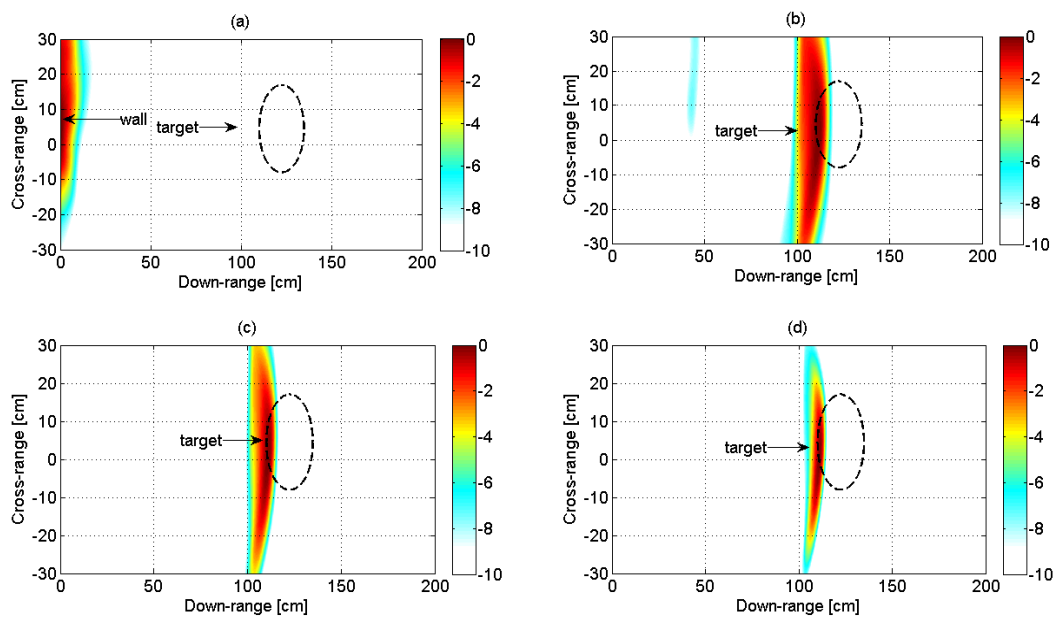
Figure 6.19 Detection of the metallic bin behind plywood wall: (a) with FMCW and BP algorithm, (b) with FMICW and BP algorithm, (c) with FMICW and DSI algorithm, and (d) with FMICW and DMSI algorithm

Figure 6.20 Fire extinguisher behind plywood wall
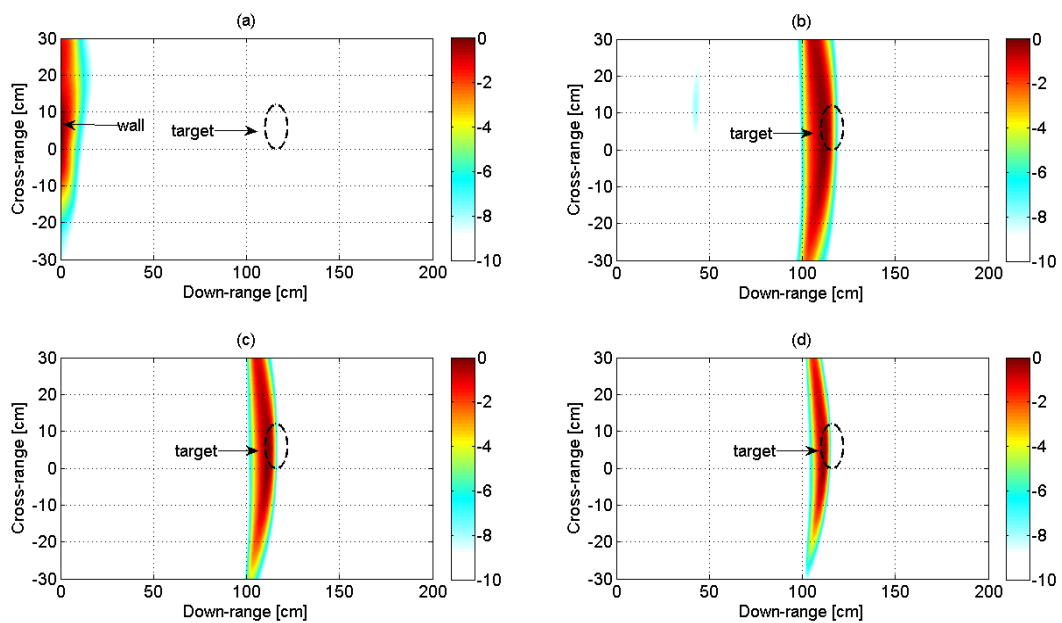
Figure 6.21 Detection of the fire extinguisher behind plywood wall: (a) with FMCW and BP algorithm, (b) with FMICW and BP algorithm, (c) with FMICW and DSI algorithm, and (d) with FMICW and DMSI algorithm

Inspecting these images some conclusions can be drawn for every target used in these experiments. The effectiveness of the FMICW waveforms as wall removal technique can be seen comparing sub-figures (a) and (b) in each figure. The application of the gating sequence allows the detection and localization of the target and removes the reflection from the wall, which is the only visible component on every FMCW image. Comparing different imaging algorithms it can be seen that DSI and even more DMSI produce images where the coloured spots are much better focused on the actual position of the targets in comparison with classic BP algorithm. In figures 6.19 and 6.21 DSI and

DMSI algorithms suppress the artefact at roughly 50 cm down-range, which is present in the images created using BP algorithm.

6.3.2 Scenario with brick wall

The measurements presented in this sub-section have been performed in the environment shown in figure 6.2. The targets are the same objects used for the tests behind the plywood wall. The thickness of the brick wall used in these measurements is 15 cm and the permittivity is assumed to be 4.6.

Figure 6.22 shows the FMCW radar profile of the scenario under test when there are no targets behind the brick wall. Two peaks can be seen at 90.4 kHz and 97.7 kHz because of the cross-talk between the antennas and the reflection from the wall, respectively. These frequency components correspond to 24.1 ns and 26.05 ns in terms of round-trip delay. Three different gating sequences have been tested in order to remove the undesired components through FMICW waveforms: 3 bit M sequence with bit duration 32 ns and delay τ_{RX2} equal to 26 ns, 3 bit M sequence with bit duration 8.5 ns and delays τ_{RX1} and τ_{RX2} equal to 1 ns, and square wave with bit duration 12 ns and delays τ_{RX1} and τ_{RX2} equal to 2 ns. The MRS patterns of these sequences are shown in figure 6.23. The first gating sequence uses the delay τ_{RX2} to increase the first blind range of the MRS to remove the undesired components, whereas the second and third gating sequence use the second blind range, which is centred at 25.5 ns and 24 ns, respectively.

For each target two figures are presented. The former compares FMCW and FMICW images with different gating sequences, but using the same imaging algorithm (BP); sub-figure (a) is created with FMCW waveform, sub-figure (b) with FMICW using the first gating sequence, sub-figure (c) with FMICW using the second sequence, and sub-figure (d) with FMICW using the third sequence. The latter figure compares results using BP and DMSI imaging algorithms for recorded data with FMICW waveforms gated by the first sequence. It should be noted that the colour scale is the same for every sub-figure in each figure and it is in decibel.
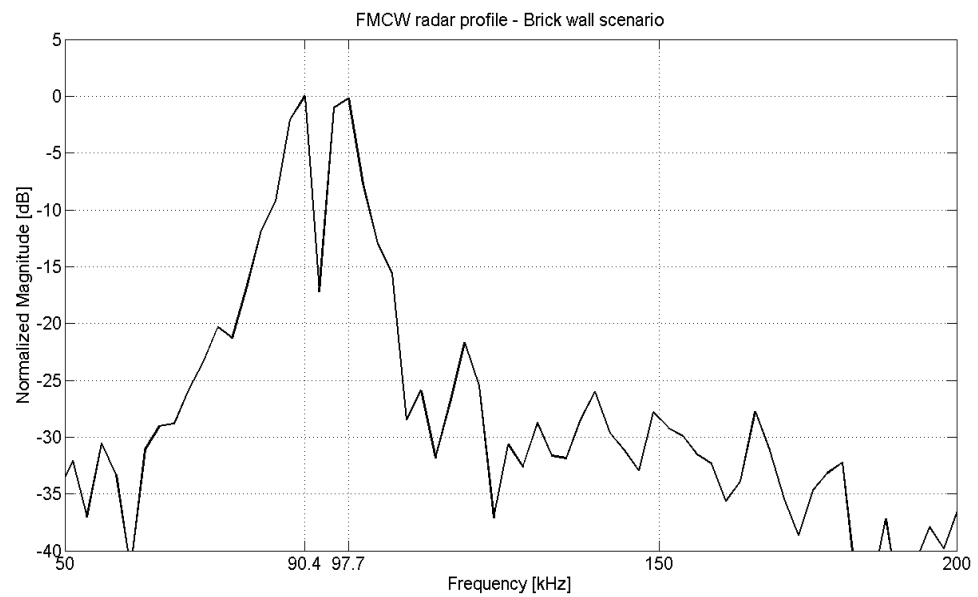
Figure 6.22 FMCW radar profile of the brick wall scenario for stationary target detection
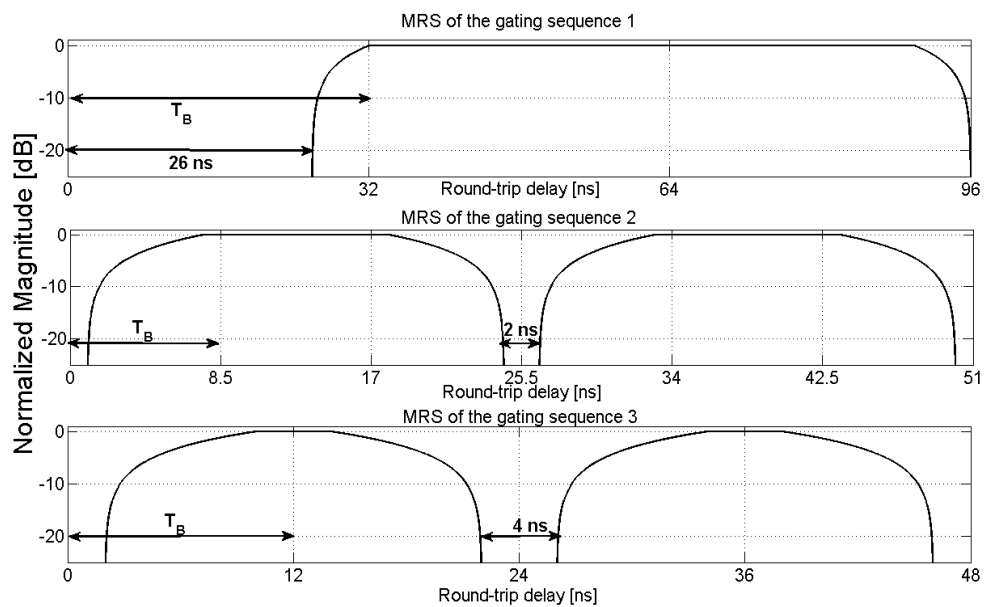
Figure 6.23 MRS of the gating sequences used for stationary target detection (brick wall scenario)
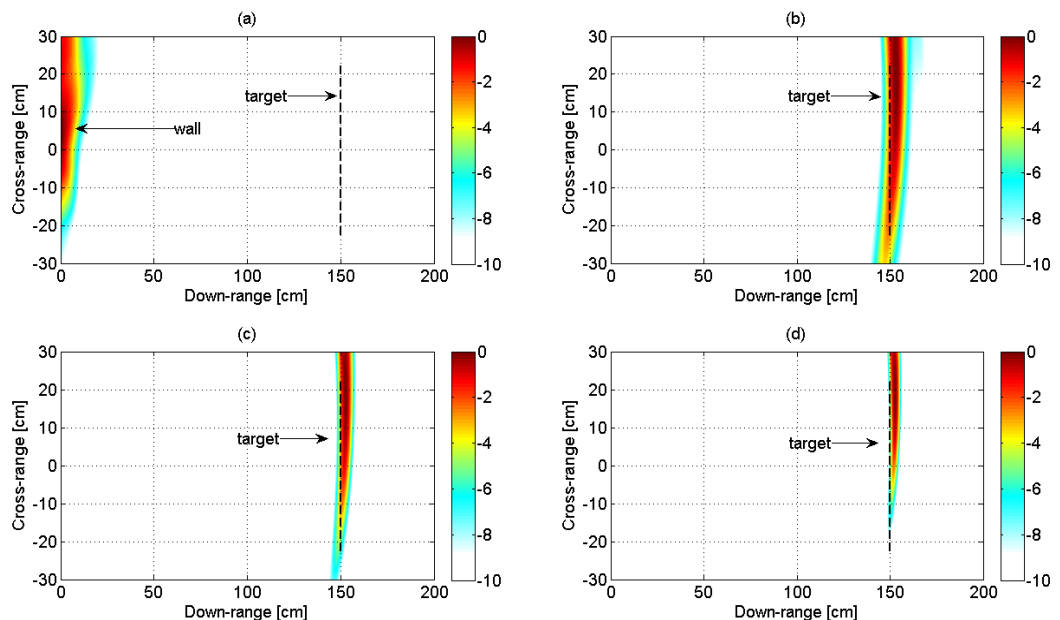
Figure 6.24 Wooden panel covered with aluminium foil behind brick wall
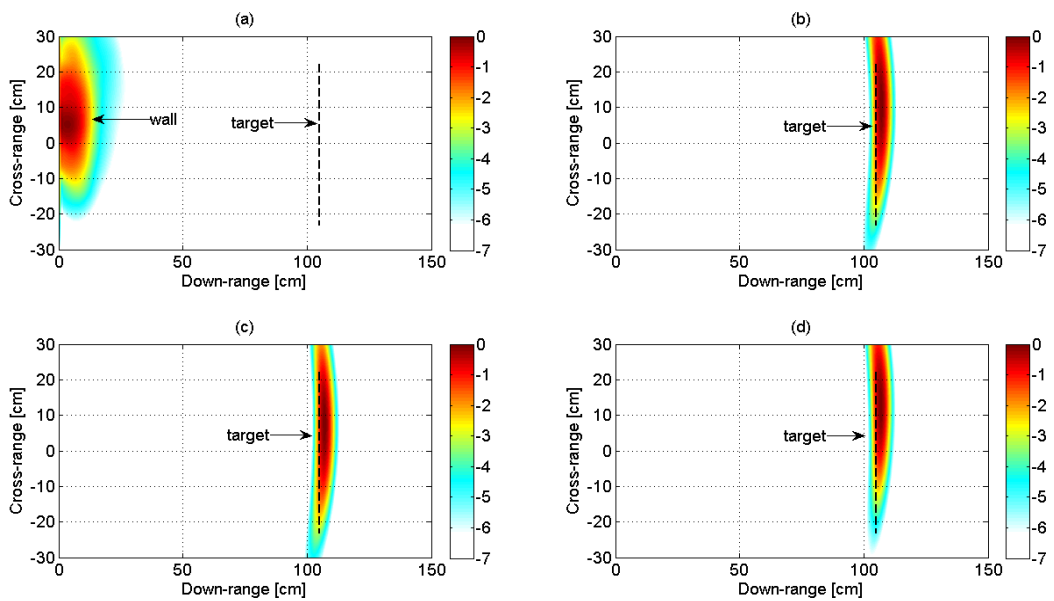
Figure 6.25 Detection of the wooden panel covered with aluminium foil behind plywood wall using BP algorithm: (a) with FMCW, (b) with FMICW gated with sequence 1, (c) with FMICW gated with sequence 2, and (d) with FMICW gated with sequence 3
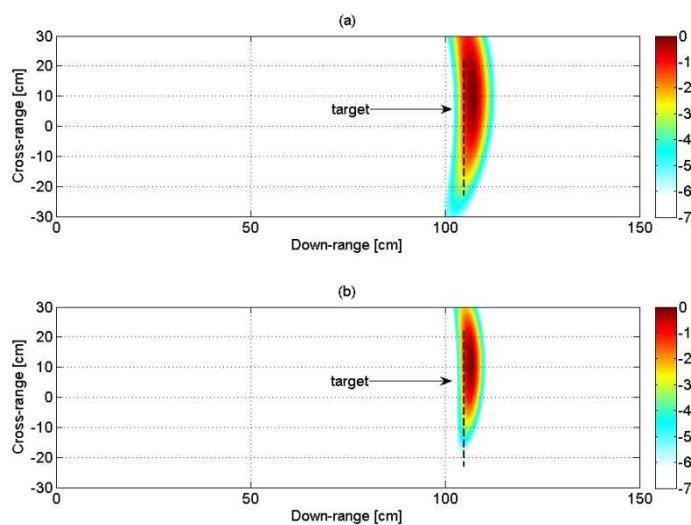
Figure 6.26 Detection of the wooden panel covered with aluminium foil behind plywood wall using FMICW data gated with sequence 1: (a) with BP, and (b) with DMSI algorithm

Figure 6.27 Cake tin behind brick wall
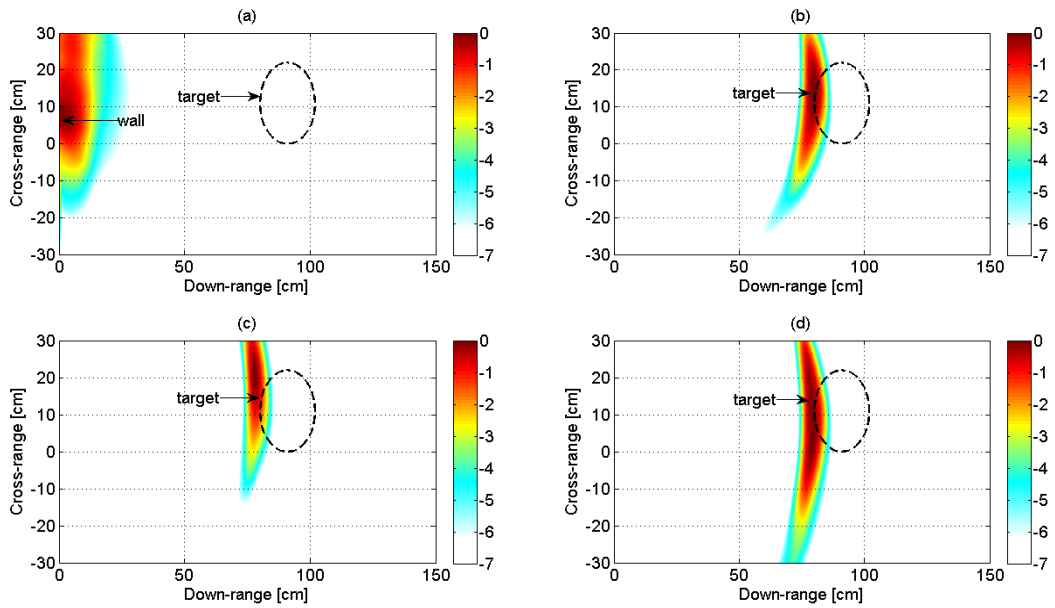
Figure 6.28 Detection of the cake tin behind plywood wall using BP algorithm: (a) with FMCW, (b) with FMICW gated with sequence 1, (c) with FMICW gated with sequence 2, and (d) with FMICW gated with sequence 3
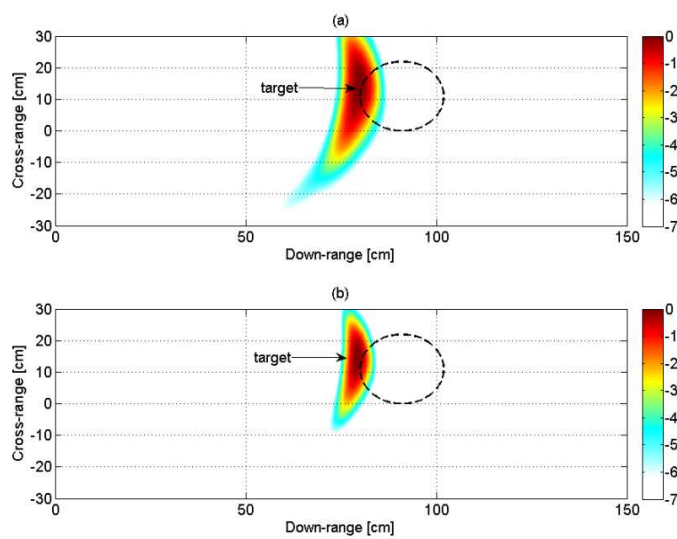
Figure 6.29 Detection of the cake tin behind plywood wall using FMICW data gated with sequence 1: (a) with BP, and (b) with DMSI algorithm

Figure 6.30 Plastic jerrycan filled with water behind brick wall
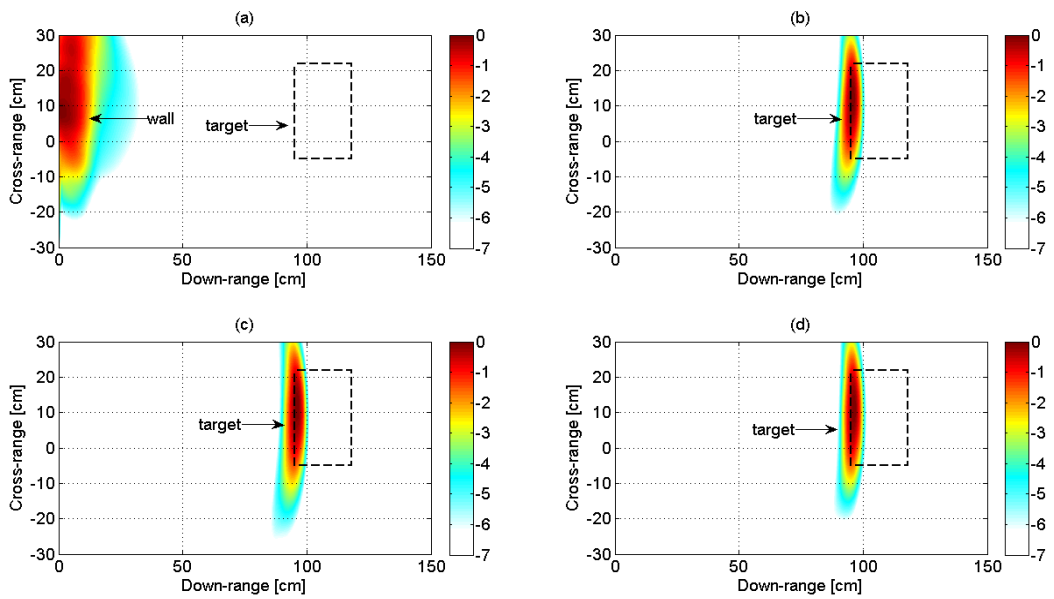
Figure 6.31 Detection of the plastic jerrycan filled with water behind plywood wall using BP algorithm: (a) with FMCW, (b) with FMICW gated with sequence 1, (c) with FMICW gated with sequence 2, and (d) with FMICW gated with sequence 3
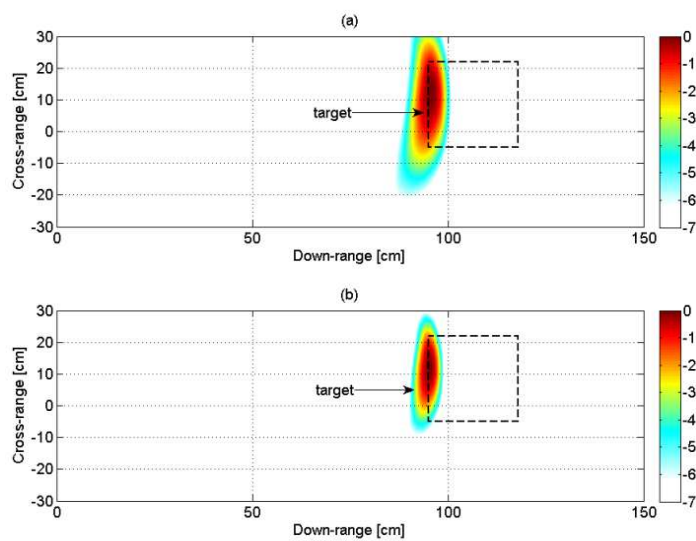
Figure 6.32 Detection of the plastic jerrycan filled with water behind plywood wall using FMICW data gated with sequence 1: (a) with BP, and (b) with DMSI algorithm

Figure 6.33 Metallic bin behind brick wall
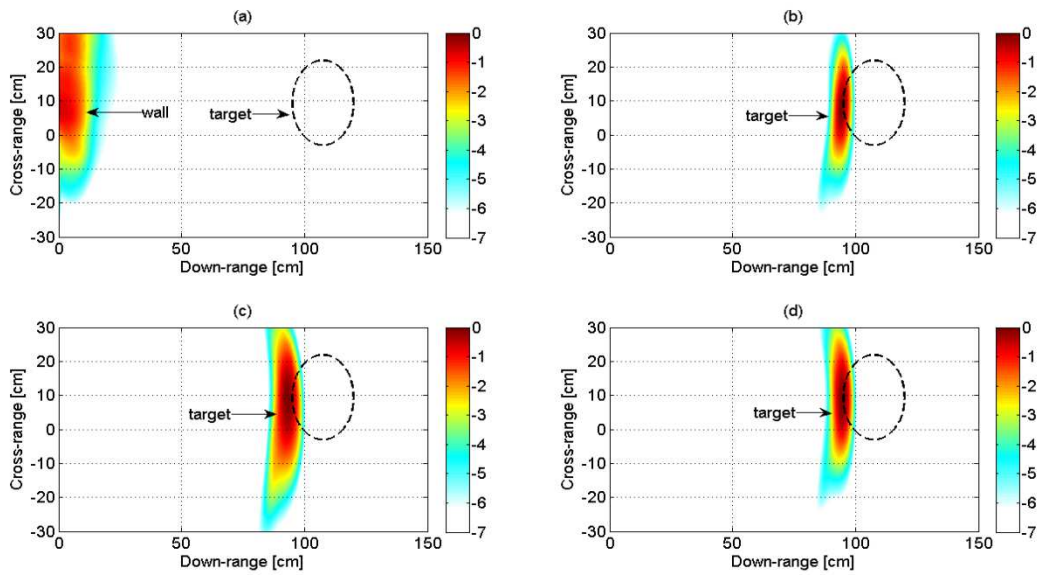
Figure 6.34 Detection of the metallic bin behind plywood wall using BP algorithm: (a) with FMCW, (b) with FMICW gated with sequence 1, (c) with FMICW gated with sequence 2, and (d) with FMICW gated with sequence 3
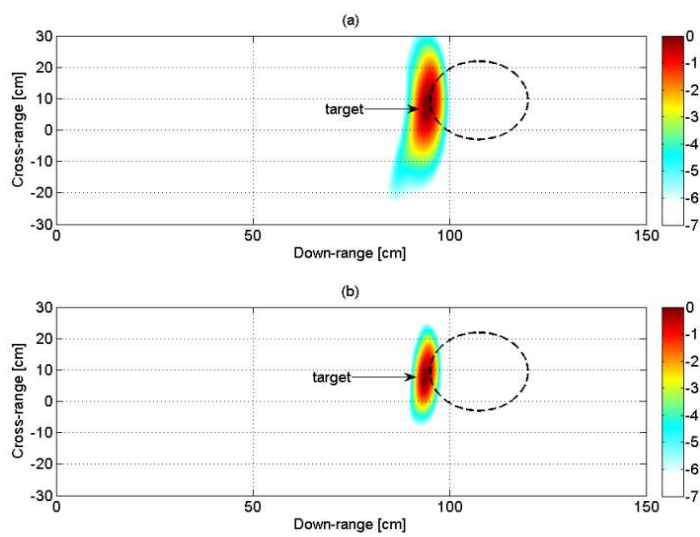
Figure 6.35 Detection of the metallic bin behind plywood wall using FMICW data gated with sequence 1: (a) with BP, and (b) with DMSI algorithm

The effectiveness of the proposed FMICW waveforms as wall removal technique is confirmed by these results even for scenarios with brick wall, which is more challenging than the plywood wall previously analyzed. The three gating sequences tested in these experiments are all successful in removing the reflection from the wall and allow the localization of the target; both approaches of using the first blind range of the MRS (as for the gating sequence number 1) and of using the second blind range (as for gating sequences number 2 and 3) prove to be suitable. In terms of imaging algorithms, DMSI gives better focused images in comparison with BP, as expected and as already observed for the tests with the plywood wall.

6.3.3 Summary of results for detection of stationary targets

In this section the effectiveness of the FMICW waveforms is shown through radar images of stationary targets created using the SAR approach (with 7 measurement positions placed 10 cm apart): only wall reflections appear in the images when normal FMCW waveforms are used, whereas FMICW waveforms gated by suitable sequences allow the detection of the targets. The targets include metallic objects with rounded shape (e.g. the cake tin and the bin), thus with smaller RCS than those with flat section, and also non-metallic objects such as the jerrycan filled with water, which has even smaller RCS.

In terms of algorithms, DSI and DMSI adapted from medical imaging show better results than classic BP algorithm: the coloured spots are better focused on the actual positions of the targets, and artefacts can be removed.

In the next sections of this chapter FMICW waveforms are similarly applied to the through-wall detection of people and their walking and breathing movement. Comparisons between results with normal FMCW waveforms and with the proposed FMICW waveforms are provided.

6.4 Experimental Results: Detection of Walking Movement

In this section results related to the detection of walking movement are presented. A person is walking inside the room under test behind the wall and the radar is placed outside, on the other side of the wall, and can detect the presence of the movement. As mentioned at the beginning of this chapter, the detection is performed through the computation of the Delay-Doppler pattern via double FFT processing, which has been described in chapter 3. Delay-Doppler patterns are presented in this thesis as bidimensional figures: on the horizontal axis the round-trip delay is shown as in radar range profiles, whereas on the vertical axis the Doppler shift due to the motion of possible targets is recorded and shown as coloured spots, with a suitable colour decibel scale to differentiate different Doppler shift intensity. When no motion is detected, thus there is no Doppler, the coloured spots are located in the middle of the vertical axis at Doppler 0 Hz; when some kind of motion is detected, coloured spots appear at some values of positive or negative Doppler and at a certain round-trip delay. The Doppler values depend on the speed of the target and the round-trip delay values depend on the distance of the target from the radar during the measurement time.

In most of the experiments presented in this section the person is walking back and forth on a radial trajectory, going closer to and farther from the wall within the measurement time, so that the expected Doppler signature of this motion is both positive and negative. The radial trajectory provides maximum Doppler shift, thus the best condition to test the different detection performance of FMCW and FMICW waveforms, which is the main focus of this thesis' work.

In some cases the change detection technique described in chapter 2 is combined with FMICW waveforms. With this approach consecutive radar range profiles from each FMCW or FMICW signal are subtracted prior to applying the second FFT on the result to extract Doppler information (coherent subtraction). This removes stationary clutter including wall reflections and enhances the detection of movements.

The methodology of these measurements is the same as in those for detection of stationary targets. FMCW waveforms are used initially; then suitable gating sequences and FMICW waveforms are applied to remove undesired components such as antenna-cross-talk and wall reflections.

In the measurements presented in this section 10 seconds of data have been recorded, corresponding to 0.1 Hz Doppler resolution, which is a good value for detection of walking movement.

6.4.1 Scenario with plastered plywood wall

The first scenario under test is the meeting room with plastered plywood walls shown in figure 6.1. Initially the Delay-Doppler pattern (figure 6.36) and the range profile (figure 6.37) for the "empty scenario" are presented when using FMCW waveforms. Nothing is moving inside the room and therefore no Doppler shifts are recorded in figure 6.36. The highest component at 102.3 kHz in the profile of figure 6.37 is caused by the antenna cross-talk and wall reflections. The corresponding round-trip delay value for this peak is 27.28 ns, where a brighter, orange spot can be seen at 0 Hz in the Delay-Doppler shown in figure 6.36.

Then the MRS of two suitable gating sequences is given in figure 6.38: a 3 bit M sequence with bit duration 9 ns and delays τ_{RX1} and τ_{RX2} equal to 3 ns, which uses the second blind range of the MRS to remove the undesired component, and again an M sequence with bit duration 35 ns and delay τ_{RX2} equal to 28 ns, which uses the first blind range for wall removal.
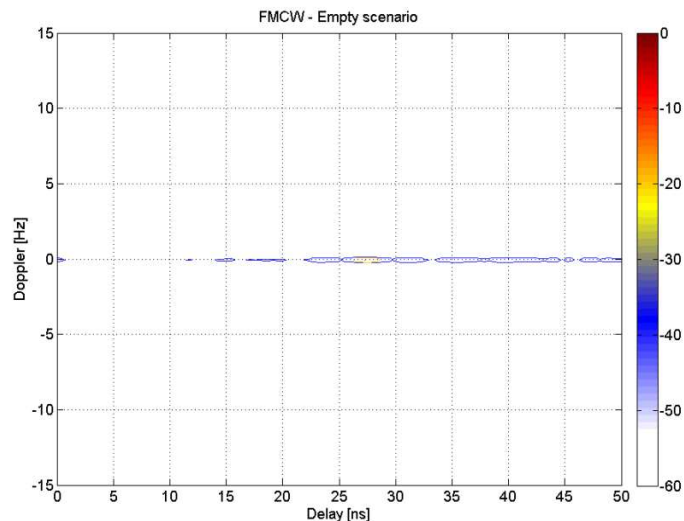
Figure 6.36 FMCW Delay-Doppler of the empty scenario with plywood wall for walking movement detection
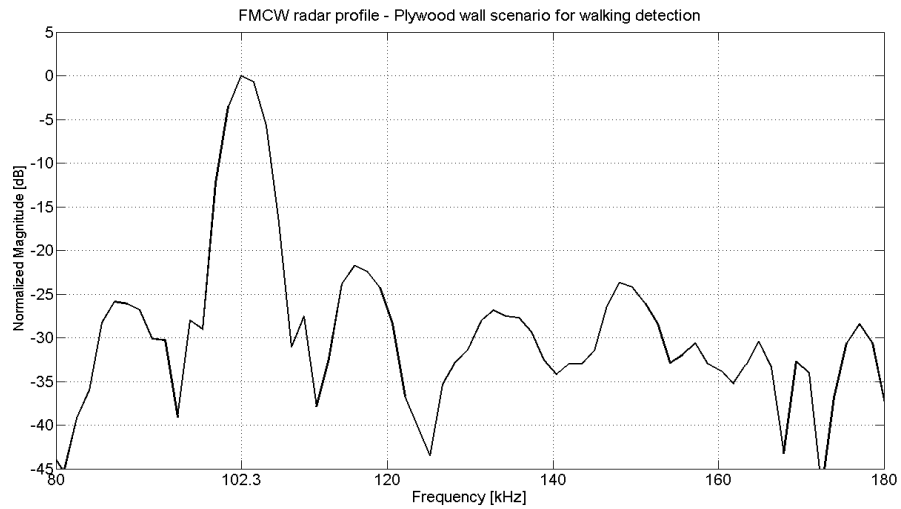
Figure 6.37 FMCW radar profile of the plywood wall scenario for walking movement detection
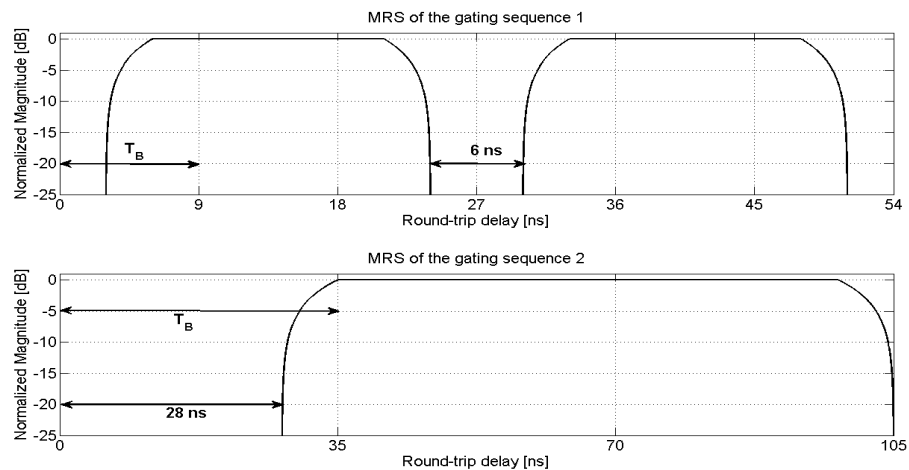
Figure 6.38 MRS of the gating sequences used for walking movement detection (plywood wall scenario)

Delay-Doppler patterns using normal FMCW and proposed FMICW waveforms are compared for measurements where a person is walking back and forth behind the wall, initially carrying a panel covered with aluminium foil to increase the overall RCS (figures 6.39-6.41), then more realistically without this panel (figures 6.42-6.44).

Figures 6.39-6.41 show the Delay-Doppler using FMCW waveforms, using FMICW waveforms gated with the first sequence of figure 6.38, and using FMICW waveforms combined with change detection, respectively.

Comparing figure 6.39 and figure 6.40, it can be seen how with FMICW waveforms the presence of the walking person can be detected: in figure 6.40 (with FMICW waveforms) a positive and negative Doppler signature can indeed be seen with the same coloured scale used in figure 6.39 (with FMCW waveforms), where nothing is detected and the room appears empty, with the same Delay-Doppler pattern as in figure 6.36. The orange spot at roughly 27.3 ns which is related to the wall reflections is removed in figure 6.40 in comparison with figure 6.39, as a consequence of the application of FMICW waveforms.

The positive and negative Doppler pattern is related to the back and forth radial movement of the person, although it contains a great deal of clutter because of the metallic panel that the person moves while walking. In figure 6.41 the combination of change detection and FMICW waveforms yields a much clearer Delay-Doppler pattern, where the stationary clutter at 0 Hz has been removed, as well as most of the clutter which is present in figure 6.40. The Doppler shift of this walking movement is centred at roughly ±10 Hz, corresponding to 2 m/s speed, which is a reasonable value for a person walking at fast pace. It should be also noted that the coloured scale of figure 6.41 has a much narrower dynamic range compared with figures 6.39-6.40.
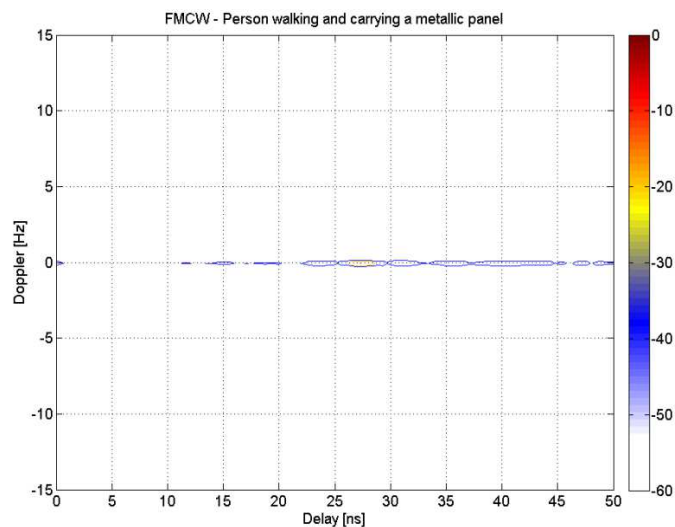
Figure 6.39 FMCW Delay-Doppler – Person walking and carrying a metallic panel behind plywood wall
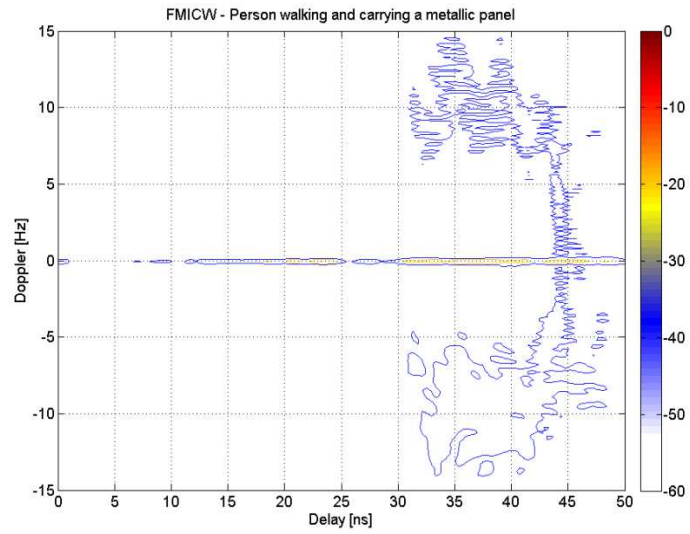
Figure 6.40 FMICW Delay-Doppler – Person walking and carrying a metallic panel behind plywood wall
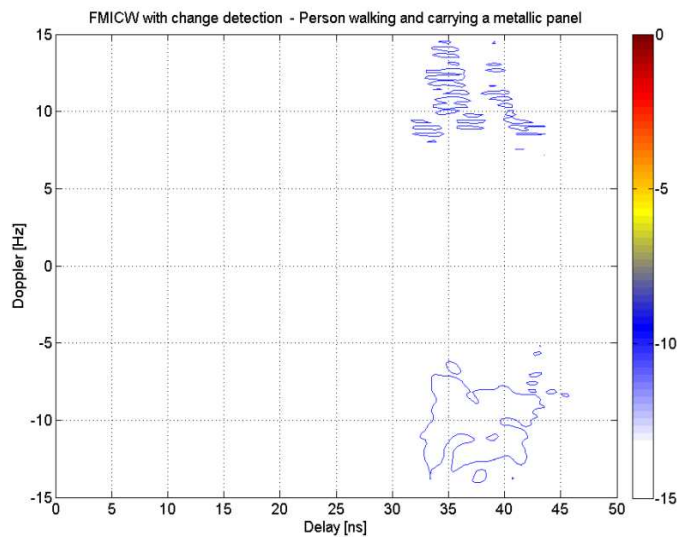
Figure 6.41 FMICW Delay-Doppler with change detection – Person walking and carrying a metallic panel behind plywood wall

Figures 6.42 and 6.43 refer to the more realistic measurement with the person walking without carrying any metallic panel.

Figure 6.42 shows the Delay-Doppler using FMCW waveforms and no difference can be seen with figure 6.36 which represents the empty scenario. Figure 6.43 shows the Delay-Doppler when FMICW waveforms are applied, in particular sub-figures (a) and (b) when the first gating sequence of figure 6.38 is used and sub-figures (c) and (d) when the second sequence is used. In sub-figures (b) and (d) change detection is combined with FMICW waveforms. We can see that both gating sequences are effective in detecting the movement and showing the Doppler signature in comparison with the normal FMCW waveform used in figure 6.42; the second gating sequence gives clear positive and negative Doppler shifts even without change detection (comparing sub-figures (a) and (c) in 6.43), and the level of clutter is reduced when change detection is applied, with better focused Doppler spots (comparing sub-figures (b) and (d) in 6.43). The values of Doppler shift (roughly ±10-15 Hz) are similar to those recorded in figure 6.41 for the previous experiment and compatible with a fast pace walking.
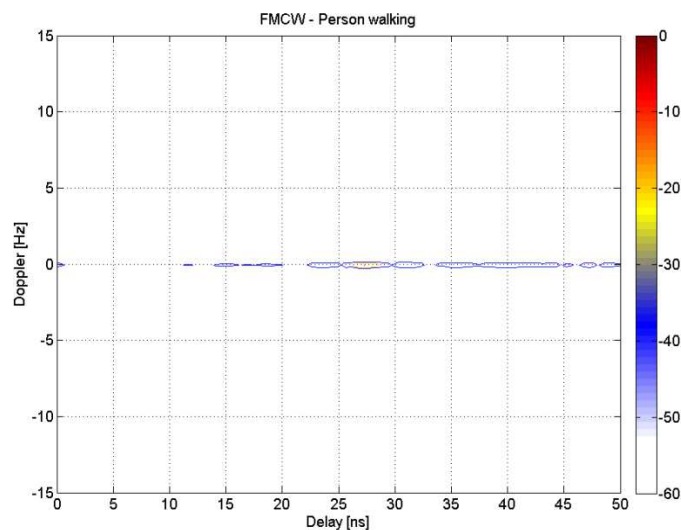
Figure 6.42 FMCW Delay-Doppler – Person walking behind plywood wall
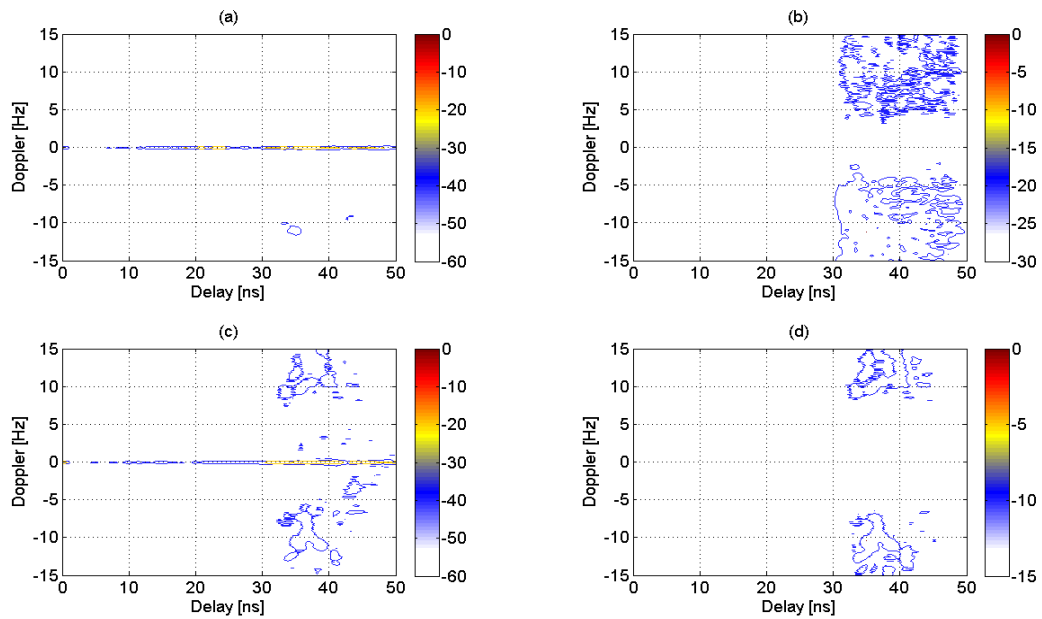
Figure 6.43 FMICW Delay-Doppler for a person walking behind a plywood wall: (a) gated with sequence 1, (b) gated with sequence 1 and combined with change detection, (c) gated with sequence 2, and (d) gated with sequence 2 and combined with change detection

Finally figure 6.44 compares two different paces of the person walking inside the room, faster in sub-figures (a) and (b), and slower in sub-figures (c) and (d). FMICW waveforms have been used for every sub-figure, and change detection is also applied to sub-figures (b) and (d). It is not worth showing figures using FMCW since no Doppler can be detected as in figures 6.42 and 6.39, and the scenario under test would appear empty. As expected the faster walking pace produces higher Doppler shifts than the slower pace (up to ±20 Hz against ±10 Hz, corresponding to roughly 4 and 2 m/s speed, respectively). Again the application of change detection gives a cleaner positive and negative Doppler pattern and allows the detection even with a narrower dynamic range of the coloured scale.
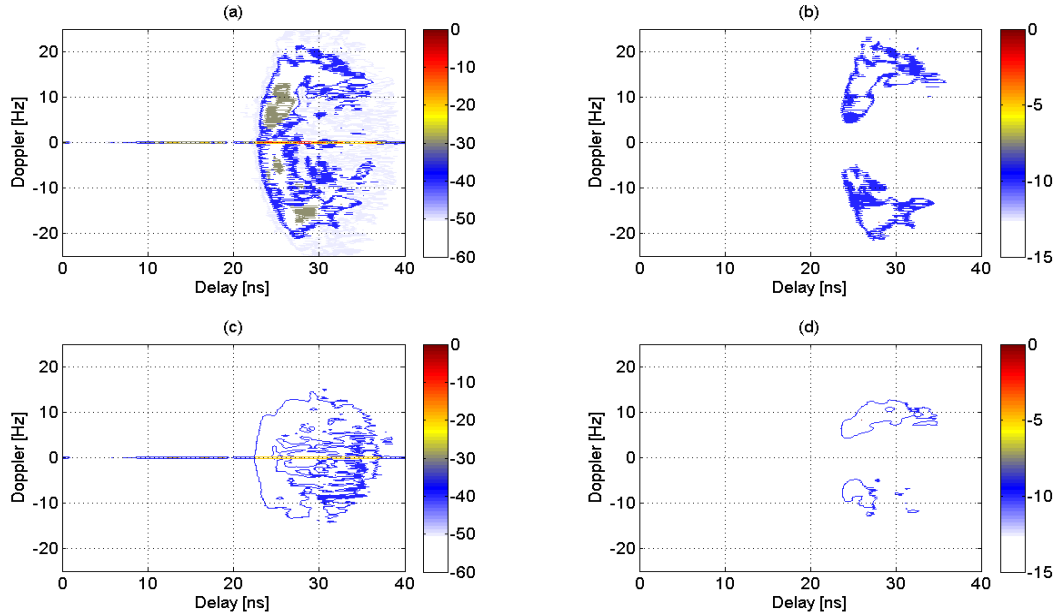
Figure 6.44 FMICW Delay-Doppler for a person walking behind a plywood wall: (a) fast walking pace, (b) fast walking pace and change detection applied, (c) slow walking pace, and (d) slow walking pace and change detection applied

6.4.2 Scenarios with brick wall

In this sub-section we present results referring to the scenarios with brick walls shown in figures 6.2 and 6.3.

The first group of measurements have been performed on the landing shown in figure 6.2 using antipodal Vivaldi antennas. Figure 6.45 shows the radar profile using FMCW waveforms for the empty scenario, where nothing is moving behind the brick wall. Two peaks related to the antenna cross-talk and to wall reflections can be seen at 82.4 kHz and 88.5 kHz, equal to 21.9 ns and 23.6 ns in terms of round-trip delay, respectively. Figure 6.46 shows the MRS of the chosen 3 bit M sequence, with bit duration 30 ns and delay τ_{RX2} equal to 24 ns, which uses the first blind range of the MRS for wall removal.

Figures 6.47-6.49 show Delay-Doppler patterns using different waveforms: the first figure uses normal FMCW, the second FMICW with the gating sequence shown in figure 6.46, and the third combines FMCW waveforms with change detection. Comparing figures 6.47 and 6.48 we can see that the Doppler signature of the walking movement is detected only using FMICW waveforms, despite the presence of clutter. In

figure 6.47 only stationary components are detected, in particular the orange spot between 20 ns and 25 ns, which is caused by cross-talk and wall reflections as already seen in the range profile in figure 6.45. Comparing figures 6.48 and 6.49, we can see that the application of change detection produces a much cleaner pattern, where both positive and negative Doppler shifts can be seen, as expected for a back and forth walking movement. The value of the Doppler is centred on roughly ±10 Hz, which is compatible with a person walking with a fairly fast pace, and consistent with the results already presented for the plywood wall scenario.

Figure 6.45 FMCW radar profile of the brick wall scenario 1 (landing) for walking movement detection

Figure 6.46 MRS of the gating sequence used for walking movement detection (brick wall scenario 1, landing)
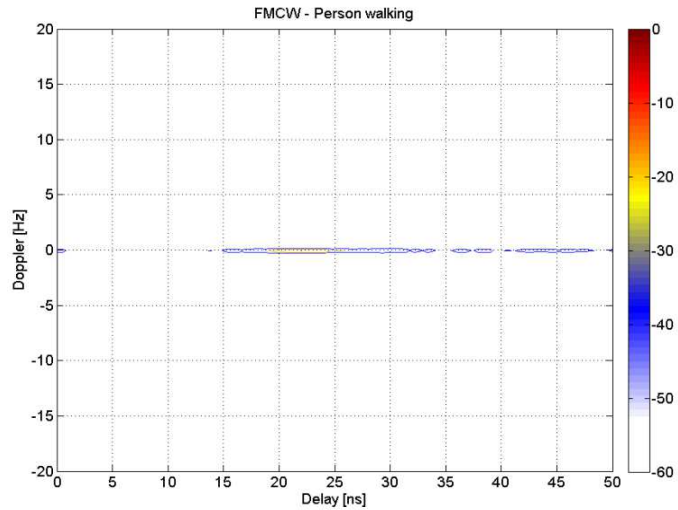
Figure 6.47 FMCW Delay-Doppler – Person walking behind a brick wall (scenario 1, landing)
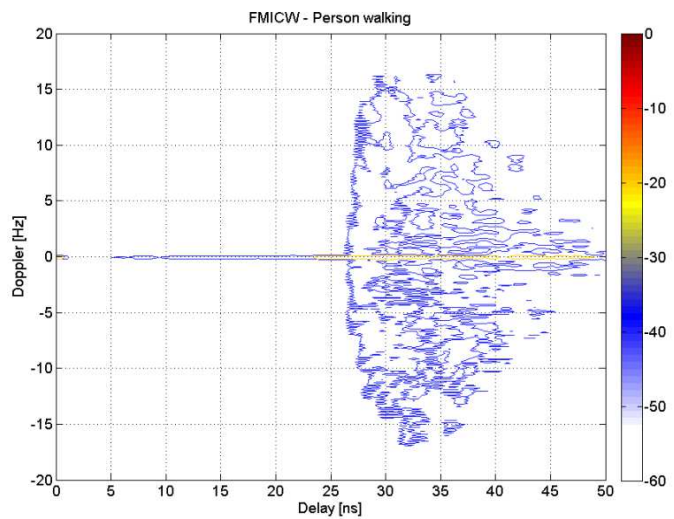
Figure 6.48 FMICW Delay-Doppler – Person walking behind a brick wall (scenario 1, landing)
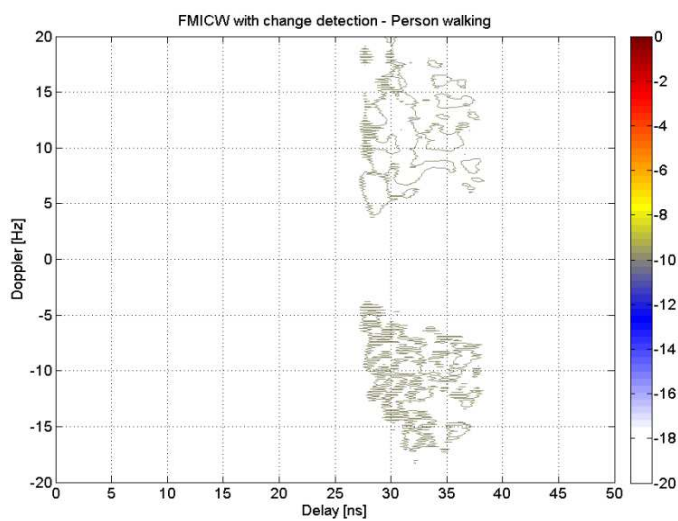
Figure 6.49 FMICW Delay-Doppler with change detection – Person walking behind a brick wall (scenario 1, landing)

167

For the second group of measurements the patch antennas developed in collaboration with the Fraunhofer IZM in Berlin have been used. They can be seen in operation on the right part of figure 6.2 next to the brick wall. Figures 6.50-6.51 show the FMCW range profile and the MRS of the chosen gating sequence, respectively. The peak at 80.6 kHz in the range profile is related to the reflection from the wall and should be removed. The corresponding time delay of this undesired component is 21.5 ns, thus a 3 bit M sequence with 26 ns delay τ_{RX2} matching this value is suitable for peak removal. The bit duration of the sequence is 26 ns.
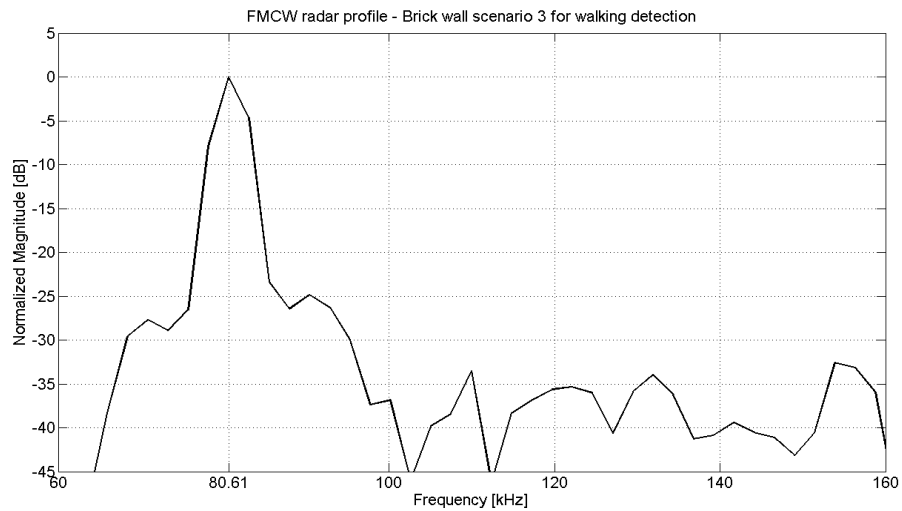
Figure 6.50 FMCW radar profile of the brick wall scenario 1 (landing) for walking movement detection – with patch antennas
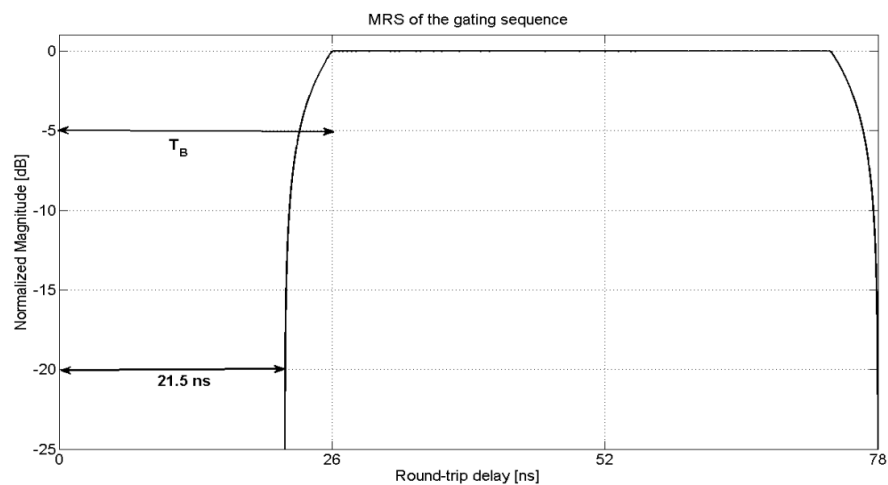
Figure 6.51 MRS of the gating sequence used for walking movement detection (brick wall scenario 1, landing) - with patch antennas

Figure 6.52 compares the Delay-Doppler in case of empty scenario when normal FMCW waveforms in sub-figure (a) and proposed FMICW waveforms in sub-figure (b) are used. In both cases no Doppler signature is recorded as expected but the two sub-figures differ. In the FMCW figure the brighter orange spot is located at roughly 21.5 ns, which is the position of the peak already seen in the FMCW range profile of figure 6.50, whereas in the FMICW figure the spot caused by the wall is removed and there is a long spot up to the highest values of round-trip delay where Doppler shifts can be detected in case of moving targets.

Figures 6.53-6.54 compare the Delay-Doppler when FMCW - in sub-figures (a) - and FMICW – in sub-figures (b) - waveforms are used for the cases of a person walking and of a person standing and swinging arms, respectively. In both cases properly gated FMICW waveforms are effective in detecting the Doppler due to the target motion, whereas nothing is detected using normal FMCW waveforms. As expected walking gives Doppler shifts with higher values than just swinging arms, since it is a faster motion. Furthermore the signature due to the motion of the arms is localized at roughly 27-28 ns delay since the person is stationary, and therefore its distance from the radar is not changing during the measurement. On the contrary the signature due to the walking motion is extended across several values of delay, roughly between 25-35 ns.

Both the antipodal Vivaldi antenna and the rectangular patch antenna have been successfully used for these through-wall measurements, and in terms of detection performance there is no particular difference to be seen. Comparing the range profiles in figures 6.45 and 6.50 the two separated peaks can be seen for cross-talk and wall reflections when the antipodal Vivaldi antennas are used, whereas a single peak is present when the rectangular patch antennas are used. However this is not consistently true for every measurement, since it depends on the stand-off distance of the antennas from the wall, on the inclination angle with which the patch antennas are placed on the wall, and also on the presence of objects like pipes, sockets, light switches which may be close to the antennas.
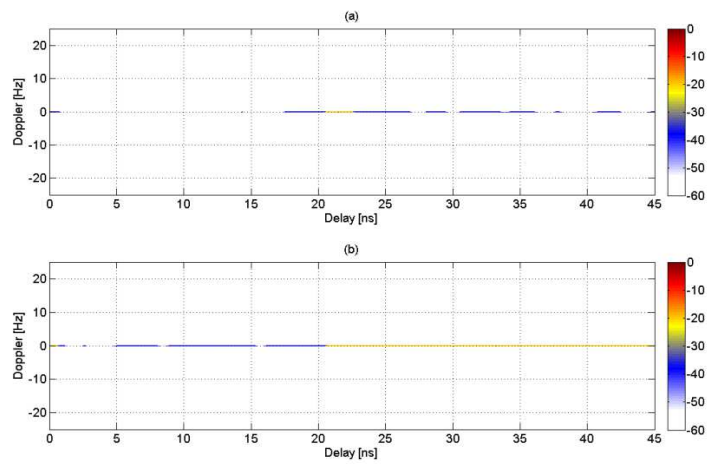
Figure 6.52 Delay-Doppler of the empty scenario 1 (landing) behind a brick wall when patch antennas are used: (a) FMCW, and (b) FMICW
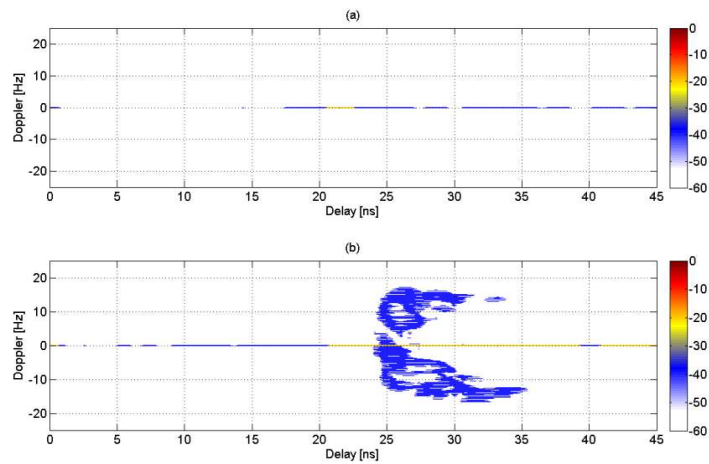
Figure 6.53 Delay-Doppler of a person walking in the scenario 1 (landing) behind a brick wall when patch antennas are used: (a) FMCW, and (b) FMICW
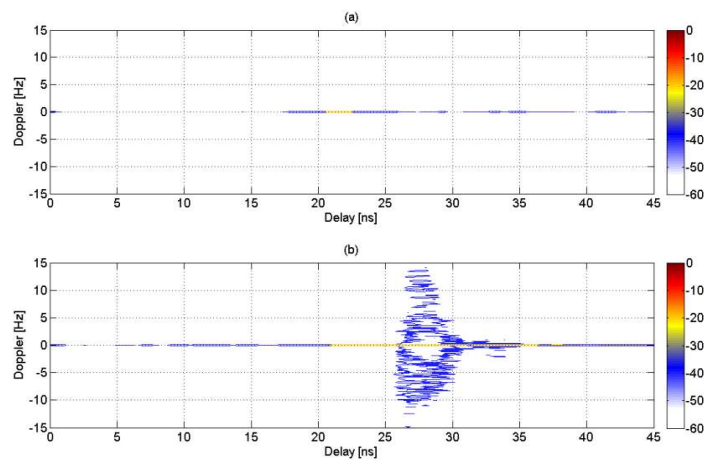
Figure 6.54 Delay-Doppler of a person standing and swinging arms in the scenario 1 (landing) behind a brick wall when patch antennas are used: (a) FMCW, and (b) FMICW

170

The last group of measurements presented in scenarios with brick walls takes place in the storage room shown in figure 6.3. Here antipodal Vivaldi antennas have been used. The FMCW range profile and the MRS of a gating sequence which is suitable for wall removal are presented, in figures 6.55 and 6.56 respectively. The undesired peak is located at 102.3 kHz, corresponding to 27.3 ns in terms of round-trip delay. FMICW waveforms are gated by a 3 bit M sequence with bit duration 35 ns and delay τ_{RX2} equal to 29 ns, so that the undesired component is removed by the first blind range of the MRS.

Figure 6.57 compares the Delay-Doppler using FMCW in sub-figure (a) and FMICW combined with change detection in sub-figure (b), in case of a person walking inside the storage room. In the former case no Doppler shift can be detected and the bright spot caused by wall reflections at Doppler 0 Hz and delay 27 ns is the strongest return. In the latter case the stationary clutter has been removed and the positive and negative Doppler shifts due to the back and forth walking movement can be seen.
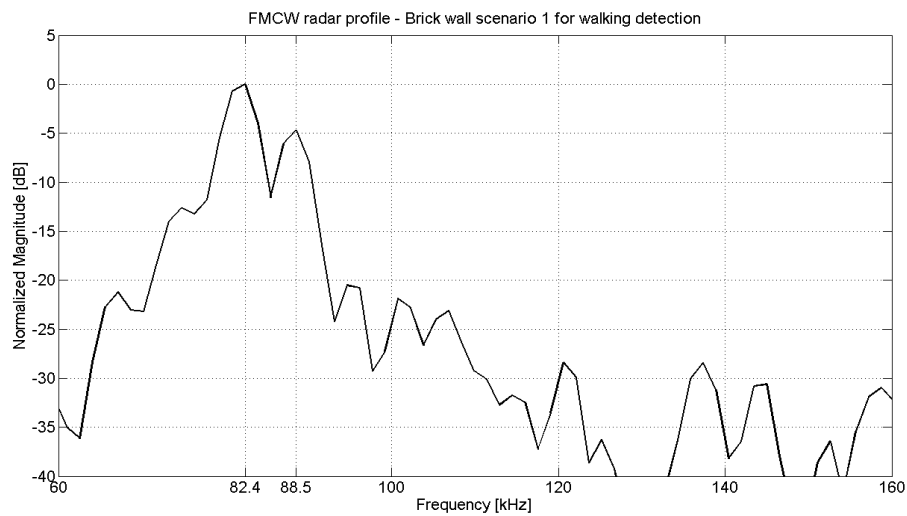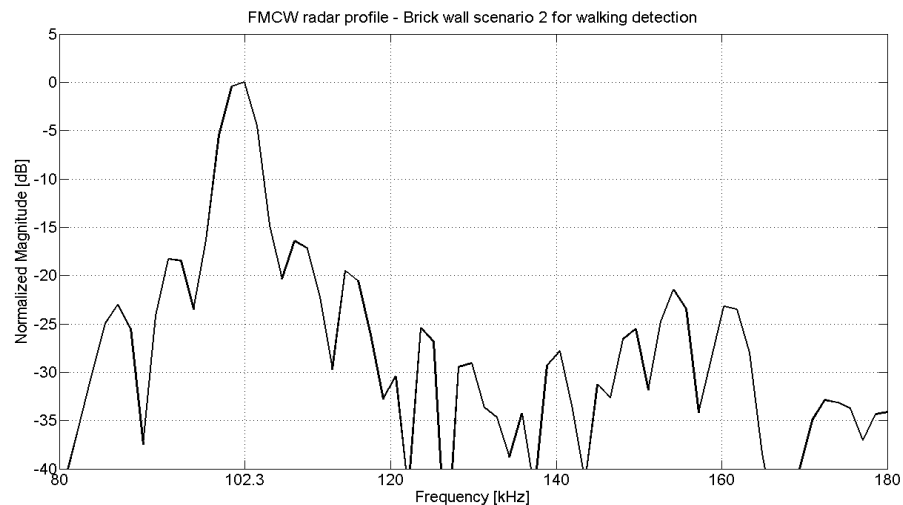

Figure 6.55 FMCW radar profile of the brick wall scenario 2 (storage room) for walking movement detection
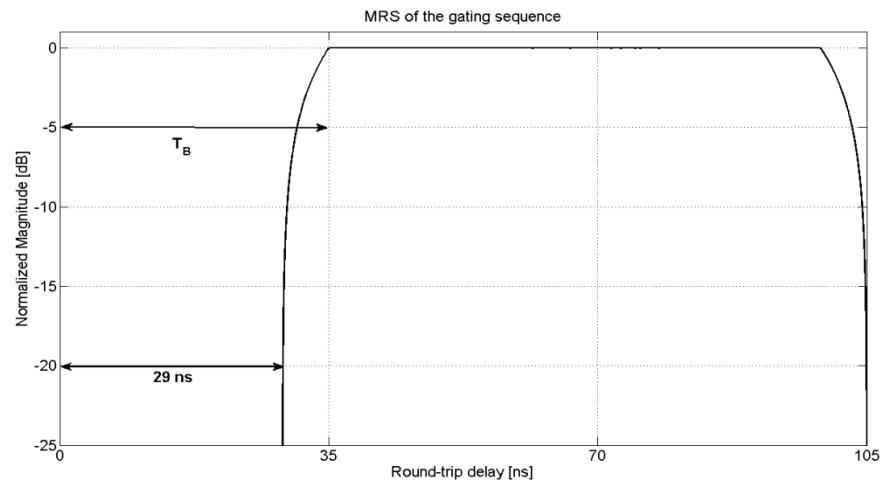
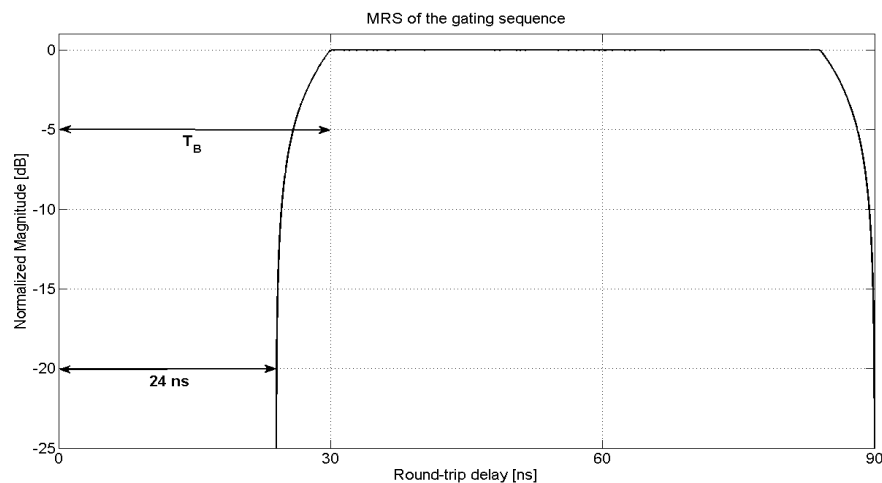**Figure 6.56 MRS of the gating sequence used for walking movement detection (brick wall scenario 2, storage room)**
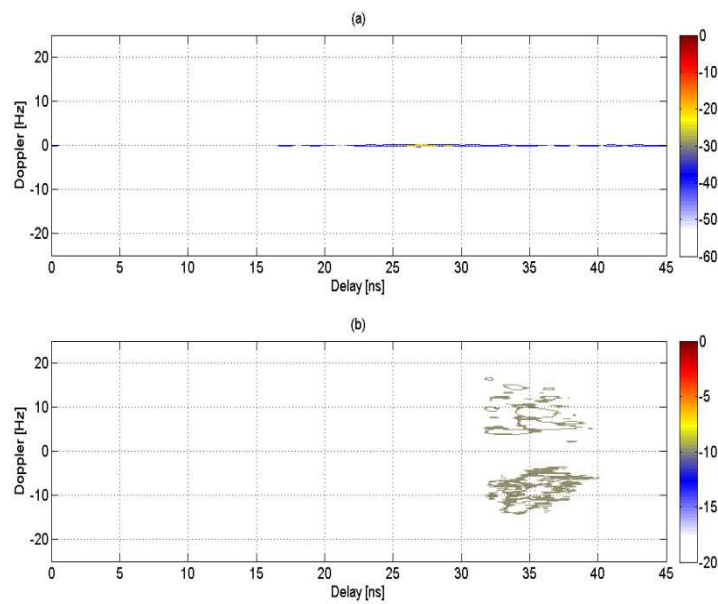
Figure 6.57 Delay-Doppler of a person walking in the scenario 2 (storage room) behind a brick wall: (a) FMCW, and (b) FMICW combined with change detection

6.4.3 Scenario with concrete wall

In this sub-section we present results referring to the third and most challenging scenario under test, the teaching room with concrete walls shown in figure 6.4.

The first set of measurements uses antipodal Vivaldi antennas. Figure 6.58 shows the FMCW profile for the empty scenario. Cross-talk and wall reflections cause in the range profile the two peaks at 83.94 kHz and 94.63 kHz, which correspond to values of round-trip delay equal to 22.38 ns and 25.24 ns, respectively. It is interesting to compare the profile in figure 6.58 for the thick concrete wall with those in figures 6.45 and 6.55 for the brick wall, using the same kind of antennas and assuming empty scenarios. We can see that the concrete wall produces a longer undesired return in comparison with the brick wall, i.e. it takes longer for the profile to decay down to more than 20 dB from the peak; for instance in figure 6.58 (concrete wall) the undesired components and relative peaks extend roughly from 84kHz to 106 kHz, thus more than 20 kHz, whereas in figures 6.45 and 6.55 they extend for roughly 10 kHz. Therefore the concrete wall is more challenging for TTWD, since it can mask targets close to the internal side of the wall and it needs longer blind ranges in the MRS of the gating sequences for effective removal.

Figure 6.59 shows the MRS of the chosen gating sequence, which is the usual 3 bit M sequence with bit duration 34 ns and τ_{RX2} equal to 26 ns. The chosen value of τ_{RX2} is enough to mitigate the first two undesired peaks of the FMCW profile, but it may be not sufficient for removal of the third peak, as it is explained later in this sub-section.
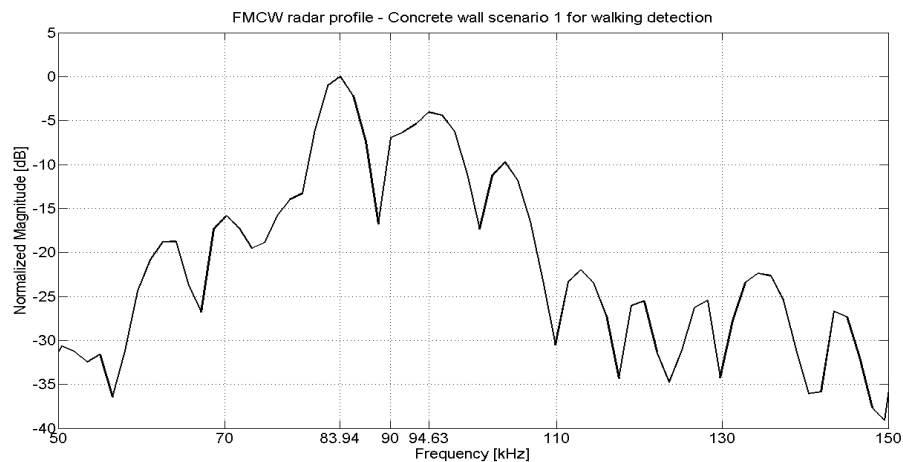
Figure 6.58 FMCW radar profile of the concrete wall scenario for walking movement detection
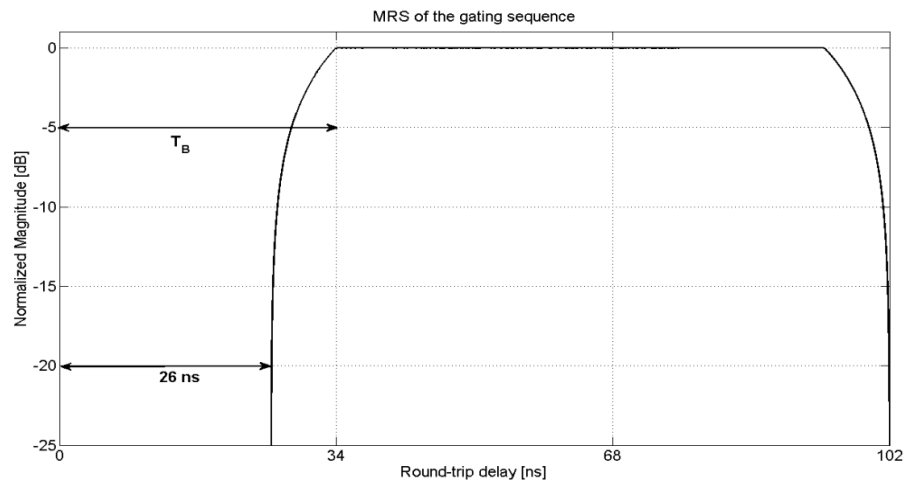
Figure 6.59 MRS of the gating sequence used for walking movement detection (concrete wall scenario)

Figure 6.60 shows the Delay-Doppler using FMCW waveforms for the empty scenario. There is no Doppler signature as expected, and the strongest return is caused by the stationary wall reflections which can be seen as bright spot at 0 Hz Doppler and delay 22-28 ns.
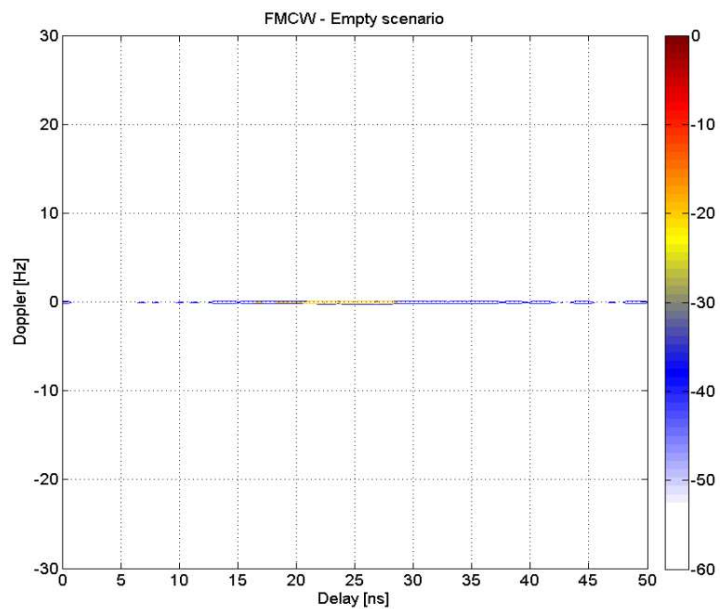
Figure 6.60 FMCW Delay-Doppler – Person walking behind concrete wall

Figures 6.61-6.64 present Delay-Doppler patterns using FMCW in sub-figures (a), and FMICW waveforms combined with change detection in sub-figures (b), in case of different walking movements behind the concrete wall. These movements are fast pace back and forth walking while carrying a metallic panel, slow pace walking with the metallic panel, fast pace walking without carrying any panel, and slow pace walking without any panel. For every case we can see the effectiveness of the FMICW waveforms and change detection in removing the stationary wall reflections and clutter and enhancing the detection of the positive and negative Doppler shifts of the movements, which are not detectable using FMCW waveforms (apart from a faint trace for the fast pace walking with metallic panel in figure 6.61). As expected the Doppler shift of the slower pace movement is smaller, below ± 20 Hz.

It is important to note that the gating sequence used for figures 6.63 and 6.64 is different from the sequence used for figures 6.61 and 6.62, whose MRS is shown in figure 6.59; the value of the delay τ_{RX2} is indeed increased from 26 to 28 ns. As previously mentioned, the former value is sufficient to mitigate the first two undesired components shown in the profile of figure 6.58, but not to deal with the third component which can compromise the detection of targets with lower RCS. The increase of the delay τ_{RX2} can solve this issue and improve the detection performance. So the first gating sequence (with delay τ_{RX2} 26 ns) allows the detection of the walking movement when the person is carrying the metallic panel and therefore has an increased RCS, but it would not be effective when the metallic panel is not used. The second gating sequence (with delay τ_{RX2} 28 ns) is instead effective in detecting the walking movement even when the person is simply walking, with no metallic panel involved.
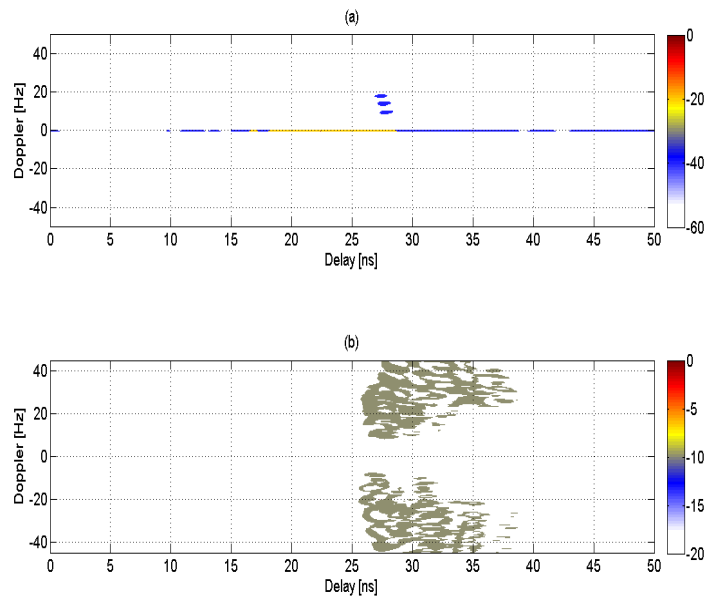
Figure 6.61 Delay-Doppler of a person walking with fast pace and carrying a metallic panel behind a concrete wall: (a) FMCW, and (b) FMICW combined with change detection
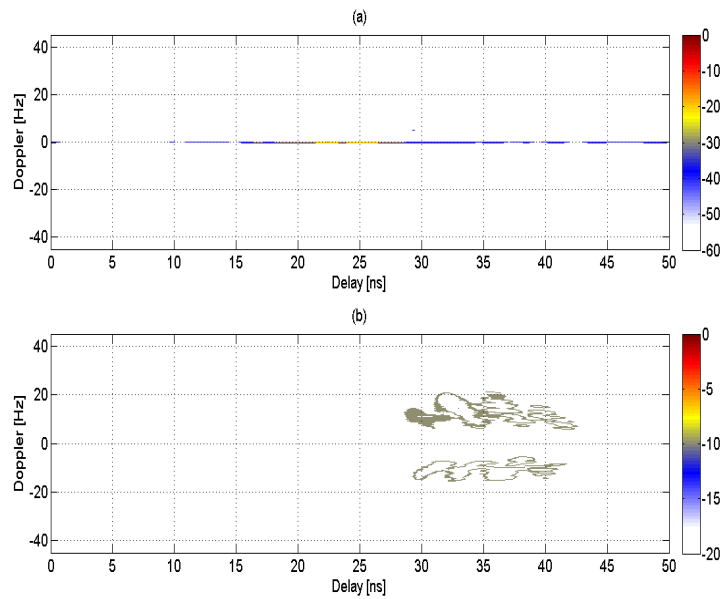
Figure 6.62 Delay-Doppler of a person walking with slow pace and carrying a metallic panel behind a concrete wall: (a) FMCW, and (b) FMICW combined with change detection
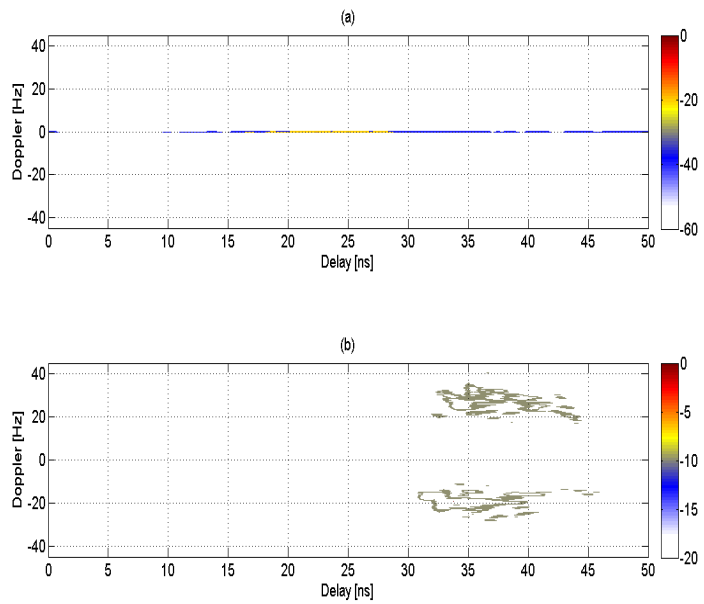
Figure 6.63 Delay-Doppler of a person walking with fast pace behind a concrete wall: (a) FMCW, and (b) FMICW combined with change detection
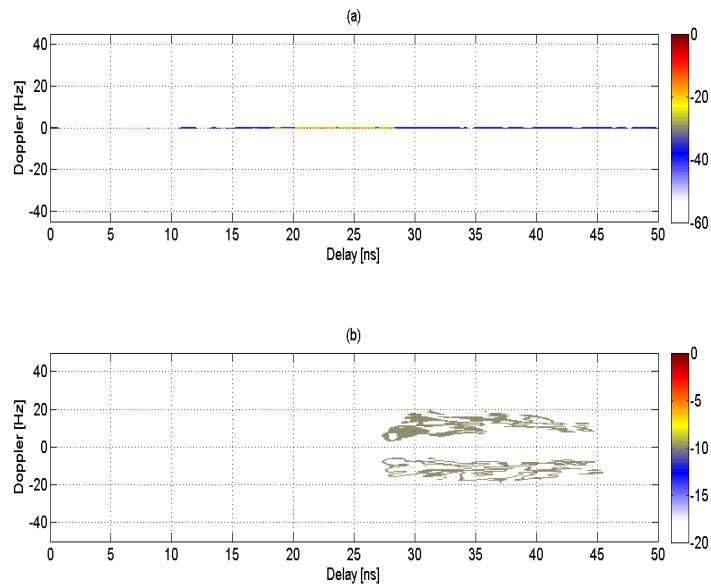
Figure 6.64 Delay-Doppler of a person walking with slow pace behind a concrete wall: (a) FMCW, and (b) FMICW combined with change detection

177

So far every Delay-Doppler is created with 10 s of recorded data, in which both the movements towards and away from the radar are detected and shown as positive and negative Doppler shifts. In figure 6.65 we show four Delay-Doppler sub-figures, created using a sub-period of data with duration 2.5 seconds from the whole amount of data lasting 10 seconds. The data refer to the fast pace walking movement with no metallic panel when FMICW waveforms combined with change detection are used. In each sub-figure we can see a single Doppler shift, either positive or negative, because there was only a movement either towards the radar or away from it during a sub-period of 2.5 seconds. It is also interesting to note how the negative Doppler shift in sub-figures (a) and (c) is smaller than the positive shift in sub-figures (b) and (d), roughly 20 Hz against 30 Hz. This is probably due to the fact that the person is walking backwards when moving away from the radar, and therefore with a slower pace because this is somewhat unnatural.
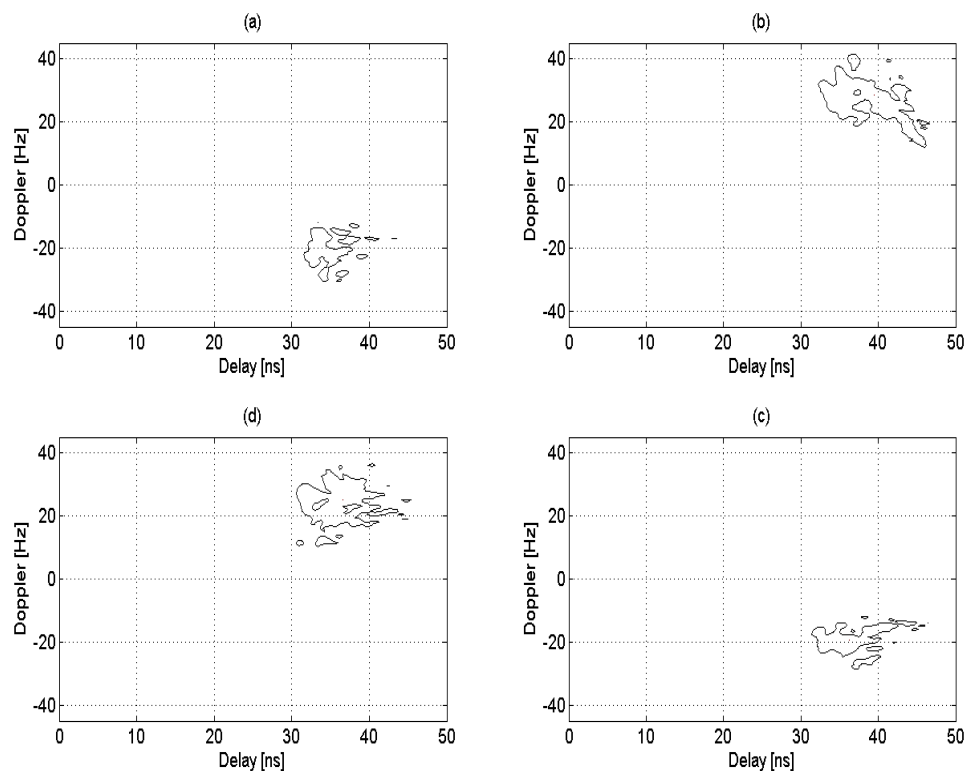
Figure 6.65 Delay-Doppler of a person walking with fast pace behind a concrete wall when FMICW combined with change detection is used: (a) sub-period 1, (b) sub-period 2, (c) sub-period 3, and (d) sub-period 4

The last results for this set of measurements are shown in figures 6.66 and 6.67. The former compares the radial – in sub-figure (a) – and the diagonal – in sub-figure (b) – walking trajectory of the person behind the concrete wall when FMICW waveforms are used. As expected the Doppler signature is much weaker for the diagonal trajectory because Doppler shifts are only caused by the radial component of the speed, and also because in the proposed system only two antennas are used and the target moves outside their main radiation beam when the trajectory is not radial.

The latter figure shows the Delay-Doppler recorded for a person standing behind the wall and moving hands back and forth as if during an animated conversation. Sub-figure (a) refers to the empty scenario, whereas sub-figure (b) refers to the scenario with the target. FMICW waveforms are used for both sub-figures. As expected we can see both positive and negative Doppler shift at values of round-trip delay around 32 ns as the person is standing, and the entity of the Doppler is only a few Hz since it is a slow movement; no Doppler shifts are detected for the empty scenario.
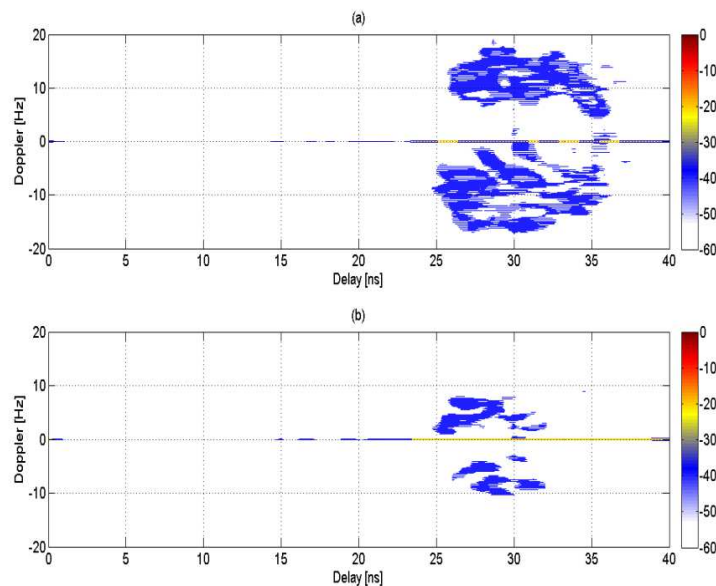
Figure 6.66 FMICW Delay-Doppler of a person walking behind a concrete wall: (a) radial trajectory, and (b) diagonal trajectory
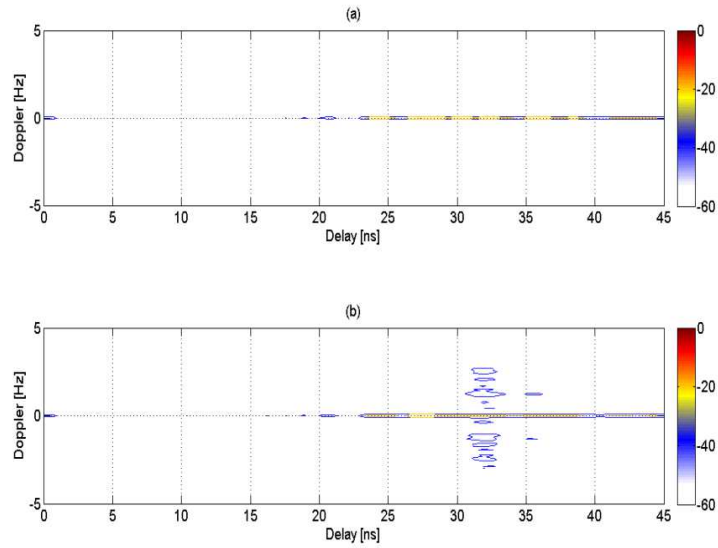
Figure 6.67 FMICW Delay-Doppler for scenario with a concrete wall: (a) empty scenario, and (b) person standing and moving hands

Another set of measurements has been performed in the same scenario with concrete walls, but using the rectangular patch antennas. Figure 6.68 shows the FMCW range profile for the empty scenario, with the main undesired component at 87.93 kHz corresponding to 23.45 ns in terms of round-trip delay. In comparison with the profile shown in figure 6.50 which refers to the brick wall scenario, we can see that the lobe of the main undesired component is larger and there is a sort of second peak at roughly 100 kHz. This seems to confirm what we have already observed about the challenge of detection through the concrete wall when commenting on the profile in figure 6.58. Figure 6.69 shows the MRS of the gating sequence used for the FMICW waveform; it is the same 3 bit M sequence with bit duration 28.5 ns and delay τ_{RX2} equal to 23.5 ns. In this case the value of τ_{RX2} is just above the position of the main undesired component in the FMCW profile, but it proves to be effective for wall removal.

Figure 6.70 and 6.71 show Delay-Doppler patterns for fast pace and slow pace walking movement of a person behind the concrete wall, respectively. In sub-figures (a) FMCW waveforms are used, in sub-figures (b) FMICW waveforms combined with change detection are used. As expected, the combination of FMICW waveforms and change detection removes wall reflections and stationary clutter and allows the detection of the

Doppler signature of the walking movement. The Doppler shift caused by the slower movement has a maximum value of roughly ±20 Hz as in figure 6.71, whereas it is higher for the movement with faster pace as in figure 6.70.

Finally, figure 6.72 shows the Delay-Doppler pattern using FMICW waveforms for the empty scenario in sub-figure (a), and for a scenario where a person is standing and moving back and forth arms and hands in sub-figure (b), similarly to what was already presented in figure 6.67. The Doppler signature of the movement is correctly detected in the bottom sub-figure: it is a shift of a few Hz, both positive and negative.
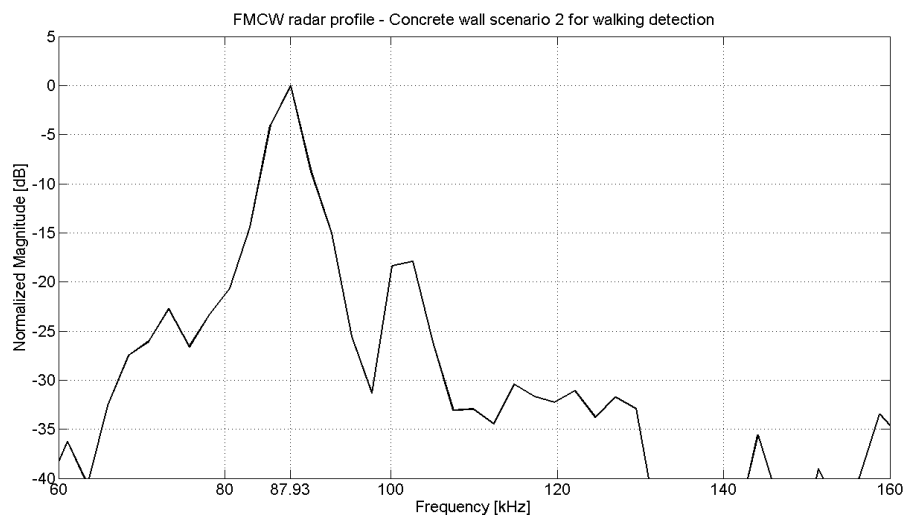
Figure 6.68 FMCW radar profile of the concrete wall scenario for walking movement detection – with patch antennas
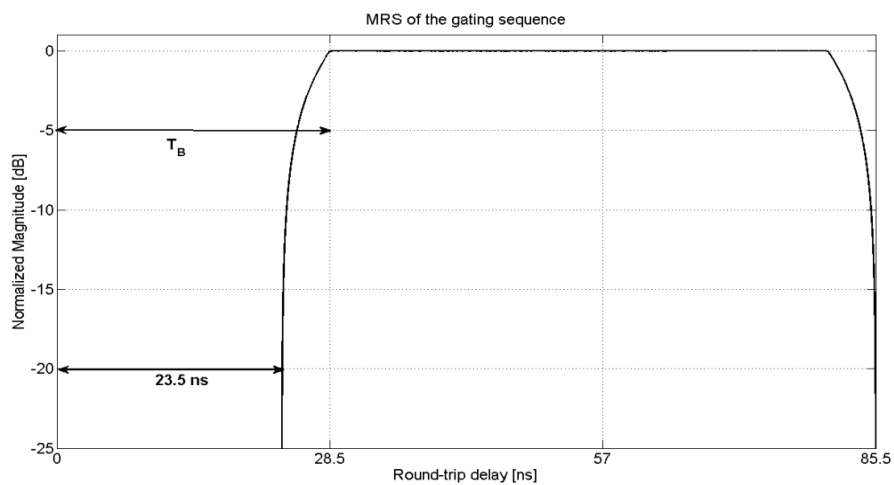
Figure 6.69 MRS of the gating sequence used for walking movement detection (concrete wall scenario) – with patch antennas
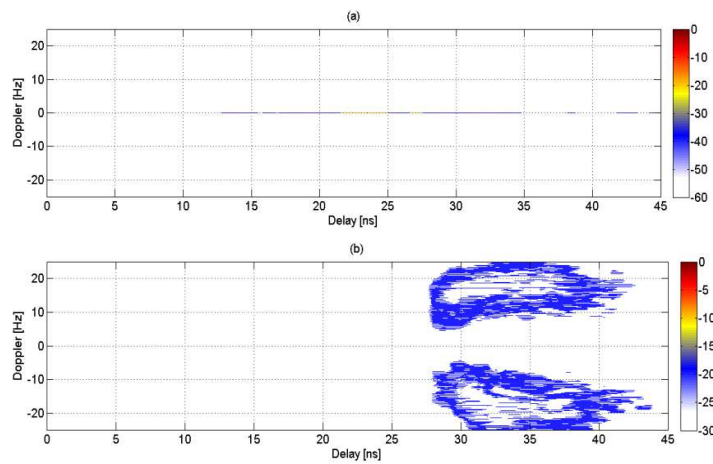
Figure 6.70 Delay-Doppler of a person walking with fast pace behind a concrete wall when patch antennas are used: (a) FMCW, and (b) FMICW combined with change detection
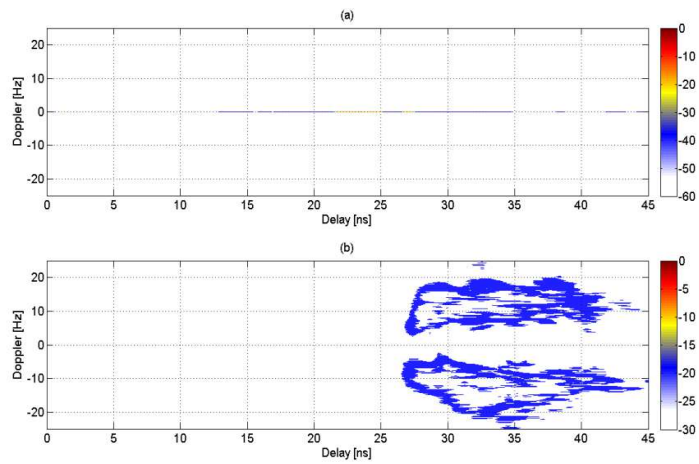
Figure 6.71 Delay-Doppler of a person walking with slow pace behind a concrete wall when patch antennas are used: (a) FMCW, and (b) FMICW combined with change detection
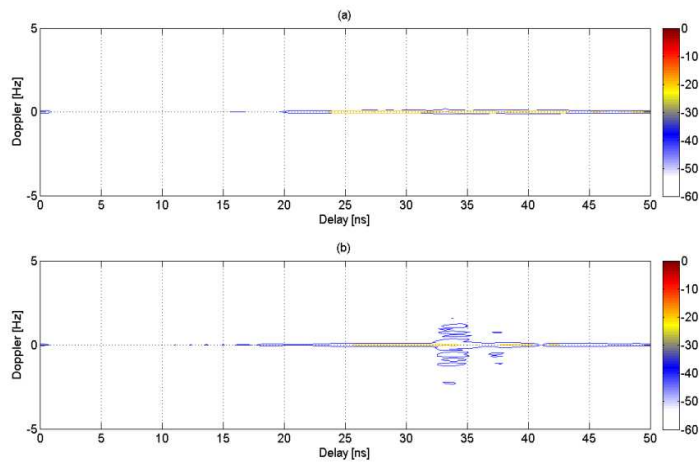
Figure 6.72 FMICW Delay-Doppler for scenario with a concrete wall when patch antennas are used: (a) empty scenario, and (b) person standing and moving hands

6.4.4 Summary of results for detection of walking movements

In this section the detection of people moving behind different walls (plywood, brick, and concrete) has been addressed and results in terms of Delay-Doppler patterns have been presented; most of the results refer to walking movement on a radial trajectory, which produces the highest Doppler shift, but diagonal trajectory and the movements of only arms and hands have been also incidentally discussed. The recorded Doppler shifts can be used to differentiate different walking paces.

The main focus of the results is showing the effectiveness of the proposed FMICW waveforms in comparison with the FMCW signal in mitigating the undesired returns from cross-talk and wall reflections, so that the Doppler shifts due to the target motion can be detected.

In many cases change detection has been combined with FMICW waveforms in order to remove the residual wall reflections and other stationary clutter, thus producing cleaner Delay-Doppler patterns and making the Doppler signature of the motion visible with narrower dynamic range of the coloured scale. It should be noted that change detection is applied on data which have been previously digitized and recorded. These data include also the strong undesired components if they have not been removed by suitable techniques, and this requires large dynamic range at the receiver and risks blocking it because of the strong signal, as discussed in chapter 2. Therefore it is convenient to combine change detection with the proposed FMICW waveforms (even if change detection may be directly applied on FMCW data); in this way FMICW mitigates or removes the strongest stationary return prior to digitization of the beat-note signal, and then change detection cancels the residual stationary clutter. The application of FMICW waveforms without change detection is sufficient in some cases to provide clean Delay-Doppler patterns, for instance in figures 6.54, 6.66, and 6.72.

6.5 Experimental Results: Detection of Breathing

In this section results related to the detection of breathing are presented. A person is standing inside the room under test facing the wall and breathing, while the radar is placed outside, on the other side of the wall to collect data. The detection approach is based on extracting Doppler shifts through double FFT processing and showing Delay-Doppler patterns, as already shown for the detection of walking movement presented in the previous section of this chapter.

However the expected Doppler shifts are far smaller, since the movement of the chest while breathing is slower and across far shorter distances (only a few centimetres) in comparison with walking or with the movements of arms and hands. The expected breathing rate for a person is around 0.2-0.4 Hz according to the literature [1-4]. This rate may change depending on the age, health, and physical condition. In order to discriminate these small Doppler shifts, the Doppler resolution of the system has been doubled from 0.1 Hz to 0.05 Hz by recording and processing 20 seconds of data in the measurements presented in this section.

The methodology of the measurements is the same used for detection of stationary objects and walking movement. Initially normal FMCW waveforms are used and undesired components caused by cross-talk and wall reflections are identified in the range profile. Then a suitable gating sequence is used for FMICW waveforms and Delay-Doppler patterns in colour decibel scale are presented for both waveforms, in order to highlight the improved detection provided by the proposed FMICW waveforms.

Before discussing the actual through-wall scenarios, it is worth presenting some preliminary results in free space where no wall is placed between the person and the radar system. These measurements have been performed in the environment shown in figure 6.1, with the person and the radar both inside the meeting room. Since there is no wall reflection, normal FMCW waveforms are used. Figure 6.73 shows the Delay-Doppler when nobody is in front of the radar in sub-figure (a), when the person is standing at 1 m away from the radar and breathing in sub-figure (b), when the person is standing at 1 m from the radar but holding breath in sub-figure (c), and when the person is standing at 1.5 m from the radar and breathing in sub-figure (d). In every sub-figure

there is a bright spot at 0 Hz Doppler and at roughly 22 ns delay. This is the stationary component caused by the cross-talk between the antennas. Another bright spot at 0 Hz Doppler appears at roughly 28.5 ns delay when the person is standing at 1 m from the radar, in sub-figures (b) and (c), or at roughly 32 ns delay when the person is standing at 1.5 m, as in sub-figure (d). These spots are caused by the reflections on the person's body. The differences in terms of round-trip delay between the cross-talk spot and the person spot in sub-figures (c) and (d) are 6.5 ns and 10 ns, which in free space are equal to distances of 0.98 m and 1.5 m. as expected.

In this free space scenario it is possible to detect the breathing Doppler shift with FMCW waveforms. In both sub-figures (b) and (d) we can see a positive and negative coloured spot at roughly ±0.4 Hz as expected. When the person is holding his breath, no Doppler shifts are detected, but only the stationary contribution at 0 Hz due to the reflections from the body.
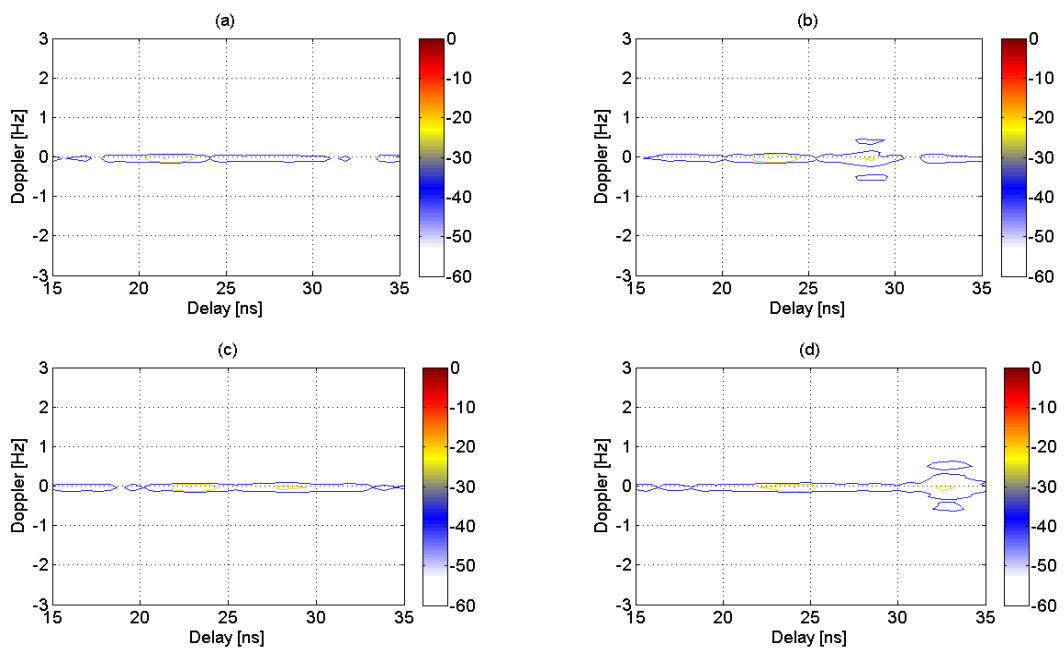
Figure 6.73 FMICW Delay-Doppler for breathing detection in free space: (a) empty scenario, (b) with a person breathing, (c) with a person holding breath, and (d) with a person located at a longer distance and breathing

Three sub-sections follow with experimental results from measurements performed in the three environments already presented for detection of walking movement: room with plywood wall, landing and storage room with brick wall, and teaching room with thick concrete wall.

6.5.1 Scenario with plastered plywood wall

In this sub-section measurements for breathing detection in the scenario with plywood wall shown in figure 6.1 are presented. Figure 6.74 shows the FMCW range profile for the empty scenario; the peak given by the undesired component is located at 90.38 kHz, corresponding to 24.1 ns in terms of round-trip delay. The MRS of the gating sequence applied in this case is the 3 bit M sequence with bit duration 28 ns and delay τ_{RX2} equal to 24.125 ns and shown in figure 6.75.
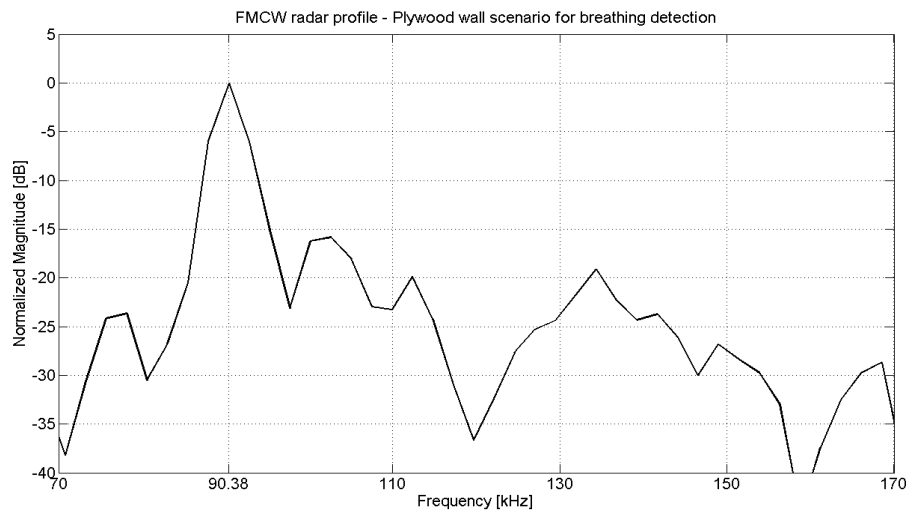
Figure 6.74 FMCW radar profile of the plywood wall scenario for breathing detection
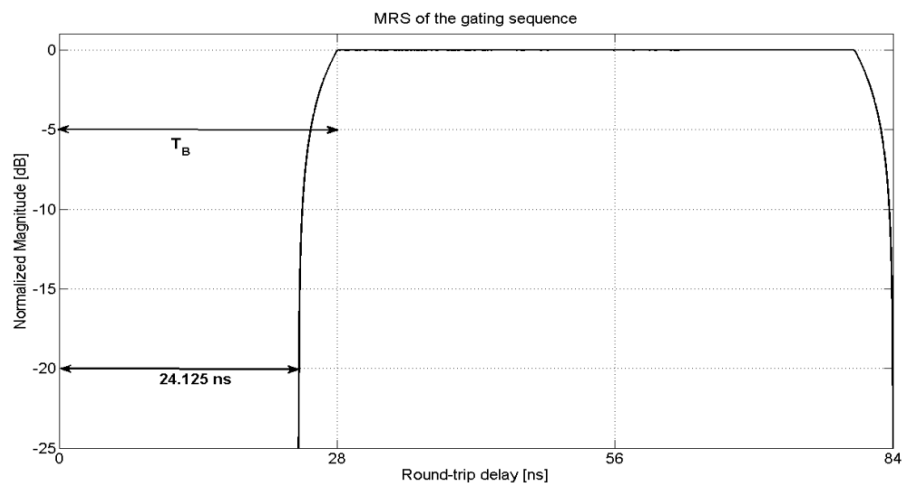
Figure 6.75 MRS of the gating sequence used for breathing detection (plywood wall scenario)

Figure 6.76 compares the Delay-Doppler when using normal FMCW waveforms in sub-figures (a) and (c) and proposed FMICW waveforms in sub-figures (b) and (d), for two different volunteers acting as targets, the first person for sub-figures (a) and (b), and the second person for sub-figures (c) and (d). The breathing Doppler signature of the first person can be detected only using FMICW waveforms, whereas normal FMCW are already able to detect the Doppler shift caused by the second person. The breathing Doppler signature is within ±0.5 Hz as expected, and it is located for both targets at roughly 29 ns delay. The difference in terms of round-trip delay between the Doppler shift and the stationary peak of the range profile due to the wall is roughly 5ns, corresponding to roughly 70 cm distance of the targets from the radar, which is close to the actual value of 60 cm.
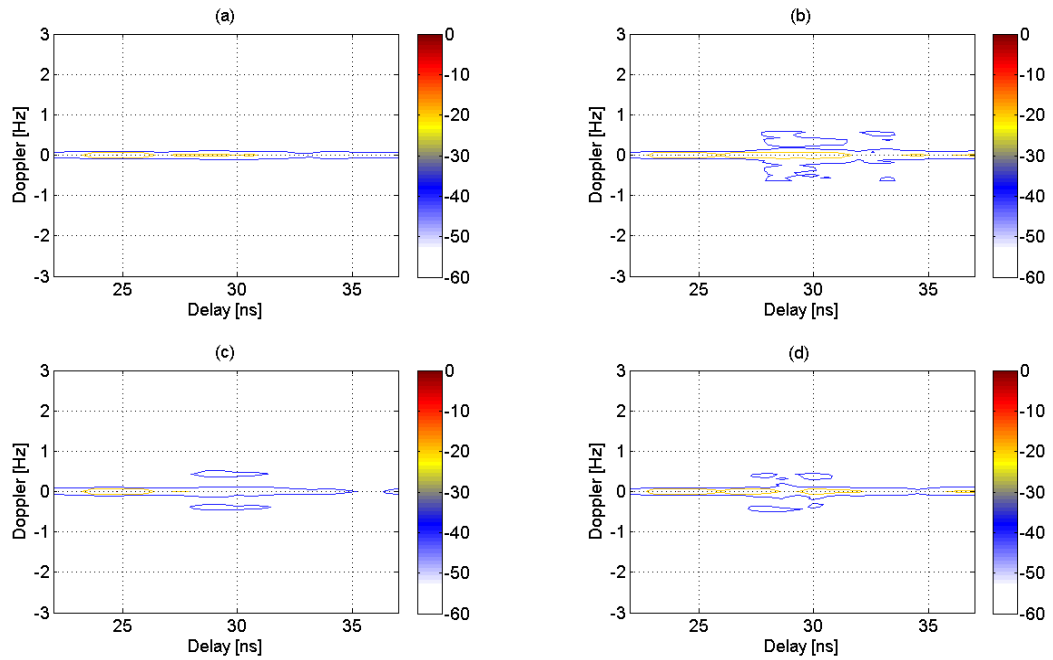
Figure 6.76 Delay-Doppler for breathing detection behind a plywood wall: (a) person 1 and FMCW signal, (b) person 1 and FMICW signal, (c) person 2 and FMCW signal, and (d) person 2 and FMICW signal

6.5.2 Scenario with brick wall

Measurements for breathing detection have been performed in scenarios with brick walls.

The first set of measurements has been performed in the storage room of figure 6.3 and used antipodal Vivaldi antennas. Figure 6.77 shows the FMCW range profile, with the undesired component at 80.61 kHz, corresponding to 21.5 ns in terms of round-trip delay. Figure 6.78 shows the MRS of the gating sequence used for FMICW waveforms; it is a 3 bit M sequence with bit duration 7 ns and delays τ_{RX1} and τ_{RX2} equal to 0.75 ns, thus using the second blind range centred at 21 ns and 1.5 ns long in order to remove the undesired component caused by cross-talk and wall reflections.
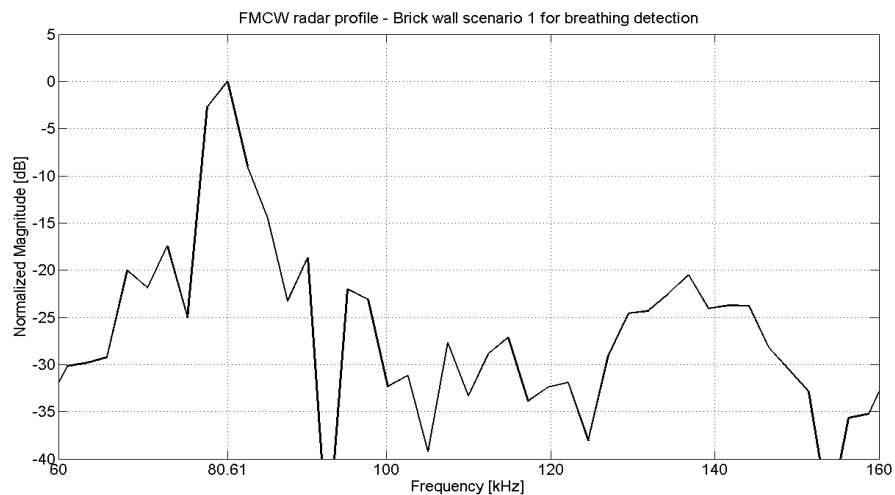
Figure 6.77 FMCW radar profile for breathing detection in the brick wall scenario (storage room)
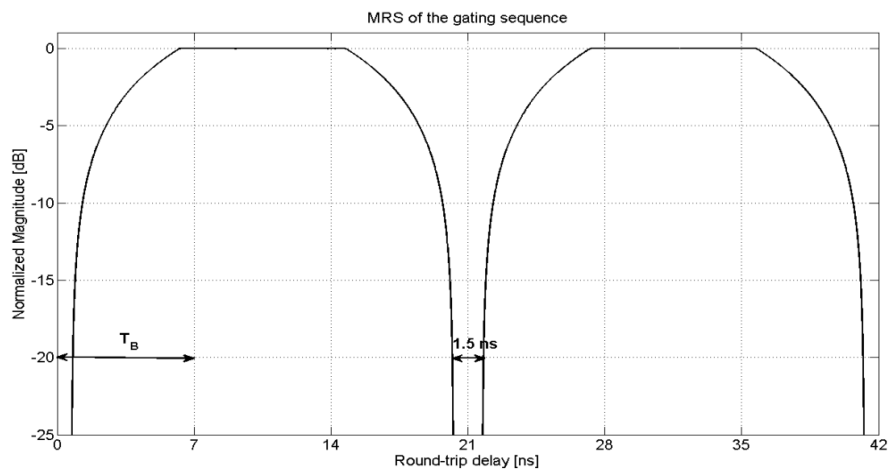
Figure 6.78 MRS of the gating sequence used for breathing detection (brick wall scenario, storage room)

Figure 6.79 shows the Delay-Doppler for two different volunteers, person 1 for sub-figures (a) and (b), and person 2 for sub-figures (c) and (d); sub-figures (a) and (c) have been created with FMCW data and they can be compared with sub-figures (b) and (d), which have been created with FMICW data. The breathing Doppler signature of both persons can be detected using FMCW waveforms, but the application of FMICW waveforms can improve the performance. For the case of the first person the Doppler shift when using FMICW waveforms is much more evident, whereas the pattern created using FMCW data could be related to an empty scenario because the coloured spots of the Doppler shifts are small. For the case of the second person the breathing Doppler shift can be detected with a narrower dynamic range of the coloured scale, so it is less likely to mistaken the shift for clutter.
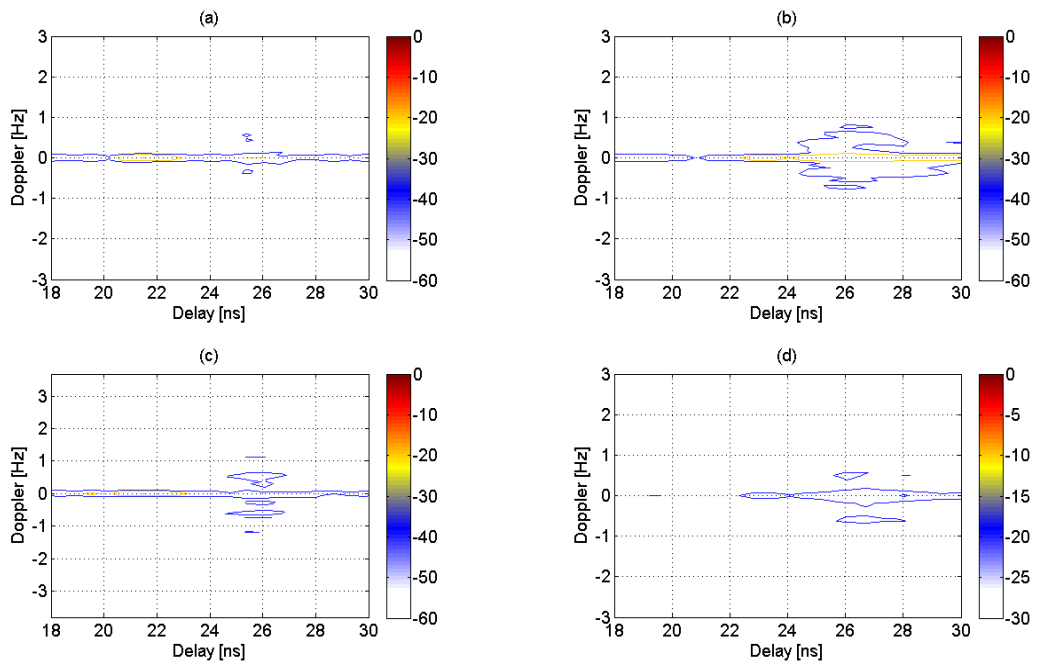
Figure 6.79 Delay-Doppler for breathing detection inside the storage room with a brick wall: (a) person 1 and FMCW signal, (b) person 1 and FMICW signal, (c) person 2 and FMCW signal, and (d) person 2 and FMICW signal

The second set of measurements has been performed on the landing of figure 6.2 and used rectangular patch antennas. In this case the FMCW profile and the MRS of the gating sequence used for the FMICW waveforms can be seen in the previous section in figures 6.50 and 6.51, respectively. The measurements for walking detection and those for breathing detection have been performed with the same experimental setup, without moving the radar system or modifying the surrounding environment, thus the gating sequence for FMICW waveforms can be the same. Figure 6.80 shows the Delay-Doppler using FMCW waveforms in sub-figures (a) and (c) and FMICW waveforms in sub-figures (b) and (d); the person is trying to breathe at two different rates – faster in sub-figures (a) and (b), and slower for sub-figures (c) and (d) – in order to investigate how different the Delay-Doppler pattern looks like. We can see the effectiveness of the FMICW waveforms in detecting the breathing Doppler signature for both breathing rates, whereas the Doppler shifts is not detected using FMCW waveforms and the Delay-Doppler appear similar to the pattern of the empty scenario, with only stationary components at 0 Hz. The difference between the two breathing rates can be appreciated: for faster rate the Doppler shift is higher than 1 Hz and the coloured spots are bigger, whereas for slower rate the Doppler is below 1 Hz with smaller spots concentrated around the values ±0.5 Hz.
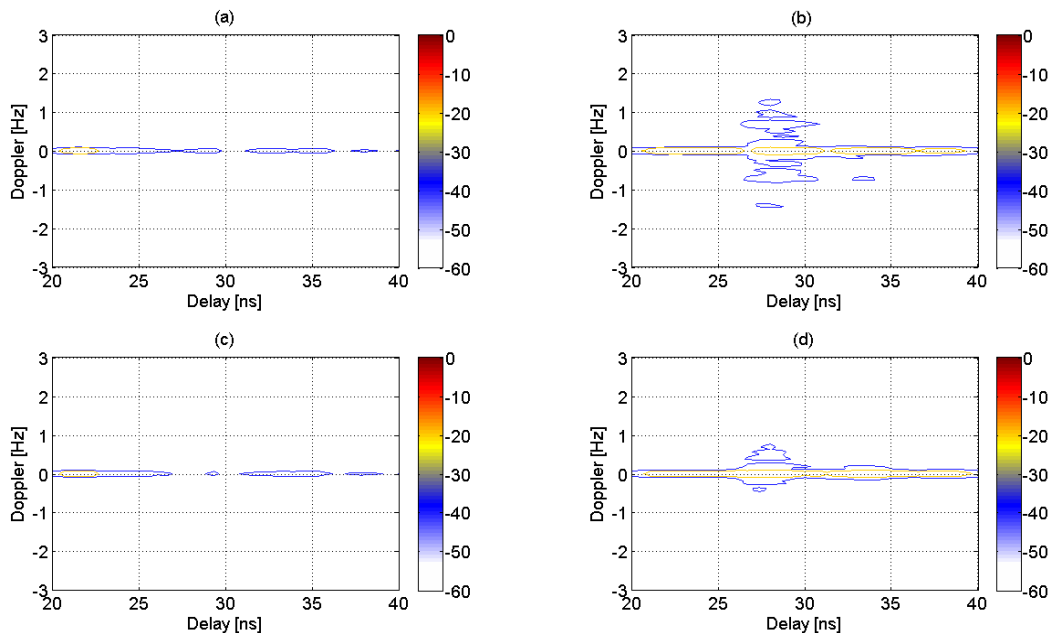
Figure 6.80 Delay-Doppler for breathing detection on the landing behind a brick wall when patch antennas are used: (a) faster breathing rate and FMCW signal, (b) faster breathing rate and FMICW signal, (c) slower breathing rate and FMCW signal, and (d) slower breathing rate and FMICW signal

6.5.3 Scenario with concrete wall

Finally, we present the results from breathing detection measurements performed in the room with concrete walls shown in figure 6.4.

For the first set of measurements antipodal Vivaldi antennas have been used. Figure 6.81 shows the FMCW range profile for the empty scenario; as previously observed, the undesired components caused by cross-talk and reflections from this kind of wall are extended across a wide set of beat-note frequencies. The frequency of the peak is 87.93 kHz, corresponding to 23.45 ns in terms of round-trip delay. Figure 6.82 shows the MRS of the gating sequence used for FMICW waveforms; it is a 3 bit M sequence with bit duration 29 ns and delay τ_{RX2} equal to 23.675 ns, thus the first blind range of the MRS is used to mitigate/remove the undesired components.
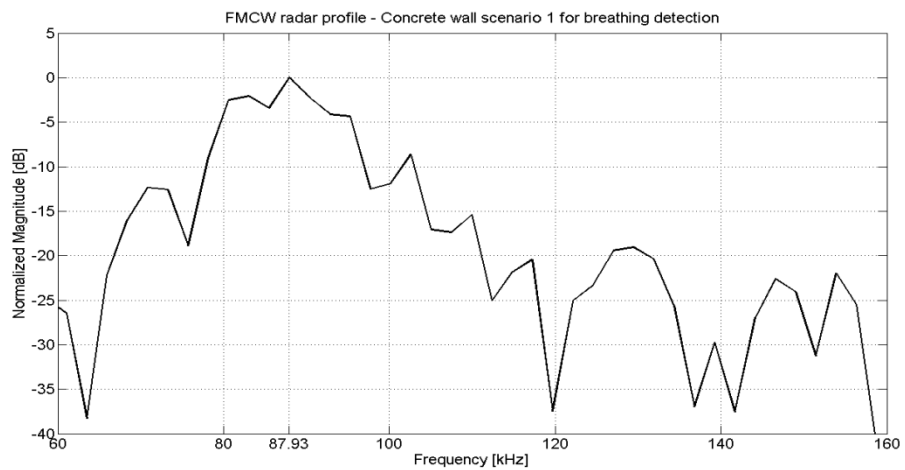
Figure 6.81 FMCW radar profile for breathing detection in the concrete wall scenario
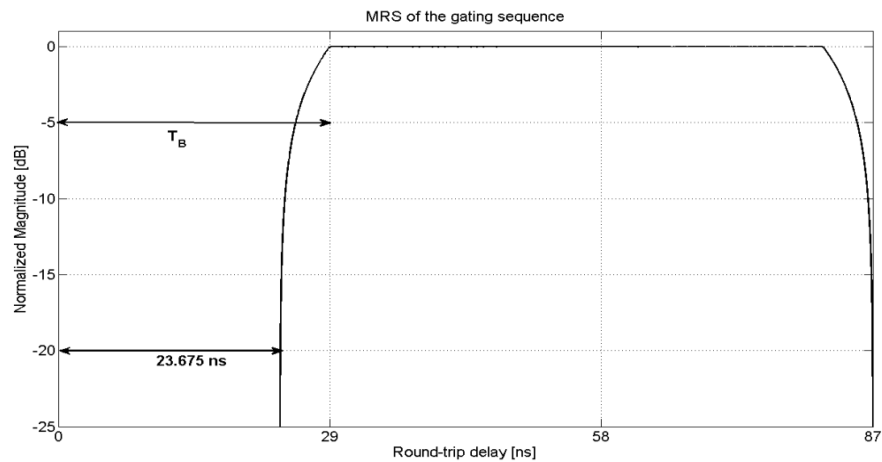
Figure 6.82 MRS of the gating sequence used for breathing detection (concrete wall scenario)

Figure 6.83 shows Delay-Doppler patterns for the empty scenario in sub-figure (a) and for the case of a person behind the concrete wall standing and breathing with different rates, i.e. faster in sub-figure (b), normal in sub-figure (c), and slower in sub-figure (d); FMICW data have been used to create every sub-figure. As expected there is no Doppler signature detected for the empty scenario, whereas positive and negative Doppler shifts are detected when the person is present; in case of the slow breathing only the positive Doppler is detected, but the pattern is clearly different from the pattern for the empty scenario. As expected the entity of the Doppler is decreasing if the breathing rate decreases, from roughly ±1.5 Hz down to roughly 0.2 Hz. It should be noted that for the fast breathing measurement the person was almost puffing, not breathing at a natural and relaxed rate, hence such high values of Doppler shift are recorded.
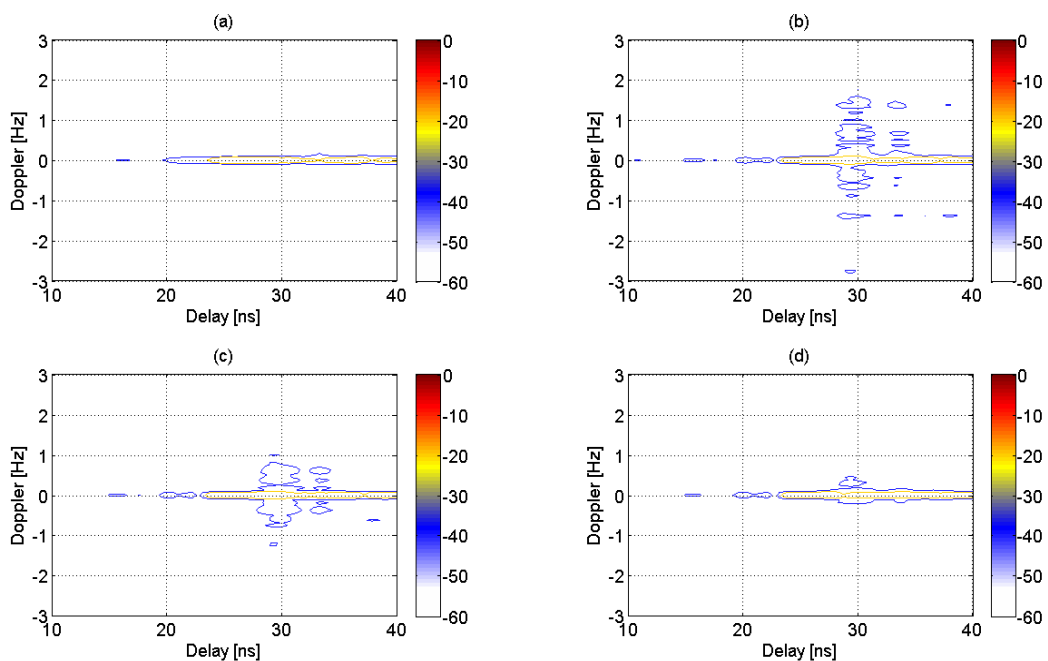
Figure 6.83 FMICW Delay-Doppler for breathing detection behind a concrete wall: (a) empty scenario, (b) with a person breathing at faster rate, (c) with a person breathing at normal rate, and (d) with a person breathing at slower rate

For the second set of measurements rectangular patch antennas have been used. The FMCW range profile and the MRS of the gating sequence used for the FMICW waveforms have been already shown in the section on walking movement detection, in figures 6.68 and 6.69 respectively. Figure 6.84 shows the Delay-Doppler using FMCW waveforms in sub-figures (a) and (c) and FMICW waveforms in sub-figures (b) and (d), for two different breathing rates of the person behind the concrete wall, namely normal rate for sub-figures (a) and (b), and slow rate for sub-figures (c) and (d). No breathing Doppler shift is detected when normal FMCW waveforms are used, whereas FMICW waveforms provide correct detection for both breathing rates. Doppler shifts of ±0.5 Hz are detected for normal breathing rate and roughly half this value for slow breathing rate, as expected.
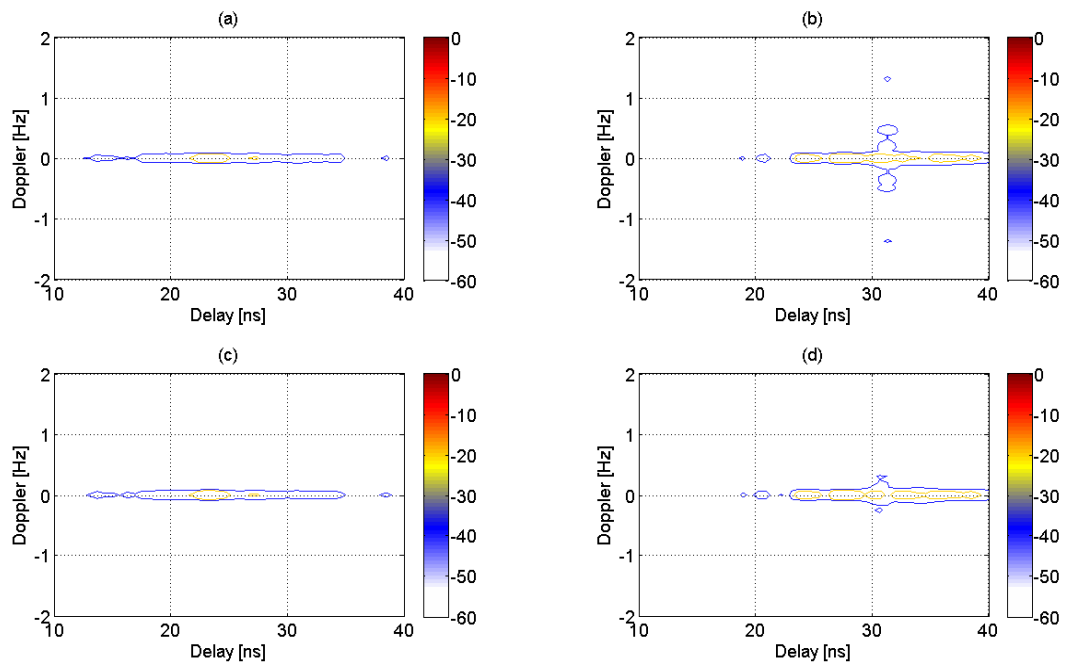
Figure 6.84 Delay-Doppler for breathing detection behind a concrete wall when patch antennas are used: (a) normal breathing rate and FMCW, (b) normal breathing rate and FMICW, (c) slower breathing rate and FMCW, and (d) slower breathing rate and FMICW

6.5.4 Summary of results for detection of breathing

In this section results on through-wall breathing detection using FMICW waveforms have been presented in scenarios with different kinds of walls. It has been highlighted by showing Delay-Doppler patterns how FMICW waveforms are effective in mitigating the stationary undesired contribution from cross-talk and wall reflections, thus

providing detection of the breathing Doppler signature when normal FMCW waveforms do not. This is a further confirmation of the good performance of the proposed FMICW waveforms as wall removal technique for TTWD, together with what we have already presented for detection of stationary targets and walking movement.

In some cases the recorded Delay-Doppler patterns are not perfect: the coloured spots related to the breathing Doppler shift are not symmetric because the negative part is missing (e.g. in sub-figures (d) of figures 6.80 and 6.83), or they span across several values of round-trip delays (e.g. in sub-figure (c) of figure 6.79). However these patterns differ from those related to the empty scenarios where no target is present and therefore the presence of the person is successfully detected.

6.6 Summary of the chapter

The aim of this chapter was providing experimental validation of the proposed FMICW waveforms as wall mitigation and removal technique in TTWD scenarios. A measurement campaign in environments of the School of Engineering and Computing Sciences at Durham University presenting three different kinds of wall, namely plastered plywood, brick, and concrete walls, has been performed. The performance of the proposed FMICW waveforms has been tested and compared with normal FMCW waveforms for detection of stationary targets and of the presence of people moving or breathing behind the wall. Images obtained using the SAR approach and Delay-Doppler patterns obtained through double FFT processing have been presented for the detection of stationary objects and for the detection of walking and breathing movement, respectively. FMICW waveforms appear to be effective in removing or at least mitigating the undesired return caused by the antenna cross-talk and wall reflections, thus enhancing the detection of actual targets if compared with normal FMCW waveforms.

Square waves and 3 bit M sequences have been used as gating sequences for FMICW waveforms in this experimental work. As already mentioned in chapter 3 the former sequences can provide maximum or minimum MRS at desired values of round-trip delay, the latter can provide flat MRS with no additional attenuation of the beat-note

signal at values of round-trip delay where potential targets are placed. The delays τ_{RX1} and τ_{RX2} have been used on the gating sequence at the receiver in order to increase the duration of the blind ranges of the MRS, thus achieving more effective attenuation of the undesired components.

In most cases 3 bit M sequences together with only the delay τ_{RX2} have been used, thus exploiting the first blind range of the MRS to mitigate/remove undesired components. The value of τ_{RX2} is set equal to the round-trip delay corresponding to the peak of the undesired component in the range profile (or slightly higher), while the bit duration is longer and determines where the flat part of the MRS starts. As already mentioned in chapter 3, a compromise should be sought when setting the values of τ_{RX2} and of the bit duration. Longer τ_{RX2} in comparison with the bit duration provide better attenuation of undesired components, which is particularly useful for scenarios with thick walls made of materials with high permittivity, as in the tests with the concrete wall presented in this chapter. However longer τ_{RX2} reduce the overall received power because of the additional off-time at the receiver, and this may compromise the system dynamic range and the detection of low RCS targets, which may be buried below the system noise floor.

6.7 References

[1]   J. Sachs, et al., "Remote vital sign detection for rescue, security, and medical care by ultra-wideband pseudo-noise radar," Ad Hoc Networks, 2012.

[2]   Y. Wang, et al., "Simultaneous localization and respiration detection of multiple people using low cost UWB biometric pulse Doppler radar sensor," in Microwave Symposium Digest (MTT), 2012 IEEE MTT-S International, 2012, pp. 1-3.

[3]   X. Yanyun, et al., "A novel method for automatic detection of trapped victims by ultra-wide-band radar," Geoscience and Remote Sensing, IEEE Transactions on, vol. 50, pp. 3132-3142, 2012.

[4]   W. Fu-Kang, et al., "Detection of concealed individuals based on their vital signs by using a see-through-wall imaging system with a self-injection-locked radar," Microwave Theory and Techniques, IEEE Transactions on, vol. 61, pp. 696-704, 2013.

7.1 Conclusions

The primary objective for this thesis was to investigate the effectiveness of the novel wall removal technique based on FMICW waveforms for through-wall detection scenarios. The proposed technique has been successfully validated through results from numerical simulations and an experimental campaign in different realistic scenarios at the School of Engineering and Computing Sciences, Durham University.

The problem of strong backscattered reflections from the air-wall interface is common for active radar systems for through-wall detection. This strong undesired signal can overshadow the reflections from actual targets and limit the dynamic range at the receiver, with the risk of saturating and blocking it. Wall removal techniques have therefore been developed in the literature, and a comprehensive review has been provided in chapter 2 in order to evaluate their advantages and disadvantages in relation to the novel technique proposed in this thesis. In comparison with algorithmic wall removal techniques, such as subspace projection and spatial filtering, FMICW mitigates wall reflections before digitizing the data, thus avoiding the limitation of the dynamic range at the receiver. Even change detection approach does not address the problem of the dynamic range and it is not suitable for detection of stationary targets. In comparison with hardware filtering for FMCW systems, the proposed implementation of our FMICW radar system does not require extra hardware components like the filter itself or additional oscillators to adjust the frequency of the beat-note signal to the fixed filter. It is true that the arbitrary waveform generators used in our system to provide FMICW waveforms are expensive and complex pieces of equipment, but they are worth it for the flexibility they provide. FMICW waveforms are therefore a promising further possibility for wall removal, and they can be also used in combination with other existing techniques, as for instance shown in chapter 6 combining FMICW waveforms with change detection approach.

FMICW waveforms have been used in the past in monostatic radar systems for ionospheric sounding and ocean surface sensing, but to the best knowledge of the author they have not been investigated so far as wall removal technique for through-wall detection. These waveforms have been analyzed in details in chapter 3, providing examples of gating sequences and corresponding MRS which have been used in the

simulated and experimental data. Particular emphasis has been given to the analysis of those parameters of the gating sequence which have an impact on the removal of wall reflections, such as bit duration and variation of the duty cycle of the gating sequence used at the receiver through the delays τ_{RX1} and τ_{RX2}.

Numerical simulations of scenarios for through-wall detection have been run using CST Microwave Studio in order to test the performance of the proposed FMICW waveforms. Normal FMCW signals are simulated within the software to produce raw data, whereas different gating sequences can be flexibly applied through MATLAB processing at a later stage. Environments with different stand-off distances and different wall materials and internal structures have been simulated in order to assess the performance of the proposed wall removal approach in different scenarios. Realistic human phantoms and metallic cabinets have been used as targets. In chapter 4 results from these simulations have been presented, focusing on the comparison between images obtained with normal FMCW waveforms and those using the proposed FMICW waveforms. The design of suitable gating sequences and corresponding MRS for each simulated scenario has been also discussed. FMICW waveforms allow to mitigate/remove undesired wall reflections, thus enhancing the detection of the actual targets. Three different algorithms have been used to create images from simulated data and their results have been compared. DSI and DMSI, which have been adapted from medical imaging, provide better focused images in comparison with classic BP algorithm. The importance of the correct estimation of the round-trip delay to avoid displacement and blurring in the final images has been discussed; a simple approximated estimation has been used as it is sufficient for the scope of this thesis.

A radar system capable of generating FMICW waveforms has been built and used for the experimental campaign. As described in chapter 5, this system integrates off-the-shelf components and ad hoc components which have been designed and manufactured to meet the requirements; LPF at 3.5 GHz to filter the output of the AWG and two models of antennas, namely antipodal Vivaldi and rectangular patch, have been developed specifically for this project. Particular effort has been made for the distribution of the same rubidium clock to every component of the system and for their synchronization in order to avoid jittering and Doppler artefacts. It is important to

highlight that the gating sequences used for FMICW waveforms are not implemented with physical switches, but via software through the AWG. This solution does not require extra hardware components (switches and related controllers) and provides great flexibility as the parameters of the gating sequence can be adapted to the particular scenario under test by simply programming the AWG.

Chapter 6 presents the results of the experiments performed to validate the proposed wall removal technique using the radar system. The measurement campaign has been performed in realistic environments in the School of Engineering and Computing Sciences, Durham University, with three different kinds of walls, namely concrete, brick, and plastered plywood. The experiments aimed at the localization of stationary targets behind walls presenting radar images created through the SAR approach, and at the through-wall detection of people presenting Delay-Doppler patterns to highlight the Doppler shifts due to motion or breathing. For both types of experiments normal FMCW and proposed FMICW waveforms have been compared, showing that the latter are effective in removing or at least mitigating the undesired contributions of antenna cross-talk and wall reflections, thus improving the detection of the actual targets. The process of designing suitable gating sequences for each scenario under test has been also described, starting from FMCW range profiles and setting the gating sequence parameters accordingly to achieve wall removal.

The results from the experimental campaign confirm the effectiveness of the proposed FMICW based wall removal technique and seem to agree with the expected performance parameters described in chapter 5 for the proposed system. The expected down-range and cross-range resolution at 1 m (10 cm and 35 cm, respectively) seem to be achieved for detection of stationary targets, especially when the DMSI imaging algorithm is applied to produce better focused images. The expected fine Doppler resolution (0.05 Hz when 20 s of data are collected and processed) can be appreciated when performing breathing detection experiments. As mentioned in chapter 5, the through-wall detection of stationary human beings is challenging given the sensitivity of the system. However the use of Doppler processing addresses successfully the issue of human targets detection and further confirms the effectiveness of the FMICW wall

removal technique. Additional possible work is discussed in the following section to improve the sensitivity and other aspects of the system.

7.2 Further work

Although the proposed radar system has successfully provided data for the experimental validation of the novel FMICW waveforms, there is undoubtedly further work which could be valuable to improve the system. The most important improvement would be the manufacturing of an array to replace the single antennas used at the transmitter and at the receiver, thus resulting in a MIMO radar system; this would also require the implementation of switching matrices and related control circuits to select different pairs of transmitting and receiving antennas during measurements. The array would provide faster creation of images for localization of stationary targets, without moving the antennas to different positions in the SAR approach. The array would also improve the performance in case of motion detection, giving the possibility to locate and track the target precisely in the area under test and to show images rather than Delay-Doppler patterns, as they are easier to understand for users.

The limited onboard memory of the AWG introduces a constraint on the maximum duration of the FMCW-FMICW chirp that can be loaded into them and prevents the possibility of loading at the same time and in different memory pages several FMICW waveforms, each of them gated with different sequences. This would make the system faster and more flexible, as it would be possible to change dynamically the waveform just by changing the memory page. An ad hoc AWG could therefore be designed to replace the current one and minimize the time to reload new waveforms and change the parameters of the gating sequences. The off-the-shelf components could be replaced by ad hoc components with enhanced performance, for instance larger bandwidth to increase the down-range resolution of the system or higher gains in the receiver chain to improve the sensitivity and dynamic range. The "signal conditioning" block developed at the Centre for Communications System, Durham University, could replace the current base-band amplifier with fixed gain; this block would provide variable gain up to 53 dB to the beat-note signal when its level is particularly low, and smaller gain when the signal is already strong in order to prevent the saturation of the ADC.

In the current system results (radar images or Delay-Doppler patterns) are generated through MATLAB processing after the measurements, therefore not in real time. It would be good to integrate in the system some unit (for instance an FPGA programmed for the purpose) to process the recorded data in real-time and provide the user with the resulting images, possibly through a friendly graphical interface.

FMICW data have been already used in conjunction with change detection approach for walking motion detection. Further research could be carried out in combining the proposed FMICW waveforms with other wall removal techniques as subspace projection or spatial filtering, which are effective also for detection of stationary targets. Different imaging algorithms (for instance Stolt or Kirchhoff migration) could be tested using the data collected in this experimental work. Finally, the estimation of the round-trip delay could be improved taking into account the refraction at the air-wall interfaces, thus reducing displacement errors and blurring in the final images.

Appendix 1.1: MATLAB programs for numerical simulations

In this appendix we present MATLAB programs which have been developed to import data from numerical simulations in CST, apply gating sequences to simulate FMICW waveforms, and produce radar images through a desired imaging algorithm as final results; the first program is a script which calls the other programs as functions.

TTWProcessing_Room3.m

```
% GUI to INSERT PARAMETERS RELATED TO THE PARTICULAR SIMULATION
row1 = 'Enter RX X coordinate [cm]';
row2 = 'Enter RX Y max coordinate (edge of the receiving array) [cm]';
row3 = 'Enter RX step in Y coordinate (distance between 2 probes)
[cm]';
row4 = 'Enter RX Z coordinate [cm]';
row5 = 'Enter wall thickness [m]';
row6 = 'Enter wall real permittivity';
row7 = 'Enter stand-off distance [cm]';
row8 = 'Enter farthest down-range distance (end of the room) [cm]';

prompt= {row1,row2,row3,row4,row5, row6,row7,row8};
dlg_title = 'Select the parameters for the CST simulation to analyze';
def = {'5','100','25','100','0.15','4.642','250','520'};
answer = inputdlg(prompt,dlg_title,1,def,'on');

xt=0;
c=3e8;
xr=str2double(answer{1});
yrmax=str2double(answer{2});
yrstep=str2double(answer{3});
zr=str2double(answer{4});
yr=-yrmax:yrstep:yrmax;
th=str2double(answer{5});
eps=str2double(answer{6});

beggrid=xr;
standoffd=str2double(answer{7});
endroom=str2double(answer{8});
begroom=beggrid+standoffd+th*100;
xp1=beggrid:1:begroom;
xp2=begroom+1:1:endroom;
xp=horzcat(xp1,xp2);
yp=-yrmax-30:1:yrmax+30;
clear row0 row1 row2 row3 row4 row5 row6 row7 row8 dlg_title  prompt
def answer
%%%%%%%%%%%%%%%%%%%%%%%%%%%%%%%%%%%%%%%%%%%%%%%%%%%%%%%%%%%%%%%%%%%%%%%%

% ROUND-TRIP DELAY COMPUTATION - Reshape in matrices to speed up
XP1=repmat(xp1,[length(yp) 1 length(zr) length(yr)]);
XP2=repmat(xp2,[length(yp) 1 length(zr) length(yr)]);
YP1=repmat(yp',[1 length(xp1) length(zr) length(yr)]);
YP2=repmat(yp',[1 length(xp2) length(zr) length(yr)]);
yr_aux=reshape(yr,1,1,1,length(yr));
YR1=repmat(yr_aux,[length(yp) length(xp1) length(zr) 1]);
```

```
YR2=repmat(yr_aux,[length(yp) length(xp2) length(zr) 1]);

TOAtx1=(sqrt((XP1-xt).^2).*(1E-2)).*(1E9)./c; %[ns]
TOArx1=(sqrt((YP1-YR1).^2+(XP1-xr).^2).*(1E-2)).*(1E9)./c;

TOAtx2=(sqrt((XP2-xt).^2).*(1E-2)+th*(sqrt(eps)-1)).*(1E9)./c; %[ns]
dwall2=th./(cos(atan((sqrt((YR2-YP2).^2))./(sqrt((XP2-xr).^2)))));
TOArx2=(sqrt((YP2-YR2).^2+(XP2-xr).^2).*(1E-2)+dwall2.*(sqrt(eps)-
1)).*(1E9)./c;

delay=horzcat(TOAtx1+TOArx1,TOAtx2+TOArx2);

disp('Finished to compute the RoundTrip delays');
clear XP1 YP1 XP2 YP2 ZP1 YR1 ZR1 YR2 ZR2;
clear TOAtx1 TOArx1 TOAtx2 TOArx2 dwall2  yr_aux zr_aux xt zp xr;
%%%%%%%%%%%%%%%%%%%%%%%%%%%%%%%%%%%%%%%%%%%%%%%%%%%%%%%%%%%%%%%%%%%%

% LOAD DATA FROM CST
timeaxis=LoadCSTData(yr,zr);
load('MyWorkspace');
timestep=timeaxis(2);
%%%%%%%%%%%%%%%%%%%%%%%%%%%%%%%%%%%%%%%%%%%%%%%%%%%%%%%%%%%%%%%%%%%%

% APPLY GATING SEQUENCES
[data_diff_cos_g,data_diff_sin_g,excit_cos_g,excit_sin_g]=ApplyGatingS
equences(yr,zr,timeaxis,data_diff_cos,data_diff_sin,excit_cos,excit_si
n);
clear data_diff_cos data_diff_sin excit_cos excit_sin
%%%%%%%%%%%%%%%%%%%%%%%%%%%%%%%%%%%%%%%%%%%%%%%%%%%%%%%%%%%%%%%%%%%%

% CORRELATION TO EXTRACT THE BEAT-NOTE
data_corr=[];
for l=1:1:length(zr)
for n=1:1:length(yr)

data_corr(:,n,l)=xcorr((data_diff_cos_g(:,n,l)+1i*data_diff_sin_g(:,n,
l)),(excit_cos_g+1i*excit_sin_g))./size(data_diff_cos_g,1);
end
end
data_corr=data_corr(length(timeaxis):size(data_corr,1),:,:);
clear data_diff_cos_g data_diff_sin_g excit_cos_g excit_sin_g
%%%%%%%%%%%%%%%%%%%%%%%%%%%%%%%%%%%%%%%%%%%%%%%%%%%%%%%%%%%%%%%%%%%%

% APPLY THE DESIRED IMAGING ALGORITHM
[myimage]=ImagingAlgorithm(data_corr,delay,timeaxis,xp,yp,yr,zr);

% IMAGE CREATION
xp_int=beggrid:0.25:endroom;
yp_int=-yrmax-30:0.25:yrmax+30;
myimage_int=interp2(xp,yp',myimage,xp_int,yp_int','cubic');

myimage_int=myimage_int./(max(max(myimage_int)));
myimage_log=20*log10(abs(myimage_int));
dynamics_ampl=10;
clims_ampl=[max(max(myimage_log))-dynamics_ampl
max(max(myimage_log))];
```

```
figure;
imagesc(xp_int,yp_int,myimage_int);
xlabel('X down-range direction [cm]');
ylabel('Y cross-range direction [cm]');
title('Radar Image - Amplitude in Lin scale');
axis([xp_int(1) xp_int(length(xp_int)) yp_int(1)
yp_int(length(yp_int))]);
grid;


figure;
imagesc(xp_int,yp_int,myimage_log,clims_ampl);
xlabel('X down-range direction [cm]');
ylabel('Y cross-range direction [cm]');
title(['Radar Image - Amplitude in Log scale (
',num2str(dynamics_ampl),'dB dynamics)']);
axis([xp_int(1) xp_int(length(xp_int)) yp_int(1)
yp_int(length(yp_int))]);
grid;

rectangle('position',[255,-115,265,230],'LineStyle','--
','LineWidth',2);
rectangle('position',[270,-100,235,200],'LineStyle','--
','LineWidth',2);
rectangle('position',[445,60,60,40],'LineStyle','--','LineWidth',2);
rectangle('position',[360,-
55,25,45],'Curvature',[0.5,1],'LineStyle','--','LineWidth',2);
```

LoadCSTData.m

```
function [timeaxis] = LoadCSTData(yr,zr)
%DIRECTORY AND FILE NAMES FOR CST DATA
basedir_cos='E:\cvxl66_F_FIORANELLI\CST_Data\3DRoom3_Cos\Result\';
basedir_sin='E:\cvxl66_F_FIORANELLI\CST_Data\3DRoom3_Sin\Result\';
basedir_cos_empty='E:\cvxl66_F_FIORANELLI\CST_Data\3DRoom3_Cos_Empty\R
esult\';
basedir_sin_empty='E:\cvxl66_F_FIORANELLI\CST_Data\3DRoom3_Sin_Empty\R
esult\';
prefix='E-field (5 ';
suffix=')(Z)(pw).prs';

filename_cos=[basedir_cos,prefix,num2str(yr(1)),'
',num2str(zr(1)),suffix];
fid_cos=fopen(filename_cos,'rt');
fseek(fid_cos,96,'bof');
timeaxis=fscanf(fid_cos, '%g %*g', [1, inf])';
timestep=timeaxis(2);
fclose(fid_cos);
disp('Timeaxis loaded')


data_cos=[];
for l=1:1:length(zr)
for n=1:1:length(yr)
    filename_cos=[basedir_cos,prefix,num2str(yr(n)),'
',num2str(zr(l)),suffix];
    fid_cos=fopen(filename_cos,'rt');
```

```matlab
    fseek(fid_cos,96,'bof');
    data_cos=horzcat(data_cos,(fscanf(fid_cos, '%*g %g', [1, inf]))');
    fclose(fid_cos);
end
end
disp('Data cos loaded')
data_cos=reshape(data_cos,length(data_cos),length(yr),length(zr));
data_cos=cast(data_cos,'single');
data_sin=[];
for l=1:1:length(zr)
for n=1:1:length(yr)
    filename_sin=[basedir_sin,prefix,num2str(yr(n)),'
',num2str(zr(l)),suffix];
    fid_sin=fopen(filename_sin,'rt');
    fseek(fid_sin,96,'bof');
    data_sin=horzcat(data_sin,(fscanf(fid_sin, '%*g %g', [1, inf]))');
    fclose(fid_sin);
end
end
disp('Data sin loaded')
data_sin=reshape(data_sin,length(data_sin),length(yr),length(zr));
data_sin=cast(data_sin,'single');


filename_cos_empty=[basedir_cos_empty,prefix,num2str(yr(1)),'
100',suffix];
fid_cos_empty=fopen(filename_cos_empty,'rt');
fseek(fid_cos_empty,96,'bof');
timeaxis_empty=fscanf(fid_cos, '%g %*g', [1, inf])';
fclose(fid_cos_empty);
data_cos_empty=[];
for n=1:1:length(yr)
    filename_cos_empty=[basedir_cos_empty,prefix,num2str(yr(n)),'
100',suffix];
    fid_cos_empty=fopen(filename_cos_empty,'rt');
    fseek(fid_cos_empty,96,'bof');

data_cos_empty=horzcat(data_cos_empty,interp1(timeaxis_empty,(fscanf(f
id_cos_empty, '%*g %g', [1, inf]))',timeaxis,'spline',0) );
    fclose(fid_cos_empty);
end
data_cos_empty=repmat(data_cos_empty,[1 1 length(zr)]);
data_cos_empty=cast(data_cos_empty,'single');
data_sin_empty=[];
for n=1:1:length(yr)
    filename_sin_empty=[basedir_sin_empty,prefix,num2str(yr(n)),'
100',suffix];
    fid_sin_empty=fopen(filename_sin_empty,'rt');
    fseek(fid_sin_empty,96,'bof');

data_sin_empty=horzcat(data_sin_empty,interp1(timeaxis_empty,(fscanf(f
id_sin_empty, '%*g %g', [1, inf]))',timeaxis,'spline',0) );
    fclose(fid_sin_empty);
end
data_sin_empty=repmat(data_sin_empty,[1 1 length(zr)]);
data_sin_empty=cast(data_sin_empty,'single');
```

```
filename_excit_cos=[basedir_cos,'plw.sig'];
filename_excit_sin=[basedir_sin,'plw.sig'];
fid_excit_cos=fopen(filename_excit_cos,'rt');
fid_excit_sin=fopen(filename_excit_sin,'rt');
fseek(fid_excit_cos,96,'bof');
excit_cos=fscanf(fid_excit_cos, '%g %g', [2, inf]);
excit_cos=excit_cos';
fclose(fid_excit_cos);
fseek(fid_excit_sin,96,'bof');
excit_sin=fscanf(fid_excit_sin, '%g %g', [2, inf]);
excit_sin=excit_sin';
fclose(fid_excit_sin);
excit_cos=interp1(excit_cos(:,1),excit_cos(:,2),timeaxis,'spline');
excit_sin=interp1(excit_sin(:,1),excit_sin(:,2),timeaxis,'spline');


data_diff_cos=data_cos-data_cos_empty;
data_diff_sin=data_sin-data_sin_empty;


clear data_cos data_sin data_cos_empty data_sin_empty;
clear suffix prefix basedir_cos basedir_sin filename_cos filename_sin
fid_cos fid_sin;
clear basedir_cos_empty basedir_sin_empty filename_cos_empty
filename_sin_empty fid_cos_empty fid_sin_empty data_cos_empty_interp
data_sin_empty_interp;
clear timeaxis_empty fid_excit_cos fid_excit_sin filename_excit_cos
filename_excit_sin;
save('MyWorkspace');
disp('Finished to load the data - I saved them into "MyWorkspace"');
end
```

ApplyGatingSequences.m

```
function
[data_diff_cos_g,data_diff_sin_g,excit_cos_g,excit_sin_g]=ApplyGatingS
equences(yr,zr,timeaxis,data_diff_cos,data_diff_sin,excit_cos,excit_si
n)


% GUI to INSERT PARAMETERS OF THE GATING SEQUENCE
row1 = 'Choose the gating sequence: 0 No Gating - 1 SquareWave - 2
Barry - 3 Salous-Nattour - 4 Msequence - 5 Experimental Sequences';
row2 = 'Enter bit duration for gating sequence [ns]';
row3 = 'Enter delays between TX and RX gating sequences [ns]';


prompt= {row1,row2,row3};
dlg_title = 'Select the parameters for your gating sequences';
num_lines = 1;
def = {'1','8','0'};
answer = inputdlg(prompt,dlg_title,num_lines,def,'on');


timestep=timeaxis(2);
SequenceType=str2double(answer{1});
BitDuration=str2double(answer{2});
DelayTxDuration=str2double(answer{3});
DelayRxDuration=DelayTxDuration;


if SequenceType == 4
```

```
rowMseq = {'Choose the number of bit for M-sequence (format 2^(N)-
1)'};
answer2 = inputdlg(rowMseq,'M-sequence Details',1,{'3'});
MSeqCoeff=str2double(answer2{1});
end;
clear row0 row1 row2 row3 row4 row5 row6 prompt rowMseq def answer
answer2

switch SequenceType %Select gating sequence
    case 0
        sequence = 1;
    case 1
        sequence = [1 0]; %Square Wave
    case 2
        sequence = [1 1 0 0 0 1 1 1 1 0 0 0 0 0 0 0]; %Barry
    case 3
        sequence = [1 1 1 0 0 0 1 1 1 1 1 1 0 0 0 0 0 0 0 0 0]; %Salous-
Nattour
    case 4
        sequenceM=mseq(2,log2(MSeqCoeff+1)); %Msequence
        for k=1:1:length(sequenceM)
        if sequenceM(k) ~= 1
        sequenceM(k)=0;
        end
        end
        sequence=sequenceM';
end

NumSampleProBit=round(BitDuration/timestep);
NumSampleProDelayTx=round(DelayTxDuration/timestep);
NumSampleProDelayRx=round(DelayRxDuration/timestep);
NumBitSequence= length(sequence);

OnePeriodSequence=reshape((sequence'*HelpMatrix1)',1,NumSampleProBit*N
umBitSequence);
SequenceTx=repmat(OnePeriodSequence,1,floor(length(timeaxis)/length(On
ePeriodSequence)));
SequenceTx=horzcat(SequenceTx,OnePeriodSequence(1:round(mod(length(tim
eaxis),length(OnePeriodSequence)))));

SequenceRx=1-SequenceTx;
HelpMatrix2=horzcat(zeros(1,NumSampleProDelayTx),ones(1,round(NumSampl
eProBit-NumSampleProDelayTx-
NumSampleProDelayRx)),zeros(1,NumSampleProDelayRx));
OnePeriodMask=reshape((ones(NumBitSequence,1)*HelpMatrix2)',1,NumSampl
eProBit*NumBitSequence);
MaskRx=repmat(OnePeriodMask,1,floor(length(timeaxis)/length(OnePeriodM
ask)));
MaskRx=horzcat(MaskRx,OnePeriodMask(1:round(mod(length(timeaxis),lengt
h(OnePeriodMask))) ));
SequenceRx=SequenceRx.*MaskRx;

% APPLICATION OF THE GATING SEQUENCE TO THE DATA
if SequenceType == 0
    data_diff_cos_g=data_diff_cos;
    data_diff_sin_g=data_diff_sin;
    excit_cos_g=excit_cos;
    excit_sin_g=excit_sin;
```

```
    disp('You chose to apply no gating functions');
else
for n=1:1:length(zr)
for index=1:1:length(yr)
    data_diff_cos_g(:,index,n)=data_diff_cos(:,index,n).*SequenceRx';
    data_diff_sin_g(:,index,n)=data_diff_sin(:,index,n).*SequenceRx';
end
end
excit_cos_g=excit_cos.*SequenceTx';
excit_sin_g=excit_sin.*SequenceTx';
disp('Finished to apply the gating functions');
end


% PLOT THE MRS OF THE SEQUENCE
MRP=corrc1(SequenceTx(1:NumSampleProBit*NumBitSequence),SequenceRx(1:N
umSampleProBit*NumBitSequence));
ax=linspace(0,NumBitSequence,NumBitSequence*NumSampleProBit);
figure;
subplot(2,1,1);
stairs(ax,SequenceTx(1:NumSampleProBit*NumBitSequence), 'linewidth',
2)
grid
ylim([-0.2 1.2]);
title('Gating sequence','FontSize',12);
xlabel('Bit','FontSize',12);
subplot(2,1,2)
plot(ax,10*log10(MRP.^0.5)-max(10*log10(abs(MRP.^0.5))),'linewidth',
2);
grid
ylim([-40 1]);
title('MRS of the sequence normalized in [dB]','FontSize',12);
xlabel('Bit','FontSize',12);
clear HelpMatrix1 HelpMatrix2 OnePeriodMask OnePeriodSequence ax
end
```

ImagingAlgorithm.m

```
function
[myimage]=ImagingAlgorithm(data_corr,delay,timeaxis,xp,yp,yr,zr)
% GUI to SELECT THE ALGORITHM
row1 = 'Select the imaging algorithm: 1 for BP - 2 for DSI - 3 for
DMSI - ';
row2 = 'Select whether activating the averaging: 0 for NO - 1 for
YES';
prompt= {row1,row2};
dlg_title = 'Imaging Algorithm';
def = {'1','0'};
answer = inputdlg(prompt,dlg_title,1,def,'on');
AlgType=str2double(answer{1});
AvgSelection=str2double(answer{2});

switch AlgType
    case 1 % Back Projection
        data_corr_avg_interpolated=[];
        data_avg_interpolated=[];
        data_avg=mean(data_corr,2);
        for n=1:1:length(yr)
```

```matlab
        for l=1:1:length(zr)

data_corr_avg_interpolated(:,:,l,n)=interp1(timeaxis,data_corr(:,n,l),
delay(:,:,l,n),'spline',0);

data_avg_interpolated(:,:,l,n)=interp1(timeaxis,data_avg(:,l),delay(:,
:,l,n),'spline',0);
        end
        end
        if AvgSelection == 1
            data_diff_interpolated=abs(data_corr_avg_interpolated)-
abs(data_avg_interpolated);%Remove the average from each response
            disp('Applied the averaging');
        else
            data_diff_interpolated=abs(data_corr_avg_interpolated);
        end
        myimage=flipdim(sum(sum(data_diff_interpolated,3),4),1);

    case 2 % Delay Sum Integration (DSI)
        myimage=[];
        data_temp=[];
        timestep=timeaxis(2);
        delay_s=ceil(delay.*(1/timestep));
        maxdel=max(max(max(max(delay_s))));
        npt=maxdel+ceil(2*0.5*1E9/(3E8*timestep));
        timeaxis=timeaxis(1:npt);
        rr=cumtrapz(timeaxis,real(data_corr(1:npt,:,:)));
        ii=cumtrapz(timeaxis,imag(data_corr(1:npt,:,:)));
        data_corr=abs(rr+1i*ii);
        data_avg=mean(data_corr,2);
        if AvgSelection == 1
            data_corr=abs(data_corr)-
abs(repmat(data_avg,1,size(data_corr,2)));
            disp('Applied the averaging');
        else
            data_corr=abs(data_corr);
        end
        integrlength=ceil((1/1.5).*(1/timestep));
        disp('For loops begun for DSI - It might take long')
        for l=1:1:length(yp)
            for m=1:1:length(xp)
                for n=1:1:length(zr)
                    for k=1:1:length(yr)
                     tau=cast(length(data_corr(:,k,n))-
delay_s(l,m,n,k),'double');
                        data_temp(:,k,n)=circshift(data_corr(:,k,n),tau);
                    end
                end
            data_temp_sum=sum((sum(data_temp,3)),2).^2;
            myimage(l,m,n,k)=timestep*1E-
9*trapz(data_temp_sum(1:integrlength));
            end
         disp(num2str(l))
        end
        myimage=flipdim(sum(sum(myimage,3),4),1);

    case 3 % Delay Multiply Sum Integration (DMSI)
        myimage=[];
        data_temp=[];
```

```
        timestep=timeaxis(2);
        delay_s=ceil(delay.*(1/timestep));
        maxdel=max(max(max(delay_s)));
        npt=maxdel+ceil(2*0.5*1E9/(3E8*timestep));
        timeaxis=timeaxis(1:npt);
        rr=cumtrapz(timeaxis,real(data_corr(1:npt,:)));
        ii=cumtrapz(timeaxis,imag(data_corr(1:npt,:)));
        data_corr=abs(rr+1i*ii);
        data_avg=mean(data_corr,2);
        if AvgSelection == 1
            data_corr=abs(data_corr)-
abs(repmat(data_avg,1,size(data_corr,2)));
            disp('Applied the averaging');
        else
            data_corr=abs(data_corr);
        end
        integrlength=ceil((1/1.5).*(1/timestep));
        disp('For loops begun for DMSI - It might take long')
        for l=1:1:length(yp)
            for m=1:1:length(xp)
               for n=1:1:length(zr)
                   for k=1:1:length(yr)
                     tau=cast(length(data_corr(:,k))-
delay_s(l,m,n,k),'double');
                       data_temp(:,k)=circshift(data_corr(:,k),tau);
                   end
               end
            data_temp_sum=zeros(size(data_temp,1),1);
            for ff=1:1:size(data_temp,2)-1
                for gg=(ff+1):1:size(data_temp,2)

data_temp_sum=data_temp_sum+data_temp(:,ff).*data_temp(:,gg);
                end
            end
           myimage(l,m,n,k)=timestep*1E-
9*trapz(data_temp_sum(1:integrlength));
            end
          disp(num2str(l))
        end
        myimage=flipdim(sum(sum(myimage,3),4),1);
end
end
```

corrc1.m

```
function [ex1] = corrc1 (o, t)
o1= fft(o);
o2 = fft(t);
ex = o1.*conj(o2);
ex1 = ifft(ex);
ex1  = abs(ex1);
[n m] = size(t);
ex1 = ex1.^2;
ex1 = ex1/(m ^2);
```

Appendix 1.2: MATLAB program to generate waveforms for the AWG

This script creates the FMCW-FMICW waveform which is then loaded into the AWG to generate the transmitted signal and its replica to drive the mixer at the receiver; the user can select the desired parameters through a graphical interface.

MyUserDefinedChirp.m

```
% This program generates a user defined excitation for Euvis AWG 801
% Two UDA files are therefore written running this script
%%%%%%%%%%%%%%%%%%%%%%%%%%%%%%%%%%%%%%%%%%%%%%%%%%%%%%%%%%%%%%%%%%%%%%%%

% GUI TO INSERT PARAMETERS OF THE FMCW-FMICW CHIRP
row1 = 'Enter start frequency [Hz]';
row2 = 'Enter bandwidth [Hz]';
row3 = 'Enter Duration [s] (Max 0.98ms)';
row4 = 'Choose the gating sequence: 0 NoGating - 1 SquareWave - 2
Barry - 3 Salous-Nattour - 4 Msequence';
row5 = 'Enter bit duration for gating sequence [s]';
row6 = 'Enter delay 1 between TX and RX gating sequences [s]';
row7 = 'Enter delay 2 between TX and RX gating sequences [s]';
row8 = 'Enter directory which the file is saved in (Use double \\ for
C++ compatibility)';
row9 = 'Window to multiply your chirp: 0 No Window - 1 Kaiser B=6 - 2
Kaiser B=4 - 3 Hamming';

prompt= {row1,row2,row3,row4,row5,row6,row7,row8,row9};
dlg_title = 'Select the parameters for your chirp';
num_lines = 1;
def = {'0.7e9','1.5e9','400e-6','0','1e-9','0e-9','0e-
9','C:\\Documents and Settings\\cvxl66\\Desktop\\','0'};
answer = inputdlg(prompt,dlg_title,num_lines,def);

fstart=str2double(answer{1});
B=str2double(answer{2});
T=str2double(answer{3});
SequenceType=str2double(answer{4});
BitDuration=str2double(answer{5});
DelayTxDuration=str2double(answer{6});
DelayRxDuration=str2double(answer{7});
filedirectory=answer{8};
WindowType=str2double(answer{9});
Tbis=T*1e6;
Bbis=B/1e9;

if SequenceType == 4
rowMseq = {'Choose the number of bit for M-sequence (format 2^(N)-
1)'};
answer2 = inputdlg(rowMseq,'M-sequence Details',1,{'3'});
MSeqCoeff=str2double(answer2{1});
end;
clear row0 row1 row2 row3 row4 row5 row6 prompt rowMseq def answer
answer2
```

```matlab
% DEFINITION OF THE CHIRP
Fs = 8e9;                        % Sampling frequency 8 [Gsps] for AWG 801
timestep = 1/Fs;
L = round(T/timestep);
t = (0:L-1)*timestep;
x=cos(2*pi*fstart.*t+pi*(B/T).*t.^2);


% INVERSE SINC FILTER
% This inverse filter is applied via software in order to get a flat
% spectrum at the output of the AWG (it compensates the decaying trend
% that normally the output of AWG presents
NFFT=L;
X = fft(x,NFFT)/L;
f = Fs/2*linspace(0,1,NFFT/2);
% A frequency FACTOR F=1.5 gives good output (see Euvis manual)
filt_pos=1./sinc(1.5.*f./8e9);
% filt_pos=ones(1,length(f)); % Optional to disable the inverse filter
filt_neg=fliplr(filt_pos);
filt_all=horzcat(filt_pos,filt_neg);
X_filtered=X.*(filt_all+1i);
x_filtered=real(ifft(X_filtered).*L);


% OPTIONAL WINDOWING
switch WindowType
    case 0
        w = ones(L,1);       % No windowing
    case 1
        w = kaiser(L,6);     %Kaiser with Beta 6
    case 2
        w = kaiser(L,4);     %Kaiser with Beta 4
    case 3
        w = hamming(L);      %Hamming
end
y=x_filtered.*w';


% GATING SEQUENCES PART
switch SequenceType
    case 0
        sequence = [1];
    case 1
        sequence = [1 0]; %Square Wave
    case 2
        sequence = [1 1 0 0 0 1 1 1 1 0 0 0 0 0 0 0]; %Barry
    case 3
        sequence = [1 1 1 0 0 0 1 1 1 1 1 1 0 0 0 0 0 0 0 0]; %Salous-
Nattour
    case 4
        sequenceM=mseq(2,log2(MSeqCoeff+1)); %Msequence
        for k=1:1:length(sequenceM)
        if sequenceM(k) ~= 1
        sequenceM(k)=0;
        end
        end
        sequence=sequenceM';
end

NumSampleProBit=round(BitDuration/timestep);
NumSampleProDelayTx=round(DelayTxDuration/timestep);
```

```
NumSampleProDelayRx=round(DelayRxDuration/timestep);
NumBitSequence= length(sequence);
HelpMatrix1=ones(1,NumSampleProBit);

OnePeriodSequence=reshape((sequence'*HelpMatrix1)',1,NumSampleProBit*N
umBitSequence);
SequenceTx=repmat(OnePeriodSequence,1,floor(L/length(OnePeriodSequence
)));
SequenceTx=horzcat(SequenceTx,OnePeriodSequence(1:round(mod(L,length(O
nePeriodSequence)))));

SequenceRx=1-SequenceTx;
HelpMatrix2=horzcat(zeros(1,NumSampleProDelayTx),ones(1,round(NumSampl
eProBit-NumSampleProDelayTx-
NumSampleProDelayRx)),zeros(1,NumSampleProDelayRx));
OnePeriodMask=reshape((ones(NumBitSequence,1)*HelpMatrix2)',1,NumSampl
eProBit*NumBitSequence);
MaskRx=repmat(OnePeriodMask,1,floor(L/length(OnePeriodMask)));
MaskRx=horzcat(MaskRx,OnePeriodMask(1:round(mod(L,length(OnePeriodMask
))) ));
SequenceRx=SequenceRx.*MaskRx;

if SequenceType == 0
    yTX_gated_del=y;
    yRX_gated_del=y;
else
yTX_gated_del=y.*SequenceTx;
yRX_gated_del=y.*SequenceRx;
end

Ldel = round(zeroeslength/timestep);
zerostring = zeros(1, Ldel);
yTX_gated = horzcat(zerostring,yTX_gated_del);
yRX_gated = yRX_gated_del;

clear HelpMatrix1 HelpMatrix2 OnePeriodMask OnePeriodSequence
SequenceTx SequenceRx MaskRx X x X_filtered x_filtered
clear filt_pos filt_neg filt_all w y

% MARKERS GENERATION
marker1 = horzcat(ones(1, round(100e-9/timestep)), zeros(1, L+Ldel-
round(100e-9/timestep)));
marker2 = horzcat(ones(1, round(5000e-9/timestep)), zeros(1, L+Ldel-
round(5000e-9/timestep)));
marker3 = horzcat(zeros(1, L+Ldel-round(4000e-9/timestep)), ones(1,
round(3999.75e-9/timestep)), 0, 0);
marker11 = marker1 + bitshift(marker2,1) + bitshift(marker3,2);
clear  marker1 marker2 marker3

% WRITE the TX DATA FILE
fullscale = hex2dec('FD0');
z1TX = round( fullscale * (yTX_gated - min(yTX_gated)) /
(max(yTX_gated)-min(yTX_gated)) );
udacontentsTX = [z1TX; marker11; (0:L+Ldel-1)];
filenameTX=horzcat('MyTXChirp_BW',num2str(B/1e9),'GHz_T',num2str(round
(T*1e6)),'us_Gated',num2str(length(sequence)),'bit_',num2str(BitDurati
on*1e9),'nsBitDuration');
filepathTX=horzcat(filedirectory,filenameTX,'.uda');
```

```
fid = fopen (filepathTX,'wt');
count = fprintf(fid, ';---- User-Defined file generated in Matlab\n');
count = fprintf(fid, '#type=5\n');
count = fprintf(fid, '#hex=1\n');
count = fprintf(fid, ';---- User-Defined file data and marker
contents\n');
count = fprintf(fid, '%03X %1o\t; [%6d]\n', udacontentsTX);
fclose (fid);
clear udacontentsTX z1TX
% WRITE the RX DATA FILE
fullscale = hex2dec('FD0');
z1RX = round( fullscale * (yRX_gated - min(yRX_gated)) /
(max(yRX_gated)-min(yRX_gated)) );
udacontentsRX = [z1RX; marker11(1,1:length(marker11)-Ldel); (0:L-1)];
filenameRX=horzcat('MyRXChirp_BW',num2str(B/1e9),'GHz_T',num2str(round
(T*1e6)),'us_Gated',num2str(length(sequence)),'bit_',num2str(BitDurati
on*1e9),'nsBitDuration');
filepathRX=horzcat(filedirectory,filenameRX,'.uda');
fid = fopen (filepathRX,'wt');
count = fprintf(fid, ';---- User-Defined file generated in Matlab\n');
count = fprintf(fid, '#type=5\n');
count = fprintf(fid, '#hex=1\n');
count = fprintf(fid, ';---- User-Defined file data and marker
contents\n');
count = fprintf(fid, '%03X %1o\t; [%6d]\n', udacontentsRX);
fclose (fid);
clear marker1 udacontentsRX  z1RX
%%%%%%%%%%%%%%%%%%%%%%%%%%%%%%%%%%%%%%%%%%%%%%%%%%%%%%%%%%%%%%%%%%%%%%%%%

figure;
plot(real(yTX_gated));
title('Signal in Time Domain')
xlabel('Samples')
grid
axis tight;
Y = fft(yTX_gated,NFFT)/(L);
figure;
semilogy(f/1e9,2*abs(Y(1:(NFFT)/2)))
axis([ 0, Fs/2e9, 1e-4, 0.1 ]);
title('Single-Sided Amplitude Spectrum of y(t)')
xlabel('Frequency (GHz)')
ylabel('|Y(f)|')
```

Appendix 1.3: MATLAB programs to process experimental data

This script load the data recorded by the ADC after performing measurements and applies the double FFT processing discussed in chapter 3 in order to extract the range profile and the Delay-Doppler pattern.

MySignatecReader.m

```
Tch= 400e-6; %Chirp Duration
BW= 1.5e9; %Chirp Bandwidth
Fsam=20e6; %Sampling frequency of ADC
```

```matlab
filename=horzcat('C:\Users\PC\Desktop\Tests Euvis Aug 10th\Data Nov
19th&Following\Data Mar 22nd 2013\FMICW MeHold 20s');
filename = [filename '.rd16'];
fid=fopen(filename);
rawdata = fread(fid,'uint16');
fclose(fid);


ch1data= rawdata(1:2:length(rawdata));
ch2data= rawdata(2:2:length(rawdata));
%Convert data values
R=2.2; %This is the pk-pk range in the ADC
if ch1data>=32768;
    ch1data = (R/2) + ((ch1data/65532)*R);
else ch1data = (-R/2) + ((ch1data/65532)*R);
end;
if ch2data>=32768;
    ch2data = (R/2) + ((ch2data/65532)*R);
else
    ch2data = (-R/2) + ((ch2data/65532)*R);
end;



SegSize=Fsam*500e-6;
BeginSize=1;
EndSize=2060-1;
ch2data = ch2data(1:end);
for k=1:floor(length(ch2data)/SegSize)-1
    ch2dataTime(:,k)=ch2data(BeginSize+SegSize*(k-1):SegSize*(k)-
EndSize);
end


figure
numofsample= 300;
stem(ch2dataTime(1:numofsample,:))
title(horzcat('First ', num2str(numofsample), ' samples of each
sweep'), 'FontSize', 16)
xlabel('Samples', 'FontSize', 16)
set(gca, 'FontSize', 16);
grid


NFFT = 2^nextpow2(size(ch2dataTime,1));
win = repmat(hamming(size(ch2dataTime,1)),1,size(ch2dataTime,2));
ch2dataFreq= fft(ch2dataTime.*win,NFFT);
ch2dataFreq=ch2dataFreq(1:round(size(ch2dataFreq,1)/2-1),:);
freqaxis=linspace(0,Fsam/2,size(ch2dataFreq,1));
figure
plot(freqaxis./1e6,20*log10(mean(abs(ch2dataFreq')))-
max(20*log10(mean(abs(ch2dataFreq')))),'k');
title('Average FFT of each sweep [dB] - Hamming win', 'FontSize', 16)
xlabel('Frequency [MHz]', 'FontSize', 16)
axis([0.05 0.15 -40 5])
set(gca, 'FontSize', 16);
grid



% Optional part to apply change detection when computing Delay-Doppler
% ch2dataFreqShift=circshift(ch2dataFreq,[0 1]);
% ch2dataFreq=ch2dataFreq-ch2dataFreqShift;
```

```matlab
ch2dataFreqAll=ch2dataFreq;
% Optional to process a sub-period of data in case
ch2dataFreq=ch2dataFreqAll(:,1:end);
ch2dataFreq=ch2dataFreq';
[NSweeps,NFreqBins] = size(ch2dataFreq);


win=hamming(NSweeps);
for k=1:1:NFreqBins
    ch2dataFreq(:,k)=ch2dataFreq(:,k).*win;
end
ch2dataDoppler=fft(ch2dataFreq);
ch2dataDoppler=ch2dataDoppler./max(max(ch2dataDoppler));
ch2dataDoppler=20*log10(abs(ch2dataDoppler));
for k=1:1:NFreqBins
    ch2dataDoppler(:,k)=fftshift(ch2dataDoppler(:,k));
end


figure;
delaxisdopp = freqaxis.*Tch/BW*1e9;
doppleraxis=(-size(ch2dataDoppler,1)/2:size(ch2dataDoppler,1)/2-
1)*(1/Tch)/size(ch2dataDoppler,1);
DoppAxisParam = 60;
ch2dataDoppler=ch2dataDoppler(round(length(doppleraxis)/2)-
DoppAxisParam:round(length(doppleraxis)/2)+DoppAxisParam,1:75);
ch2dataDoppler=ch2dataDoppler-max(max(ch2dataDoppler));
contour( delaxisdopp(1:75),doppleraxis(round(length(doppleraxis)/2)-
DoppAxisParam:round(length(doppleraxis)/2)+DoppAxisParam),ch2dataDoppl
er )
grid
xlabel('Delay [ns]', 'FontSize', 14)
ylabel('Doppler [Hz]', 'FontSize', 14)
set(gca, 'FontSize', 14);
```

Appendix 2: VERILOG program to generate trigger signals

This VERILOG code is used to program the FPGA chip in order to divide the SYNCO signals from the AWG and generate the triggers signals accordingly; in this example the SYNCO signals at 125 MHz are divided down to 2 kHz, corresponding to 500 μs period for the trigger signals. This program can be used as source file to generate the actual files to be loaded into the FPGA through the software suite QUARTUS from Altera.

TriggerGeneration.v

```
//Code for trigger generation
module TimeSyncAdnan(  clk,triggerOut, temp, temp2, temp3, clkdiv,
clk2n, triggerOut2n, temp2n, temp22n, temp32n, clkdiv2n);

input clk, clk2n;
output triggerOut, temp, temp2, temp3, clkdiv, clkdiv2n, triggerOut2n,
temp2n, temp22n, temp32n, clkdiv2n;

reg triggerOut, triggerOut2n, clkdiv ;
reg temp, temp2, temp3, temp2n, temp22n, temp32n ;

integer dcountr, dcountr2n ;

initial
begin
triggerOut = 1'b0 ;
temp = triggerOut ;
clkdiv = 1'b0 ;
triggerOut2n = 1'b0 ;
temp2n = triggerOut2n ;
clkdiv2n = 1'b0 ;
end

      always @ (posedge clk) // activate at the positive edge of the
input clock
      begin

      dcountr = dcountr + 1 ;

            if ( dcountr == 62500/2) //at half desired period change
the level of triggerOut
            begin
            triggerOut = 1'b1;
//          temp = triggerOut ;
//          temp2 = triggerOut ;
//          temp3 = triggerOut ;
            end

            if ( dcountr == 62500 ) //at the desired period change the
level of triggerOut again...
            begin
```

```
               triggerOut = 1'b0;
//             temp = triggerOut ;
//             temp2 = triggerOut ;
//             temp3 = triggerOut ;
               dcountr = 0; //... and reset the counter
               end

 clkdiv = ~clkdiv;
       end

//Part for the D flip flop as suggested by Euvis support
always @ (negedge clk )
begin
      temp = triggerOut;
      temp2 = triggerOut ;
      temp3 = triggerOut ;
end




// Replica for the division of the second input clock
      always @ (posedge clk2n)
      begin

      dcountr2n = dcountr2n + 1 ;

            if ( dcountr2n == 62500 /2)
            begin
            triggerOut2n = 1'b1;
//          temp2n = triggerOut2n ;
//          temp22n = triggerOut2n ;
//          temp32n = triggerOut2n ;
            end

            if ( dcountr2n == 62500 )
            begin
            triggerOut2n = 1'b0;
//          temp2n = triggerOut2n ;
//          temp22n = triggerOut2n ;
//          temp32n = triggerOut2n ;
            dcountr2n = 0;
            end

 clkdiv2n = ~clkdiv2n;
       end

//Part for the D flip flop as suggested by Euvis support
always @ (negedge clk2n)
begin
      temp2n = triggerOut2n;
      temp22n = triggerOut2n ;
      temp32n = triggerOut2n ;
end


endmodule
```

Appendix 3: C++ program to control the AWG

This C++ program controls the AWG while performing measurements. Initially this program calls MATLAB and runs the script presented in appendix 1.2 to generate files with the values of the desired waveform. Then the AWG are initialized and accordingly set to load these files and wait for trigger signals to actually generate the waveform. The user can dynamically recall MATLAB and generate new waveforms, which is particularly flexible to change some parameters of the FMICW waveform.

MyEuvis_32bitSystems_Chirp1Sweep

```cpp
#include "stdafx.h"
#include <stdio.h>
#include <stdlib.h>
#include <string.h>
#include <windows.h>

#include <engine.h>
#include "matrix.h"

using  namespace      MOL;
using  namespace      MOL::AWG;
using  namespace       System::Threading;
using                 System::String;

#include "ftd2xx.h"
#pragma comment(lib, "FTD2XX.lib")


int main()
{
        int mempage;
        for (mempage=0; mempage>=0; mempage++) {

        Engine *ep;
        ep = engOpen(NULL);
        if (ep == NULL)
        {printf("Error: not found");}

        printf("MATLAB script begun\n");
        engEvalString(ep, "MyUserDefinedChirp");
        printf("MATLAB script finished\n");
        Sleep(7000);

        mxArray *MyArray1 = NULL, *MyArray2 = NULL, *MyArray3 = NULL;
        MyArray1 = engGetVariable(ep, "filepathTX");
        MyArray2 = engGetVariable(ep, "filepathRX");
        if (MyArray1 == NULL || MyArray2 == NULL)
        {printf("\nError: MATLAB had problems in writing the files... you should
stop!\n");}

        char *filepathTX, *filepathRX;
        double* chirpdur;
        filepathTX = mxArrayToString(MyArray1);
```

```cpp
    filepathRX = mxArrayToString(MyArray2);
    MyArray3 = engGetVariable(ep, "Tbis");
    chirpdur = (double *) mxGetPr(MyArray3);
    printf("Value of chirp duration is %f [us]\n\n", *chirpdur);

    mxDestroyArray(MyArray1);
    mxDestroyArray(MyArray2);
    mxDestroyArray(MyArray3);
    engClose(ep);
    ///////////////////////////// End part to call MATLAB


AWG_Group_API    awg_group;
    AWG_API                     awg30;
    AWG_API                     awg25;

    //---- Check if there is at least one AWG module connected
    if( awg_group.number == 0 )
    {printf( "No Euvis Module Exists:error, close the program!\n" );}
    else
    {printf("\nFound %d devices\n", awg_group.number);}

    //---- Get the module series number for both AWG801 SN 25 and 30
    int    SeriesNumber1 = awg_group.get_sn(0);
    if (SeriesNumber1 == 30)
    {printf("Found Device with SN: %d\n", SeriesNumber1);}
    else
    {SeriesNumber1 = awg_group.get_sn(1);
    if (SeriesNumber1 == 25)
    {printf("Found Device with SN: %d\n", SeriesNumber1);}
    else
    {printf("No AWG Board 30 has been found!\n");}
    }
    int    SeriesNumber2 = awg_group.get_sn(1);
    if (SeriesNumber2 == 25)
    {printf("Found Device with SN: %d\n", SeriesNumber2);}
    else
    {SeriesNumber2 = awg_group.get_sn(0);
    if (SeriesNumber2 == 25)
    {printf("Found Device with SN: %d\n", SeriesNumber2);}
    else
    {printf("No AWG Board 25 has been found!\n");}
    }

//--- Initialize the AWG
    if (SeriesNumber1 == 30)
    {awg30.ini( SeriesNumber1);
    printf( "Module %d initialized\n", SeriesNumber1);
    printf( "Module model id: %X and model name: %s\n\n", awg30.module_id_number,
awg30.module_name);}
    if (SeriesNumber2 ==25)
    {awg25.ini( SeriesNumber2);
    printf( "Module %d initialized\n", SeriesNumber2);
    printf( "Module model id: %X and model name: %s\n\n", awg25.module_id_number,
awg25.module_name);}

    //--- AWG ID Check
    if( SeriesNumber2 == 25 && awg25.module_id_number != (unsigned)
MODULE_ID::AWG801)
    {
```

```
        printf( "Wrong Module for Series Number 25!\n" );
        return 1;
    }
    if ( SeriesNumber1 == 30 && awg30.module_id_number != (unsigned)
MODULE_ID::AWG801 )
    {       printf( "Wrong Module for Series Number 30!\n" );
        return 1;
    }

    //--- Initialize AWG signature
    awg25.signature_ini( );
    awg30.signature_ini( );

    //--- Set the clock frequency
    awg25.Clock_Frequency = 4e9;
    awg30.Clock_Frequency = 4e9;

    //--- Select one sweep to be generated for each trigger event
    int SweepNum25=1, SweepNum30=1;
    awg25.loop_count = SweepNum25;
    awg30.loop_count = SweepNum30;
    printf ("\nYou have chosen %d sweep per trigger for both waveform
generators\n", SweepNum25);

    int NumOfPoints25 = 0;
    int NumOfPoints30 = 0;
    String^ filepathTX2 = gcnew String(filepathTX);
    String^ filepathRX2 = gcnew String(filepathRX);

    NumOfPoints25 = awg25.user_define_file(filepathTX2, 4e9);
    NumOfPoints30 = awg30.user_define_file(filepathRX2, 4e9);
    printf("\nThe file for AWG801-25 has %x points. If 0, you've got problems!\n",
NumOfPoints25);
    printf("The file for AWG801-30 has %x points. If 0, you've got problems!\n",
NumOfPoints30);

    //--- Set data length to number of points from user_define_file method
    awg25.data_length = NumOfPoints25;
    awg30.data_length = NumOfPoints30;

    //--- Set waveform code to user-defined file
    awg25.code = (unsigned) WAVEFORM_CODE::USER_DEFINED;
    awg30.code = (unsigned) WAVEFORM_CODE::USER_DEFINED;

    //--- Download the waveform to module
    if (SeriesNumber2 == 25) {
    awg25.user_page = mempage;
    awg25.stop();
    printf( "Downloading on AWG-25 mem page %d...\n", mempage );
    awg25.download();
    printf( "Download Done!!\n" );
    awg25.user_page = mempage;
    awg25.stop();
    awg25.flush();}

    if (SeriesNumber1 == 30) {
    awg30.user_page = mempage;
    awg30.stop();
    printf( "Downloading on AWG-30 mem page %d ...\n", mempage );
    awg30.download();
```

```
printf( "Download Done!!\n" );
awg30.user_page = mempage;
awg30.stop();
awg30.flush();}


int myflag=2; //just a flag to keep the do-while loop running

do {
//--- Arm the AWG: they are waiting for a trigger signal
if (SeriesNumber2 == 25) {
awg25.arm();
printf("\nBoard AWG801-25 waiting for trigger\n");
}
if (SeriesNumber1 == 30) {
awg30.arm();
printf("\nBoard AWG801-30 waiting for trigger\n\n");
}

//--- Scanf put the system on hold until the user decides if changing waveform
int stopsweep = 0;
printf("Insert 1 to stop sweeping; decide whether you want to change
waveform\n");
scanf("%d", &stopsweep);
if (stopsweep == 1)
{printf("Sweep is stopped\n");
if (SeriesNumber2 == 25) {
awg25.stop();
awg25.flush();
awg25.arm();}
if (SeriesNumber1 == 30) {
awg30.stop();
awg30.flush();
awg30.arm();}
}
Sleep(2000);

int wfselect;
printf("Would you like to keep this waveform? YES insert 0, NO insert 1\n");
scanf("%d", &wfselect);
if (wfselect == 0) { //if keeping the waveform just short pause and loop again
Sleep(1000);}
else {
        myflag = -1; //this breaks the do-while loop
        printf("Reloading MATLAB to create new waveform\n");
        } //end else
} // end of the do section

while (myflag >0);

if(mempage>=9)
{mempage=0;}
}//end of the big for loop
```

Appendix 4: Step-by step guide for measurements

This appendix is meant to be a sort of simple step-by-step guide for inexperienced users who approach the through-wall radar system described in this thesis. A list of steps to perform measurements is given, assuming that the system is located at the intended position and with every component correctly interconnected.

The manuals contain additional information on the interfaces of the AWGs (http://www.euvis.com/products/mod/awg/awg801.html) and on those of the ADC (http://www.signatec.com/products/pdf/Signatec-PCIe-Digitizer-PX14400A-Data-Sheet.pdf).

1. Switch on the rubidium clock module and wait until all the LEDs on the front panel are green, meaning that the output waveforms are correctly locked and stable.

2. Switch on the power supply (12 V) for the phased-locked-loop modules generating the 4 GHz clock for the AWGs. They may need some time to be ready and stable, especially if the environment is cold (as a rule of thumb they are ready when the total current absorption for both units is around 700 mA).

3. Switch on the two AWGs. They output a 125 MHz sine wave if they are working correctly.

4. Run the C++ program to load the desired waveform into the AWGs.

5. Provide 5 V to the FPGA board to start the generation of the trigger signals for the AWGs, and therefore the measurement.

6. Record and save the data using the ADC, which is also triggered from the FPGA board. MATLAB can be used to process the data or more data can be recorded at different positions.

7. The parameters of the waveforms can be changed by following the instructions on the C++ program, which reloads the new waveforms into the AWGs.

There may be now and then a synchronization problem caused by the way the AWGs lock to the 4 GHz clock. The overall effect of this issue is the jittering in the beat-note signal at the receiver, which can be observed using an oscilloscope which is triggered by the same trigger signal for the ADC. This jittering produces artefacts in the Delay-Doppler pattern as if there were moving targets, even if the measurement is taken in an empty scenario or it is a back-to-back configuration.

This problem can be solved by changing some internal parameters of the AWGs, as described in details in the application note "*Adjusting the AWG Timing Signature*" released by Euvis. Here we describe shortly the steps, assuming to check the beat-note signal on the oscilloscope during the procedure.

1. Open the graphical interface for both AWGs.

2. Type "*TCV enabled*" in the CMD text box. Go to the "Signature" section of the interface and tick "Writable" to allow modifications of the TV parameters.

3. The only parameter of interest for the jittering problem is TV0, which can be adjusted separately for both units until the jittering is no longer seen on the oscilloscope trace. The new values of the TV0 parameter can be saved by clicking on "Record Signature".

Appendix 5: Publications and other outputs

- F.Fioranelli, S.Salous, and X.Raimundo, "Frequency modulated interrupted continuous wave as wall removal technique in through-the-wall imaging", submitted to IEEE Transactions on Geoscience and Remote Sensing and accepted for publication in the next available issue.

- F.Fioranelli, S. Salous, and I. Ndip, "Optimized patch-like antennas for through the wall radar imaging and preliminary results with frequency modulated interrupted continuous wave", presented at International Symposium on Signals, Systems, and Electronics (ISSSE), Potsdam, Germany, October 2012.

- F. Fioranelli, S. Salous, and X. Raimundo, "Through-the wall radar imaging using UWB signals", poster presented at the 2nd IET Technical Enterprise Workshop on "Today's RF Tomorrow's Medicine", Queen Mary University, London, February 2013.

- F. Fioranelli, "Through-the wall radar imaging using UWB signals", presented at Durham University Research Day, School of Engineering and Computing Sciences, December 2012

- F. Fioranelli, and S. Salous, "Through-the wall radar imaging using UWB signals", presented at UK URSI Festival of Radio Science, Durham University, April 2012

- F. Fioranelli, "Through-the wall detection using UWB signals", presented at Durham University Research Day, School of Engineering and Computing Sciences, June 2011

- F. Fioranelli, and S. Salous, "A review on through-the-wall radar: numerical simulations and imaging algorithms", presented at UK URSI Festival of Radio Science, University of Leicester, January 2011.